



Unione Europea



*Ministero dell'Istruzione,
dell'Università e della Ricerca*



Università degli Studi di Salerno

DIPARTIMENTO DI INGEGNERIA INDUSTRIALE

Dottorato di Ricerca in Ingegneria Meccanica

XII Ciclo N.S. (2011-2013)

***“Advances in lubrication technology and
modelling”***

***Novel nanoscale friction modifiers - Piezoviscosity effect in
EHL contacts***

Ing. Vincenzo Petrone

Tutor:

Ch.mo Prof. Vincenzo D'Agostino

Coordinatore:

Ch.mo Prof. Vincenzo Sergi

THANKS TO

Eccomi di nuovo giunto alla fine di un percorso di studi ma soprattutto di crescita personale e scientifica, percorso che non sarei stato in grado intraprendere e concludere senza il contributo di alcune persone alle quali sento il bisogno di esprimere la mia più sincera gratitudine.

In primis il mio Tutor, il Prof. D'Agostino, verso il quale sento di voler esprimere il mio più profondo riconoscimento e ringraziamento. Nel corso degli anni trascorsi insieme è stato una guida non solo accademica e scientifica ma anche e soprattutto una figura "paterna" cui potermi rivolgere in ogni occasione e una bussola con cui orientarmi nelle scelte.

Un ringraziamento particolare deve andare al Prof. Senatore, nel tempo diventato semplicemente Adolfo. Lui per primo ha creduto in me, fin dalla tesi di primo livello, fino a quella magistrale ed oltre. Una persona con cui ho condiviso la passione per la ricerca scientifica, le idee, i successi, ed anche qualche buona birra a valle dei lavori di qualche conferenza di cui ho impagabili ricordi. E' per me diventato un amico e un importante punto di riferimento lavorativo cui debbo moltissimo.

Ringrazio anche il gruppo di Chimica Industriale, con cui ho condiviso parte della ricerca e che mi hanno fatto scoprire molto del mondo della Chimica. Sento di dover ringraziare, inoltre, il Prof. Mitjan Kalin e il gruppo di ricerca del Laboratory for Tribology and Interface Nanotechnology (TINT) di Ljubljana per la straordinaria esperienza e per l'enorme fiducia riposta in me e nel mio lavoro.

Ancora, sento di voler ringraziare gli amici e i colleghi che, seppur in tempi diversi, hanno contribuito al raggiungimento di questo obiettivo, contribuendo a rendere speciali gli anni universitari.

Lascio alla fine il ringraziamento più sentito, quello alla **mia famiglia**, che con il suo affetto, ha partecipato e partecipa al raggiungimento di tutti i miei traguardi professionali ma soprattutto umani. Ai miei genitori, che mai per un secondo mi hanno fatto mancare il loro supporto e il loro amore, con cui sento di dover dividere equamente tutti i risultati raggiunti come studente e come uomo. A mio fratello, da sempre preso a modello, perché intraprendere questo cammino di ricerca è stato anche voler seguire le sue orme. Leggere nei loro occhi quella impagabile espressione di felicità e soddisfazione che nel mio piccolo sento di avergli dato è il miglior titolo di cui possa fregiarmi. **GRAZIE.**

**“Chi non è disposto ad imparare per tutta la vita,
non ha imparato la cosa più grande”**

(R. Haak)

TABLE OF CONTENTS

LIST OF FIGURES	VI
LIST OF TABLES	XIV
INTRODUCTION	1

CHAPTER 1 Lubrication, nanoadditives and tools

1.1	Tribology: Friction and wear	7
1.2	Lubrication regimes	8
1.2.1	Boundary lubrication	9
1.2.2	Hydrodynamic lubrication	10
1.2.3	Elastohydrodynamic lubrication	12
1.2.4	Mixed lubrication	13
1.3	Stribeck curve	13
1.4	Nanoparticles as lubricant additives	15
1.5	Carbon based nanoadditives	16
1.5.1	Graphene and carbon nanotube	16
1.5.2	Fullerene C60	18
1.5.3	Lubrication mechanism of carbon-based additives	18
1.6	Nanoparticles of metal dichalcogenides	19
1.6.1	IF- MoS ₂ and IF- WS ₂	20
1.6.2	IF-MX ₂ nanoparticles: lubrication mechanism	24
1.7	Tools and methods	29
1.7.1	Friction test-Stribeck curve	30
1.7.2	Friction and wear in steady-state tests	34
1.7.3	Surface analysis	35
	References	37

CHAPTER 2 Nanoparticles as additives for lubricant

1.1	Inorganic Nanoadditives: IF-MoS ₂	43
2.1.1	The sample	45
2.1.2	Friction test—Stribeck curve	46
2.1.3	Friction and wear in steady-state tests	50
2.1.4	Comparison with base oil lubricant	58
2.1.4.1	Friction test—Stribeck curve	59
2.1.4.2	Friction and wear in steady-state tests	66
2.1.5	Numerical simulations	71
2.1.6	Conclusion	78
2.2	Rhenium doped fullerene-like MoS ₂ nanoparticles	80
2.2.1	Nanoparticles synthesis	80
2.2.1.1	Preparation of the Re doped molybdenum oxide	80
2.2.1.2	Determination of the rhenium content in the IF-MoS ₂ nanoparticles	81
2.2.1.3	Sedimentation experiments of the nanoparticles in PAO-4 oil	82
2.2.1.4	X-ray absorption spectroscopy measurements and analysis	83
2.2.2	Friction test-Stribeck curve	88
2.2.3	Friction and wear in steady-state tests	95
2.2.4	Surface analysis	100
2.2.5	Discussion	104
2.2.6	Conclusions	106
2.3	Organic nanoadditives: Graphene and graphite	107
2.3.1	Introduction	107
2.3.2	Nanosheets preparation and characterization	108
2.3.2.1	Materials	108
2.3.2.2	Characterization techniques	109
2.3.2.3	Tribological tests description	109
2.3.2.4	Graphite and GO characterization	110

2.3.3	Friction test—Stribeck curve	113
2.3.4	Friction and wear in steady-state tests	119
2.3.5	Surface analysis	125
2.3.5.1	Raman spectrum of the worn surface	125
2.3.5.2	Optical profiler of the rubbed surfaces	128
2.3.6	Discussion	130
	References	132

CHAPTER 3 Nanoparticles in lubricating greases

3.1	Introduction	139
3.2	Greases with nanosized inorganic based additives	141
3.2.1	Synthesis of 2D MS ₂ @oleylamine nanosheet crystals	143
3.2.2	Rheological characterization	144
3.2.3	Tribological tests	148
3.2.4	Tribological tests at Nanomaterials facilities on Rilub greases with 2 wt% MoS ₂ nanoparticles synthesized by Nano_Mates	157
3.2.5	Fretting test	159
3.2.6	Discussion on the greases formulated with nanosized inorganic based additives	162
3.3	greases with hybrid nanosheets of MoS ₂ on CNT	163
3.3.1	Experimental Section	163
3.3.1.1	Synthesis of carbon nanotubes	163
3.3.1.2	Preparation of OA@MoS ₂ -CNT nanocomposite	163
3.3.1.3	Preparation of OA@CNT-MoS ₂ nanocomposite	166
3.3.1.4	Preparation of nanoadditivated lubricant grease	166
3.3.1.5	Physico-chemical characterization	166
3.3.2	Results and discussion	167
3.3.2.1	X-ray diffraction analysis	167
3.3.2.2	Scanning electron microscopy analysis	168
3.3.2.3	Transmission electron microscopy analysis ³	170

3.3.2.4	TG-DTG-DSC-MS analysis	171
3.3.2.5	Raman spectroscopy analysis	175
3.3.2.6	Tribological characterization	175
3.3.2.7	Tribological results	176
	References	179

CHAPTER 4 Modelling Elastohydrodynamic lubrication: Piezoviscoisty and surface roughness

4.1	Introduction	185
4.2	History of EHL Research	186
4.3	Theoretical model	192
4.3.1	Solution Domain	192
4.3.2	The Reynolds Equation	193
4.3.3	The Film Thickness Equation	198
4.3.3.1	Line contact	198
4.3.3.2	Point contact	199
4.3.4	The load balance equation	199
4.3.5	Dimensionless Equations	199
4.3.6	Piezoviscous lubricant models	204
4.3.6.1	Barus model	204
4.3.6.2	Roelands model	204
4.3.6.3	Free-volume model	204
4.4	Numerical discretization	207
4.5	Numerical results	210
4.5.1	EHL line contact	210
4.5.2	EHL pint contact	213
4.5.2.1	Numerical results with Doolittle pressure viscosity model: Pressure distribution	217
4.5.2.2	Numerical results with Doolittle pressure-viscosity model: Film thickness	219
4.5.3	Discussion	225

4.6	The influence of the roughness parameters	226
4.6.1	Numerical results	227
4.6.2	Discussion	234
	Appendix A	235
	References	237

CHAPTER 5 Investigation on nanoparticle mechanical behaviour through finite element simulation

5.2.4	Introduction	243
5.2.1	Effect of pressure and shear on the structural behavior of MoS ₂ nanoparticles	245
5.2.2	Numerical model	245
5.2.3	Numerical simulated testing procedure	248
5.2.4	Comparison of the load at a nanoparticle in FEM simulation and loads in typical macroscopic tribological experiments	250
5.2.3	Numerical Results	251
5.2.4	Hollow-core MoS ₂ nanoparticle: Compression phase	251
5.2.4.1	Hollow-core MoS ₂ nanoparticle: shear phase	253
5.2.4.2	Full-core bulk MoS ₂ nanoparticle: Compression phase	255
5.2.4.3	Full-core bulk MoS ₂ nanoparticle: shear phase	256
5.2.4.4	Effect of nanoparticles structure (hollow-core vs. full-core) on their mechanical response to external loads	258
5.2.4.5	Friction behavior of hollow- and full-core nanoparticles	262
5.2.4.6	Analysis of the MoS ₂ nanoparticle deformation and motion behavior: the influence of a soft rough surface	266
5.3	Experimental simulation: Surfaces and nanoparticle	266
5.3.1	Numerical simulation testing procedure	268
5.3.2	Numerical results	268
5.3.3	Compression phase	268
5.3.3.1	Numerical results: shear phase	270
5.3.3.2	Comparison between rough and smooth surfaces	272

5.3.4	References	276
CHAPTER 6	Conclusion s	281
ANNEX A		285
	Papers on Journals and Conference Proceedings	

LIST OF FIGURES

- Fig. 0.1** - Physical-chemical system of a tribological pair
- Fig. 1.2** - Stribeck diagram for a generic coupling
- Fig. 1.3** - Graphene and SWNT
- Fig. 1.4** - Crystal structure of (a) SWCNT and (b) MWCNT
- Fig. 1.5** - Crystal structure of C60
- Fig. 1.6** - HRTEM images of IF-MoS₂ nanoparticles
- Fig. 1.7** - TEM images of a single IF-MoS₂ nanoparticle
- Fig. 1.8** - TEM images of IF-WS₂ nanoparticles
- Fig. 1.9** - The three main friction mechanism of multilayered IF-NO which are discussed in literature: rolling (a), sliding (b), and exfoliation (c). The bottom surface is stationary while the upper surface is moving to the left. The red mark is a point of reference.
- Fig. 1.10** - Possible tribochemical mechanism of IF-MoS₂ nanoparticles on steel surfaces
- Fig. 1.11** - Tribopair functional scheme. Different 3D view (a) and (b)
- Fig. 1.12** - (a) Wazau TRM 100 rotational tribometer; (b) triobological contact, (c) ball specimen and holder; (d) steel disk
- Fig. 1.13** - Graphs superposition: friction coefficient μ and sliding speed (vs) ramp.
- Fig. 1.14** - Hysteresis cycles in μ measuring for two tests.
- Fig. 1.15** - Confocal profiler Sensofar Neox PLu
- Fig. 2.1a** - Stribeck curve from the sweep test; p=1.17 GPa, T=25 °C
- Fig. 2.1b** - Stribeck curve from the sweep test; p=1.17 GPa, T=50 °C
- Fig. 2.1c** - Stribeck curve from the sweep test; p=1.17 GPa, T=80 °C
- Fig. 2.2a** - Stribeck curve from the sweep test; p=1.47 GPa, T=25 °C
- Fig. 2.2b** - Stribeck curve from the sweep test; p=1.47 GPa, T=50 °C
- Fig. 2.2c** - Stribeck curve from the sweep test; p=1.47 GPa, T=80 °C
- Fig. 2.3a** - Stribeck curve from the sweep test; p=1.68 GPa, T=25 °C
- Fig. 2.3b** - Stribeck curve from the sweep test; p=1.68 GPa, T=50 °C
- Fig. 2.3c** - Stribeck curve from the sweep test; p=1.68 GPa, T=80 °C

Fig. 2.4a - Evolution of friction coefficient, 1-hour test in boundary lubrication steady condition; $p=1.68$ GPa, $T=25$ °C, $v=5$ mm/s.

Fig. 2.4b - Evolution of friction coefficient, 1-hour test in boundary lubrication steady condition; $p=1.68$ GPa, $T=80$ °C, $v=5$ mm/s.

Fig. 2.4c - Evolution of friction coefficient, 1-hour test in mixed/EHL lubrication steady condition; $p=1.68$ GPa, $T=25$ °C, $v=0.5$ m/s.

Fig. 2.4d - Evolution of friction coefficient, 1-hour test in mixed/EHL lubrication steady condition; $p=1.68$ GPa, $T=80$ °C, $v=0.5$ m/s.

Fig. 2.5a - Friction coefficient in boundary regime ($v = 5$ mm/s; $p = 1.68$ GPa)

Fig. 2.5b - Wear scar diameter [μm] in boundary regime ($v = 5$ mm/s; $p = 1.68$ GPa)

Fig. 2.5c - Friction coefficient in mixed-EHL regime ($v = 0.5$ m/s; $p = 1.68$ GPa)

Fig. 2.5d - Wear scar diameter [μm] in mixed-EHL regime ($v = 0.5$ m/s; $p = 1.68$ GPa)

Fig. 2.6a - Stribeck curve from the sweep test for different contact pressures at $T=25$ °C

Fig. 2.6b - Stribeck curve from the sweep test for different contact pressures at $T=50$ °C

Fig. 2.6c - Stribeck curve from the sweep test for different contact pressures at $T=80$ °C

Fig. 2.6d - Stribeck curve from the sweep test for different temperatures at $p=1.17$ GPa

Fig. 2.6e - Stribeck curve from the sweep test for different temperatures at $p=1.47$ GPa

Fig. 2.6f - Stribeck curve from the sweep test for different temperatures at $p=1.68$ GPa

Fig. 2.7a - ARL1 Base oil and ARL1_E11_0.5 comparison at $p=1.17$ GPa, $T=25$ °C

Fig. 2.7b - ARL1 Base oil and ARL1_E11_0.5 comparison at $p=1.17$ GPa, $T=50$ °C

Fig. 2.7c - ARL1 Base oil and ARL1_E11_0.5 comparison at $p=1.17$ GPa, $T=80$ °C

Fig. 2.7d - ARL1 Base oil and ARL1_E11_0.5 comparison at $p=1.47$ GPa, $T=25$ °C

Fig. 2.7e - ARL1 Base oil and ARL1_E11_0.5 comparison at $p=1.47$ GPa, $T=50$ °C

Fig. 2.7f - ARL1 Base oil and ARL1_E11_0.5 comparison at $p=1.47$ GPa, $T=80$ °C

Fig. 2.7g - ARL1 Base oil and ARL1_E11_0.5 comparison at $p=1.68$ GPa, $T=25$ °C

Fig. 2.7h - ARL1 Base oil and ARL1_E11_0.5 comparison at $p=1.68$ GPa, $T=50$ °C

Fig. 2.7i - ARL1 Base oil and ARL1_E11_0.5 comparison at $p=1.68$ GPa, $T=80$ °C

Fig. 2.8a - Evolution of friction coefficient, 1-hour test in boundary lubrication steady condition; $p=1.68$ GPa, $T=25$ °C, $v=5$ mm/s.

Fig. 2.8b - Evolution of friction coefficient, 1-hour test in boundary lubrication steady condition; $p=1.68$ GPa, $T=80$ °C, $v=5$ mm/s.

Fig. 2.8c - Evolution of friction coefficient, 1-hour test in mixed/EHL lubrication steady condition; $p=1.68$ GPa, $T=25$ °C, $v=0.5$ m/s.

Fig. 2.8d - Evolution of friction coefficient, 1-hour test in mixed/EHL lubrication steady condition; $p=1.68$ GPa, $T=80$ °C, $v=0.5$ m/s.

Fig. 2.9 - Formulation of the sample ARL_N10_0.75

Fig. 2.10 - Structure of the Artificial Neural Network

Fig. 2.11a - Friction coefficient in boundary regime at 25 °C ($v = 5$ mm/s; $p = 1.68$ GPa)

Fig. 2.11b - Friction coefficient in boundary regime at 80 °C ($v = 5$ mm/s; $p = 1.68$ GPa)

Fig. 2.11c - Friction coefficient in Mixed/EHL regime at 80 °C ($v = 0.5$ m/s; $p = 1.68$ GPa)

Fig. 2.11d - Friction coefficient in Mixed/EHL regime at 80 °C ($v = 0.5$ m/s; $p = 1.68$ GPa)

Fig. 2.11e - Wear Scar Diameter in boundary regime at 25 °C ($v = 5$ mm/s; $p = 1.68$ GPa)

Fig. 2.11f - Wear Scar Diameter in boundary regime at 80 °C ($v = 5$ mm/s; $p = 1.68$ GPa)

Fig. 2.11g - Wear Scar Diameter in Mixed/EHL regime at 25 °C ($v = 0.5$ m/s; $p = 1.68$ GPa)

Fig. 2.11h - Wear Scar Diameter in Mixed/EHL regime at 80 °C ($v = 0.5$ m/s; $p = 1.68$ GPa)

Fig. 2.12 - Reactor for the preparation of the Re-doped molybdenum oxide

Fig. 2.13 - XRD patterns of IF-MoS₂ powder and Re-doped IF-MoS₂ powder

Fig. 2.14 - Optical microscopy image of through the bottom of the oil suspension 1 day after the initial mixing: a. Re doped IF-MoS₂ suspension; b. undoped IF-MoS₂. c. Sedimentation curve for the IF powder in PAO-4 oil (specific gravity- 0.86 g cm⁻³; viscosity- 0.027 Pa*s): black- undoped IF-MoS₂; purple- Re (0.12 at%) doped IF-MoS₂.

Fig. 2.15a - XANES and EXAFS data obtained for Re L₃ edge.

Fig. 2.15b - XANES and EXAFS data obtained for Mo K edge

Fig. 2.15c/d - Schematic of the nearest neighbor environment around Re in ReS₂ (left) and substituting for Mo in the MoS₂ (right) structures. Re is blue, Mo is green/blue and S is yellow

Fig. 2.15e - Frequency distribution of the bond lengths Re-S and Re-Re in the two models of Re environment: MoS₂ and ReS₂. The latter model has same number of Re-S bonds (6) but more broadly distributed, and the smaller number of Re-Mo bonds (3 vs 6) in the second nearest neighbor range, are also broadly distributed.

Fig. 2.16 - Typical high resolution scanning electron microscope (a) and transmission electron microscopy (b) image of Re:IF-MoS₂ NP. The interlayer spacing of the NP (0.624 nm) coincides with that of the undoped IF-MoS₂ NP (which is not much different from the values of the bulk material)

Fig. 2.17a - Stribeck curve from the sweep-speed test; $p=1.17$ GPa, $T=25$ °C

Fig. 2.17b - Stribeck curve from the sweep-speed test; $p=1.17$ GPa, $T=50$ °C

Fig. 2.17c - Stribeck curve from the sweep-speed test; $p=1.17$ GPa, $T=80$ °C

Fig. 2.18a - Stribeck curve from the sweep-speed test; $p=1.47$ GPa, $T=25$ °C

Fig. 2.18b - Stribeck curve from the sweep-speed test; $p=1.47$ GPa, $T=50$ °C

Fig. 2.18c - Stribeck curve from the sweep-speed test; $p=1.47$ GPa, $T=80$ °C

Fig. 2.19a - Stribeck curve from the sweep-speed test; $p=1.68$ GPa, $T=25$ °C

Fig. 2.19b - Stribeck curve from the sweep-speed test; $p=1.68$ GPa, $T=50$ °C

Fig. 2.19c - Stribeck curve from the sweep-speed test; $p=1.68$ GPa, $T=80$ °C

Fig. 2.20a - Evolution of friction coefficient; 1-hour test in boundary lubrication steady

condition; $p=1.68$ GPa, $T=25$ °C, $v=5$ mm/s.

Fig. 2.20b - Evolution of friction coefficient; 1-hour test in boundary lubrication steady condition; $p=1.68$ GPa, $T=80$ °C, $v=5$ mm/s.

Fig. 2.21 - SEM micrographs wear scar of steel ball for each lubricant sample: (a) 2H-MoS₂, (b) IF-WS₂, (c) Re:IF-MoS₂ and (d) IF-MoS₂.

Fig. 2.22 - XRD patterns of the wear-scar for all the tested samples. The (0 0 0 2) peak is related to MS₂ (M=Mo,W). The peaks marked with asterisk (*) are related to the steel ball

Fig. 2.23 - SEM micrograph of a typical dimples on the wear scar of steel ball, filled with the IF

Fig. 2.24 - SEM images of Graphite (a), GO (b)

Fig. 2.25 -TEM image of GO at different magnification

Fig. 2.26 - X-ray diffraction patterns of Graphite and GO

Fig. 2.27 - TG-DTG analysis of Graphite (a) and GO (b)

Fig. 2.28 - TG-DTG analysis and the MS evaluation of the dispersant

Fig. 2.29- Stribeck curves comparison from the sweep-speed test (SN150 - black, SN150 with 0.1 w.t. % Graphite – red, SN150 with 0.1 w.t. % GO - violet)

Fig. 2.30 - Friction coefficient in 1-hour steady state test with average hertzian contact pressure 1.68 GPa and sliding speed 5.0 mm/s (boundary regime): oil temperature 25° C (a) and 80 °C: (b); sliding speed 0.50 m/s (mixed/EHL regime): oil temperature 25° C (c) and 80 °C: (d); (SN150 - black, SN150 with 0.01 w.t.% GO – red)

Fig. 2.31 - Friction coefficient in steady boundary (a) and EHL (b) lubrication conditions at 25 °C and 80 °C

Fig. 2.32 - Wear scar diameter (WSD) after 1-hour boundary (a) and EHL (b) regime test at 25 °C and 80 °C

Fig. 2.33 - Raman spectra of graphite, GO and further exfoliated GO on the ball wear after 1 hour test at $p=1.68$ GPa, $T=25$ °C, $v=0.5$ m/s

Fig. 2.34 - Raman spectra of GO, SN150, GSN150_1h and GO on the ball wear scar after 1 hour test at $p=1.68$ GPa, $T=25$ °C, $v=0.5$ m/s

Fig. 2.35 - Raman spectra of original graphite and graphite on the ball wear scar

Fig. 2.36 - 3D surface morphologies of the wear scars: (a) after 1 hour test at $p=1.68$ GPa, $T=25$ °C, $v=0.5$ m/s with base oil SN150; (b) after 1 hour test at $p=1.68$ GPa, $T=25$ °C, $v=0.5$ m/s with GSN150; (c) on the wear scar in (b) after a thermal oxidation to remove GO

Fig. 3.1 – (a) WS₂@oleylamine nanosheet highlighted in a TEM image, (b) schematic representation of WS₂ nanosheets covered by a “brush of oleylamine”

Fig. 3.2 - SEM and TEM images of WS₂ nanosheets synthesized in oleylamine

Fig. 3.3 - Grease samples Lithium based: (a) Lithium based grease NLGI 3, (b) Lithium based grease formulated with 4% NanoLub GH paste, (c) Lithium based grease

formulated with 4% w.t. MoS₂ nanoparticles (NM26O16Mo4-NLGI3), (d) Lithium based grease formulated with 4% w.t. WS₂ nano-particles (NM28O16W4-NLGI3), (e) Lithium based grease formulated with 2% w.t. MoS₂ nano-particles

Fig. 3.4 - Grease samples Calcium based: (a) Calcium based grease NLGI 2, (b) Calcium based grease formulated with 4% NanoLub GH paste, (c) Calcium based grease formulated with 4% w.t. WS₂ nanoparticles (NM27O16W4-NLGI2), (d) Calcium based grease formulated with 2% w.t. MoS₂ nano-particles

Fig. 3.5 - PHYSICA MCR 301 Anton Paar for the rheological characterization

Fig. 3.6 - Storage Modulus (G') and Loss Modulus G'' vs frequency for the Lithium based grease

Fig. 3.7 - Storage Modulus (G'), Loss Modulus G'' and Complex Viscosity (η^*) vs frequency for the Calcium based grease NLGI 2 and the Calcium based grease – NLGI 2 with 4 wt % WS₂ nanosheets. T= 25 °C

Fig. 3.8 - Storage Modulus (G'), Loss Modulus G'' and Complex Viscosity (η^*) vs frequency for the Calcium based grease NLGI 2 and the Calcium based grease – NLGI 2 with 4 wt % WS₂ nanosheets. T=100°C

Fig. 3.9 - Calcium based grease and calcium formulated samples comparison

Fig. 3.10 – Lithium based grease and calcium formulated samples comparison

Fig. 3.11 - Four balls and DIN 51834 test setups

Fig. 3.12 - Weld load test result using 4 Ball test

Fig. 3.13 - Scar Diameter test result using 4 Ball test

Fig. 3.14 - The Brugger value test result using 4 Ball test

Fig. 3.15 – Fretting wear process

Fig. 3.14 - The Brugger value test result using 4 Ball test

Fig. 3.16 - Schematic representation of hybrid MoS₂/CNT coaxial nanotubes: carbon nanotubes are externally coated with MoS₂ nanosheets. Oleylamine molecules cover the inorganic core, improving the dispersibility in grease and corresponding TEM image of nano hybrid material

Fig. 3.17 - XRD patterns of CNT (black) , OA@CNT-MoS₂ (blue), OA@MoS₂-CNT (red), OA@MoS₂ (green)

Fig. 3.18 - SEM images at different magnification (500x, 1000x, 5000x and 15000x) of OA@MoS₂-CNT nanocomposite

Fig. 3.19 - SEM images of OA@CNT-MoS₂ nanocomposites at different magnification (500x, 1000x, 5000x and 10000x)

Fig. 3.20 - TEM images of OA@MoS₂-CNT at different magnification

Fig. 3.21 - TEM images of OA@CNT-MoS₂ (a, b, c) and CNT (d).at different magnification

Fig. 3.22 - TG-DTG-DSC and relevant total ion current signals of OA@MoS₂-CNT (a) and OA@CNT-MoS₂ (b)

-
- Fig. 3.23** - TG-DTG of CNT and the relevant total ion current signal showing the formation of CO₂ from carbon oxidation
- Fig. 3.24** - Raman spectra of OA@CNT-MoS₂, OA@CNT-MoS₂_TG_384, OA@CNT-MoS₂_TG_460, OA@CNT-MoS₂_TG_4
- Fig. 4.1** - (a) Elastohydrodynamic contact and (b) pressure distribution in the meatus
- Fig. 4.2** - (a) Pressure profile and (b) Film thickness profile in the case of pure rolling for an EHL point contact problem
- Fig. 4.3** - Film thickness and pressure distribution along the contact in the case of pure rolling for an EHL line contact problem
- Fig. 4.4** - Two surfaces in relative motion
- Fig. 4.5** - Forces on an element
- Fig. 4.6** - Flow through a column
- Fig. 4.7** - Geometry of the gap in an EHL point contact for $y=0$
- Fig. 4.8** - Comparison between the improved Yasutomi free-volume model and experimental data for a squalane at $T=25^{\circ}\text{C}$
- Fig. 4.9** - Film thickness profile and pressure distribution using Doolittle model
- Fig. 4.10** - Film thickness profile and pressure distribution comparison using Doolittle model with $U_{ID}=1.5\times 10^{-11}$ (solid line); $U_{ID}=2.0\times 10^{-11}$ (dashed line), $U_{ID}=2.5\times 10^{-11}$ (dot line)
- Fig. 4.11** - Film thickness profile and pressure distribution comparison using Doolittle model with $W_{ID}=2.5\times 10^{-4}$ (dot line); $W_{ID}=3.5\times 10^{-4}$ (solid line), $W_{ID}=4.5\times 10^{-4}$ (dashed line)
- Fig. 4.12** - Film thickness profile and pressure distribution using Doolittle model (solid line) and Roelands law (dashed line) with $W_{ID}=3.0\times 10^{-4}$, $U_{ID}=2.0\times 10^{-11}$
- Fig. 4.13** - 3D Pressure distribution for $U=2.6\times 10^{-11}$ and $W=1.1\times 10^{-6}$, with Doolittle pressure-viscosity model
- Fig. 4.14** - 3D Pressure distribution for $U=2.6\times 10^{-11}$ and $W=1.1\times 10^{-6}$, with Roelands pressure-viscosity model
- Fig. 4.15** - Pressure distribution level curves for $U=2.6\times 10^{-11}$ and $W=1.1\times 10^{-6}$, with Doolittle pressure-viscosity model
- Fig. 4.16** - Pressure distribution level curves for $U=2.6\times 10^{-11}$ and $W=1.1\times 10^{-6}$, with Roelands pressure-viscosity model
- Fig. 4.17** - Film thickness level curves for $U=2.6\times 10^{-11}$ and $W=1.1\times 10^{-6}$, with Doolittle pressure-viscosity model
- Fig. 4.18** - Film thickness level curves for $U=2.6\times 10^{-11}$ and $W=1.1\times 10^{-6}$, with Roelands pressure-viscosity model
- Fig. 4.19** - Pressure distribution level curves for $U=1.1\times 10^{-11}$ and $W=3.5\times 10^{-7}$, with Doolittle pressure-viscosity model

-
- Fig. 4.20** - Pressure distribution level curves for $U=5.3\times 10^{-12}$ and $W=3.5\times 10^{-7}$, with Doolittle pressure-viscosity model
- Fig. 4.21** - Pressure distribution level curves for $U=5.3\times 10^{-12}$ and $W=8.6\times 10^{-7}$, with Doolittle pressure-viscosity model
- Fig. 4.22** - Pressure distribution level curves for $U=2.6\times 10^{-11}$ and $W=1.1\times 10^{-6}$, with Doolittle pressure-viscosity model
- Fig. 4.23** - Film thickness level curves for $U=1.1\times 10^{-11}$ and $W=3.5\times 10^{-7}$, with Doolittle pressure-viscosity model
- Fig. 4.24** - Film thickness level curves for $U=5.3\times 10^{-12}$ and $W=3.5\times 10^{-7}$, with Doolittle pressure-viscosity model
- Fig. 4.25** - Film thickness level curves for $U=5.3\times 10^{-12}$ and $W=8.6\times 10^{-7}$, with Doolittle pressure-viscosity model
- Fig. 4.26** - Film thickness level curves for $U=2.6\times 10^{-11}$ and $W=1.1\times 10^{-6}$, with Doolittle pressure-viscosity model
- Fig. 4.27a** - Pressure distribution and film thickness behavior with a RMS of 1 μm
- Fig. 4.27b** - Pressure distribution and film thickness behavior with a RMS of 0.5 μm
- Fig. 4.27c** - Pressure distribution and film thickness behavior with a RMS of 0.1 μm
- Fig. 4.28a** - Pressure distribution and film thickness behavior with a kurtosis of 3.5 (solid line) compared with the results for smooth surfaces (dot line)
- Fig. 4.28b** - Pressure distribution and film thickness behavior with a kurtosis of 3 (solid line) compared with the results for smooth surfaces (dot line). The value of RMS is 0.1 μm
- Fig. 4.28b** - Pressure distribution and film thickness behavior with a kurtosis of 2.5 (solid line) compared with the results for smooth surfaces (dot line). The value of RMS is 0.1 μm
- Fig. 4.29a** - Pressure distribution and film thickness behavior with a skewness of 0.768. The value of RMS is 0.1 μm
- Fig. 4.29b** - Pressure distribution and film thickness behavior with a skewness of -0.300. The value of RMS is 0.1 μm
- Fig. 4.30** - Pressure distribution and film thickness behavior obtained using an exponential autocorrelation function (solid line) and a Gaussian autocorrelation function (dot line). The value of RMS is 0.1 μm
- Fig. 4.31a** - Pressure distribution and film thickness behavior with correlation length of 0.1 μm and RMS of 0.1 μm
- Fig. 4.31b** - Pressure distribution and film thickness behavior with correlation length of 1 μm and RMS of 0.1 μm
- Fig. 4.32** - Pressure distribution and film thickness behavior obtained using the free volume piezoviscosity model (solid line) and the Roelands model (dot line). The value of RMS is 0.1 μm

Fig. 5.1 - (a) Undeformed geometry of the hollow and the bulk (b) MoS₂ nanoparticle used for the finite element simulations

Fig. 5.2 - Displacements scheme performed in the finite element simulation: uniaxial compression and shearing

Fig. 5.3 - Displacement-time curves. The solid curves represent different time-Y displacement resulting in different contact pressures, (a) from 1.1 GPa up to 2.0 GPa for the hollow-core nanoparticle and (b) up to 4.0 GPa for the bulk-core (b), while the dashed line represents the displacement in X direction (300 nm) during the shearing phase

Fig. 5.4 - Force-time curves as function of testing time for different contact pressure used

Fig. 5.5 - Sliding snapshots of the hollow nanoparticles at different sliding times for the different presented contact pressure. The white point in the different snapshots allows to follow the rolling of the hollow nanoparticle

Fig. 5.6 - Slide to roll ratio at different sliding times for the presented pressure contact

Fig. 5.7 - Force-time curves as function of testing time for different contact pressure used

Fig. 5.8 - Sliding snapshots of the hollow nanoparticles at different sliding times for the different presented contact pressure. The white point in the different snapshots allows to follow the rolling of the hollow nanoparticle

Fig. 5.9 - Slide to roll ratio at different sliding times for the presented contact pressure

Fig. 5.10 - Normal load comparison for the different core structure (hollow and bulk) of the particle for the presented contact pressure

Fig. 5.11 - Upper surface displacement comparison for the different core structure (hollow and bulk) of the particle for the presented contact pressure

Fig. 5.12 - Shear stress snapshots comparison at the end of test (t=5s) for the different presented contact pressures

Fig. 5.13 - Shear stress comparison for the different core structure (hollow and bulk) of the particle for the presented contact pressure

Fig. 5.14 - Slide to roll ratio for the different nanoparticle core structures (hollow and bulk) for the presented contact pressure in steady state sliding (time: 5 sec)

Fig. 5.15 - (a) Surface roughness profile acquired through AFM. The average arithmetic roughness measured by the microscope is 0.005 μm . The acquired data cover a width of 20 μm , in red the roughness profile chosen for the finite element simulations. (b) Particular of the surface roughness chosen for the finite element simulations.

Fig. 5.16 - Undeformed geometry of the hollow MoS₂ nanoparticle used for the finite element simulations. The area interested by the hollow MoS₂ nanoparticle displacements used for the finite element simulations is highlighted in red

Fig. 5.17 - Normal force comparison at different sliding times between the roughness surface (solid lined) and the ideal smooth surface (dashed line) for the hollow nanoparticle

Fig. 5.18 - Pressure comparison at different sliding times between the roughness surface (solid lined) and the ideal smooth surface (dashed line). In the red circle is possible to observe the failure point of particle. At that pressure the nanoparticle collapse and the finite element problem does not converge to a solution

Fig. 5.19 - Sliding snapshots of the hollow nanoparticles at different sliding times for the presented contact pressure with a $Ra=0.005\mu\text{m}$. The white point in the different snapshots allows to follow the rolling of the hollow nanoparticle

Fig. 5.20 - Slide to roll ratio comparison at different sliding times between the roughness surface (solid lined) and the ideal smooth surface (dashed line) for the hollow nanoparticle

Fig. 5.21a - Finite element results of Von Mises equivalent stress for the hollow core structure during the compression phase

Fig. 5.21b - Finite element results of Von Mises equivalent stress for the hollow core structure during the shearing/sliding phase

LIST OF TABLES

Tab. 1.1- Confocal objective profiler characteristics

Tab. 2.1- Composition of the ARL

Tab. 2.2- Friction coefficient in boundary lubrication steady condition; sliding speed: 5.0 mm/s

Tab. 2.3- Friction coefficient in mixed lubrication steady condition; sliding speed: 0.5 m/s

Tab. 2.4- Optical micrograph and wear scar diameter (WSD) after boundary lubrication steady condition test; sliding speed: 5.0 mm/s

Tab. 2.5- Optical micrograph and wear scar diameter (WSD) after mixed lubrication steady condition test; sliding speed: 0.5 m/s

Tab. 2.6- Lubricant (ARL1) physical and chemical properties

Tab. 2.8- Friction coefficient in mixed lubrication steady condition; sliding speed: 0.5 m/s

Tab. 2.9 - Profiler image acquisition and wear scar diameter (WSD) after boundary lubrication steady condition test; sliding speed: 5.0 mm/s

Tab. 2.10- Profiler image acquisition and wear scar diameter (WSD) after mixed lubrication steady condition test; sliding speed: 0.5 m/s

Tab. 2.11 - Sample ARL_N10_0.75 Characteristic

Tab. 2.12 - Initial network parameters

Tab. 2.13 - Importance of input parameters on the output

Tab. 2.14 - Sensitivity of input parameters on the output

Tab. 2.15 - EXAFS data analysis results

Tab. 2.16 - Typical size and shape of the platelets and fullerene-like nanoparticles

Tab. 2.17 - Friction coefficient in boundary lubrication steady condition; sliding speed: 5.0 mm/S

Tab. 2.18 - Friction coefficient in mixed lubrication steady condition; sliding speed: 0.50 m/s

Tab. 2.19 - Optical micrograph and wear scar diameter (WSD) after boundary lubrication steady condition test; sliding speed: 5.0 mm/s

Tab. 2.20 - Optical micrograph and wear scar diameter (WSD) after mixed lubrication steady condition test; sliding speed: 0.50 m/s

Tab. 2.21 - EDS (energy dispersive X-ray spectroscopy) analysis of the wear scar (small magnification). The steel ball for each lubricant sample was prepared by 1-h sliding wear test in steady-state conditions, such that the average hertzian pressure was 1.68 GPa, temperature 25 °C and sliding speed 0.50 m/s

Tab. 2.22 - Friction coefficient in boundary lubrication steady condition; sliding speed: 5.0 mm/s. Average hertzian contact pressure: 1.68 GPa

Tab. 2.23 - Friction coefficient in Mixed/EHL lubrication steady condition; sliding speed: 0.5 mm/s. Average hertzian contact pressure: 1.68 GPa

Tab. 2.24 - Optical micrograph and wear scar diameter (WSD) after boundary lubrication steady condition test; sliding speed: 5.00 mm/s

Tab. 2.25 - Optical micrograph and wear scar diameter (WSD) after mixed/EHL lubrication steady condition test; sliding speed: 0.50 m/s

Tab. 3.1 - NLGI Grease classification for lubricating greases

Tab. 3.2 - Lithium grease properties

Tab. 3.3 - Calcium grease properties

Tab. 3.4 - Friction coefficient values for Calcium based grease and Calcium grease samples formulated with nanoparticles in boundary and mixed/EHL lubrication regimes

Tab. 3.5 - Friction coefficient values for Lithium based grease and Lithium grease samples formulated with nanoparticles in boundary and mixed/EHL lubrication regimes

Tab. 3.6 – Values of the Wear scar diameter and the optical micrographs of the wear circle collected on the steel ball after 1-hour test for Calcium based grease and Calcium grease samples formulated with nanoparticles in boundary lubrication regime

Tab. 3.7 – Values of the Wear scar diameter and the optical micrographs of the wear circle collected on the steel ball after 1-hour test for Lithium based grease and Lithium grease samples formulated with nanoparticles in boundary lubrication regime

Tab. 3.8 – Values of the Wear scar diameter and the optical micrographs of the wear circle collected on the steel ball after 1-hour test for Calcium based grease and Calcium grease samples formulated with nanoparticles in Mixed/EHL lubrication regime

Tab. 3.9 – Values of the Wear scar diameter and the optical micrographs of the wear circle collected on the steel ball after 1-hour test for Lithium based grease and Lithium grease samples formulated with nanoparticles in Mixed/EHL lubrication regime

Tab. 3.10 - Operating conditions used for the fretting test

Tab. 3.11 - Values of the Wear scar diameter and the optical micrographs of the wear circle collected on the steel ball after 2-hour test for Lithium and Calcium grease samples formulated with tungsten disulphide

Tab. 3.12 - Composition of grease samples tested (Ca= Calcium, Li=Lithium)

Tab. 3.13 - Friction tests results in both boundary and mixed regimes

Tab. 3.14 - Wear tests results in both boundary and mixed regimes

Tab. 4.1 - Central and minimum film thickness on four different grids with 2 cycles in FMG algorithm. $U=1.11 \cdot 10^{-11}$ $W=3.46 \cdot 10^{-7}$ with Doolittle model

Tab. 4.2 - Central and minimum film thickness on four different grids with 2 cycles in FMG algorithm. $U=1.11 \cdot 10^{-11}$ $W=1.04 \cdot 10^{-6}$ with Doolittle model

Tab. 4.3 - Doolittle and Roelands predicted central film thickness H_c versus calculated values with Dowson-Higginson equation, for different values of dimensionless speed and applied load

Tab. 4.4 - Doolittle and Roelands predicted minimum film thickness H_m versus calculated values with Dowson-Higginson equation, for different values of dimensionless speed and applied load

Tab. 5.1 - Mechanical properties of the materials used to model the surfaces (steel) and the nanoparticle (molybdenum disulphide)

Tab. 5.2 - Deformation ratio, maximum average contact pressure and hertzian deformation width for different presented Y-displacements obtained for the hollow nanoparticle just at the end of compression phase (at $t \sim 2s$), where the maximum normal load is applied

Tab. 5.3 - Deformation ratio, Y-displacement and hertzian deformation width for different maximum average contact pressures presented obtained for the bulk nanoparticle

INTRODUCTION

Lubricant additives have an important influence on the lubrication performances. These additives are active ingredients which can be added during a blending process to base oils in order either to enhance the existing performance of the base fluids or to impart new properties that the base fluids lack. In modern industry, the ever growing demand on the duration and efficiency of machineries stimulates the research for lubricant additives with better performance. At the same time, industry is facing increasingly rigorous environmental regulations. Compared with the traditional organic lubricant additives that contain P, S and Cl elements, novel additives with environmental friendly feature are certainly becoming more desirable in the future, and research for the novel lubricant additives with good tribological properties and low environmental impact becomes important.

Most of lubricant oils at present contain several critical additives, including antiwear additive, dispersant, detergent, friction modifier, viscosity index improver and antioxidant. Traditionally, lubricant oils are presented as a single phase material in order to maintain a good consistency and dispersibility of the additives in the base oil. However, a great amount of research has been focused on introducing solid particles as a friction reduction or antiwear additive over recent years due to a number of incomparable advantages of the two-phase lubricant oils (liquid-solid), such as the superior thermal conductivity, the high pressure standing ability, high resistance to decomposition at temperature, low environmental impact, etc. Some of the solid lubricant additives, particularly in nano or submicron size, have even demonstrated better tribological performances than the traditional organic additives, Zinc dialkyldithiophosphates (ZDDP) for instance.

Due to the diversity of the materials, there are still many controversies about their behaviour in a base lubricant and their lubricating mechanisms although many potential candidates have been tested as the solid lubricant additives and many of them has shown the

excellent tribological properties. The major drawback of solid lubricant additives, the intrinsic poor stability in liquid base lubricant systems, has considerably restrained them from applications. Therefore the research on exploring novel solid lubricant additives and the techniques that would improve their dispersibility in base lubricants is certainly required.

Furthermore, many machine elements, lubricated by fluid film have surfaces that do not conform to each other, so small lubricated areas must then carry the load. The lubrication area of a nonconformal conjunction is typically three orders of magnitude less than that of a conformal conjunction. In general, the lubrication area between nonconformal surfaces enlarges considerably with increasing load, but it is still smaller than the lubrication area between conformal surfaces. Accordingly, the lubrication regime, known as elastohydrodynamic lubrication (EHL) is the typical regime of lubrication characterized by high contact pressures and, therefore, significant elastic deformation and piezoviscous increase in lubricant viscosity. For this reason, a good and accurate prediction of the EHL behaviour, in several different applications, requires consideration of the constitutive equation for the lubricant. Actually, the EHL has two primary aspects: the increase of viscosity with pressure, and the elastic deformation, caused by high pressure, which is comparable to that of the film thickness. Due to the high pressure and the limited contact area, elastic deformation of the surfaces will occur and it is not negligible, as well as the pressure dependence of viscosity play a crucial role in EHL simulation because the viscosity at the inlet has crucial influence on film formation.

. In particular, for applications involving lubricants that exhibit shear-thinning behaviour, the use of an appropriate pressure-viscosity relationship for the lubricant is required to predict the EHL behaviour more accurately. Hence, this Ph.D. thesis aims, also, to emphasize the importance of implementing piezoviscous models with accurate treatment methods in EHL applications.

In order to a better modelling of the lubricant rheology Doolittle developed the first free-volume model based on a physical meaning, that the resistance to flow in a liquid depends upon the relative volume of molecules present per unit of free volume. Using an exponential function, Doolittle related viscosity to the fractional free volume.

Summarizing, this research aimed to study:

- Firstly, the influence of different solid lubricant additives (organic additives, such as graphene nanosheets, and inorganic additives, such as inorganic fullerene-like tungsten and molybdenum disulphide nanoparticles) on friction and wear properties of the base lubricants.
- Secondly, by means of numerical simulations:
 - a) The effects of different pressure–viscosity relationships (including the exponential model, the Roelands model and overall the so called Yasutomi-Doolittle free-volume model) for different operating parameters and surface characterization in EHL lubrication
 - b) The lubrication mechanism of a perfectly spherical nanoparticle, with size and shape close to those of the inorganic fullerene like nanoparticle (IF-NPs), in order to understand the lubrication mechanism and how this kind of solid additive could affect the tribological performance of mating surfaces.

The above presented research fields have been studied in different ways:

- Exploring the influence of different types of solid lubricant additives on the friction and wear properties of the base lubricants.
- Interpreting the mechanisms of the effects of these solid lubricant additives on tribological performances through tribochemical analysis.
- Using numerical simulations techniques (such as full multigrid numerical code and finite element simulations) to investigate the lubricant piezoviscous property in EHL regime and to understand IF-NPs deformation and lubrication mechanism at nanoscale.

Dissertation outline

This thesis begins, in the first part of the Chapter 1, with a literature survey which aims to provide an understanding of the background knowledge and theories in tribology. In the second part of the Chapter 1 a review regarding the different types of solid lubricant additives, most of these tested in this Ph.D. thesis is provided. The tribological properties of different types of solid lubricant additives and the various mechanisms, proposed to explain their tribological behaviors, are also discussed.

Chapter 2 describes firstly the experimental techniques used to characterize the solid lubricant and, subsequently, the experimental results, obtained both for organic and inorganic additives. Test results have been also presented in order to investigate the friction and wear behaviors of the solid lubricant additives in base lubricants. Testing materials involved in this thesis have been also introduced in this chapter.

Chapter 3 presents the experimental results obtained using inorganic nanoadditive in lubricating greases. In the second part of the Chapter the results obtained on grease samples formulated with innovative hybrid additives made up by nanosheets of MoS₂ and carbon nanotube synthesized at Nano_Mates centre (University of Salerno) have been presented.

In Chapter 4 a model for the characterization of the elastohydrodynamic lubrication is proposed. The aim of this numerical approach is to investigate the effects of different piezoviscous lubricant behavior on the EHL results. In particular, the application of the free-volume viscosity model in a Newtonian elastohydrodynamic line and point contact simulation is presented. Moreover, in the second section of this chapter the simulation results of elastohydrodynamic lubrication (EHL) contact between two rough surface cylinders are discussed. Random rough surfaces with Gaussian and exponential statistics have been generated using a method outlined where an uncorrelated distribution of surface points using a random number generator is convolved with a Gaussian filter to achieve correlation. The maximum pressure and average film thickness are studied at different values of RMS, skewness, kurtosis, autocorrelation function and correlation length.

The aim of the Chapter 5 is to investigate the structural response of IF-MoS₂ particles under uniaxial compression and shear stress, and to analyze the potential friction mechanisms of fullerene-like nanoparticles. Hollow and full-core nanoparticles were studied using numerical approach of finite element model (FEM) analysis. In particular, in the first section this research has been focused on the comparison of the hollow-core nanoparticle, while in the second part of the chapter the behavior of a hollow core nanoparticle is investigated under loading and shearing condition in the case of a real rough steel surface, acquired by means of an atomic force microscope (AFM).

Finally, Chapter 6 summarizes the main findings of this Ph.D. thesis and makes some suggestions for the future research in this area.

CHAPTER 1

Lubrication, nanoadditives and tools

1.1. Tribology: Friction and wear

The “tribology” is defined as the science and technology of interacting surfaces in relative motion and of the practices related thereto. A better definition might be the lubrication, friction, and wear of moving or stationary parts [1-3].

Friction reduces the relative motion between the two bodies or resists the tendency to motion between the two bodies in contact. The main reason for wear and energy losses is friction. The friction between the two mating surfaces depends upon the geometry, macroscopic contact points, elastic properties, adhesive forces, deformation of the surface during movement. There are basically two types of friction: internal friction and external friction. External friction is the mechanical force which resists or hinders movement between two surfaces whereas the internal friction is the friction between lubricant molecules [4,5].

The visible consequences of friction on surface are called wear. Wear is mainly caused by the progressive loss of surface material from relative tangential motion at the contact between two solid bodies. It arises from the friction forces created by the resultant interactions of these bodies surface roughness features. When the phenomenon of interaction, that causes the removal of material remains a local phenomenon and not generalized to any surface, it is called moderate “mild wear” and it is usually tolerated and sometimes even desirable (the phenomenon of running that involves an adaptation of real surfaces in relative motion). In these circumstances, the wear debris consists of particles with the size of few microns. In other cases, especially when the temperature is too high, it is possible to have rapid removal of the surface at the metal-metal that produces a fairly rapid formation of particles of hundreds of microns.

This phenomenon, called severe wear, results most of the time destructive [5].

Lubrication is an important component of Tribology; its act is to have between the surfaces a layer of a different material that reduces the friction force between them, either by being softer than the surfaces, or by being a coherent liquid lubricant or gas, entrained between the two surfaces by their relative movement. Relative motion between two elements of a fluid is retarded by intermolecular interactions caused by viscosity, a real fluid property. This property is the most essential feature of lubricants, as it enables them, given the right conditions, to separate two solid bodies in relative motion. Furthermore, most engineering structures are not in vacuum conditions, so the primary friction reducing layer is a low shear strength oxide film formed naturally by the interaction of the surfaces with the atmosphere, Figure 1.1 [6].

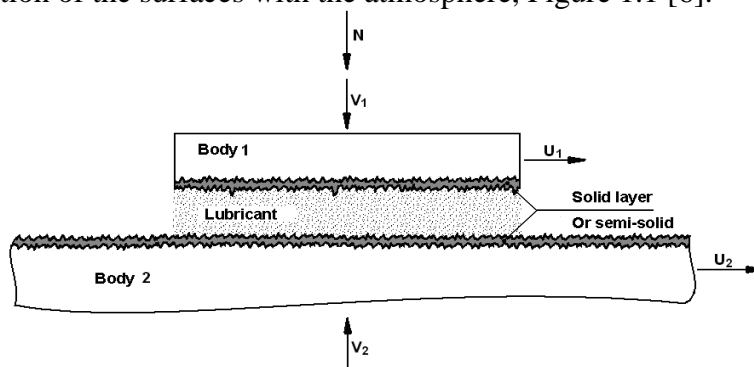


Fig. 0.2 - Physical-chemical system of a tribological pair

Actually, in this chapter, it will be showed the possible lubrication regimes commonly encountered in lubricated tribopair. While, in the second part a brief description of the nanoparticles (both organic and inorganic) nowadays mostly used as lubricant additives and tested in the experimental part of this Ph.D. thesis is given.

1.2 Lubrication regimes

Among the kinematic elements of a pair in contact and in relative motion manifests a force that opposes the motion itself, due to dissipation of mechanical energy and wear of the surfaces. The lubrication of the

mechanical parts is carried out to separate and protect the surfaces in relative motion in order to minimize the effects of friction and wear.

The kinematic pairs in lubricated contacts are subjected to varying loads, which implies the continuous variation of the lubrication regime between the tribopair. In dependence on the thickness of lubricant, the surface finishing, geometry of the surfaces (weak or high curvature), the loads, the relative speed between the elements of the kinematic pair, it can be possible to distinguish different lubrication mechanisms, normally indicated under the general classification [6]:

- Boundary lubrication
- Hydrodynamic lubrication
- Elastohydrodynamic lubrication
- Mixed lubrication

An index of the type of lubrication realized in a tribological coupling is provided by the ratio between the minimum value of the thickness of the lubricant film and the surface roughness. For values of this ratio greater than 5, the kinematic pair is operating in conditions of fluid film lubrication, since the height of the meatus fluid is such as to ensure that between the roughnesses of the two surfaces does not occur any contact. For values lower than 5 the roughness of the two surfaces are regularly in contact, thereby tearing the film interposed fluid and preventing the development of a full lubricant film. In such conditions, the lubrication is boundary [7].

1.2.1 Boundary lubrication

In boundary lubrication the surfaces of the solids are separated, at least for part of their extension, by a few molecular layers of lubricant , constituting an extremely thin film that remains anchored to each surface with a complex of chemical-physical phenomena such as adsorption, the polar properties of the molecule, the surface tension.

The reduction in friction compared to the coupling in direct contact comes from the fact that the slip does not take place in

correspondence of the solid surfaces in which the molecular bonds are intense, but inside the film of lubricating oil, where the molecular actions are weaker. The thickness of the fluid film is not such as to ensure the complete separation of the surface irregularities of the surfaces. In fact, the lubricating oil has the main function of reducing the size of the microjoints, reducing the friction and the speed of wear of the components coupled.

Because in boundary lubrication the solids are not separated by the lubricant, fluid film effects are negligible and there is considerable asperity contact. The contact lubrication mechanism is governed by the physical and chemical properties of thin surface film of molecular proportions. The properties of the bulk lubricant are of minor importance, and the friction coefficient is essentially independent of fluid viscosity.

Actually, the viscosity of the lubricant, which typically must be greater as greater is the load and the lower the speed, not representing the element of greatest weight in the choice of the lubricant itself, since the reduction of friction and wear depend mainly on the so-called lubricity, or by the ability of the oil to form a veil highly adherent to metal surfaces.

The frictional characteristics are determined by the properties of the solids and the lubricant film at the common interfaces. The surface films vary in thickness from 1 to 10 μm , depending on the molecular size. The mechanisms of surface film formation boundary lubrication could be described in two different ways [6]:

- physical adsorption. This occurs most under very mild sliding conditions. Note that no special additives are needed for physical adsorption, and that all of the lubricants have some potential for forming boundary films by this mechanism.
- chemical adsorption. In the chemical adsorption, fatty acids can react with metals to form metal soaps which may or may not be attached to a surface. With polar and paraffinic molecules, chemical adsorbed lubricant can be very closely packed on a surface.
- chemical reaction involving or not the substrate.

1.2.2 Hydrodynamic lubrication

Hydrodynamic lubrication (HL) is generally characterized by conformal

surfaces and characterized by the presence of a continuous film of lubricant which separates the surfaces of the solids in relative motion.

A positive pressure develops in a hydrodynamically lubricated journal or thrust bearing because the bearing surfaces converge and the relative motion and the viscosity of the fluid separate the surfaces. The existence of this positive pressure implies that a normal applied load may be supported. The magnitude of the pressure developed is not generally large enough to cause significant elastic deformation of the surfaces.

In hydrodynamic lubrication the films are generally thick so that the opposing solid surfaces are prevented from coming into contact. This condition is often referred to as “the ideal form of lubrication”, since it provides low friction and high resistance to wear. The lubrication of the solid surfaces is governed by the bulk physical properties of the lubricant, notably the viscosity, and the frictional characteristics arise purely from the shearing of the viscous lubricant.

The lubricant, in other words, is interposed between the surfaces being dragged by these in their motion: the drag action is due to the existence of viscous forces, for which it is understood that the viscosity μ has, in this lubrication, a role decisive. In a Newtonian fluid the shear stress τ is proportional to the velocity gradient in the sense of motion through the dynamic viscosity of the fluid [2.3]:

$$\tau_{xy} = \mu \frac{dv_x}{dy} \quad (1.1)$$

where v_x is the velocity in the x-direction, perpendicular to the direction in which the gradient is calculated.

The hydrodynamic lubrication regime was studied experimentally and theoretically by many authors that have provided models that interpret in a more or less approximated way this complex phenomenon. Of particular interest are the general principles set out by Reynolds at the end of the nineteenth century [8]. These principles are summarized in the well-known Reynolds equation, introduced in (1.2), which is obtained, under certain assumptions, by applying the continuity and momentum equation to a fluid element:

$$\frac{\partial}{\partial x} \left(\frac{\rho h^3}{\mu} \frac{\partial p}{\partial x} \right) + \frac{\partial}{\partial y} \left(\frac{\rho h^3}{\mu} \frac{\partial p}{\partial y} \right) = 6U \frac{\partial(\rho h)}{\partial x} + 12 \frac{\partial h}{\partial t} \quad (1.2)$$

1.2.3 Elastohydrodynamic Lubrication

Elastohydrodynamic lubrication (EHL) is a form of hydrodynamic lubrication where elastic deformation of the lubricated surfaces becomes significant. According to this theory can be a condition of hydrodynamic lubrication even in the presence of heavy loads. The features important in a hydrodynamically lubricated slider bearing (converging film thickness, sliding motion, and a viscous fluid between the surfaces) are also important here. Elastohydrodynamic lubrication is normally associated with nonconformal surfaces. There are two distinct form of EHL: hard and soft EHL.

Hard EHL relates to materials of high elastic modulus such as metals. In this form of lubrication the elastic deformation and the pressure-viscosity effects are equally important. The maximum pressure is typically between 0.5 and 3 GPa; the minimum film thickness normally exceeds 0.1 μm . These conditions are dramatically different from those found in hydrodynamically lubricated conjunction. At loads normally experienced in nonconformal machine elements the elastic deformations are several orders of magnitude larger than the minimum film thickness. Furthermore, the lubricant viscosity can vary by as much as 10 orders of magnitude within the lubricating conjunction [9].

Soft EHL relates to materials of low elastic modulus such as rubber. The maximum pressure for soft EHL is typically 1 MPa, in contrast to 3 GPa for hard EHL. This low pressure has a negligible effect on the viscosity variation throughout the conjunction. The minimum film thickness is a function of the same parameters as in hydrodynamic lubrication with the addition of the effective elastic modulus.

The minimum film thickness for soft EHL is typically 1 μm [6]. Engineering applications in which elastohydrodynamic lubrication is important for low elastic-modulus materials include seals, human joints, tires and a number of lubricated machine elements that use rubber as a material. The common features of hard and soft EHL are that the local elastic deformation of the solids provides coherent fluid film and that

asperity interaction is largely prevented. This implies that the frictional resistance to motion is due to lubricant shearing.

1.2.4 Mixed lubrication

If the pressures in elastohydrodynamically lubricated machine elements are too high or the running speeds are too low, the lubricant film will be penetrated. Some contact will take place between the asperities, and mixed, or partial, lubrication will occur.

The behavior of the conjunction in a mixed lubrication regime is governed by a combination of boundary and fluid film effects. Interaction takes place between one or more molecular layers of boundary-lubricating films. The average film thickness in a mixed lubrication conjunction is less than 1 and greater than 0.01 μm .

It is important to recognize that the transition from elastohydrodynamic to mixed lubrication does not take place instantaneously as the load increases, but rather a decreasing portion of the load is carried by pressures within the fluid that fills the space between the opposing solids [6]. Actually, as the load increases, a larger part of the load is supported by the contact pressure between the asperities of the solids.

1.3 Stribeck curve

A useful concept for the understanding of the role of different lubrication regimes is the Stribeck curve. Historically, the Stribeck curve was first widely disseminated because of Stribeck systematic and definitive experiments that explained friction in journal bearings [10].

The ordinate in Figure 1.2 is the coefficient of friction under steady state conditions. The abscissa is a dimensionless number, sometimes referred to as the lubrication number, Λ , (or service number, SP), and is given as:

$$\Lambda = \eta V/P \quad (1.3)$$

η = absolute viscosity, Pa·s

ω =rotational speed, rps

p = pressure, Pa.

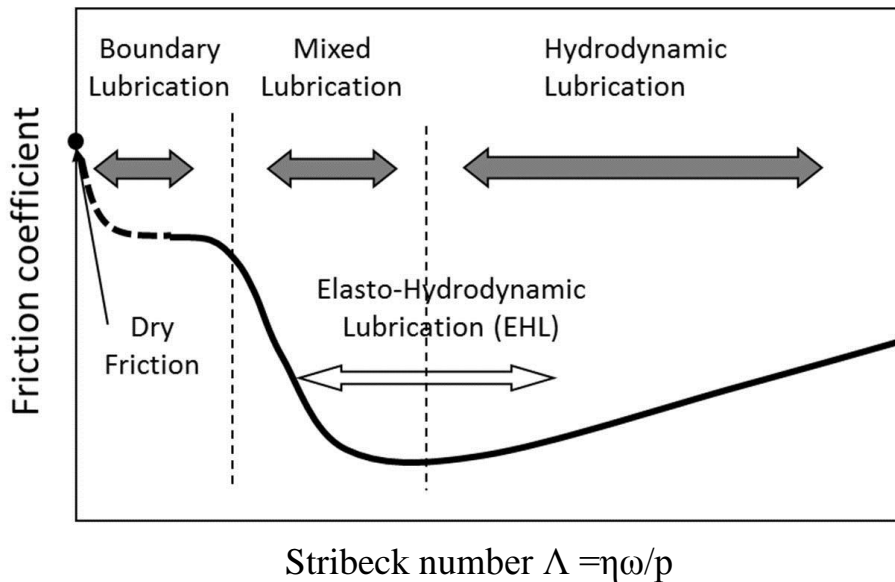


Fig. 1.2- Stribeck diagram for a generic coupling

A high Stribeck number usually means a relatively thick lubricant film, whereas a small number results in a very thin film. The lubrication regimes have been indicated in Fig. 1.2 and can be inferred from the friction behavior of the bearing system. At an extremely low Stribeck number, no real lubrication film can develop and there is significant asperity contact, resulting in high friction.

This represents the dominance of boundary lubrication in determining load transfer and friction between surfaces. As the Stribeck number increases, a noticeable and rapid decrease in friction values is observed.

This is explained by an increasing lubricant film thickness and shared load support between the surfaces asperities and the pressurized liquid lubricant present in the conjunction. With a further increase in Stribeck number, friction reaches a lower plateau value, corresponding to the onset of hydrodynamic lubrication.

At this point, the surfaces are effectively separated by the liquid lubricant, and asperity contact has negligible effect on load support and friction [4,6].

1.4 Nanoparticles as lubricant additives

This section introduces the study on the possibility of reducing wear and frictional losses in lubricated pairs through special additives, known as friction modifiers. Actually, it will be described different types of additives frequently encountered in the scientific literature and matter of study in the experimental section of this thesis. In the first part, a brief state of the art will be presented about theoretical and experimental results obtained in recent years with the use of organic (carbon based) nanoparticles as lubricant additives to improve frictional performances, while in the second part of this section the inorganic nanoadditives (based on metal dichalcogenides nanoparticles) and their more recent use as friction modifiers have been described.

Nanoparticles are very attractive novel lubricant additives because of their nanoscale size, which allows them to penetrate contacts of diverse geometries, fill the gaps between contact asperities and ultimately form a protective boundary film, persistent under high pressure. For this reason, a vast array of nanoparticles has been used in published research to investigate their effect on friction or wear in tribological contacts [11-13]. Compared to the common micro-metric additives, nanoparticles present several major advantages:

- Their nanometer size allows them to enter the contact area easily;
- They are often efficient at ambient temperature. Thus, no induction period is necessary to obtain interesting tribological properties;
- Several types of nanoparticles can be envisaged as lubricant additives.

The following sections describe different possible nanolubricants: nested nanoparticles (fullerenes, nanosheets and nanotubes) made on metal dichalcogenides or carbon. However, dispersion of nanoparticles in

oil is not always simple. Thus, in a first part, the dispersion of solid nanoparticles in a liquid has been discussed.

A colloidal sol is generally a substance (liquid or gel) containing dispersed solid particles. To obtain a homogeneous and stable system, the size of the nanoparticles has to be small, below 100 nm. A sol is composed of two phases: a continuous phase and a dispersed phase. In the present case, the continuous phase is lubricant (oil or grease) and the dispersed phase is a solid (nanoparticles). A good stability of dispersion is not easy to obtain, and several phenomena lead to instability [4,5]:

- Aggregation of the particles;
- Sedimentation of particles.

Accordingly, particles in suspension in a liquid medium are subjected to three kinds of forces: (a) gravitation forces the particles to fall down, (b) viscosity of the liquid decreases the speed of their displacement and (c) Archimedes force is opposed to gravitation force in this case. By applying fundamental relation of dynamics, the expression of the steady state sedimentation speed of a particle, V , is obtained:

$$V = \frac{2}{9} \frac{R^2}{\eta} (\rho - \rho') g \quad (1.4)$$

with:

R radius of the particle

η dynamic viscosity of the liquid

ρ density of the particles

ρ' density of the liquid

It is important to notice that the speed varies in proportion to the square of the radius of the particle. Therefore, particles with large radius will sediment much faster than small ones. Fortunately, other effects can allow for a better stability of a suspension, i.e. the Brownian motion [6].

1.5 Carbon based nanoadditives

1.5.1 Graphene and carbon nanotube

Graphene is another carbon allotrope whose structure is a single planar sheet of sp^2 -bonded carbon atoms that are densely packed in

a honeycomb crystal lattice. The term *graphene* was coined as a combination of graphite and the suffix *-ene* by Hanns-Peter Boehm, who described single-layer carbon foils in 1962. In this material, carbon atoms are arranged in a regular hexagonal pattern. The carbon-carbon bond length in graphene is about 0.142 nanometers and graphene sheets stack to form graphite with an interplanar spacing of 0.335 nm. Graphene is the basic structural element of some carbon allotropes including graphite, charcoal, carbon nanotubes and fullerenes [14,15].

High-quality graphene is very strong, light, nearly transparent, and an excellent conductor of heat and electricity and its interaction with other materials and with light, and its inherently two-dimensional nature, produce unique properties.

Carbon nanotubes can be described as a rolling-up of graphene planes. Because of its relations to graphene as well as its nanometer size and one dimensionality, this material has unique properties, Figure 1.3.

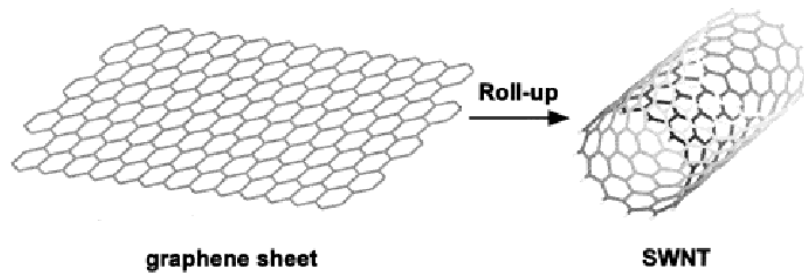


Fig. 1.3– Graphene and SWNT

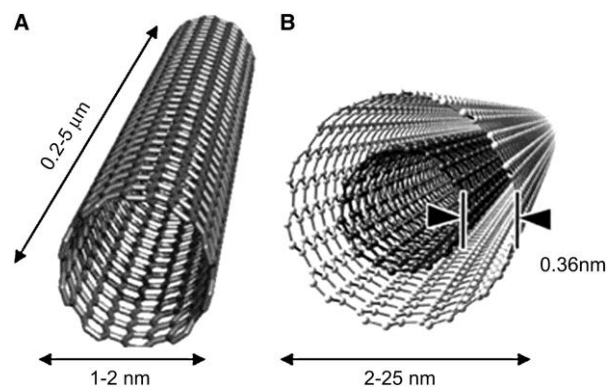


Fig. 1.4- Crystal structure of (a) SWCNT and (b) MWCNT

Nanotubes, above in Figure 1.4, can be distinguished as single-walled nanotubes (SWNTs) and multi-walled nanotubes (MWNTs). Single-walled nanotubes were observed in 1993 and can be described as a sheet of graphene rolled-up, while multi-walled nanotubes can be described as nested nanotubes that can slip one inside the other [16].

1.5.2 Fullerene C₆₀

The structure of the fullerene C₆₀, another carbon allotrope, is that of an icosahedron which has been truncated vertices and replaced by pentagons as shown in Figure 1.5. In the structure of C₆₀ each carbon atom is bonded with three other atoms by two single bonds and one double. The C₆₀ exists in the solid state form of fullerite: this at room temperature fits in a face-centered cubic structure, in which in place of each atom there is a fullerene molecule [17,18].

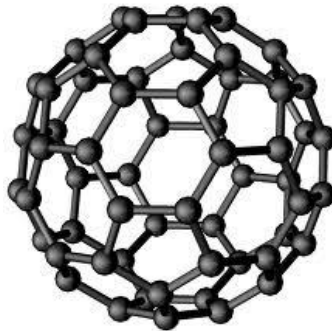


Fig. 1.5- Crystal structure of C₆₀

1.5.3 Lubrication mechanism of carbon-based additives

The C₆₀ fullerene structure has interested tribologist for long time. Because their structure looks like a ball, C₆₀ was supposed to have interesting tribological properties. It was suppose that fullerenes could “roll” in the contact, the system being like a ball bearing on a nanometer scale [19]. In fact, results obtained are contradictory: some studies report low friction with C₆₀ films [20], but other authors found that it is higher than the coefficient for amorphous carbon or diamond [21]. A study using

atomic force microscopy (AFM) also showed that the rotation of C_{60} does not reduce the friction [22]. Miura and Kamiya studied the behavior of a single layer of C_{60} between two layers of graphite [23,24] and this system can be compared to a ball bearing. A stick-slip motion of C_{60} is observed. A low friction is measured, which suggests a future use of this system could be in micromachines.

Even if it is difficult to know whether the fullerenes or nanotubes are exfoliated or not and whether graphene sheets are produced inside the contact area, an important point is that carbon based nanoadditives play more important tribological roles than graphite (particularly as an antiwear additive).

Furthermore, a hypothesis to explain the good friction-reducing properties of nanotubes is the formation of graphene single sheets inside the contact area, by unwinding of the nanotubes.

Nevertheless, it is important to mention that dispersion of graphite is not stable. It can be explained by the micrometric size of the graphite particles, which leads to a rapid sedimentation of the particles [25].

1.6 Nanoparticles made of metal dichalcogenides

By analogy to carbon which can form closed structures (fullerenes and nanotubes), Tenne and co-authors synthesized the same type of closed structures with metal dichalcogenides, lamellar compound of MS_2 ($M=Mo, W, Ti$) formula [26,27]. One of the principal advantages of these structures is the absence of edges of the crystals. These particles are called “inorganic fullerene-like nanoparticles” or IF- MS_2 and can be described as several hollow spheres with different diameters fitted together to form a structure that looks like an onion. Thereafter, we will use the term IF to describe the inorganic structure “fullerene-like” and 2H for the corresponding lamellar structure.

The discovery of inorganic fullerene-like, IF, nanoparticles of WS_2 in 1992 and, subsequently, that of MoS_2 in 1993 marked the start of a new field in inorganic synthesis of nanomaterials and their applications. This field has been reviewed by a number of authors in recent years [28-30]. Initially, much of the research effort was focused on the need to elucidate the growth mechanism of IF- MS_2 from the respective metal

oxide precursors, which formed the basis for further study of their properties.

The transfer of promising nanotechnology research results into new industrial technologies still represents a bottleneck. If IF's can be manufactured at commercial-scale, incorporated in a stable fashion into full formulations, and their performance benefits can be sustained under those circumstances, they offer the prospect for some performance breakthroughs not seen since the development of the now ubiquitous anti-wear additives, Zinc Dialkyl Dithiophosphates (ZDDP's), around 70 years ago.

There would indeed then be the potential that the IF nano-materials might facilitate reduction in the use of ZDDP's in lubricants. For engine oil (crankcase) applications, this in turn can assist in the durability and performance of exhaust-treatment and accordingly reduce harmful emissions. Exhaust catalysts tend to become poisoned by the Sulphur and Phosphorous in the conventional additives. Within engine oils and other lubricant applications, such as transmission fluids, and for greases used in rotational bearings, the potential exists for lubricants containing nano-materials to significantly reduce friction and enhance machine durability. This can contribute to substantial energy savings, reduced equipment maintenance and longer machine lifetime.

1.6.1 IF- MoS₂ and IF- WS₂

Tungsten disulphide nanoparticles (WS₂) have received particular interest because, apart from being highly effective in reducing friction and wear between moving parts [31-33], they are inert, non-toxic, non-magnetic and have high resistance to oxidation and thermal degradation [34]. Their positive influence is especially visible in mixed or boundary lubrication regimes [35] when the most severe wear and damage occur.

WS₂ NPs have a multi-layered structure and exist in two forms: 2H and IF (inorganic fullerene-like). In 2H-WS₂, the layers are flat and present 'dangling bonds'(edge effects that cause deterioration of the nanoparticle through oxidation or burnishing) [36], while in IF-WS₂ NPs, the layers are rounded up to form closed, 'onion-like' cages [37]. In the latter, the edge effects are no longer present and the particles are more inert to chemicals. From the tribological point of view, it has been

reported that under high PV (pressure and velocity) conditions, as encountered in most engineering applications, 2H-WS₂ outperform IF-WS₂ NPs, while in relatively low PV, IF are better [38].

Manufacturing of IF-WS₂ nanoparticles (NPs) involves higher temperatures and also reduces their availability to functionalization. For these reasons, 2H-WS₂ NPs could be more convenient to employ as lubricant nanoadditives in high-pressure tribological applications.

Molybdenum disulphide (MoS₂) has been used for many years as a solid lubricant because of its interesting friction-reducing properties related to its crystalline structure. MoS₂ is a lamellar compound made of a stacking of S-Mo-S layers. In each of them, the molybdenum atom is surrounded by six sulfur atoms located at the top a trigonal prism. The distance between two sulfur atoms from two adjacent layers is equal to 0.349 nm [39]. This characteristic was often used to explain easy cleavage between the layers and therefore the lubricating properties of the MoS₂. Atoms inside a layer are strongly bonded (covalent bonds) whereas the sulfur atoms between two consecutive layers are slightly bonded (Van der Waals bonds).

According to some researchers, these weak interlayer bonds are responsible for an easy slip between the layers and could thus explain the friction-reducing properties of MoS₂. On the contrary Sokoloff showed that the slip of two layers one on another is not possible without the presence of dislocations [40]. Figure 1.6 shows a TEM picture of a typical group of IF-MoS₂ nanoparticles. One can clearly notice the asymmetric-oval shape of some of the nanoparticles. The typical size of the nanoparticles is about 50–70 nm, appreciably smaller than the ubiquitous IF-WS₂ obtained by the fluidized-bed reactor which measure about 120 nm [26].

Also, there is almost no observable hollow core in the center of the IF-MoS₂. In contrast the hollow core in the IF-WS₂ nanoparticles occupies almost 30% and in the case of the INT-WS₂ up to 70% of their volume. Another noticeable difference between the two kinds of nanoparticles is that the IF-MoS₂ phase shows a much smaller tendency for agglomeration. The IF-WS₂ phase consists of agglomerates larger than 10 microns containing thousands of nanoparticles each. Furthermore, the forces holding the nanoparticles in the agglomerates together are quite

strong and consequently can not be fully broken even under the action of an ultrasonic horn [40].

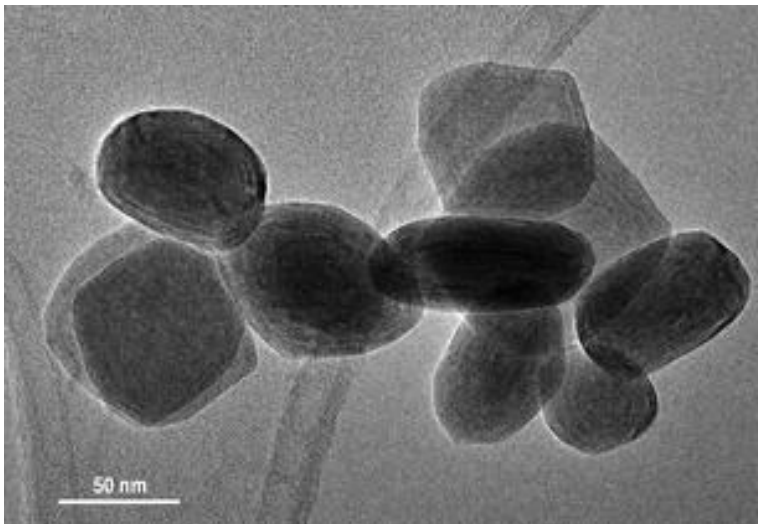


Fig. 1.6 - HRTEM images of IF-MoS₂ nanoparticles

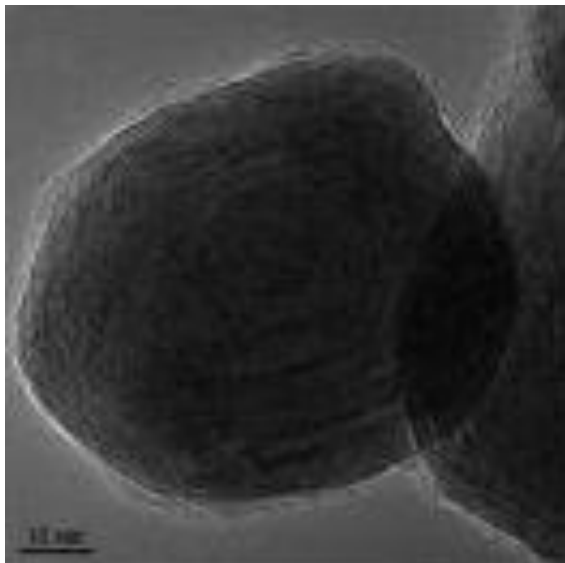


Fig. 1.7 - TEM images of a single IF-MoS₂ nanoparticle

In contrast, the IF-MoS₂ nanoparticles seem to be held by much weaker forces and consist of appreciably smaller agglomerates. This difference can be associated with the apparent better crystallinity and conductivity of the IF-MoS₂ as compared to their tungsten-based counterparts, but further research is under way aiming to quantify these differences. Figure 1.7 shows a TEM image of an individual oval shaped IF-MoS₂ nanoparticle.

It is rather remarkable that, in contrast to the IF-WS₂, the former nanoparticles have almost no empty core and the sulfide layers span the entire volume.

Both graphite and WS₂ (MoS₂) structures belong to the same space group, P6₃/mmc. Figure 1.8 shows the transmission electron microscope (TEM) image of a hollow multiwall and polyhedral IF-WS₂ nanoparticle. The diameter of the hollow void in the center of the multilayered WS₂ nanoparticle is about half the overall diameter of the nanoparticle [42].

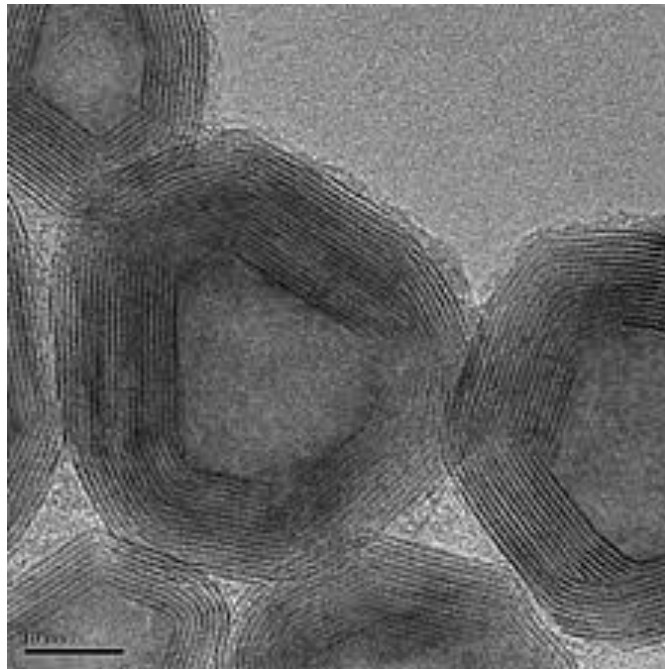


Fig.1.8 - TEM images of IF-WS₂ nanoparticles

1.6.2 IF-MX₂ nanoparticles: lubrication mechanism

The interest of the scientific research is to elucidate the mechanism by which these particular additives act in order to replace those currently in use as anti-friction anti-wear additives.

As in the case of C₆₀, the quasi-spherical closed structure of the IF presents several advantages:

- The absence of edges;
- The size of these objects which is at least twenty times smaller than the 2H-MS₂ powder.

Lamellar structures are often used because adhere easily to surfaces by their flexibility, leading them to conform easily to the topography of asperities.

On the other hand, according to some authors [43] the mechanism of action of inorganic fullerene-like format additives is much more complicated compared to the initial hypotheses. The particles consist of multilayer structures and hollow inside subjected to a load uniaxial compression deform and begin to delaminate releasing of the layers to cover the area of contact; exfoliation involves the change of the shape from spherical to ellipsoidal and finally the particle collapses. Furthermore, the nanometer size of the particles also enables them to penetrate in the asperities and porosities of surfaces. These asperities thus act as reservoirs and can regularly supply the contact area during friction. Rapoport et al. have already expressed this hypothesis [44,46].

Three main mechanisms which lead to reduced friction and wear are discussed in the literature (43):

- **Rolling:** the IF nanoparticle acts as a ball bearing between the mating surfaces, as shown in Figure 1.9a.
- **Sliding:** Given the low surface energy of its basal (001) plane and its robustness, the IF nanoparticle acts as a separator providing low friction and facile shearing between the mating surfaces, as shown in Figure 1.9b.

- **Exfoliation and transfer of films:** exfoliated layers from the IF NP are deposited on the asperities of the mating surfaces providing easy shearing, as shown in Figure 1.9c.

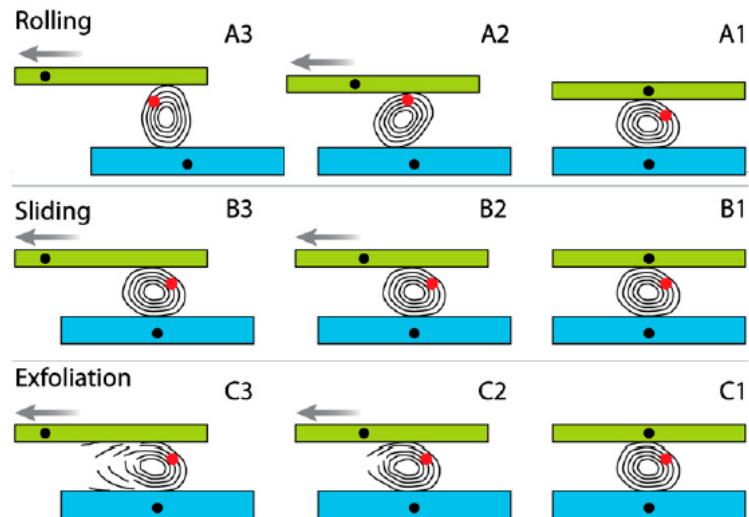


Fig. 1.9- The three main friction mechanism of multilayered IF-NP which are discussed in literature: rolling (a), sliding (b), and exfoliation (c). The bottom surface is stationary while the upper surface is moving to the left. The red mark is a point of reference.

The main action mode of IF-MoS₂ is probably based on an exfoliation of their external sheets to release single sheets inside the contact area. These sheets lead to a reduction of the friction coefficient. The results of recent scientific works [47,48] show that the action mechanism of IF-WS₂ is identical to that of IF-MoS₂, namely an exfoliation of the layers external to the IF and the formation of very thin films on surfaces.

Schwarz et al. [49] studied the effect of adhesion due to Van der Waals forces on the tribological properties of fullerenes. These forces are proportional to the radius of the particles and independent of the number of layers. Adhesion supports the exfoliation of the particles, but does not trigger it. The exfoliation of fullerenes is due to the pressure exerted on the particle, which destabilizes the structure, so that a critical pressure being necessary. Exfoliation occurs only under adhesion conditions and

concerns only the first layers. Layers then adhere on surfaces, which minimizes the edge effects and leads to the formation of film on surfaces.

The structural deformation gives rise to dislocation and dislodging of MS_2 nanosheets from the NP surface. The external nanosheets of the IF-NP, a few monolayers thick each [50], are gradually transferred onto the substrate, thus reducing the friction between the two mating surfaces. Furthermore, this process reduces the local heating, and hence the plastic deformations of the underlying metal surface and its oxidation, thereby slowing down the wear [51]. Extensive exfoliation eventually damages the IF-NP and causes degradation of the tribological behavior. However, oxidation of the sulfide NP transforms it into a tungsten oxide film, which by itself is a good lubricant, Figure 1.10.

During the sliding motion the IF NP preserves its shape under normal and shear stress without rolling or exfoliation. Sliding is regarded as a very low friction mechanism when it occurs between weakly interacting, smooth surfaces [52].

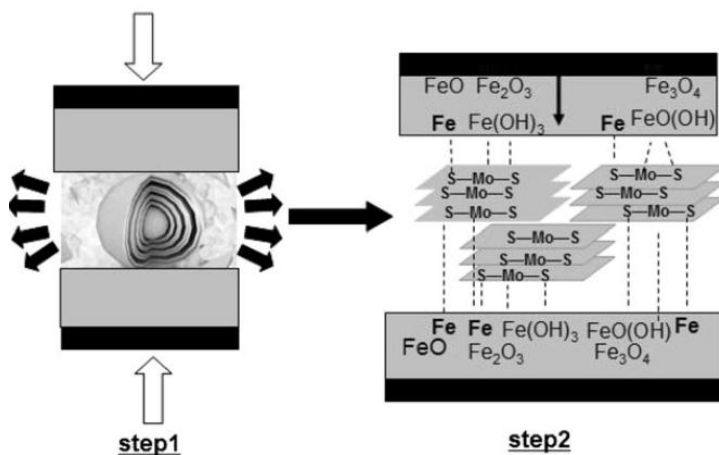


Fig. 1.10- Possible tribochemical mechanism of IF-MoS₂ nanoparticles on steel surfaces

Nonetheless if the sliding particles are made of a hard material, degradation of the mating surfaces by abrasion, plowing, or indentation is inevitable [53]. In this case the friction and wear may increase dramatically with time.

The possibility to have a rolling process that is able to enhance the lubricating properties of the spherical particles has already been advanced by Tenne [54]. This mechanism could be increasingly possible in light of the results presented in this thesis. Actually, this mechanism of lubrication is related to the spherical (or spheroidal) shape of the fullerenes that would allow them to behave as microscopic ball bearings. Thus, the authors suggested that an additional rolling friction process could also play a role and enhance the good lubricating properties of the particles. According to the authors, this process could play a more predominant role for well-crystallized particles. These nanoparticles would present higher mechanical resistance and would behave as genuine nano-ball bearings precluding gradual deformation and exfoliation.

It was postulated that the quasi-spherical IF NP are ideally suited to provide this kind of friction mechanism [55]. However, no direct evidence to that effect has been established, so far. In fact, in latter works, the rolling mechanism was debated and considered to be of minor relevance. Recently, in situ uniaxial nanocompression tests of individual IF-WS₂ (MoS₂) NP using TEM [56] and high resolution scanning electron microscope (HRSEM), were published. These works renewed the discussion on the significance of rolling friction on the tribological behavior of IF NP.

Moreover, Lahouij et al [57] investigated the influence of the crystallinity on the lubricating properties of IF-MoS₂ nanoparticles in the presence of steel surfaces. The authors highlighted that the lower the crystallinity of the particles, the better their lubricating properties. The explanation for this finding was that both the amorphous character of the particles and the presence of defects facilitate the exfoliation of the outer layers under external pressure and, therefore, ameliorate the tribological performance of the particles. This finding is consistent with the exfoliation lubrication mechanism of the IF structures.

Nowadays, the use of techniques that are able to visualize in real time the behavior of individual nanoparticles within the tribological contact and during the mechanical sollicitation and access the mechanical properties of nanoparticles is necessary to further our understanding of the dominant lubrication mechanism(s) of these nanoparticles. Recently, some research groups have developed new original techniques based on electron microscopy to observe in real time the behavior of nanoparticles

within the contact and to elucidate the tribological mechanisms of individual nanoparticles. Thus, Tevet et al [58] used a high resolution scanning electron microscope (HRSEM) associated with an AFM probe to apply to individual nanoparticles in situ axial nanocompression and shearing forces. The authors concluded from their experiments that rolling was an important lubrication mechanism for IF-WS₂ in the relatively low range of normal stress (0.96 ± 0.38 GPa). Sliding was shown to be relevant under slightly higher normal stress, where the spacing between the two mated surfaces does not permit free rolling of the nanoparticles. Exfoliation of the IF nanoparticles would become the dominant mechanism for higher pressure (1.2 GPa) and shear. Still using HRSEM, Tevet et al [43] showed that layered inorganic materials, such as WS₂ and MoS₂ that form seamless hollow closed nanostructures are, due to their small size and layered structure, able to withstand very high elastic stress. The compression failure strength of these nanoparticles was found to be as high as 1–2.5 GPa.

Moreover, the stiffness of the faceted nanoparticles was found to be lower than that of a spherical nanoparticle, due to higher stress concentration at the corners. These studies provide very interesting information in the form of mechanical properties and behavior of nanoparticles in the contact. Unfortunately, the use of HRSEM does not offer a good image quality for the observation of any structural modification of the nanoparticles under compressive and/or shear stress.

The use of a high resolution transmission electron microscope (HRTEM) is much more appropriate for very detailed observations at the atomic scale. Recently, Lahouij et al [57, 59] investigated in real time the deformation and degradation behavior of spherical and well crystallized single inorganic fullerene nanoparticles of MoS₂ under compression and shear stress using an HRTEM equipped with a nanoindentation holder.

For the first time, the exfoliation of the outer sheets of a fullerene nested structure was imaged. However, it was found that well crystallized and round shaped nanoparticles were difficult to exfoliate. Under 1–1.5 GPa uniaxial pressure, it was found that the shape of single IF-MoS₂ nanoparticles was preserved and only external layers were exfoliated. A uniaxial pressure higher than 1.5 GPa was necessary to crush the particles. The resistance of the IF-MoS₂ to exfoliation was attributed to its good mechanical properties due to its well crystallized structure and the round shape of the particle. These results are consistent with those

obtained by Tevet et al [58] which suggest higher compression failure strength for spherical particles compared to faceted particles.

1.7 Tools and methods

A rotational disc tribometer was used in this thesis to explore the tribological behavior of the different testing samples (Figure 1.11a and b).

This tribometer setup allows applying different tribopair parameters, which is desirable in order to study the different regimes in the Stribeck curve, i.e., boundary, mixed and elastohydrodynamic lubrication conditions. The normal force was applied on the mating surfaces by a lever system and could be varied in the range of 0–100 N.

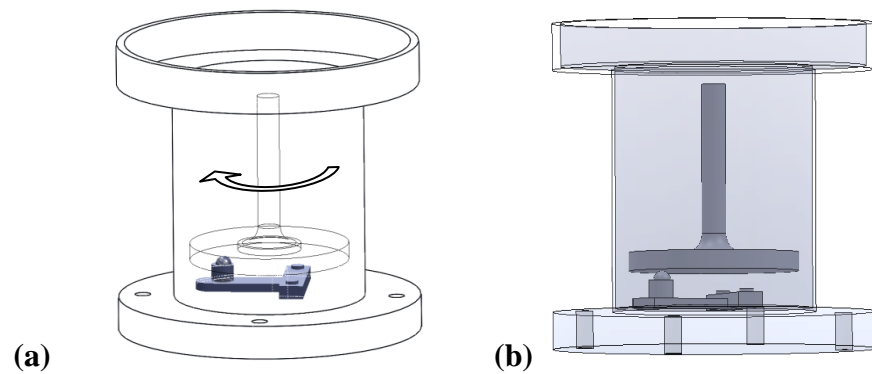


Fig. 1.11-Tribopair functional scheme. Different 3D view (a) and (b).

The spinning shaft was driven by a brushless motor with speed variable up to 3000 rpm. The measurement of the normal force was performed through a force sensor arranged between the load lever and the lower specimen holder. The lubricant average temperature has been controlled through a NiCr-Ni thermocouple in the oil reservoir and an electric resistance. The investigated contact type was composed of an upper rotating X155CrVMo12-1 steel disc of hardness 60 HRC, roughness of $R_a=0.5$ μm and 105 mm in diameter. A lower X45Cr13 steel ball, 52–54 HRC, 8 mm diameter was immersed completely in a temperature-controlled 220 ml lubricant bath (Figure 1.12a-d). The following average hertzian pressures were used at the ball/disc interface

with normal load given in brackets: 1.17 GPa (30 N), 1.47 GPa (60 N), 1.68 GPa (90 N).

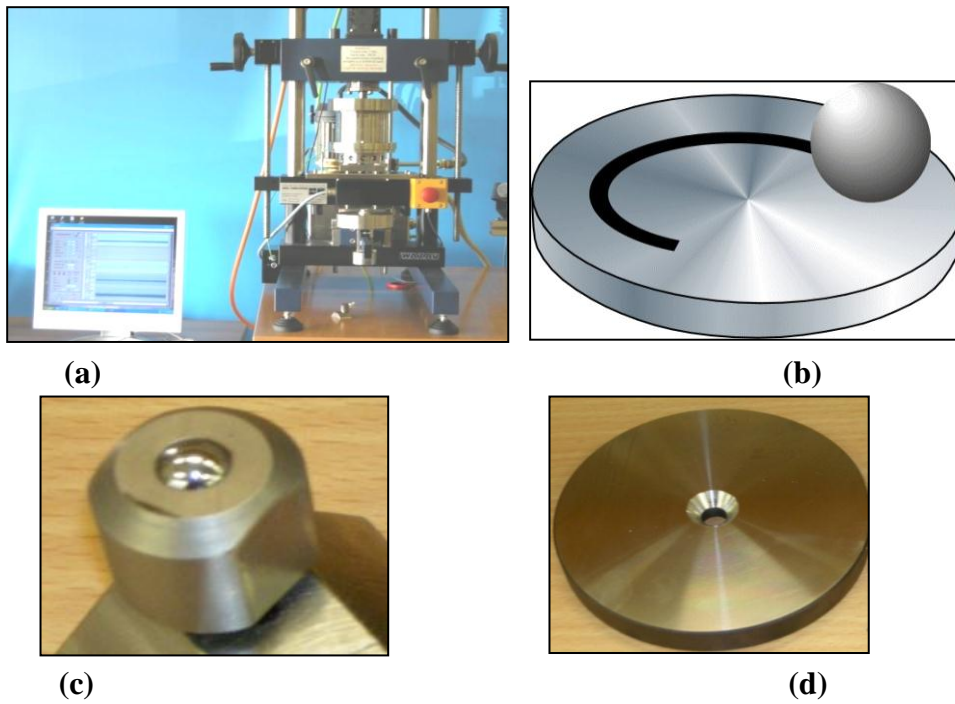


Fig. 1.12- (a) Wazau TRM 100 rotational tribometer; (b) tribological contact, (c) ball specimen and holder; (d) steel disk

1.7.1 Friction test-Stribeck curve

A speed-sweep test at constant load on a wide speed range has been designed to cover broad operating conditions with the purpose of minimizing the modification of the tribopair steel surfaces in order to get frictional results in comparable surface topography conditions. For this reason, the time extension of the tests was limited to 16 min. The disc speed rose up to 2.1 m/s in the first 4 min and dropped to zero in the following 4 min and this speed pattern was repeated twice. The tests were performed for three different temperatures, i.e., 25, 50 and 80 °C.

The current design of this experiment allowed to cover slow to high speed range and to obtain a complete Stribeck frictional graph. In this way, it was possible to investigate two different lubrication regimes. In fact, according to the theory, boundary lubrication regime is expected to appear at the lowest speed as well as mixed lubrication as superposition of boundary and elastohydrodynamic regimes at higher ones [4,5].

Another advantage of this setting was the high reproducibility of the friction coefficient (CoF) in several ramps and the good averaging-out of the noise-level. Also, since the sliding acceleration was very low along each speed ramp there was no relevant fluid inertial phenomena and transducers dynamic effect, i.e., each “CoF vs. speed” curve was obtained in a quasi-steady state condition.

The friction coefficient is the average value calculated on twenty successive samples acquired within a narrow range around selected speed values. Standard deviation calculations are also depicted on the plots.

About the speed control of the upper steel disc, obtained thanks to the good tracking of a brushless motor, a specific test with linearly variable speed with a ramp shape has been designed. It aimed at cover a wide range of sliding velocity between the mating steel surfaces avoiding long running - minutes or more – for a given velocity level, in the same time. In fact, previous tests in similar hertzian pressure have shown a naturally decreasing friction loss factor over a long duration test with marked effect for higher normal load, due to a long term surface running-in.

In some case, the load “history” of a given pattern tests could lead a similar effect of the additive coating formation on steel surfaces: a friction coefficient decreasing with respect to the benchmark lubricant. The experimenter could conclude with not-physical conjecture and weak explanation of friction diminishing phenomenon. For a better understanding of the tribometer dynamic response over a speed “sweep” test, a ring sample in Teflon with known properties has been used as benchmark material for dry frictional tests to measure the instrument delay introduced by the torque sensor. In fact, frictional torque acting on the specimen holder is acquired by a set of strain gages with uncertainty less than 1% and fed to a digital board for computer data processing and indirect friction coefficient calculation.

Since the tests aimed at comparing friction behaviour for mating

surfaces with unmodified roughness, their time extension was limited to 12-24-60-120 s. The Figure 1.13 shows a ramp test completed in 120 s; the disk speed raised from 0 to 800 rpm ($v_s = 2.3$ m/s) in the first 60 s and dropped to zero again in the second 60 s-part. The friction coefficient (μ) of the Teflon exhibited no dependence regard sign of sliding acceleration.

Furthermore, different sloped-flat speed profiles allowed an estimation of the time required by friction coefficient to attain the asymptotic value at constant speed. The overall response of the frictional torque measuring may be approximated by a first order system time response with 0.5s time constant. Dynamic response and instrument hysteresis effects, shown in Figure 1.14 at 0.04 (solid line) and 0.08 (dot line) m/s^2 sliding acceleration, have been investigated to get assessment about transducers delays.

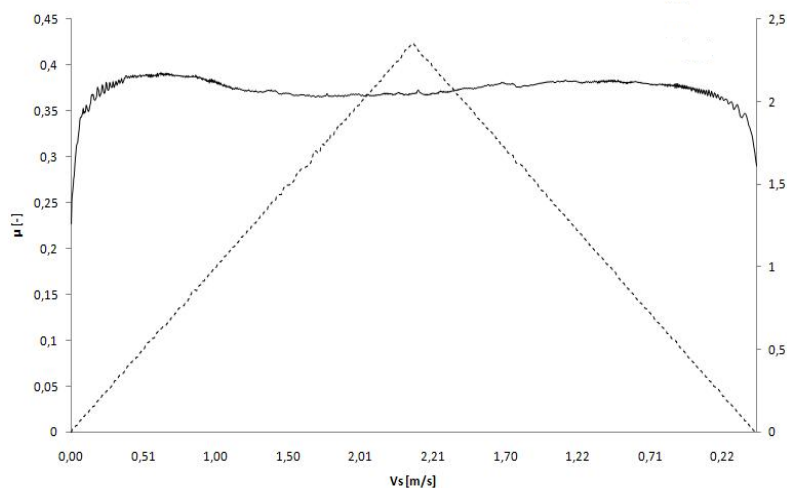


Fig. 1.13- Graphs superposition: friction coefficient μ (solid line) and sliding speed (dot line) ramp.

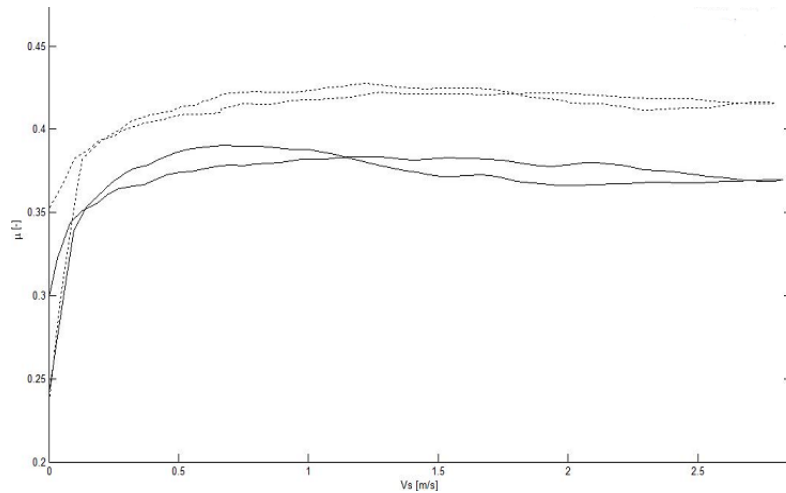


Fig. 1.14- Hysteresis cycles in μ measuring for two tests

According to the theory and the characteristic parameters of such a test protocol, no inertial effects of the fluid appear as well as no dynamic effect of transducers have been exhibited. In fact, since acceleration is equal to $1.7 \cdot 10^{-2} \text{ ms}^{-2}$, the frictional torque acquired during the sliding motion test along a speed ramp from 60 mm/s to 2.1 m/s may be considered as the steady state one. As will be clearer in the results section, the minimum sliding speed value does not allow the test campaign to cover boundary lubrication regime (Figure 1.14).

The benchmark tests test provided a high grade of reproducibility since the standard deviation of friction coefficient calculated on a set of 20 data at the same sliding speed was of 10^{-3} order of magnitude.

The main advantages of the frictional experiments designed in such a way are the following:

- Test duration for a complete characterization of each sample around 2 hours;
- High speed range covered;
- No relevant fluid inertial phenomena and transducers' dynamic effect, since acceleration is very low along each speed ramp, i.e., each couple CoF/speed is taken in quasi-steady state condition;
- Low effect of the progressive tribo-pair surface conforming, that strongly influence the "delta", i.e. the actual gain of nanoparticles;

- High reproducibility of CoF on several ramps;
- Good averaging of measurement noise;
- Good correlation between CoF and wear.

The measured data have been presented according to the Stribeck curves representation, by collecting the couples sliding speed/friction coefficient in which the latter is the average value calculated on twenty measures at the same speed value. Each measure was obtained through a set of ten upward/downward “sweep” operations, i.e. speed ramps.

In the canonical Stribeck curve the friction coefficient is related to a Stribeck number $\eta v/p$ where η is the dynamic viscosity, v is the sliding velocity, and p is the mean contact pressure at the sliding interface. The general shape of the Stribeck curve depicting the three main lubrication regimes (boundary, mixed and hydrodynamic) is common for every lubricated sliding system, but the Stribeck numbers at which the transition from a certain regime to another appears are characteristic for each individual tribopair. Since the CoF plots are given in this report with sliding speed on the abscissa. The range of the Stribeck number for the presented results is: $4.0 \cdot 10^{-13} \text{ m}^{-1}$ - $1.8 \cdot 10^{-1} \text{ m}^{-1}$. In the case of the experiments of this section, an useful indication for the average Stribeck number calculation is given by the formula $3.6 \cdot 10^{-11} \cdot v [\text{m}^{-1}]$, with v in m/s. Due to the high contact pressures of these tests, mixed lubrication regimes was obtained for the the great part of the sliding velocity range, with no transition to fully thin film lubrication that in these test conditions should be introduce characteristic pressure shape and frictional behaviour of EHL regime.

1.7.2 Friction and wear in steady-state tests

Long running frictional tests have been performed to analyze the influence of the nanoparticles on wear behavior of the steel ball/disc pair. For this test, constant values for average hertzian pressure, temperature and speed were 1.68 GPa, 25–80°C, 5.0 mm/s–0.50 m/s, respectively, resulting in four combinations.

This friction/wear test has proven to produce for a given lubricant sample, after a brief running-in, friction coefficient values with low variance around the average [26].

1.7.3 Surface analysis

The worn surface of the steel ball has been analysed by means of both an optical microscope, at the beginning of the present research, and later with a confocal profiler (Figure 1.15) to measure the wear scar diameter (WSD), the contact surface roughness and to acquire the ball worn surface topography.

Confocal profilers have been developed to measure the surface height of smooth to very rough surfaces. A confocal imaging system provides high contrast images by eliminating out-of-focus light. The sample is scanned vertically in steps so that every point on the surface passes through the focus. The height of the surface at each pixel location is found by detecting the peak of the narrow axial response. As only local areas of the surface are illuminated simultaneously, in-plane raster scanning is required to build up the axial response (i.e. the confocal image) at each vertical step.



Fig. 1.15- Confocal profiler Sensofar Neox PLu

In Table 1.1 are reported the specification of the 100X objective used for the surface acquisition in this report.

Confocal objective 100X	
Working Distance (mm)	1.0
NA	0.90
FOV (μm)	127.32 x 95.45
Spatial sampling (μm)	0.17
Optical Resolution (L&S) (μm)	0.15
Maximum Slope	51°
Vertical Resolution (nm)	<2
Scanning speed ($\mu\text{m/s}$)	1 – 16
Confocal Frame rate (frame/s)	12.5 fps

Tab. 1.1- Confocal objective profiler characteristics

Finally, in some cases for the surface analysis of the wear scar, with the aid of Industrial Chemistry Department at University of Salerno the following tools were used for the surface analysis:

- Scanning electron microscope (SEM) model ‘LEO Supra-55 VP, ZEISS, 7426’ at 10 kV;
- Energy dispersive X-ray spectroscopy (EDS)—model ‘Oxford INCA’;
- X-ray diffractometer (XRD) model ‘Ultima 3 Rigaku X-ray diffractometer’, The XRD data was analyzed with the assistance of MDI Jade 7.0 program.

SEM and EDS analysis were used in order to quantify and determine the spreading uniformity of the IF and the platelets on the wear scar. For this purpose, all the area of the wear scar was mapped and scanned using 20–50 μm spots. XRD was used for verifying the EDS quantitative results.

In particular, I would like to thank **Prof. Maria Sarno**, for the great contribution to in this part of my research activity.

References

- [1] Bowden, F. P., Tabor, D., *The Friction and Lubrication of Solids*, Clarendon Press, Oxford, 1950.
- [2] Bhushan, B., *Handbook of Micro/Nano Tribology*, Second Edition. CRC Press, Technology & Engineering, 1998.
- [3] Bhushan, B., *Introduction to Tribology*, Wiley, 1st edition, 2002.
- [4] *Handbook of Lubrication and Tribology: Theory and Design*, Second Edition, Volume 2, CRC Press, 2012.
- [5] N. Ohmae, S. Mori, J.M. Martin, *Micro and nanotribology*, Amer Society of Mechanical, 2005.
- [6] Martin, J. M., Ohmae, N., *Nanolubricants*, Tribology in Practice Series-Tribology series, Volume 13, Wiley, 2008.
- [7] Bhushan, B., *Modern Tribology Handbook Mechanics & Materials*, CRC Press; 1st edition, 2000.
- [8] Reynolds, O., *On the Theory of Lubrication and Its Application to Mr. Beauchamp Tower's Experiments, Including an Experimental Determination of the Viscosity of Olive Oil*. Phil. Trans. R. Soc. Lond., 1886.
- [9] Gohar, R., *Elastohydrodynamics*, Computing in Engineering Mechanical Engineering Series, World Scientific Ed., 2001.
- [10] Andersson, S., Söderberg, A., Björklund, S., *Friction models for sliding dry, boundary and mixed lubricated contacts*, Tribology International, Volume 40, Issue 4, pp. 580–587, 2007.
- [11] Buschow, K.H.J., Cahn, R.W., Flemings, M.C., Ilshner, B., Kramer, E.J., Mahajan, S., “Inorganic Nanotube Materials”, *Encyclopedia Mater., Sci. Tech.*, Eds. Subj. Ed. P. Day, Elsevier, Amsterdam, 5, 4108-4110, 2001.
- [12] Chinas-Castillo F., Spikes H.A., *Mechanism of action of colloidal solid dispersion*, Journal of Tribology, Vol. 125 pag. 552-557, 2003.
- [13] Tenne, R., Zettl, A., *Nanotubes from Inorganic Materials*, in *Carbon Nanotubes*, Topics in Appl. Phys., 80, 81-112, Eds. M.S. Dresselhaus and P. Avouris, Springer Verlag, 2000.
- [14] Iijima, S., *Direct observation of the tetrahedral bonding in graphitized carbon black by high resolution electron microscopy*,

- Journal of Crystal Growth, Volume 50, Issue 3, Pages 675-683, 1980.
- [15] Savage, R. H., Graphite lubrication, *Journal of Applied Physics*, 19 (1), 1–10, 1948.
- [16] Abe, M., Kataura, H., Kira, H., Kodama, T., Suzuki, S., Achiba, Y., Kato, K., Takata, M., Fujiwara, A., Matsuda, K. and Maniwa, Y., Structural transformation from single-wall to double-wall carbon nanotube bundles, *Physical Review B*, 68, 041405, 2003.
- [17] Kroto W., Heath J.R., O’Brein S.C., R.F. Curl, and R.E. Smalley: C₆₀: Buckminster fullerene, *Nature* 318, 162, 1985.
- [18] Pierson, O., *Handbook of Carbon, Graphite, Diamonds and Fullerenes*, 1993.
- [19] Tzeng, Y., Very low friction for diamond sliding on diamond in water, *Applied Physics Letters*, 63, 3586, 1993.
- [20] Grill, A., Tribology of diamondlike carbon and related materials: an updated review, *Surface and Coatings Technology*, 94–95, 507–513, 1997.
- [21] Erdemir, A. and Donnet, C., Tribology of diamond and diamond-like carbon films: an overview, in *Wear– Materials, Mechanisms and Practice* (ed. G. W. Stachowiak), John Wiley & Sons, Ltd, Chichester, 2005.
- [22] Kroto, H.W., Heath, J.R., O’Brien, S.C., Curl, R.F. and Smalley, R.E., C₆₀: Buckminsterfullerene, *Nature*, 318, 162–163, 1985.
- [23] Ugarte, D., Curling and closure of graphitic networks under electron-beam irradiation, *Nature*, 359, 707–709, 1992.
- [24] Qin, L.C., Iijima, S., Onion-like graphitic particles produced from diamond, *Chemical Physics Letters*, 262, 252–258, 1996.
- [25] Tomita, S., Burian, A., Dore, J. C., LeBolloch, D., Fujii, M. and Hayashi, S., Diamond nanoparticles to carbon onions transformation: X-ray diffraction studies, *Carbon*, 40(9), 1469–1474, 2002.
- [26] Cohen S., Feldman Y., Cohen H., Tenne R., Nanotribology of novel metal dichalcogenides, *Applied Surface Science* 144–144, 1994.
- [27] Tenne R., Remskar M., Enyashin A., Seifert and G., *Inorganic Nanotubes and Fullerene-Like Structures (IF)*, 2008.

- [28] Tenne, R., Inorganic Nanoclusters with Fullerene-Like Structure and Nanotubes, in *Progress in Inorganic Chemistry*, Ed. Kenneth D. Karlin, John Wiley&Sons, 50, 269-315, 2001.
- [29] R. Tenne, L. Margulis, M. Genut, G. Hodes, Polyhedral and cylindrical structures of WS₂, *Nature*, 360, 23, 1992.
- [30] L. Rapoport, Y. Bilik, Y. Feldman, M. Homyonfer, S.R. Cohen, R. Tenne, Hollow nanoparticles of WS₂ as potential solid-state lubricants, *Nature*, 387, 791-793, 1997.
- [31] L. Rapoport, Y. Bilik, Y. Feldman, M. Homyonfer, S.R. Cohen, R. Tenne, Hollow nanoparticles of WS₂ as potential solid-state lubricants, *Nature*, 387, 791-793, 1997.
- [32] Deepak, F.L., Margolin, A., Bar-Sadan, M., Feldman, Y., Tenne, R., Fullerene-Like (IF) WS₂ Nanoparticles and Nanotubes by the Vapor-Phase Synthesis of WCl₆ and H₂S, *Nanotechnol.* 19, 095601, 2008.
- [33] Moshkovith, A., Perfiliev, V., Verdyan, A., Popovitz-Biro, R., Tenne, R., Rapoport, L., Sedimentation of IF-WS₂ Aggregates and a Reproducibility of the Tribological Data, *Tribol. Int.* 40, 117-124, 2007.
- [34] Wiesel, I., Arbel, H., Albu-Yaron, A., Popovitz-Biro, R., Gordon, J.M., Feuermann, D., Tenne R., Synthesis of WS₂ and MoS₂ Fullerene-Like Nanoparticles from Solid Precursors, *Nano Res.* 2, 416-424, 2009.
- [35] Rapoport L., Leshchinsky V., Lapsker I., Volovik Y., Nepomnyashch O., Lvovsky M., Popovitz-Biro R., Feldman Y., Tenne R., Tribological properties of WS₂ nanoparticles under mixed lubrication, *Wear*, 255, 78-12, 785-793, 2003.
- [36] Rapoport L., Moshlovich A., Perfilyev V., Tenne R., On the efficacy of IF-WS₂ nanoparticles as solid lubricant: The efficacy of the loading scheme, *Tribol. Lett.* 28, 81-87, 2007.
- [37] Drummond C., Alcantar N.A., Israelachvili J., Tenne R., Golan Y., Microtribology and Friction-Induced Material Transfer in WS₂ Nanoparticle Additives, *Adv. Funct. Mater.*, 11, 348-354, 2001.
- [38] Rapoport L., Nepomnyashchy O., Lapsker I., Verdyan A., Moshkovich A., Feldman Y., Tenne R., Behavior of fullerene-like WS₂ nanoparticles under severe contact conditions, *Wear*, 259, 2005.

- [39] Deepak, F.L., Margolin, A., Bar-Sadan, M., Popovitz-Biro R., Tenne, R., MoS₂ Fullerene-Like Nanoparticles and Nanotubes Using Gas Phase Reaction with MoCl₅, *Nano* 1, 167-180, 2006.
- [40] Enyashin, A.N., Gemming, S., Bar-Sadan, M., Popovitz-Biro, R., Hong, S.Y., Prior, Y., Tenne, R., Seifert, G., Structure and Stability of Molybdenum Sulfide Fullerenes, *Angew. Chem. Int. Ed.* 46, 623-627, 2007.
- [41] C. Altavilla, P. Ciambelli, M. Sarno, M.R. Nobile, C. Gnerre, E. Somma, V. D'Agostino, A. Senatore, V. Petrone, Tribological and rheological behaviour of lubricating greases with nanosized inorganic based additives, in: Proc. of the 3rd European Conference on Tribology, Ecotrib 2011 and 4th Vienna International Conf. on Nano-Technology Vienanno, pp. 903-908, 2011 Vienna 2011.
- [42] M. Bar-Sadan, A.N. Enyashin, S. Gemming, R. Popovitz-Biro, S.Y. Hong, Yehiam Prior, G. Seifert and R. Tenne, Structure and Stability of Molybdenum Sulfide Fullerenes, *J. Phys. Chem. B* 110, 25399-25410, 2006.
- [43] Tevet, O., Von-Hute, P., Popovitz-Biro, R., Rosentsveig, R., Wagner H. D., Tenne, R., Friction Mechanism of Individual Multilayered Nanoparticles. *Proc. Natl. Acad. Sci.* 108, 19901-19906, 2011.
- [44] Rapoport L., Bilik Y., Feldman Y., Homyonfer M., Cohen S.R., Tenne R., Hollow nanoparticles of WS₂ as potential solid-state lubricants, *Nature*, 387, 791-793, 1997.
- [45] Rapoport L., Feldman Y., Homyonfer M., Cohen S.R., Sloan J., Hutchison J.L., Tenne R., Inorganic fullerene-like material as additives to lubricants: structure-function relationship, *Wear*, 225-229, 975-982, 1999.
- [46] L. Joly-Pottuz, F. Dassenoy, M. Belin, B. Vacher, J. Martin, N. Fleischer, Ultralow-friction and wear properties of IF-WS₂ under boundary lubrication, *Tribology letters*, 18, 477-485, 2005.
- [47] M. Chowalla, G.A.J. Amaratunga, Thin films of fullerene-like MoS₂ nanoparticles with ultralow friction and wear, *Nature*, 407 164-167, 2000.
- [48] J. Tannous, F. Dassenoy, A. Bruhacs, W. Tremel, Synthesis and Tribological Performance of Novel Mo_xW_{1-x}S₂ (0≤x≤1) Inorganic Fullerenes, *Tribology letters*, 37, 83-92, 2010.

- [49] Schwarz, U.S., Komura, S., Safran, S. A., Deformation and tribology of multi-walled hollow nanoparticles, *Europhys. Lett.*, 50, 6, pp. 762–768, 2000.
- [50] R. Rosentsveig, A. Gorodnev, N. Feuerstein, H. Friedman, A. Zak, N. Fleischer, J. Tannous, F. Dassenoy, R. Tenne, Fullerene-like MoS₂ Nanoparticles and Their Tribological Behavior, *Tribology Letters*, 36, 175-182, 2009.
- [51] R. Greenberg, G. Halperin, I. Etsion, R. Tenne, The Effect of WS₂ Nanoparticles on Friction Reduction in Various Lubrication Regimes, *Tribology Letters*, 17, 179-186, 2004.
- [52] Moshkovith, A., Perfiliev, V., Lapskerm, I., Fleischer, N., Tenne, R. and Rapoport, L., Friction of fullerene-like WS₂ nanoparticles: effect of agglomeration, *Tribology Letters*, 24, 2006.
- [53] Cizaire, L., Vacher, Le Mogne, B. T., Martin, J. M., Rapoport, L., Margolin, A., Tenne, R., Mechanism of ultra-low friction by hollow inorganic fullerene-like MoS₂ nanoparticles, *Surface and Coating Technology*, 160, 2002.
- [54] Rapoport, L. Moshkovich, A. Perfiliev, V. Laikhtman, A. Lapsker, I. Yadgarov, L. Rosentsveig R. and Tenne, R., High Lubricity of Re-Doped Fullerene-Like MoS₂ Nanoparticles, *Trib. Lett.* 45, 257-264, 2012.
- [55] Rosentsveig, R., Tenne, R., Gorodnev, A., Feuerstein, N., Friedman, H., Fleischer, N., Tannous Dassenoy, J. F., Fullerene-Like MoS₂ Nanoparticles and Their Tribological Behavior, *Tribology Lett.* 36, 175-182, 2009.
- [56] Lahouij, I., Dassenoy, F., de Knoop, L., Martin, J.M., Vacher, B., In situ TEM observation of the behavior of an individual fullerene-like MoS₂ nanoparticle in a dynamic Contact. *Tribol Lett.*, 42:133–140, 2011.
- [57] Lahouij, I., Dassenoy, F., Vacher, B., Martin, J.M., Real time TEM imaging of compression and shear of single fullerene like MoS₂ nanoparticle, *Tribol Lett* 45, 131-141, 2012.
- [58] Tevet, O., Goldbart, O., Cohen, S. R., Rosentsveig, R., Popovitz-Biro, R., Wagner, H.D., Tenne, R., Nanocompression of individual multilayered polyhedral nanoparticles. *Nanotechnology*, 21, 365705 –365711, 2010.

- [59] Lahouij, I., Bucholz, W., Vacher, E., Sinnott, B., Martin, S. M., Dassenoy, F., Lubrication mechanisms of hollow-core inorganic fullerene-like nanoparticles: coupling experimental and computational works, *Nanotechnology*, 23, 37, 375701, 2012.

CHAPTER 2

Nanoparticles as additives for lubricant

Due to growing environmental concerns and fuel efficiency demands, investigations of low-friction materials and lubricants have increased in the last two decades. A significant portion of these research activities has been directed towards the use of nanoparticles (carbon based structures, inorganic fullerenes and metal nanoparticles) [1–7]. These nanoparticles are very attractive novel lubricant additives because of their nanoscale size, which allows them to penetrate contacts of diverse geometries, fill the gaps between contact asperities and ultimately form a protective boundary film, persistent under high pressure. For this reason, a vast array of nanoparticles has been used in published research to investigate their effect on friction or wear in tribological contacts [8,10]. In this chapter, the tribological performances obtained for oil lubricant formulated with inorganic (IF-WS₂), inorganic-doped (IF-Mo:ReS₂) and organic (graphene) nanoparticles have been presented.

2.1 INORGANIC NANOADDITIVES: IF-MOS₂

Over the past few years, inorganic fullerene-like (IF) nanoparticles of metal dichalcogenide MX₂ (M = Mo, W, etc.; X = S, Se), materials with structures closely related to nested carbon fullerenes and nanotubes, have been synthesized [10-12]. The IF are multi-walled hollow nanoparticles, seamless, quasi-spherical, highly elastic and chemically stable [13]. Due to their low surface energy, high chemical stability, nanometric size, spherical shape, and weak intermolecular bonding, their use as lubricant additives was suggested [14]. Their efficacy for tribological applications was demonstrated in many papers [15,16]. It was shown that the addition of small amounts of IF-MoS₂ or IF-WS₂ into a lubricating oil greatly improve the tribological properties of the lubricant.

The present research activity has been developed in the context of the “AddNano” project, this project is partially funded by European Commission within the 7th Framework Programme (NMP-2008-1.2.1,

under grant agreement n° 229284). The AddNano consortium combines technological expertise and industrial representation from all parts of the prospective value chain to investigate the development of new nano-based lubricants. The AddNano Project aim is to develop, scale-up and prove pilot lines to produce optimised nano-materials which may then be straightforwardly dispersed into oils. Advanced dispersing and stabilising technologies have been developed in this project, and also extended into practical “full-formulation” technology according to the end-user applications. The overall objective of the tribological activities is to assess the tribological characteristics of newly formulated lubricants under realistic conditions, i.e. similar to those experienced in the final application, and thus establish their performance in comparison to traditional lubricants. The specific objectives in relation to the crankcase application are to:

- study the tribological properties of newly formulated engine oils containing nanoparticles with the aim of establishing the mechanism through which they act in fully formulated oils;
- evaluate the impact of the chemical nature of the base oil and different additives such as dispersants, anti-wear, anti-friction, anti-foam agents, antioxidants;
- study the effect of the environment on the performance of the fully formulated product by evaluating the performance of fully formulated product under realistic conditions for the crankcase application.

Other objectives are:

- to develop environmentally well-managed production methods that avoid potential for impact on production-workers health, and release of harmful chemicals into the environment;
- to identify and use raw materials for the synthesis of IFs that are suitable for mass production of IF-based lubricants;
- to prepare new process design methods based on improved understanding of the effects of powder and liquid properties on dispersion and de-agglomeration operations (scale-up of mixing equipment from laboratory scale to industrial scale);

- to design and select process equipment for the industrial scale production of lubricants incorporating nanoparticles using design rules and numerical models developed within the project.

2.1.1 The samples

The tested samples are named as ARL1_XX_YY, where XX represents the code for the additive concentrate and YY represents the nanoparticles concentration, while ARL1 is the lubricant oil. The base oil has been provided by Fuchs, the inorganic nanoparticles have been synthesized by CIDETEC and Nanomaterials Ltd. (NML), while the dispersion have been made by BHR. The tested samples are reported below in the Table 2.1.

SAMPLE ID	COMPOSITION
ARL1	Reference 5W30 oil from Fuchs
ARL1_N10_0.5	a dilution at 0.5% wt of nanoparticles NML in Fuchs oil ARL1. Original concentrate (prepared from BHR) N10: 23% wt of NML particles in PAO6, with 5.7% wt C9268 and 5.7% wt C9232.
ARL1_N11_0.5	a dilution at 0.5% wt of nanoparticles NML in Fuchs oil ARL1. Original concentrate (prepared from BHR) N11: 23% wt of NML particles in PAO6, with 5.7% wt C9268.
ARL1_N13_0.5	a dilution at 0.5% wt of nanoparticles NML in Fuchs oil ARL1. Original concentrate (prepared from BHR) N13: 23% wt of NML particles in PAO6, with 5.7% wt C9268.
ARL1_E11_0.5	a dilution at 0.5% wt of nanoparticles Cidetec in Fuchs oil ARL1. Original concentrate (prepared from BHR) E11: 23% wt of NML particles in PAO6, with 5.7% wt C9268 and 5.7% wt C9232.

Tab. 2.1- Composition of the samples

2.1.2 Friction test-Stribeck curve

In the group of graphs below are reported the results obtained for the frictional tests on the formulated samples, at different temperatures and average hertzian contact pressures (test operating conditions and tools have been described in Chapter 1). The first group of graphs (Figures 2.1) represents the friction coefficient at the lowest value of the pressure contact, $p=1.17$ GPa.

$p=1.17$ GPa

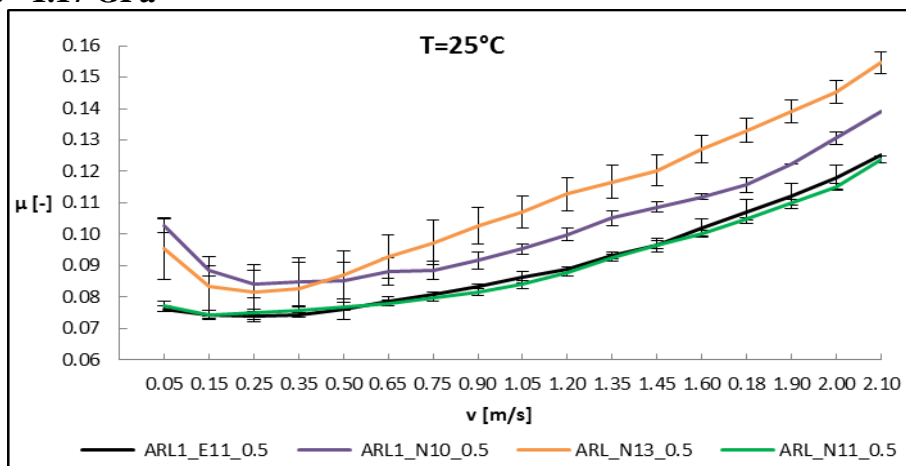


Fig. 2.1a- Stribeck curve from the sweep test; $p=1.17$ GPa, $T=25^\circ\text{C}$

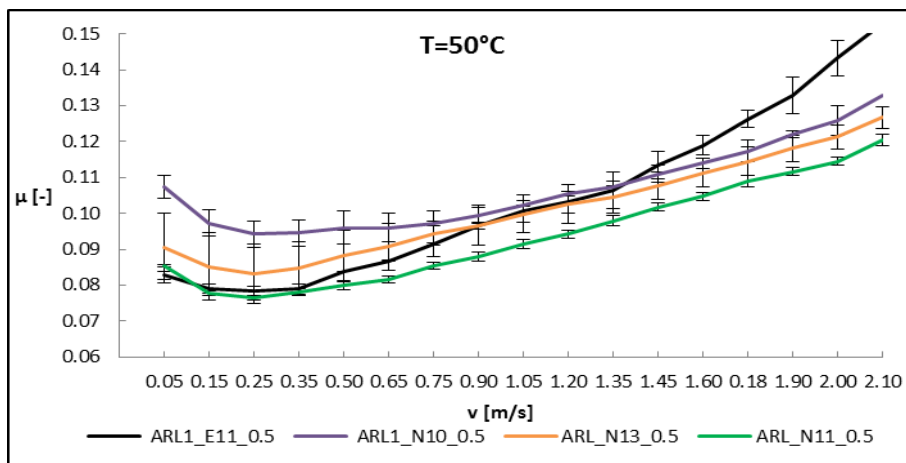
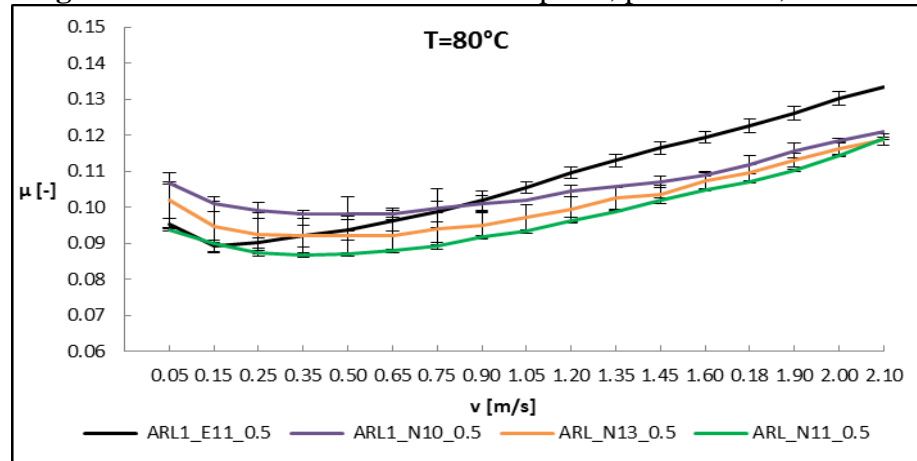
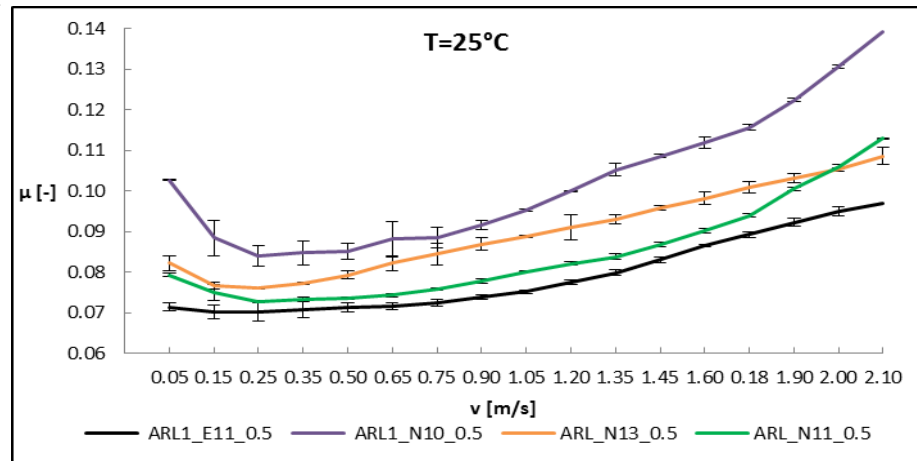


Fig. 2.1b- Stribeck curve from the sweep test; $p=1.17$ GPa, $T=50$ °C**Fig. 2.1c-** Stribeck curve from the sweep test; $p=1.17$ GPa, $T=80$ °C

The group of graphs (Figures 2.2) represents the friction coefficient at the medium value of the pressure contact, $p=1.47$ GPa.

$p= 1.47$ GPa

**Fig. 2.2a-** Stribeck curve from the sweep test; $p=1.47$ GPa, $T=25$ °C

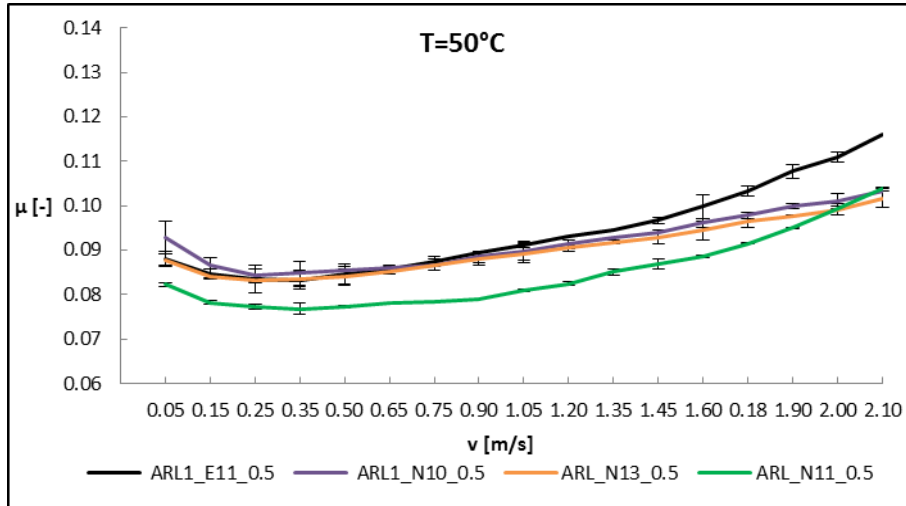


Fig. 2.2b- Stribeck curve from the sweep test; $p=1.47$ GPa, $T=50^{\circ}\text{C}$

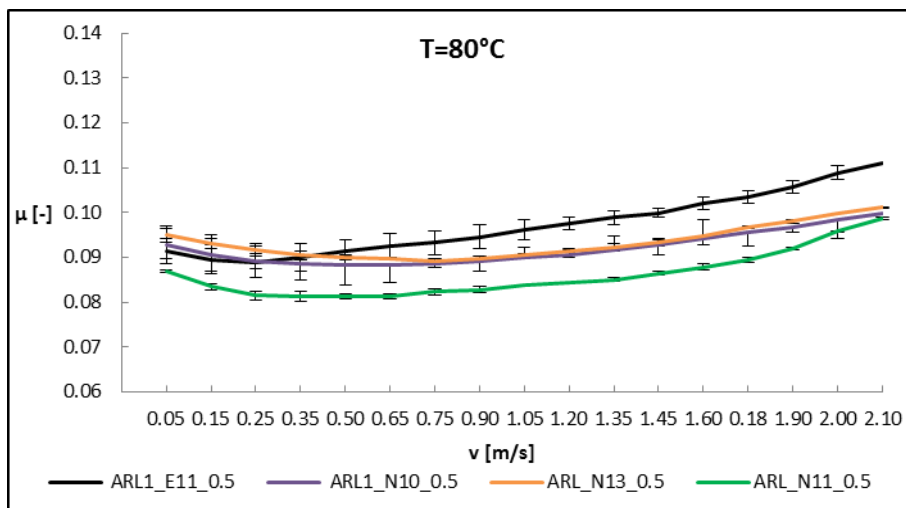


Fig. 2.2c- Stribeck curve from the sweep test; $p=1.47$ GPa, $T=80^{\circ}\text{C}$

Finally, in the Figures 2.3, the Stribeck curves for the highest value of the pressure contact, $p=1.68$ GPa, are plotted.

$p= 1.68$ GPa

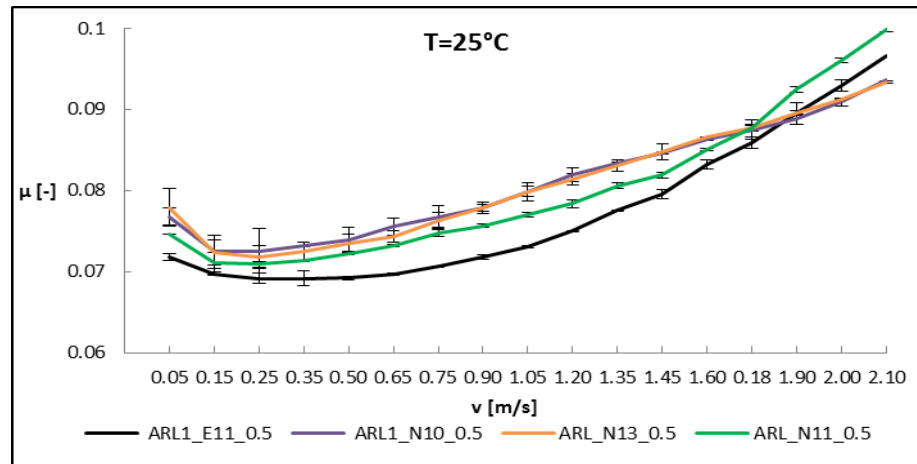


Fig. 2.3a- Stribeck curve from the sweep test; $p=1.68$ GPa, $T=25^{\circ}\text{C}$

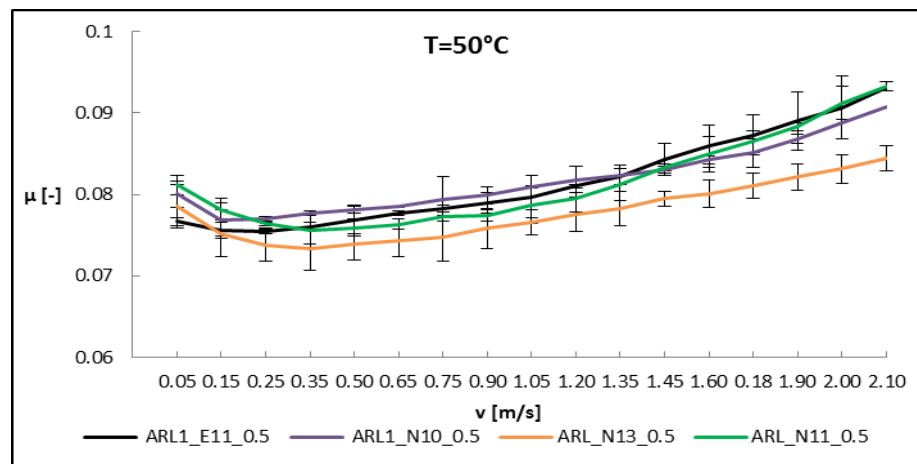


Fig. 2.3b- Stribeck curve from the sweep test; $p=1.68$ GPa, $T=50^{\circ}\text{C}$

All the presented samples exhibit good performance in terms of coefficient of friction (CoF). The best results have been achieved by the samples ARL_E11_0.5 (formulated with Cidetec nanoparticles) and ARL_N13_0.5 (formulated with Nanomaterials nanoparticles). For all the tested samples, the CoF shows a tendency to decrease with increasing contact pressure. According to previous works [8-10] which studied the friction under elasto-hydrodynamic (EHL) conditions the shear stress

increased less rapidly in proportion to the contact pressure. This leads to a slight reduction of the friction with increasing pressure. Additionally, in all studied samples the CoF increased with the temperature.

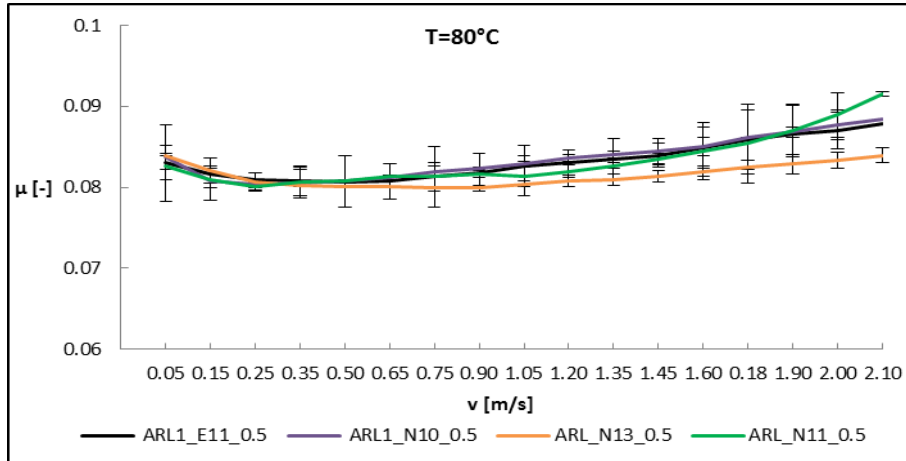


Fig. 2.3c- Stribeck curve from the sweep test; $p=1.68$ GPa, $T=80$ °C

This observation is attributed mainly to the effect of the lower lubricant viscosity in the boundary lubrication regime. Good results, comparable with the other samples, have been obtained also for the samples ARL_N11_0.5 and ARL_N12_0.25, this one formulated with a lower concentration of additive. The sample ARL_N10_0.5 appears to work better in boundary lubrication regime in almost all combinations of operating conditions, while it shows an increase of the coefficient of friction at higher value of sliding speed, instead the sample ARL_N10_1.0 seems to be less sensitive to the variation of sliding speed

2.1.3 Friction and wear in steady-state tests

As showed in Chapter 1, long running frictional tests (60 minutes) were also performed to analyze the behavior of the lubricating samples with regard to the wear of the mating materials (ball and disc). In particular, the worn surfaces of the steel ball have been analyzed by means of an optical microscope to measure the wear scar diameter (WSD).

These friction/wear steady tests have proven to produce a stable value of the friction coefficient with low variance and they are also in

good agreement with those measured with the frictional speed-sweep tests.

As for the friction tests, the experimental investigation on wear effect has been done under constant values for the average hertzian pressure, the temperature and the speed, respectively: 1.68 GPa, 80 °C, 5.0 mm/s and 0.5 m/s.

Thus, it was possible investigating both boundary and mixed – EHL lubrication regimes (Figures 2.4).

p= 1.68 GPa

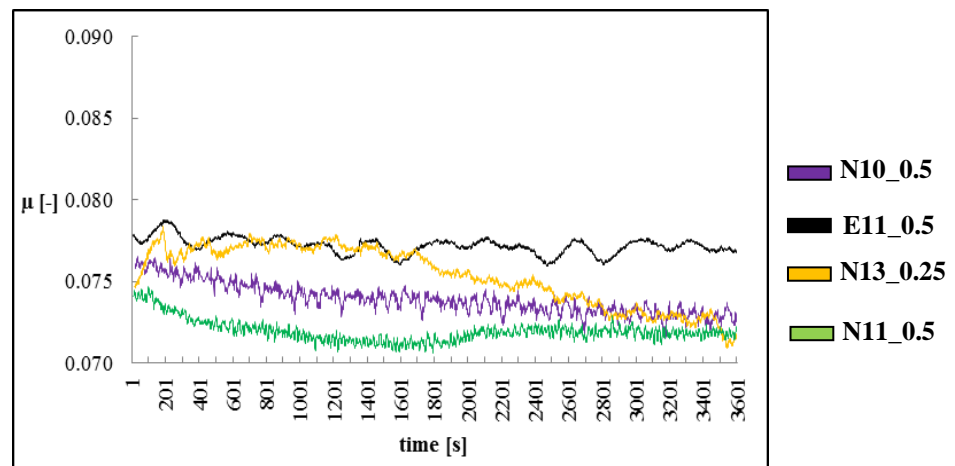


Fig. 2.4a- Evolution of friction coefficient, 1-hour test in boundary lubrication steady condition; p=1.68 GPa, T=25 °C, v=5 mm/s.

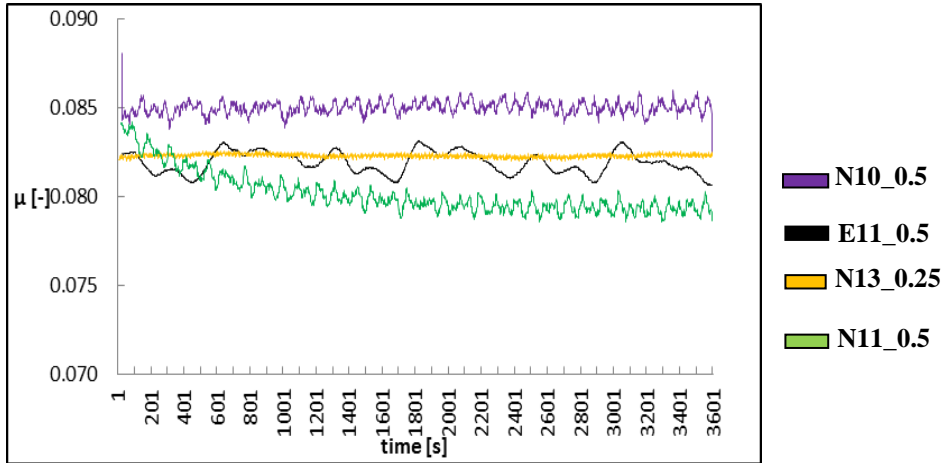


Fig. 2.4b- Evolution of friction coefficient, 1-hour test in boundary lubrication steady condition; $p=1.68$ GPa, $T=80$ °C, $v=5$ mm/s.

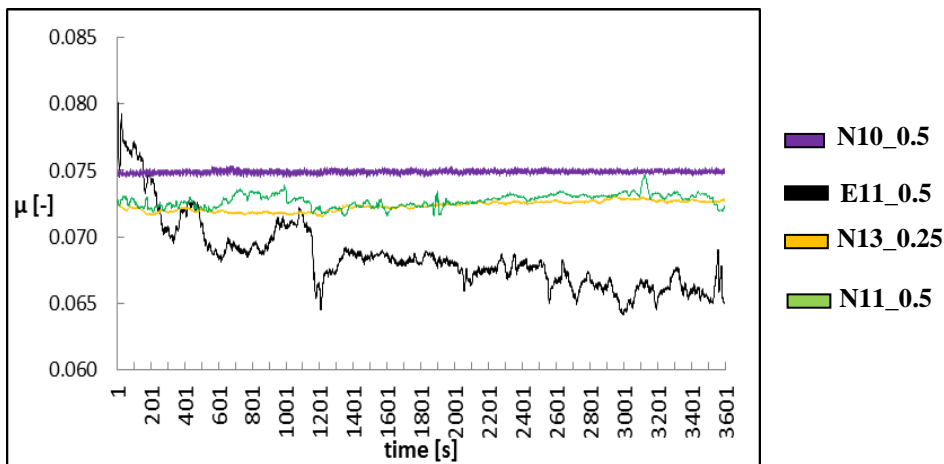


Fig. 2.4c- Evolution of friction coefficient, 1-hour test in mixed/EHL lubrication steady condition; $p=1.68$ GPa, $T=25$ °C, $v=0.5$ m/s.

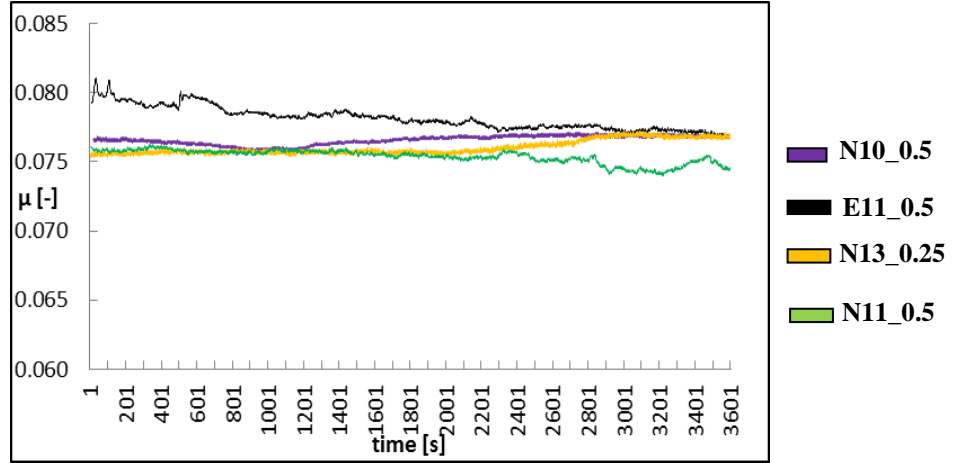


Fig. 2.4d- Evolution of friction coefficient, 1-hour test in mixed/EHL lubrication steady condition; $p=1.68$ GPa, $T=80$ °C, $v=0.5$ m/s.

According to ISO/IEC Guide 98-3:2008, the friction coefficient in the Tables 2.2 and 2.3 are presented with an expanded uncertainty equal to $5.0 \cdot 10^{-3}$, coverage factor $k = 2.3$.

Sample	Friction coefficient[-] in boundary lubrication at 25°C	Friction coefficient[-] in boundary lubrication at 80°C
ARL1_N10_0.5	0.075	0.085
ARL1_N11_0.5	0.072	0.080
ARL1_N13_0.5	0.074	0.083
ARL1_E11_0.5	0.077	0.083

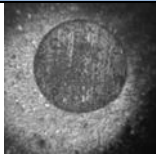
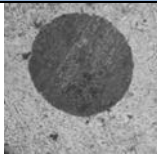
Tab. 2.2- Friction coefficient in boundary lubrication steady condition; sliding speed: 5.0 mm/s.

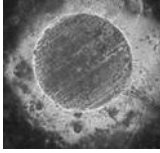

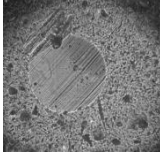
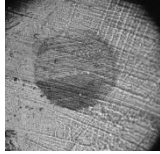
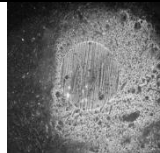
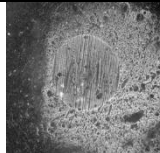
The Tables 2.2 and 2.3 show CoF values in good agreement with those measured with the frictional speed-sweep tests previously described and represented by the Stribeck curves.

Sample	Friction coefficient [-] in Mixed/EHL lubrication at 25°C	Friction coefficient [-] in Mixed/EHL lubrication at 80°C
ARL1_N10_0.5	0.075	0.077
ARL1_N11_0.5	0.073	0.076
ARL1_N13_0.5	0.073	0.076
ARL1_E11_0.5	0.069	0.079

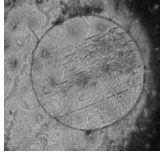
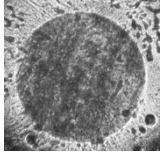

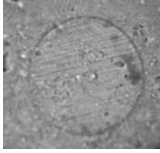
Tab. 2.3- Friction coefficient in mixed lubrication steady condition; sliding speed: 0.5 m/s.

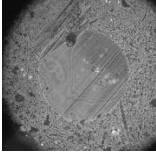
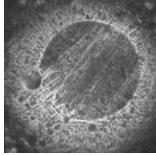
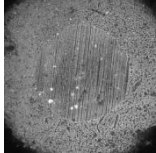
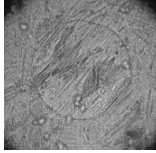
Furthermore, Tables 2.4 and 2.5 illustrates the optical micrograph and the diameter of the wear circles observed on the steel ball specimens after 1-hour steady conditions wear test. According to ISO/IEC Guide 98-3:2008, the wear scar diameter (WSD) measurements in the Tables 2.4 and 2.5 are presented with an expanded uncertainty equal to 20 μm , coverage factor $k = 2$.

Sample	Ball wear scar diameter [μm] in boundary lubrication at 25 °C	Ball wear scar diameter [μm] in boundary lubrication at 80 °C
ARL1_N10_0.5	 510	 530

<p>ARL1_N11_0.5</p>	 <p>490</p>	 <p>510</p>
<p>ARL1_N13_0.5</p>	 <p>480</p>	 <p>530</p>
<p>ARL1_E11_0.5</p>	 <p>490</p>	 <p>510</p>

Tab. 2.4- Optical micrograph and wear scar diameter (WSD) after boundary lubrication steady condition test; sliding speed: 5.0 mm/s.

<p>Sample</p>	<p>Ball wear scar diameter [μm] in mixed lubrication at 25 °C</p>	<p>Ball wear scar diameter [μm] in mixed lubrication at 80 °C</p>
<p>ARL1_N10_0.5</p>	 <p>610</p>	 <p>630</p>
<p>ARL1_N11_0.5</p>	 <p>600</p>	 <p>640</p>

ARL1_N13_0.5		
	600	610
ARL1_E11_0.5		
	580	600

Tab. 2.5- Optical micrograph and wear scar diameter (WSD) after mixed lubrication steady condition test; sliding speed: 0.5 m/s.

The samples exhibit good anti-wear properties, in particular, the best performances in terms of reduction of the wear scar diameter (WSD) are obtained with the samples ARL_E11_0.5 and ARL_N13_0.5.

For the other lubricant sample, the anti-wear performance based on the WSD reduction is practically the same for the different samples.

Below are reported some schematic graphs for a better understanding of the final results obtained for each tested samples in the long-running tests (Figures 2.5).

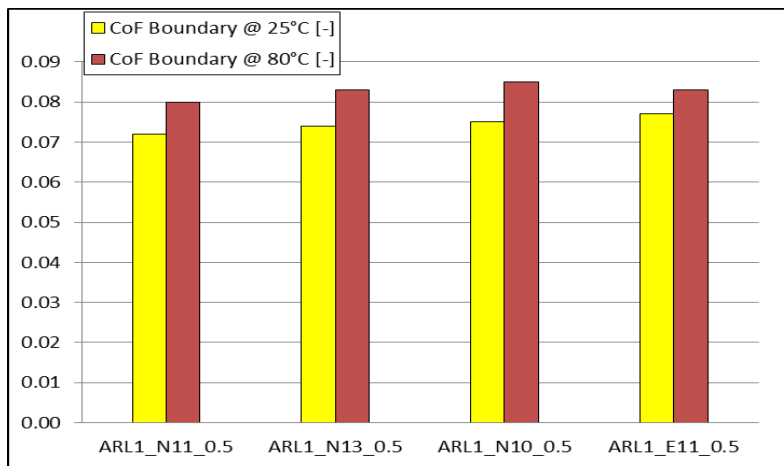


Fig. 2.5a - Friction coefficient in boundary regime ($v = 5 \text{ mm/s}$; $p = 1.68 \text{ GPa}$)

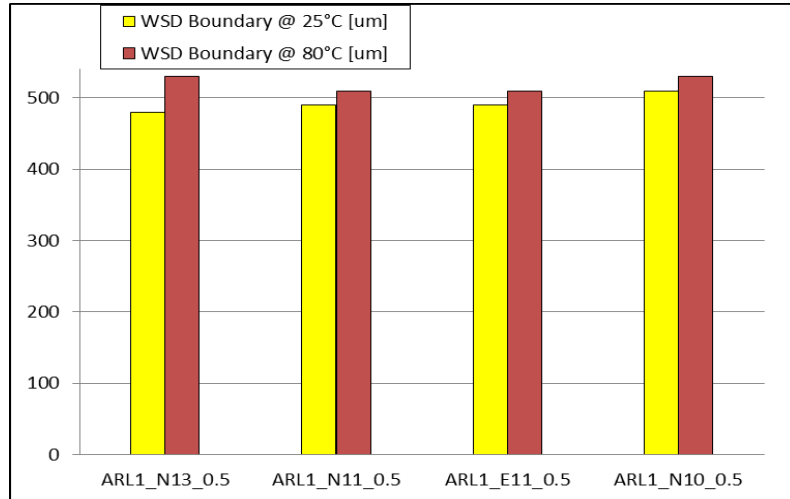


Fig. 2.5b - Wear scar diameter [μm] in boundary regime ($v = 5 \text{ mm/s}$; $p = 1.68 \text{ GPa}$)

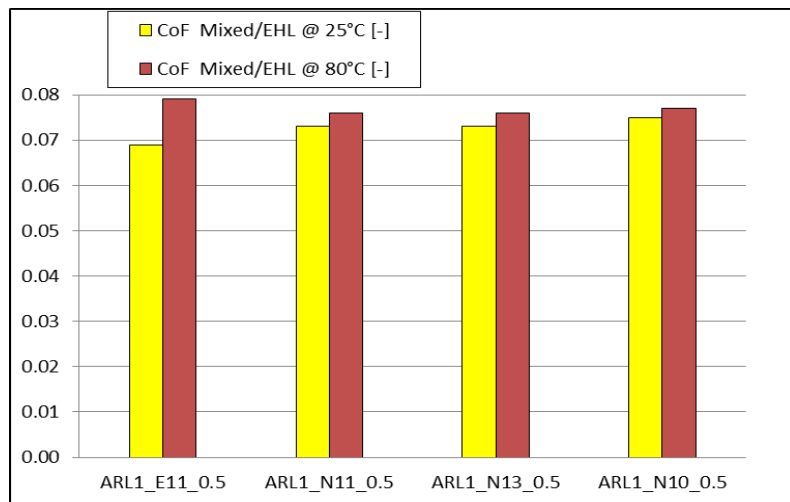


Fig. 2.5c - Friction coefficient in mixed-EHL regime ($v = 0.5 \text{ m/s}$; $p = 1.68 \text{ GPa}$)

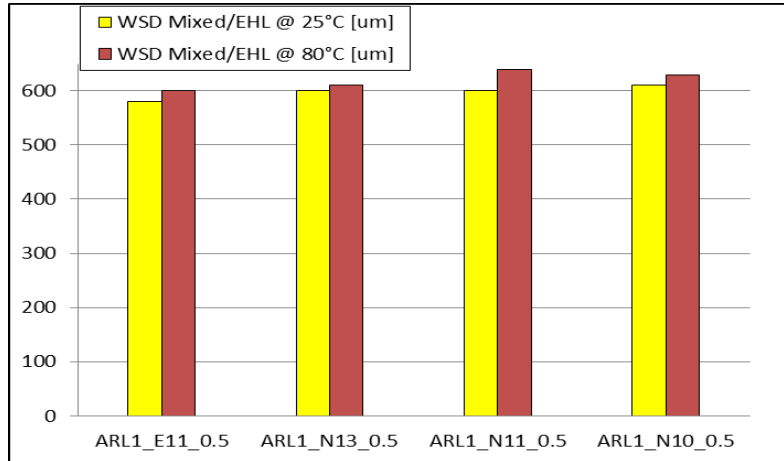


Fig. 2.5d - Wear scar diameter [μm] in mixed-EHL regime ($v = 0.5 \text{ m/s}$; $p = 1.68 \text{ GPa}$)

2.1.4 Comparison with base oil lubricant

In order to complete the task on lubricant tribological tests, the base oil, used for all the formulated samples analyzed in the previous paragraph, has been tested in terms of its frictional and wear behavior.

The physical and chemical properties of the base oil are reported below, in Table 2.6:

Physical and chemical Properties	
Form	Liquid
Colour	Brown
Flash point	220 °C (EN ISO 2592)
Density at 15 °C	0.86 g/cm ³ (DIN 51 757)
Viscosity kinematic at 40 °C	61 mm ² /s (DIN 51 562)
Solvent content	0.0 %

Tab. 2.6- Lubricant (ARL1) physical and chemical properties

The base oil has been compared with the tribological results previously obtained with the most performing formulated sample, ARL1_E11_0.5, in order to highlight the improvement reached with the addition of nanoparticles and dispersant on the tribological performance of the lubricant.

2.1.4.1 Friction test—Stribeck curve

The measured data are presented according to the Stribeck curves representation, i.e. friction coefficient vs. sliding speed. Below are shown the results obtained for the base oil ARL1 sample for different level of average hertzian contact pressure and temperature, Figures 2.6.

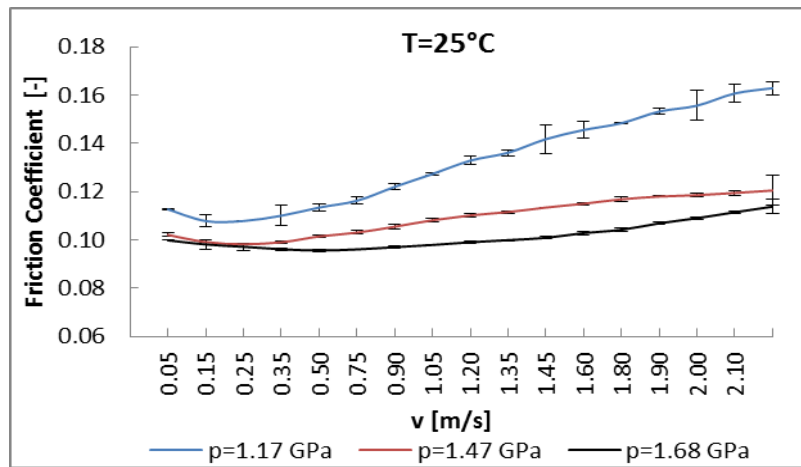


Fig. 2.6a- Stribeck curve from the sweep test for different contact pressures at T=25 °C

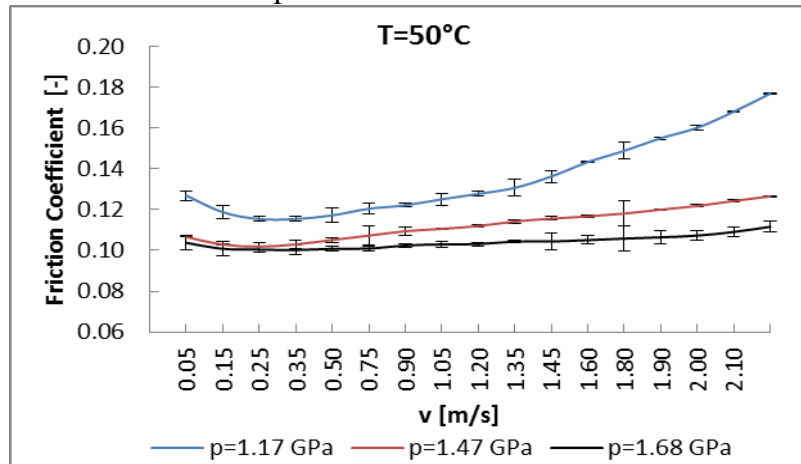


Fig. 2.6b- Stribeck curve from the sweep test for different contact pressures at T=50 °C

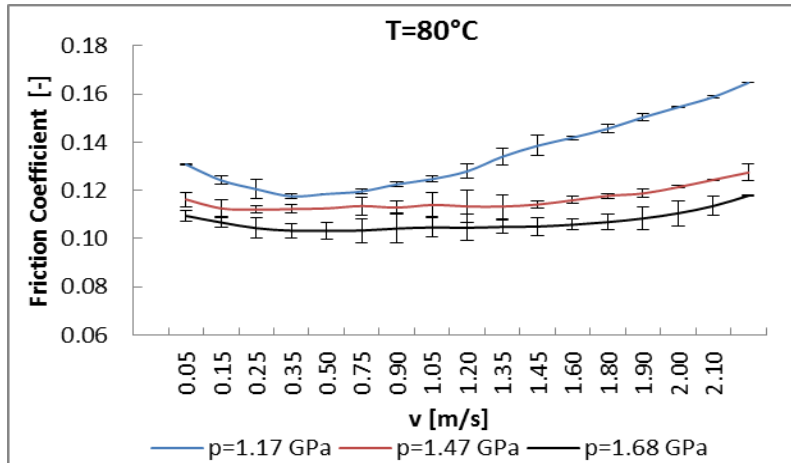


Fig. 2.6c- Stribeck curve from the sweep test for different contact pressures at $T=80$ °C

In all studied samples the CoF increased with the temperature. This observation is attributed mainly to the effect of the lower lubricant viscosity of the lubricant.

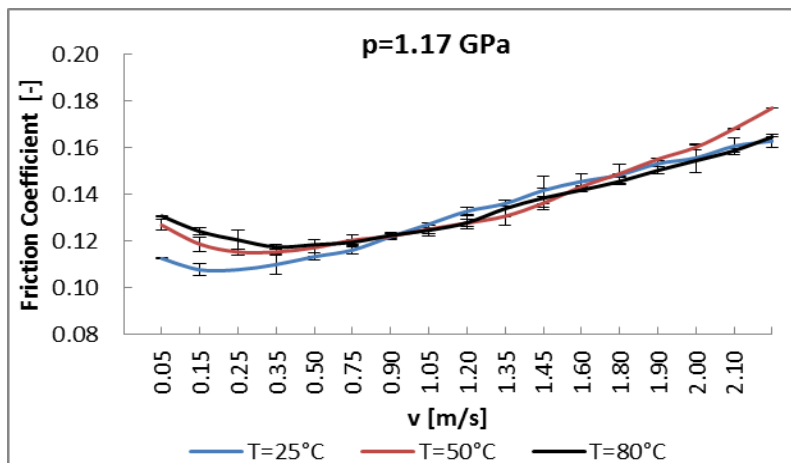


Fig. 2.6d- Stribeck curve from the sweep test for different temperatures at $p=1.17$ GPa

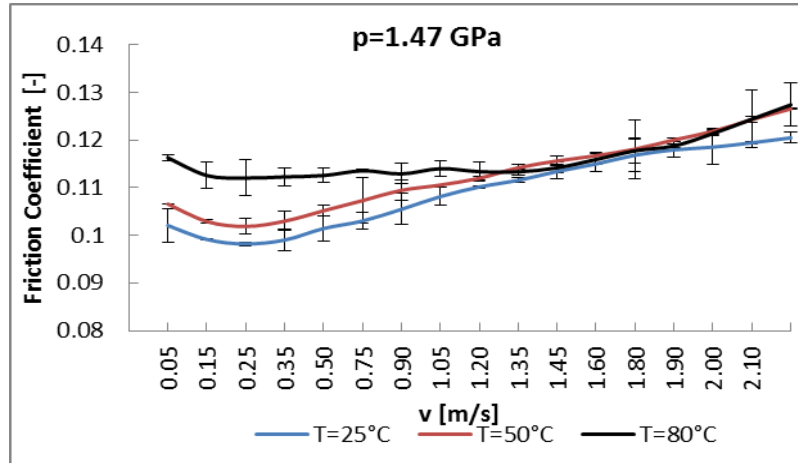


Fig. 2.6e- Stribeck curve from the sweep test for different temperatures at $p=1.47$ GPa

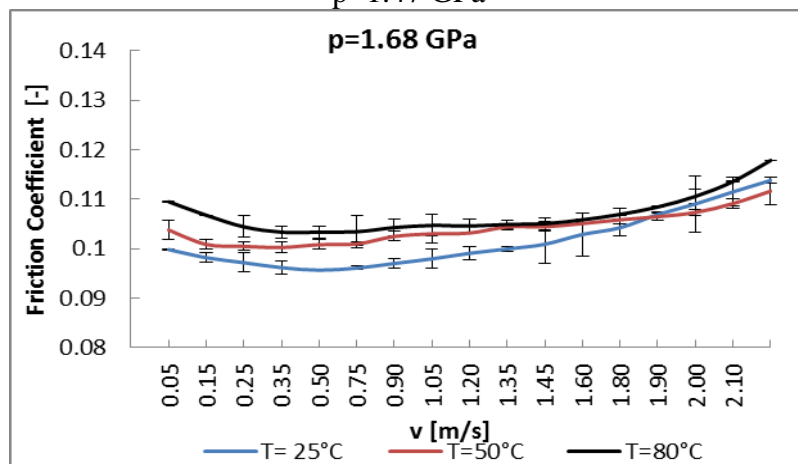


Fig. 2.6f- Stribeck curve from the sweep test for different temperatures at $p=1.68$ GPa

For all the tested samples, the CoF showed a tendency to decrease with increasing contact pressure, due to increase of the shear stress less rapidly in proportion to the contact pressure. A comparison between the sample ARL1_E11_0.5 with 0.5 w.t.% of Cidetec nanoparticles and the ARL1 base oil has been made in order to show the difference in terms of tribological results between the used base oil and the most performing formulated sample tested during this project. The comparison shows that reduction of the friction coefficient for the sample with nanoparticles

addition is quite remarkable. The tribological results are presented in Figures 2.7. These tests confirm that using inorganic fullerene nanoparticles in lubricants enhances the friction reduction in boundary and mixed lubrication regimes. In the group of graphs below are reported the results obtained through the frictional tests on samples, at different temperatures and average hertzian contact pressures. The first group of graphs (Figures 2.7a-c) represents the friction coefficient at the lowest value of the pressure contact, $p=1.17$ GPa.

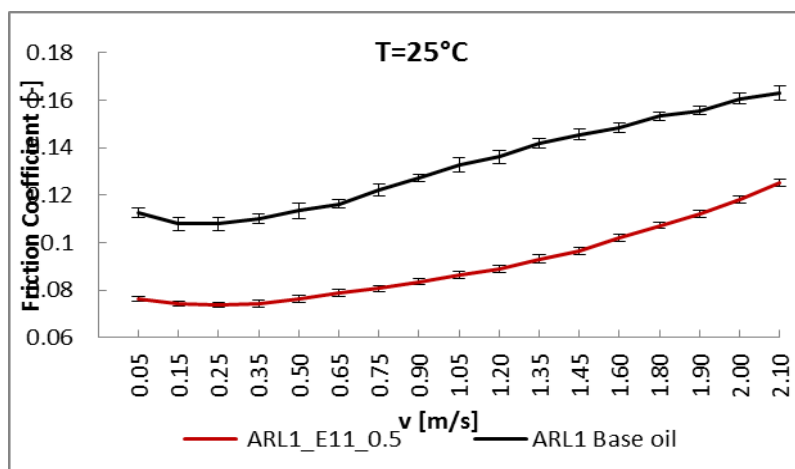


Fig. 2.7a- ARL1 Base oil and ARL1_E11_0.5 comparison at $p=1.17$ GPa, $T=25^{\circ}\text{C}$

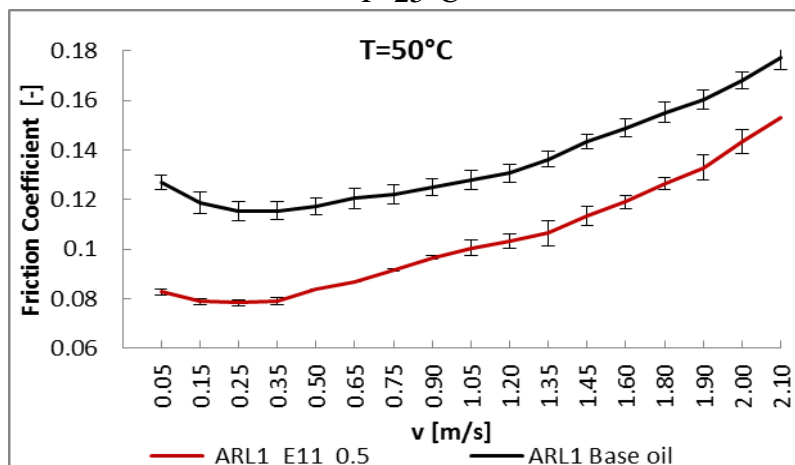


Fig. 2.7b- ARL1 Base oil and ARL1_E11_0.5 comparison at $p=1.17$ GPa, $T=50^{\circ}\text{C}$

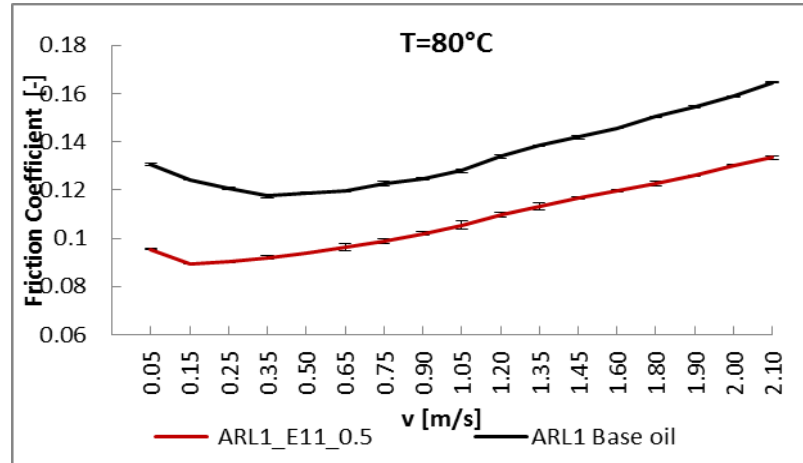


Fig. 2.7c- ARL1 Base oil and ARL1_E11_0.5 comparison at $p=1.17$ GPa, $T=80$ °C

The graphs in Figures 2.7 d-f represents the friction coefficient at the medium value of the pressure contact, $p=1.47$ GPa

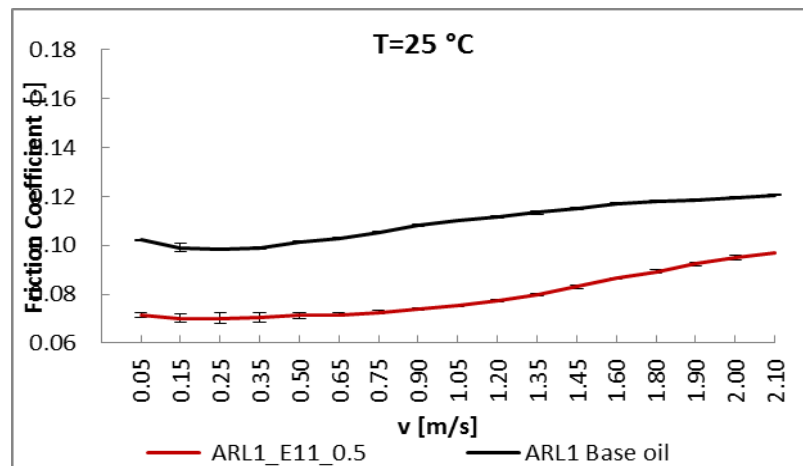


Fig. 2.7d- ARL1 Base oil and ARL1_E11_0.5 comparison at $p=1.47$ GPa, $T=25$ °C

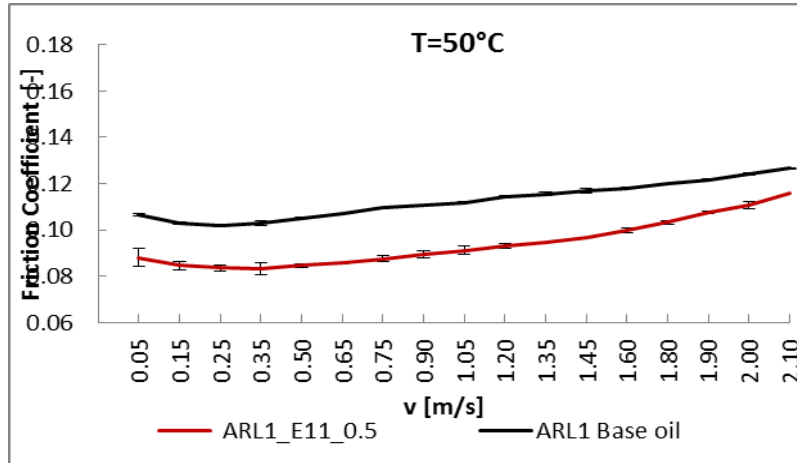


Fig. 2.7e- ARL1 Base oil and ARL1_E11_0.5 comparison at $p=1.47$ GPa, $T=50^\circ\text{C}$

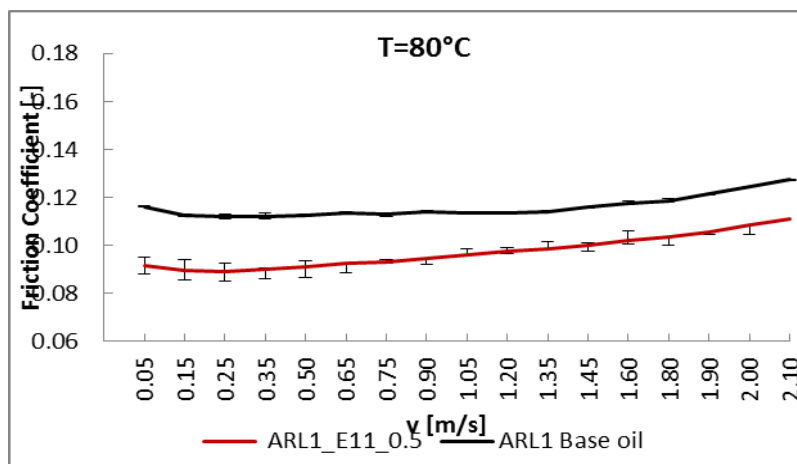


Fig. 2.7f- ARL1 Base oil and ARL1_E11_0.5 comparison at $p=1.47$ GPa, $T=80^\circ\text{C}$

Finally, in the Figures 2.7g-i, the Stribeck curves for the highest value of the pressure contact, $p=1.68$ GPa, are plotted.

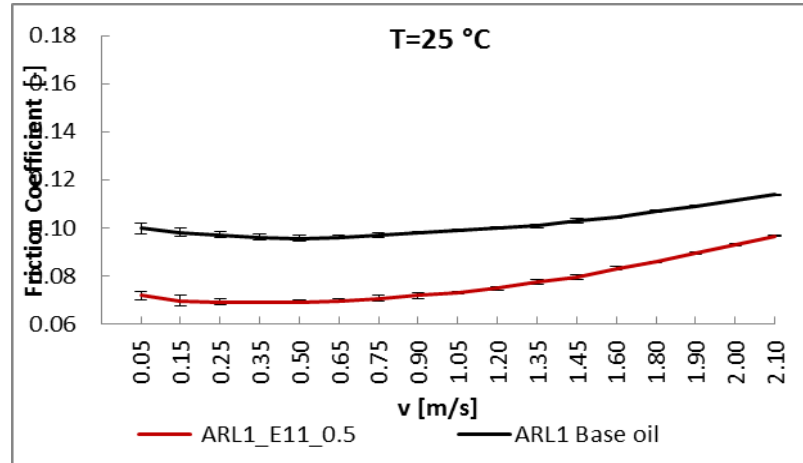


Fig. 2.7g- ARL1 Base oil and ARL1_E11_0.5 comparison at $p=1.68$ GPa, $T=25^{\circ}\text{C}$

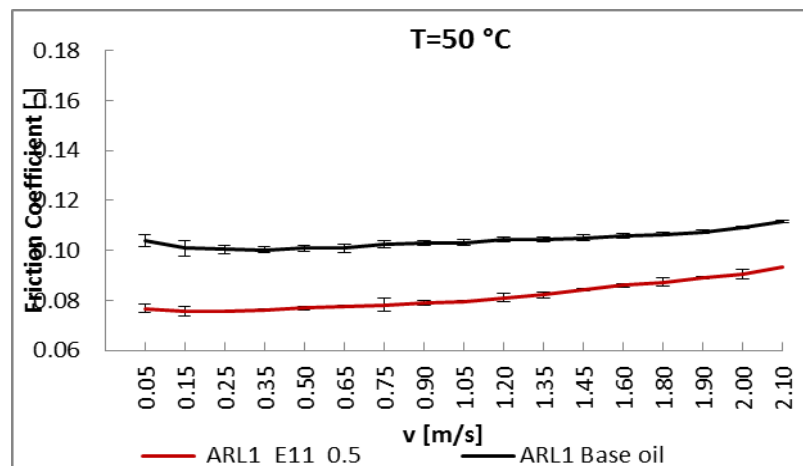


Fig. 2.7h- ARL1 Base oil and ARL1_E11_0.5 comparison at $p=1.68$ GPa, $T=50^{\circ}\text{C}$

The formulated sample exhibits good performance in terms of coefficient of friction (CoF) compared to the ARL1 base oil

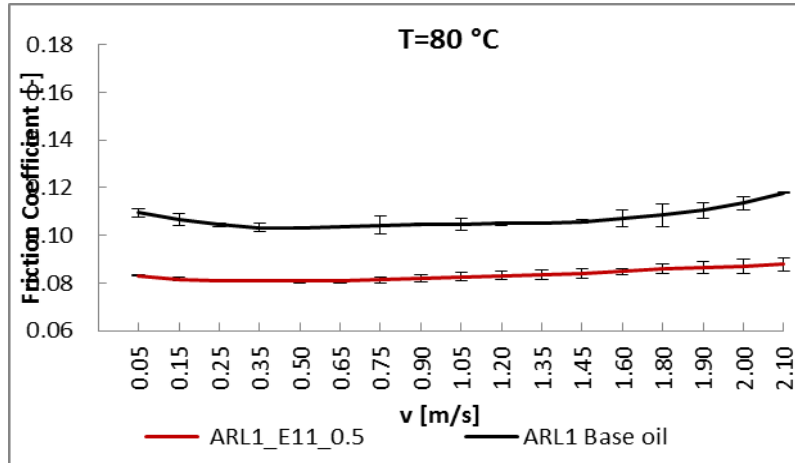


Fig. 2.7i- ARL1 Base oil and ARL1_E11_0.5 comparison at $p=1.68$ GPa, $T=80^\circ\text{C}$

The results show that the gain in terms of friction coefficient reduction is remarkable for both the lubrication regime and in all the tested operating condition. The gain for the friction coefficient ranges from 15% to 25 % for the different combination of contact pressure and temperature.

2.1.4.2 Friction and wear in steady-state tests

As for the previous tested samples, friction/wear steady tests have proven to produce a stable value of the friction coefficient with low variance and they are also in good agreement with those measured with the frictional speed-sweep tests.

As for the friction tests, the experimental investigation on wear effect has been done under constant values for the average hertzian pressure, the temperature and the speed, respectively: 1.68 GPa, 80 °C, 5.0 mm/s and 0.5 m/s (Figures 2.8 a-d).

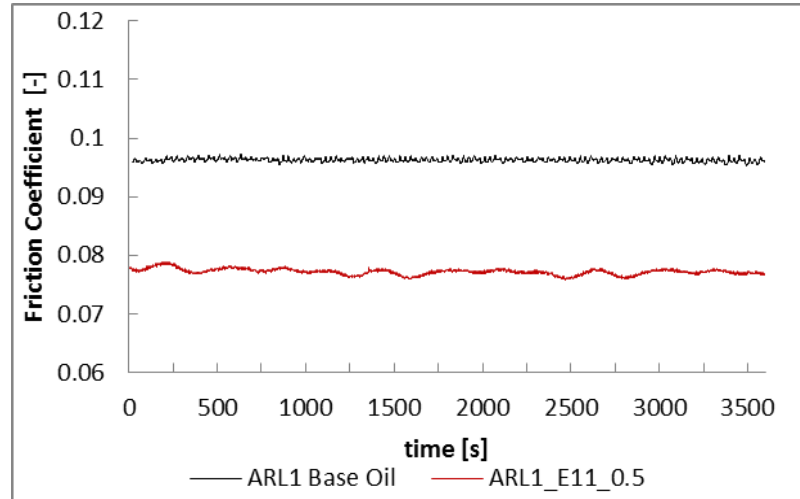


Fig. 2.8a- Evolution of friction coefficient, 1-hour test in boundary lubrication steady condition; $p=1.68$ GPa, $T=25$ °C, $v=5$ mm/s.

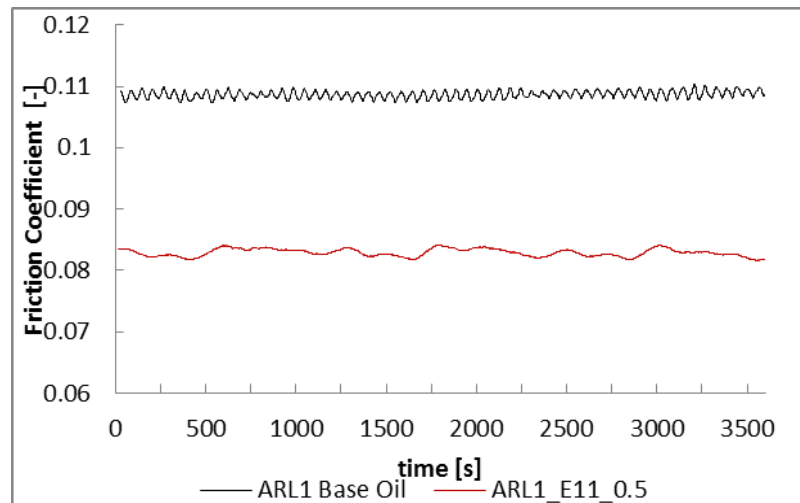


Fig. 2.8b- Evolution of friction coefficient, 1-hour test in boundary lubrication steady condition; $p=1.68$ GPa, $T=80$ °C, $v=5$ mm/s.

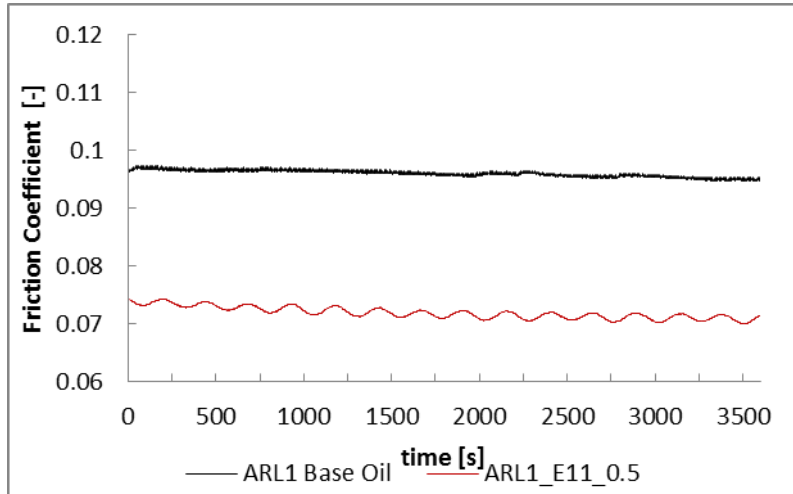


Fig. 2.8c- Evolution of friction coefficient, 1-hour test in mixed/EHL lubrication steady condition; $p=1.68$ GPa, $T=25$ °C, $v=0.5$ m/s.

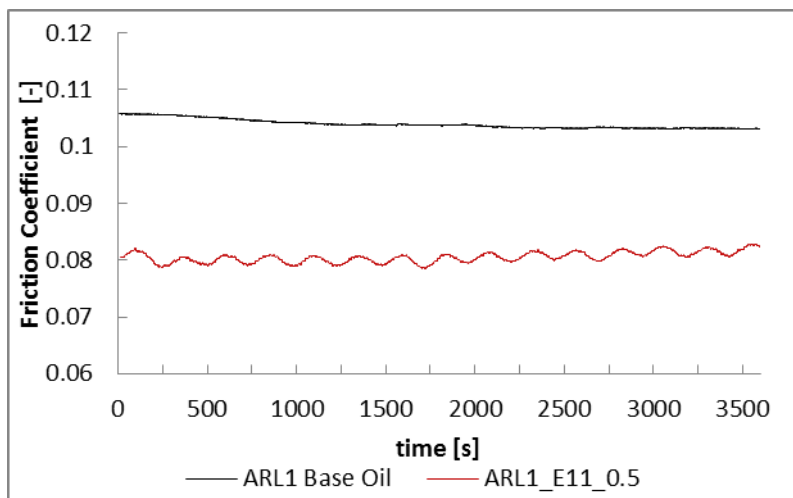


Fig. 2.8d- Evolution of friction coefficient, 1-hour test in mixed/EHL lubrication steady condition; $p=1.68$ GPa, $T=80$ °C, $v=0.5$ m/s.

The results of the long running frictional tests show as for the sweep test a good improvement in terms of tribological performances with a remarkable reduction of the friction coefficient, ranged from 17% in boundary lubrication to 25% in mixed/EHL lubrication.

According to ISO/IEC Guide 98-3:2008, the friction coefficient in

the Tables 2.7 and 2.8 are presented with an expanded uncertainty equal to $5.0 \cdot 10^{-3}$, coverage factor $k = 2$.

Sample	Friction coefficient[-] in boundary lubrication at 25°C	Friction coefficient[-] in boundary lubrication at 80°C
ARL1 Base Oil	0.097	0.110
ARL1_E11_0.5	0.077	0.083

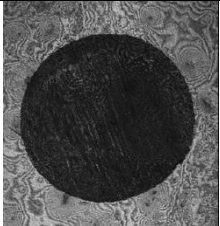
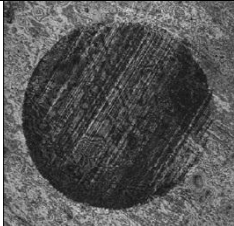


Tab. 2.7- Friction coefficient in boundary lubrication steady condition; sliding speed: 5.0 mm/s.

Sample	Friction coefficient [-] in Mixed/EHL lubrication at 25°C	Friction coefficient [-] in Mixed/EHL lubrication at 80°C
ARL1 Base Oil	0.096	0.105
ARL1_E11_0.5	0.069	0.079

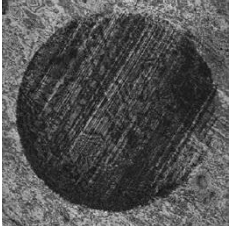
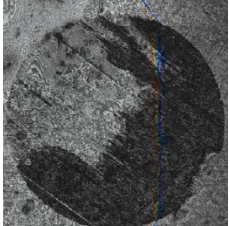
Tab. 2.8- Friction coefficient in mixed lubrication steady condition; sliding speed: 0.5 m/s.

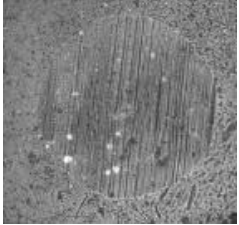
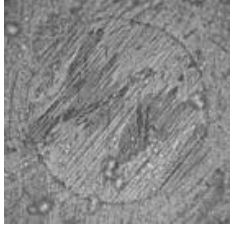
The reduction of the wear scar diameter is equal to 34% and 55% in boundary lubrication at 25° C and 80°C, respectively. Furthermore, the trend is different in mixed/EHL lubrication in which the WSD reduction is 36% and 20% at 25°C and 80°C.

The Tables 2.9 and 2.10 illustrates the profiler acquisitions of the diameter of the wear circles observed on the steel ball specimens after 1-hour steady conditions wear test.

Sample	Ball wear scar diameter [μm] in boundary lubrication at 25 °C	Ball wear scar diameter [μm] in boundary lubrication at 80 °C
ARL1 Base Oil	 507	 540
ARL1_E11_0.5	 490	 510

Tab. 2.9- Profiler image acquisition and wear scar diameter (WSD) after boundary lubrication steady condition test; sliding speed: 5.0 mm/s.

Sample	Ball wear scar diameter [μm] in mixed lubrication at 25 °C	Ball wear scar diameter [μm] in mixed lubrication at 80 °C
ARL1 Base Oil	 602	 612

ARL1_E11_0.5	 <p style="text-align: center;">580</p>	 <p style="text-align: center;">600</p>
--------------	---	--

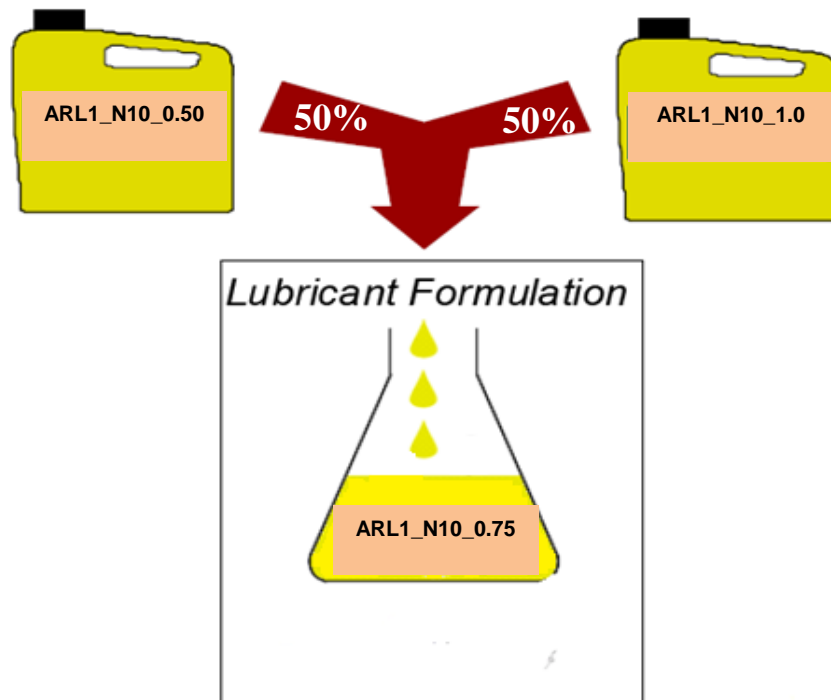
Tab. 2.10- Profiler image acquisition and wear scar diameter (WSD) after mixed lubrication steady condition test; sliding speed: 0.5 m/s.

As for the friction coefficient comparison results, the sample formulated with Cidetec nanoparticles exhibits good anti-wear properties.

2.1.5 Numerical simulations

Numerical simulations based on the obtained test data have been carried out, using an artificial neural network, to point out the best NPs concentration for a given set of the other operating parameters.

In order to be able to obtain a significant amount of input data to build the neural network, it is thought to create a sample with a concentration of nanoparticles equal to 0.75 w.t.% (Figures 2.9), through a simple mixing of two samples that we have already been tested with the addition of 0.5 w.t.% and 1 w.t.% of Nanomaterials nanoparticles. The characteristics of this new sample are shown in Table 2.11.



NPs	NML 0.75 w.t.%
Dispersant 1	0.18 w.t.% C9268
Dispersant 2	0.18 w.t.% C9232
Base oil for the concentrate (PAO 6)	2.1 w.t.%
Fuchs formulated engine oil	96.8 w.t.%

Tab. 2.11 - Sample ARL_N10_0.75 Characteristic

For this task a multilayer perceptron (MLP) Artificial Neural Network (ANN) has been set up to obtain a comprehensive view of the influence of the main sliding physical parameters. ANN also provided the prediction of the friction coefficient and wear scar diameter dependence on the nanoparticles concentration over the limit imposed by our samples.

The Multi-Layer Perceptron (MLP) network has been selected because it can be considered an “universal approximator” of nonlinear functions that transform the inputs space in the space of outputs (applying the technique of the gradient descent, also called Back-Propagation rule). The data acquired during the tests have been split into two sets: training data set, validation data. The number of training data and validation data set was equal to 16 for each one (4 for each samples with 0.25-0.5-0.75 and 1 w.t.%); the second was used to monitor the quality of neural network training [17,18].

The splitting into two different sets of data was based on the previous experience on neural networks, in order to avoid drawbacks due to poor generalization ability of the model caused by the so-called overfitting.

Each neuron transfers the data or signal to the next neuron, which is manipulated by the ‘transfer function’, ‘weight’ embedded in the neuron. The software performs a weighted sum of inputs and computes the sigmoidal function values; the outputs of the network are used to determine the cost function that will be compared with the limit error defined by the user. Subsequently, various weights with respect to learning rate and momentum set according to the delta rule are calculated.

Figure 2.10 shows the architecture of the ANN obtained after the optimization process. The ANN algorithm has been trained with a target error less or equal to the experimental measurements uncertainty [19-21]. After the learning stage, the ANN performances were calculated; see Tables 2.12-2.14. The ANNs offer also the possibility to investigate the hierarchy influence of the input parameters on the friction coefficient. The relative importance parameter is the sum of the absolute input weights to reflect the impact of that input variable on the output.

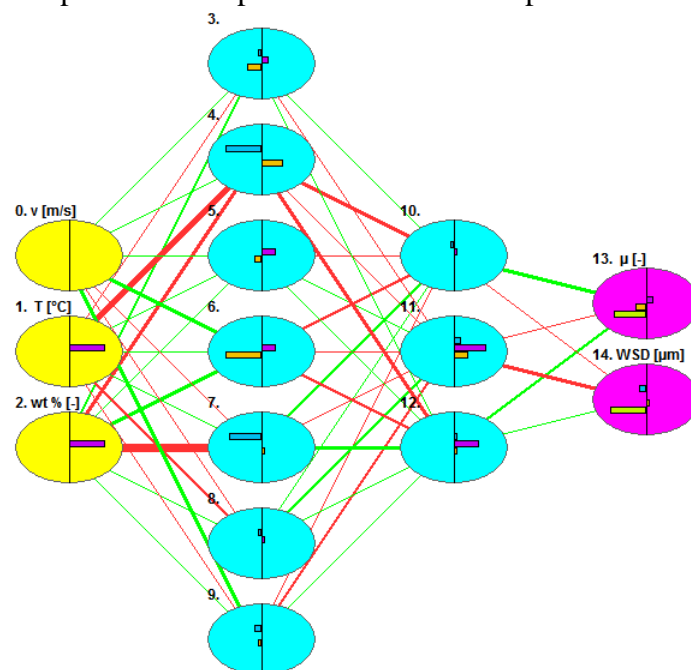


Fig. 2.10– Structure of the Artificial Neural Network

The Sensitivity shows how much an output changes when the inputs are changed. The inputs are all set to the median values and then each in turn is increased from the lowest value to the highest value. The change in the output is measured as each input is increased from lowest to highest to establish the sensitivity to change. Insensitive inputs are not shown.

The inputs are shown in the descending order of sensitivity from the most sensitive input. The Input Importance, instead, shows the importance and the relative importance of each input column. The Importance is the sum of the absolute weights of the connections from the

input node to all the nodes in the first hidden layer. The inputs are shown in the descending order of importance from the most important input [22-24].

Parameter	Value
Target error	1.0×10^{-3}
Maximum error	3.5×10^{-3}
Average error	1.0×10^{-3}
Minimum error	1.0×10^{-4}
Learning cycles	1233
Momentum	0.80
Learning rate	0.60

Tab. 2.12 – Initial network parameters

Input name	Importance
w.t. [%]	29.8
v [m/s]	20.6
T [°C]	17.4

Tab. 2.13– Importance of input parameters on the output

Input name	Sensitivity
w.t. [%]	0.074
v [m/s]	0.289
T [°C]	0.059

Tab. 2.14–Sensitivity of input parameters on the output

The ANN predictions show a good agreement with the acquired data and indicates the best NPs concentration is around 0.5-0.6 w.t.% both for the CoF and WSD values. Only for the heaviest operating condition ($p=1.68$ GPa and $T=80$ °C) the best performance is predicted for higher NPs concentration (> 0.75 w.t. %) (Figure 2.11).

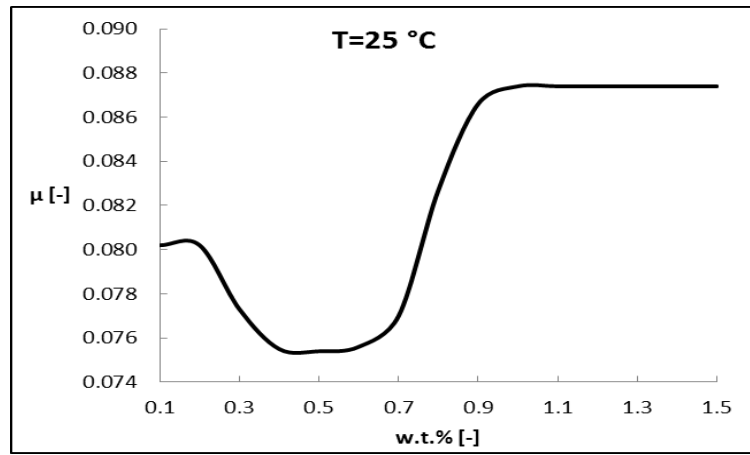


Fig. 2.11a- Friction coefficient in boundary regime at 25 °C ($v = 5$ mm/s; $p = 1.68$ GPa)

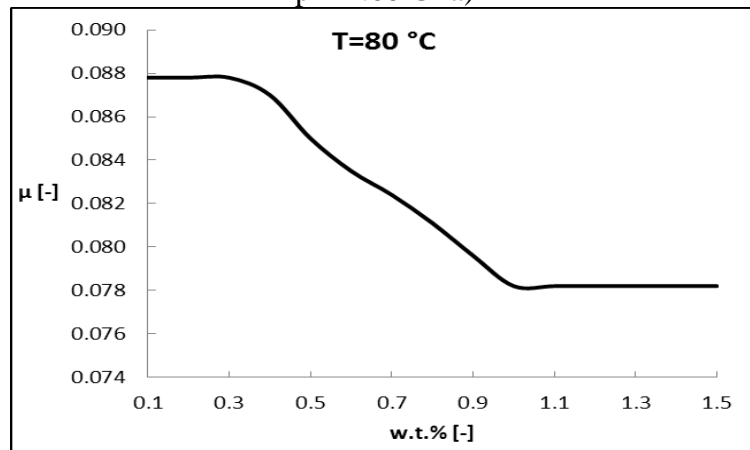


Fig. 2.11b- Friction coefficient in boundary regime at 80 °C ($v = 5$ mm/s; $p = 1.68$ GPa)

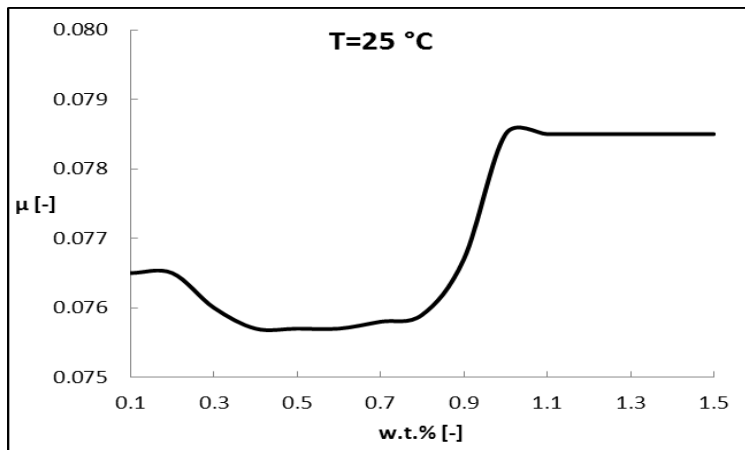


Fig. 2.11c- Friction coefficient in Mixed/EHL regime at 80 °C ($v = 0.5\text{ m/s}$; $p = 1.68\text{ GPa}$)

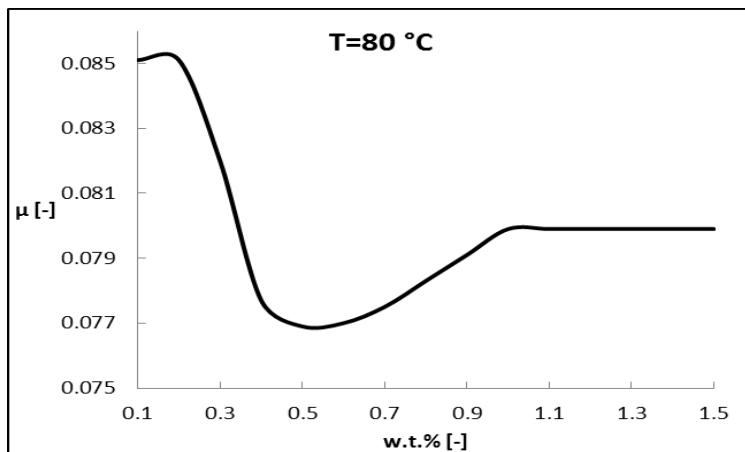


Fig. 2.11d- Friction coefficient in Mixed/EHL regime at 80 °C ($v = 0.5\text{ m/s}$; $p = 1.68\text{ GPa}$)

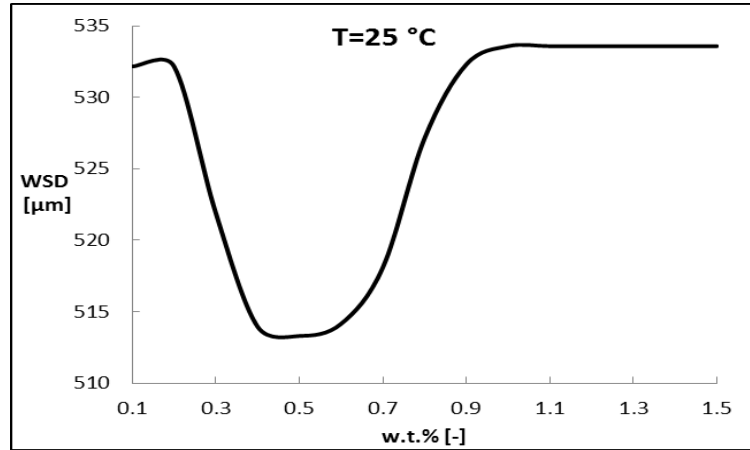


Fig. 2.11e- Wear Scar Diameter in boundary regime at 25 °C ($v = 5$ mm/s;
 $p = 1.68$ GPa)

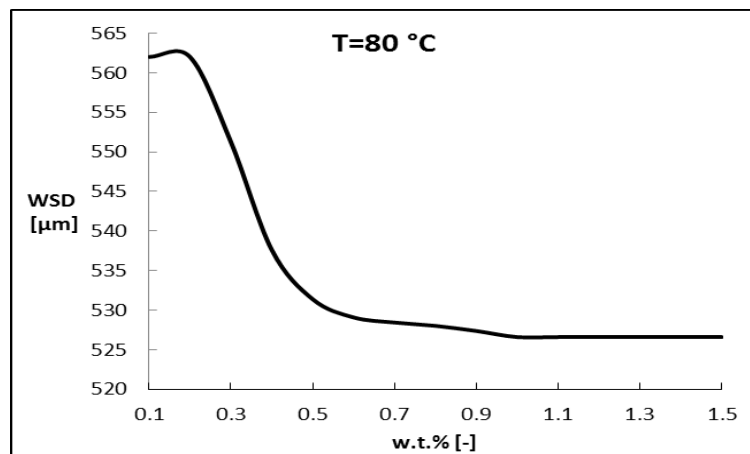


Fig. 2.11f- Wear Scar Diameter in boundary regime at 80 °C ($v = 5$ mm/s;
 $p = 1.68$ GPa)

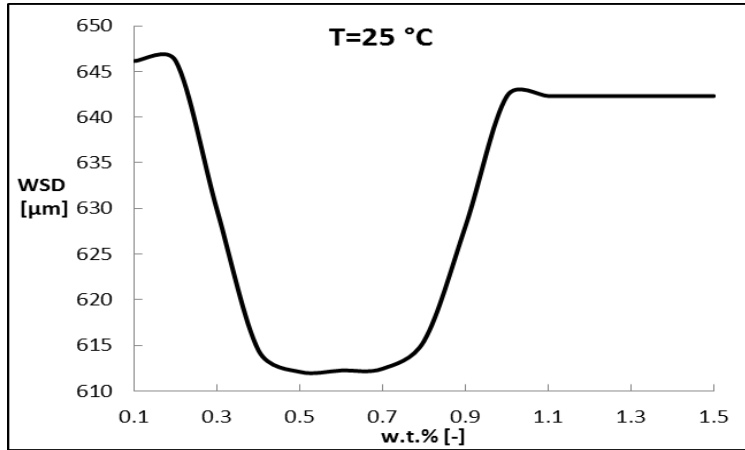


Fig. 2.11g- Wear Scar Diameter in Mixed/EHL regime at 25 °C ($v = 0.5$ m/s; $p = 1.68$ GPa)

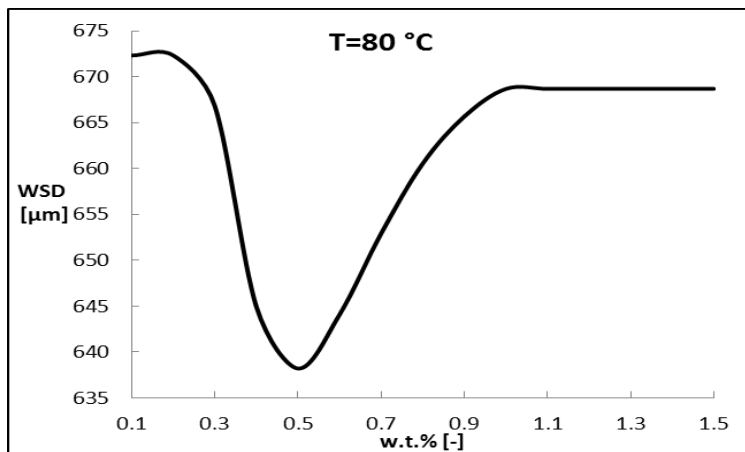


Fig. 2.11h -Wear Scar Diameter in Mixed/EHL regime at 80 °C ($v = 0.5$ m/s; $p = 1.68$ GPa)

2.1.6 Conclusion

The first part of this chapter, showing the results obtained for the samples formulated with inorganic nanoparticles, figured out the role of the MoS₂ nanoparticles as lubricating additive. The ability of the particles to exfoliate is directly related to the fast formation of a tribofilm made of MoS₂ nanosheets that protects the surface against wear and contributes to

reduce friction. For all the tested samples, the CoF showed a tendency to decrease with increasing contact pressure; the major reason is that the shear stress increased less rapidly in proportion to the contact pressure leading to a slight reduction of the friction with increasing pressure. Additionally, in all studied samples the CoF increased with the temperature.

This observation is attributed mainly to the effect of the lower lubricant viscosity in the boundary lubrication regime. The sample ARL1_N13_0.5 (Nanomaterials Ltd. nanoparticles) provides a very good result for the friction coefficient and wear scar diameter parameters compared to all the other tested samples, very similar with the sample ARL1_E11_0.5. Very close to the best results the sample ARL1_N11_0.5. About the sensitivity to the sliding speed, the samples ARL1_N13_0.5 and ARL1_N10_0.5 work better of others in boundary lubrication regime in a broad range of operating conditions. But they show an increase of the coefficient of friction at higher value of sliding speed.

On the other hand, the sample ARL1_E11_0.5 shows the best results compared to the other samples in Mixed/EHL lubrication regime. The sample ARL1_N12_0.25 (NPs @ 0.25 wt %) provides similar performance of the sample ARL1_N10_1.0 (NPs at 1 wt%). Thus, 0.5 wt% seems to be the favorite concentration. On the sensitivity to dispersant agent: the sample ARL1_N11_0.5 with NML nanoparticles and InS dispersant shows reduction in friction and wear with reference to other samples with the same NPs.

Since the formation of tribofilm/nanocoating on steel surface needs a characteristic time-dynamics as proved by CRF tests, the more realistic interpretation of the benefits in CoF and WSD here shown should be related to the mating surface sliding along XS2 planes with lower shear stress of the metal-to-metal contact [13-15]. Other mechanisms recently discussed in the literature in relation with “mending effect” (NPs ability to modify the metal surface topography) and electrostatic interaction between NPs and steel surface should be explored (Mo/W comparison).

About the stability of nanoparticles particle in ARL1 base oil with different dispersants, the samples N11_0.5 and N12_0.25 showed with one and two dispersants, respectively, all showed excellent stability. Both NML and CIDETEC particles showed acceptable stability.

2.2 RHENIUM DOPED FULLERENE-LIKE MOS₂ NANOPARTICLES

2.2.1 Nanoparticles synthesis

In this section the results obtained using a new kind of nanoparticles, inorganic fullerene-like molybdenum disulfide doped rhenium as lubricant additives have been shown [24-28].

Actually, for the experiments reported here Re-doped IF-MoS₂ NPs were prepared by Tenne and his co-workers at the Weizmann Institute (Israel) in situ, i.e., during the NP synthesis. Following is reported a quite brief description of the Re_xMo_{1-x}O₃ powder synthesis method.

2.2.1.1 Preparation of the Re doped molybdenum oxide

Firstly, the two weighted powders are grinded carefully in air, afterwards, ethanol is added to the mixture in the ratio 2:1 ethanol/powder ratio and left in an ultrasonic bath for 5 min under high intensity irradiation.

After drying in air, the powder is grinded and again put in crucibles and is inserted to an auxiliary horizontal reactor, Figure 2.12. The temperature is gradually raised from 300 °C to 735 °C (1 deg min⁻¹) under nitrogen atmosphere and remains there for 45 min. At this point the heating is stopped and the sample cools down to room temperature by a natural cooling process.

The crucible is then inserted to the main reactor for the sulfidization reaction.

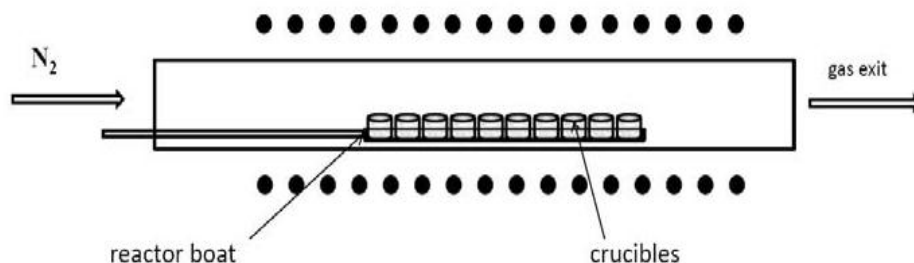


Fig. 2.12- Reactor for the preparation of the Re-doped molybdenum oxide

2.2.1.2 Determination of the rhenium content in the IF-MoS₂ nanoparticles

Standard methods, like energy dispersive X-ray spectroscopy (EDS) were used within the SEM and the TEM to estimate the Re content in the nanoparticles. Electron energy loss spectroscopy (EELS) was also used in the HRTEM to estimate the Re content in the nanoparticles and X-ray photoelectron spectroscopy was also used for this purpose.

The sensitivity of all these methods is about 0.1 at% and therefore their reliability in this case was limited. However, all three methods and in particular those used within the electronmicroscopes (EDS and EELS) showed variation of the Re content from one nanoparticle to another, with some nanoparticles not showing any Re signal, while others showed more signal than the formal concentration. In order to gain better confidence two other methods were used to measure the rhenium content in the MoS₂ nanoparticles, Figure 2.13.

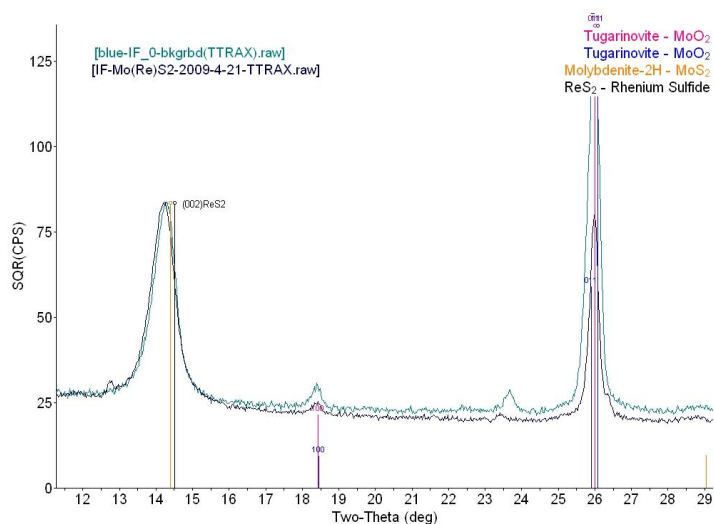


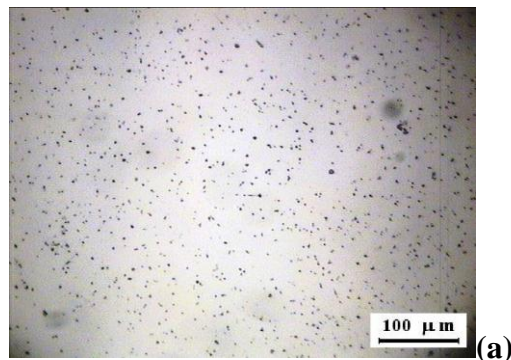
Fig. 2.13- XRD patterns of IF-MoS₂ powder and Re-doped IF-MoS₂ powder. The XRD pattern of the undoped and the Re (0.12 at%)-doped IF-MoS₂ NP are almost indistinguishable, Figure 2.13.

Both methods are sensitive to parts per million (ppm) and below, but they are not free of their own limitations due to issues of sample preparation and homogeneity of the sample. Both methods gave quite a consistent picture which can be summarized as follows:

- The overall atomic concentration of the Re in the nanoparticles is about one third to half of the formal concentration, i.e. the amount of ReO_3 weighed into the MoO_3 precursor powder.
- The Re concentration is not fully uniform with variations from batch to batch and from one measured point to the other (TOF-SIMS). The standard deviation was larger in the case of the TOF-SIMS measurement (0.1 vs. 0.05), due possibly to issues related to sample preparation.

2.2.1.3 Sedimentation experiments of the nanoparticles in PAO-4 oil

Paraffin oil with a viscosity of 60 cSt at 20 °C was used as a base oil. 1wt% of the IF-MoS₂ nanoparticles with an average size close to 80 nm was added to the paraffin oil. A magnetic mixer and spinbar magnetic stir bars have been used with a mixing time of 1 hour and the sedimentation analysis was performed during 24 h. A weight of the IF sediments was measured with an accuracy of 0.1 mg. Furthermore, no surfactants were applied for dispersion of the IF nanoparticles in the lubricant, Figure 2.14 a-c.



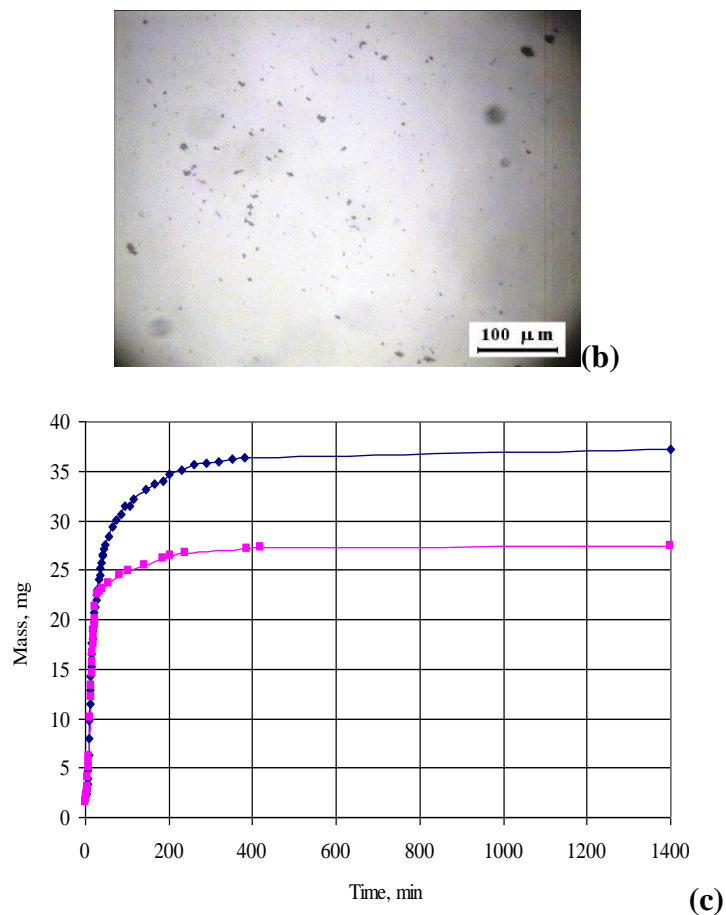


Fig. 2.14 - Optical microscopy image of through the bottom of the oil suspension 1 day after the initial mixing: a. Re doped IF-MoS₂ suspension; b. undoped IF-MoS₂. c. Sedimentation curve for the IF powder in PAO-4 oil (specific gravity- 0.86 g cm⁻³; viscosity- 0.027 Pa*s): blue- undoped IF-MoS₂; purple- Re (0.12 at%) doped IF-MoS₂.

2.2.1.4 X-ray absorption spectroscopy measurements and analysis

The raw XANES and EXAFS data collected at Mo-K edge showed virtually identical results for the pure IF MoS₂ and the Re-doped samples,

confirming that the structure around Mo is the same in all the samples. Both XANES and EXAFS data collected at the Re L_3 edge demonstrate distinct differences between the electronic structure and atomic arrangements of the Re-doped IF samples and ReS_2 . The area under the main XANES peak (also known as the white line) caused by the 2p-5d transition is proportional to the unoccupied d-state density. The higher white line intensity in the IF samples compared to ReS_2 indicative the greater degree of charge transfer in the former samples that, in turn, may be caused by the difference in their bonding geometries between these two systems. This hypothesis was verified by EXAFS analysis.

The first peak in r-space near 2 Å is due to Re-S coordination. In ReS_2 six Re-S bonds have lengths that range from ca. 2.3 to 2.5 Å (Figures 2.15) and thus the first peak intensity is relatively small due to the destructive interference in the EXAFS signal because of the split.

In MoS_2 , the first Mo-S shell is 6-fold degenerate, with the same distance for each S neighbor to Mo, Figure 2.15a. Thus, if Re substitutes for Mo in this system, its environment will be more ordered than in ReS_2 , and it will result in the higher peak intensity.

Also, ReS_2 has a group of second nearest neighbor Re-Re distances split in several sub-shells, (Figure 2.15b shows the first of such sub-shells containing 3 Re-Re bonds per Re). In MoS_2 , there is no split in the Mo-Mo bond distances.

Thus, in the substitutional model, Re-Mo distances should: 1) have the same length, 2) be 6-fold degenerate and 3) contribute to a relatively long distance range. In the ReS_2 structure, on the other hand, the Re-Re distances should: 1) be spread in the distances, 2) their first group should have only 3 Re-Re bonds per Re and 3) contribute to the relatively short distance range.

All these effects, predicted from the structural considerations of the two models (Figures 2.15c and d) are evident in the raw EXAFS data (Figure 2.15e). We also note that in the 0.12% Re concentration sample we have larger peak intensities compared to the 0.71% sample. It is consistent with the latter sample containing a small sub-mixture of ReS_2 phase.

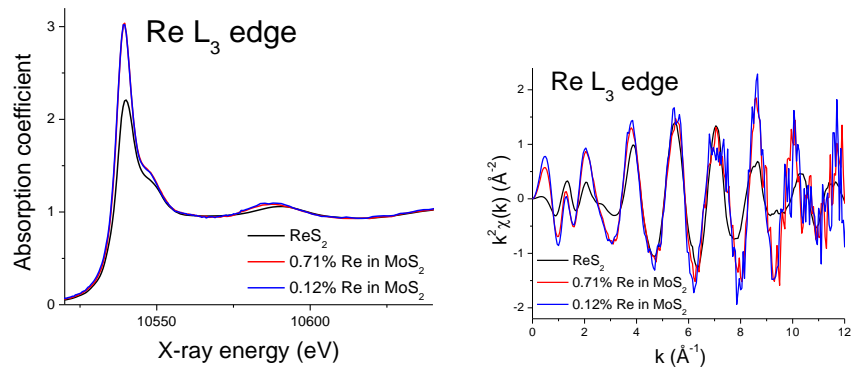


Fig. 2.15a- XANES and EXAFS data obtained for Re L₃ edge.

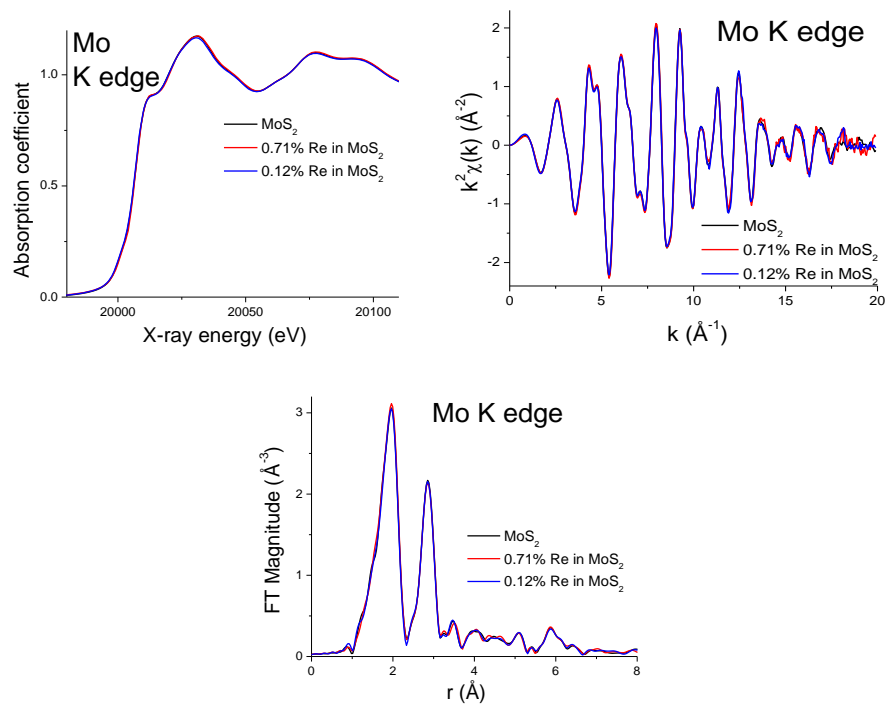


Fig. 2.15b- XANES and EXAFS data obtained for Mo K edge

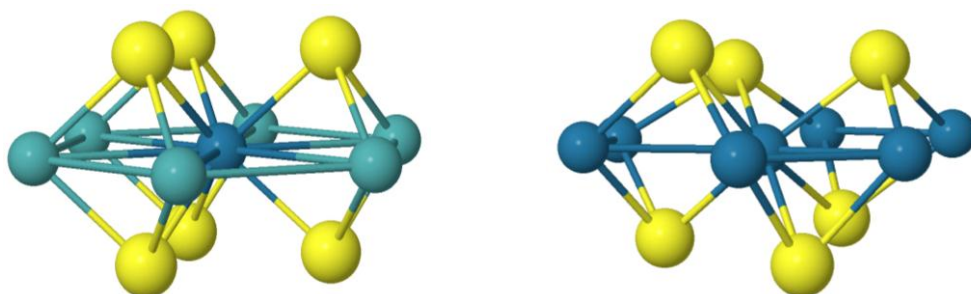


Fig. 2.15c and d - Schematic of the nearest neighbor environment around Re in ReS₂ (top) and substituting for Mo in the MoS₂ (bottom) structures. Re is blue, Mo is green/blue and S is yellow.

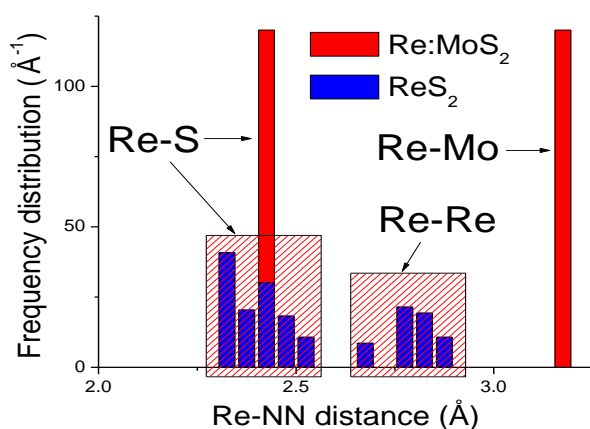


Fig. 2.15e - Frequency distribution of the bond lengths Re-S and Re-Re in the two models of Re environment: MoS₂ and ReS₂. The latter model has same number of Re-S bonds (6) but more broadly distributed, and the smaller number of Re-Mo bonds (3 vs 6) in the second nearest neighbor range, are also broadly distributed.

In the quantitative data analysis using FEFF6, we constructed a model where Re was embedded in MoS₂ structure substitutionally.

For that model, Re-S (1NN) and Re-Mo (2NN) contributions were used in the fit, and their distance corrections and the bond disorder parameters were varied. In addition, the coordination number of Re-Mo

bonds was varied as well, to account for a possible submixture of ReS_2 phase (it should be equal to 6 in MoS_2 structure).

The fits were done with k , k^2 and k^3 weightings. The model with Re in ReS_2 structure resulted in poor fit quality and non-physical fit results for the Re-Re contributions.

From the data analysis, the local environment around Mo was obtained to be the same, within the small uncertainties, as that in bulk MoS_2 , as expected.

The best fit results are shown in the Table 2.15. Coordination numbers, distances, and their mean square disorder values for Re-S and Re-Mo bonds confirm the substitutional model of Re incorporation in MoS_2 structure in the both samples.

Bond length(Å)	ReS_2	Re:MoS_2 (0.71%)	Re:MoS_2 (0.12%)	IF MoS_2
Re-S (1NN)	2.380(8) ^{S2}	2.377(6)	2.381(7)	-
Re-Re (2NN)	2.80(1) ^{S2}	-	-	-
Re-Mo (2NN)	-	3.13(1)	3.15(1)	-
Mo-S (1NN)	-	2.404(3)	2.403(4)	2.404(4)
Mo-Mo (2NN)	-	3.168(3)	3.167(4)	3.168(3)

Tab. 2.15- EXAFS data analysis results

These latest results suggest that when the dopant concentration exceeds 0.5 at% segregation of ReS_2 islets within and on the surface of the MoS_2 NP takes place. This phenomenon is not surprising in view of the very different unit cells of the two compounds. It is likely that non-uniform doping exists also for the lower doping levels, nonetheless it does not lead to a resistive behavior of individual NP [29-34]. Finally, typical high resolution scanning electron microscopy (HRSEM) and transmission electron microscopy (HRTEM) micrographs of the doped fullerene-like nanoparticles are shown in Figure 2.16.

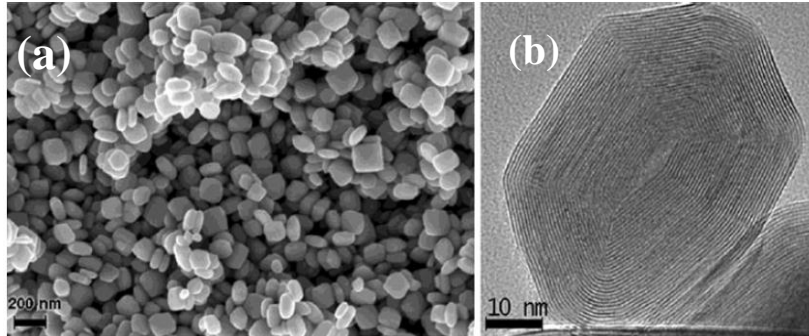


Fig. 2.16 - Typical high resolution scanning electron microscope (a) and transmission electron microscopy (b) image of Re:IF-MoS₂ NP. The interlayer spacing of the NP (0.624 nm) coincides with that of the undoped IF-MoS₂ NP (which is not much different from the values of the bulk material).

The IF NP consists of about 30 closed MoS₂ layers and has shape of a squashed ellipsoid, like a pita bread. No impurity, like oxides, or platelets could be found in the product powder and the layers seem to be evenly folded and closed with very few defects and cusps, demonstrating the IF are crystalline.

2.2.2 Friction test—Stribeck curve

The tribological equipment used to test the performance of the IF-Mo:ReS₂ is the same used for the previous section of this chapter with rotational disc tribometer. In order to explore the effectiveness of the rhenium dope on the tribological behavior of poly alpha-olefin (PAO-6), the sample have been compared to the same base oil lubricant formulated with undoped IF-MoS₂, IF-WS₂ and platelets (bulk) of 2H-MoS₂ additives. Furthermore, the main properties of the base oil were: kinematic viscosity, 30.5 cSt at 40 °C, 5.9 cSt at 100 °C; specific gravity, 0.823. The size and shape of these nanoparticles and platelets is presented in Table 2.16. The tested samples were obtained by mixing the additive in a granular form with PAO-6 base oil for 30 min, using a mechanical stirrer IKA T25 Ultra-Turrax disperser. No surfactant was added to the suspensions. The investigated contact type was composed of an upper rotating X155CrVMo12-1 steel disc of hardness 60 HRC, roughness of Ra=0.5 mm and 105 mm in diameter. A lower X45Cr13 steel ball, 52–54

HRC, 8 mm diameter was immersed completely in a temperature-controlled 220 ml lubricant bath. The test conditions in terms of contact pressure, temperature, sliding speed and running-in time are the same reported in Chapter 1.

	Re:IF-MoS ₂	IF-MoS ₂	IF-WS ₂	2H-MoS ₂
Median size	100 nm	100 nm	120 nm	< 2 μm
Typical size distribution	50–150 nm	50–150 nm	60–200 nm	
Typical shape	Rectangular, oblate	Rectangular, oblate	Polyhedral, faceted	Platelet

Tab. 2.16- Typical size and shape of the platelets and fullerene-like nanoparticles

Most of the Stribeck graphs in Figures 2.17-2.18 for hertzian pressure equal to 1.17 GPa and 1.47 GPa show a shape with a well-developed minimum, that is considered the transition from mixed lubrication regime to EHL regime for increasing speed [35]. This frontier divides the region with concurrent phenomena of solid-to-solid contacts, adhesion and interaction between friction modifier additives and steel surface (mixed lubrication) from the other with predominant viscous stress and elastic deformation of the tribopair surfaces (EHL). For instance, the transition appears at sliding speed of 0.40 m/s (0.80 m/s) for the test with hertzian pressure of 1.17 GPa (1.47 GPa) at the lower temperature, 25°C. According to the definition in [27], these transitions match in both cases the value $0.7 \cdot 10^{-3} \text{ m}^{-1}$ for the Stribeck parameter. The lower oil viscosity at higher temperature results in transition between mixed and EHL regime at higher sliding speed, on average around 1.5 m/s, and a Stribeck parameter of approximately $0.35 \cdot 10^{-3} \text{ m}^{-1}$. Due to the higher contact pressure of the tests with hertzian pressure of 1.68 GPa (90 N) and the lower oil viscosity at 50 and 80°C, only the boundary and the mixed lubrication regimes are prevailing in Figures 2.19a-c.

The reduction of the friction coefficient for the sample with 2H-MoS₂ as compared to the pure PAO-6 oil is rather low. Its effectiveness could depend on the precipitation tendency of the solid, especially for high temperatures.

Thus, at high temperatures the friction results for pure PAO-6 and PAO-6 formulated with 2H-MoS₂ were virtually identical. IF-WS₂ was found to work well exhibiting substantial reduction of the CoF compared to that of a pure PAO-6. For all the tested samples, the CoF showed a tendency to decrease with increasing contact pressure. According to previous works [26-41] which studied the friction under elastohydrodynamic conditions, the shear stress increased less rapidly in proportion to the contact pressure.

This leads to a slight reduction of the friction with increasing pressure. Additionally, in all studied samples the CoF increased with the temperature. This observation is attributed mainly to the effect of the lower lubricant viscosity in the boundary lubrication regime. In general, the samples with Re:IF-MoS₂ nanoparticles presented the best results in boundary, mixed and elasto-hydrodynamic lubrication regimes.

Below are shown the results obtained for the considered lubricant samples. The first group of graphs (Figures 2.17) represents the friction coefficient at the lowest value of the pressure contact, $p=1.17$ GPa.

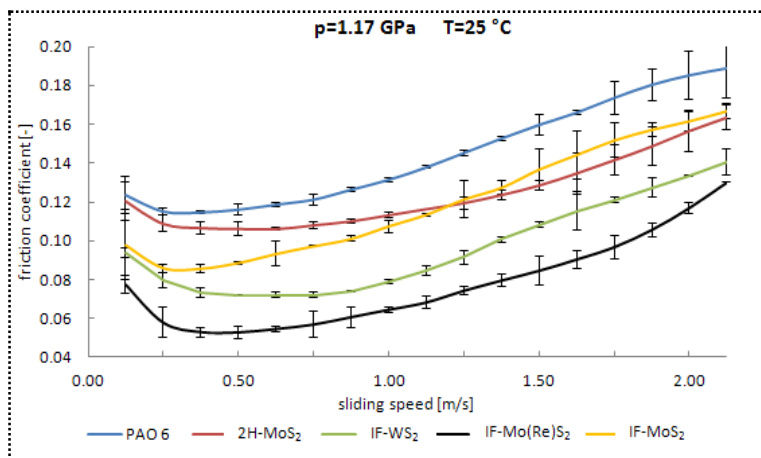


Fig. 2.17a- Stribeck curve from the sweep-speed test; $p=1.17$ GPa, $T=25$ °C

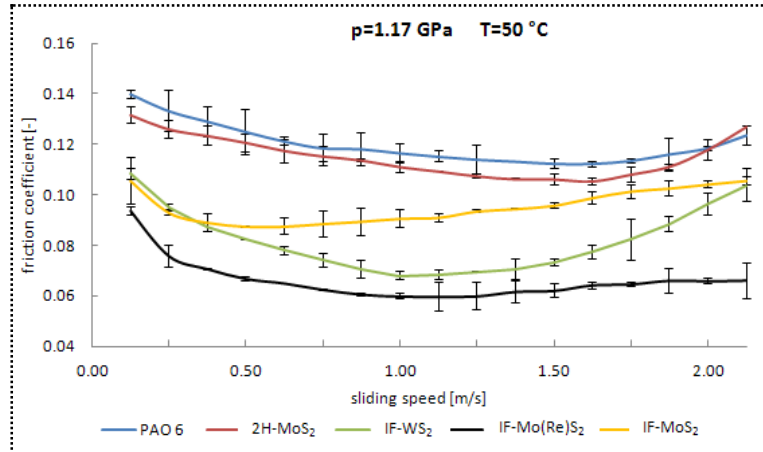


Fig. 2.17b- Stribeck curve from the sweep-speed test; $p=1.17$ GPa, $T=50$ °C

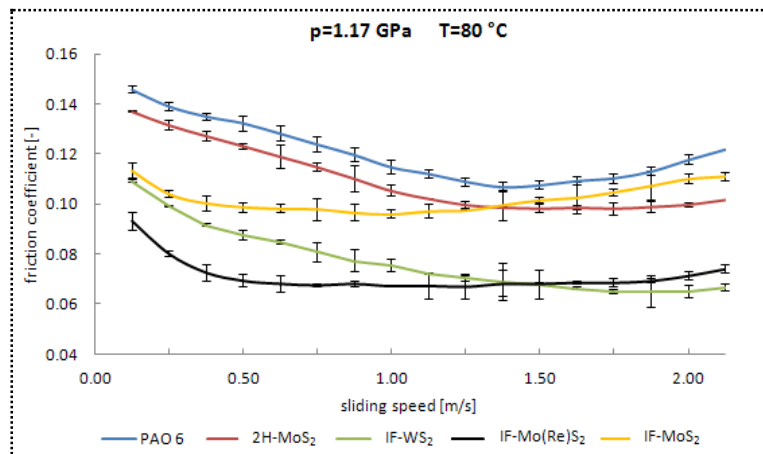


Fig. 2.17c- Stribeck curve from the sweep-speed test; $p=1.17$ GPa, $T=80$ °C

The second group of graphs (Figures 2.18) represents the friction coefficient at the middle value of the pressure contact, $p=1.47$ GPa.

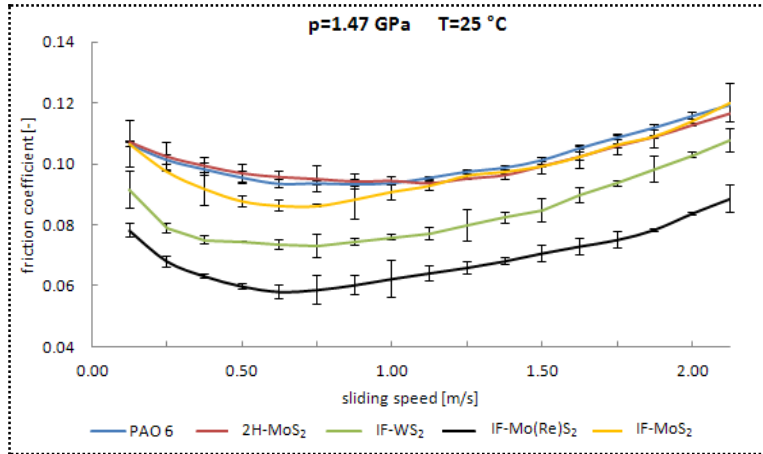


Fig. 2.18a- Stribeck curve from the sweep-speed test; $p=1.47$ GPa, $T=25$ °C

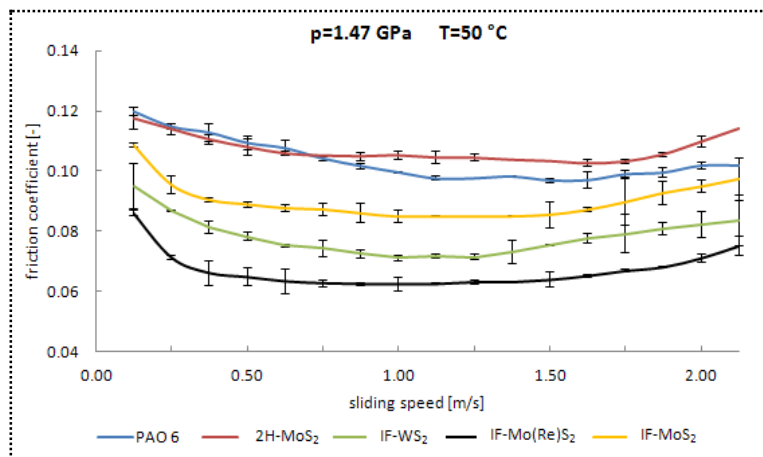


Fig. 2.18b- Stribeck curve from the sweep-speed test; $p=1.47$ GPa, $T=50$ °C

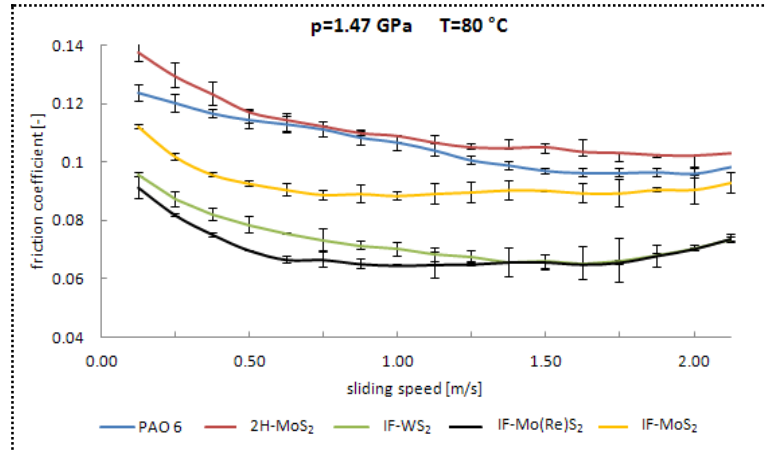


Fig. 2.18c- Stribeck curve from the sweep-speed test; $p=1.47$ GPa, $T=80$ °C

Finally, in the Figures 2.19 the third group of Stribeck curves are plotted for the highest value of the pressure contact, $p=1.68$ GPa.

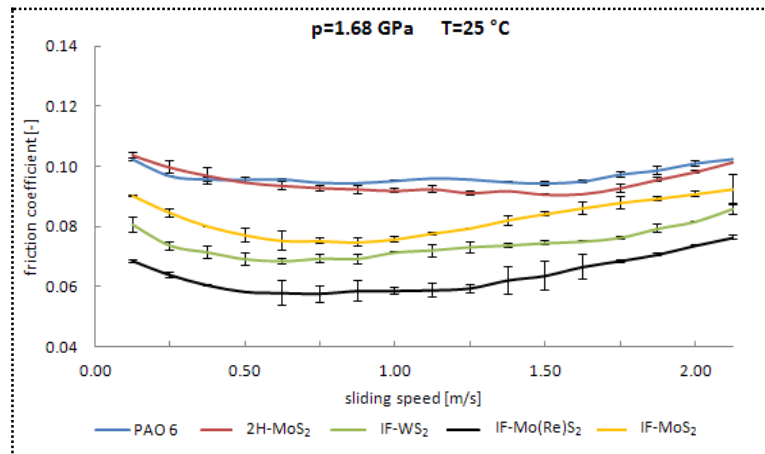


Fig. 2.19a- Stribeck curve from the sweep-speed test; $p=1.68$ GPa, $T=25$ °C

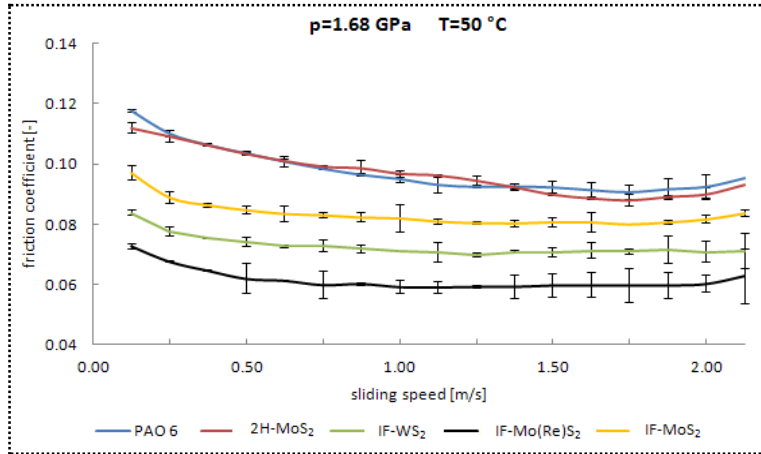


Fig. 2.19b- Striebeck curve from the sweep-speed test; $p=1.68$ GPa, $T=50$ °C

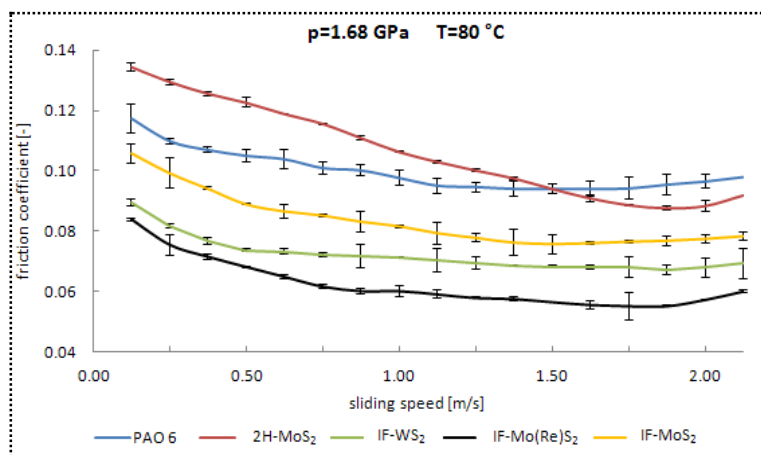


Fig. 2.19c- Striebeck curve from the sweep-speed test; $p=1.68$ GPa, $T=80$ °C

The reduction of the friction coefficient for the sample with 2H-MoS₂ is rather low. Its effectiveness could depend on the precipitation tendency, especially for high temperatures (that would explain why at high temperatures the friction results for PAO 6 and PAO 6 with 2H-MoS₂ are virtually identical).

Furthermore, it must be emphasized the very low settlement of the IF-based samples. IF-WS₂ works well with good reductions compared to PAO 6 friction coefficient. In particular, for all the tested samples, it is possible to identify a trend of reduction in friction with increasing contact

pressure, while it increases with increasing temperature, as expected, mainly due to the effect of the lower lubricant viscosity on the boundary lubrication component.

IF-Mo(Re)S₂ presents the best results in both lubrication regime (boundary and mixed), with reduction up to 60% in comparison with PAO 6 base oil.

These results are comparable to those of IF-WS₂; the former powder exhibits a very poor precipitation tendency, i.e., high stability of the mixture, even inspecting it after several hours.

2.2.3 FRICTION AND WEAR IN STEADY-STATE TESTS

Longer running frictional tests have been performed in order to analyse wear behaviour of the tribological steel pair ball/disc by using the lubricant samples described above and the obtained results are show in Figures 2.20(a) and 2.20(b). In particular, the worn surface of the steel ball has been analysed after 1-hour sliding test by means of an optical microscope to measure the wear circles diameter. For these tests, constant values for average hertzian pressure, temperature and speed have been chosen: 1.68 GPa, 25 °C – 80 °C, 5.0 mm/s – 0.50 m/s. Thus, it was possible investigating both boundary and mixed-EHL lubrication regimes. This test pattern has already proven to produce after a brief running-in a stable value of the friction coefficient with low variance.

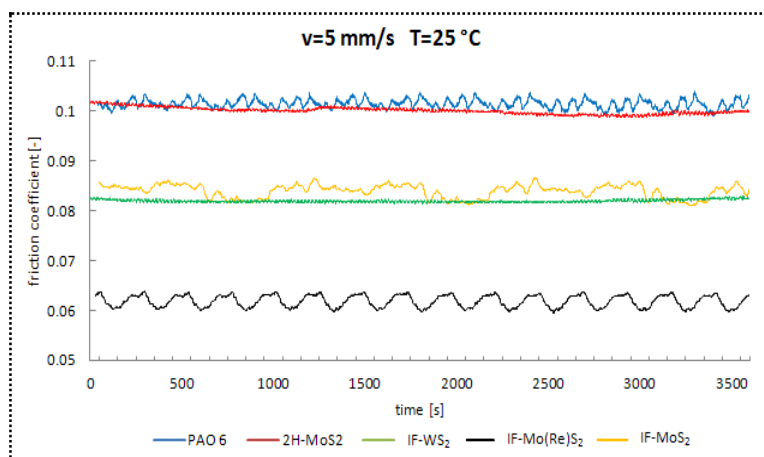


Fig. 2.20a-Evolution of friction coefficient; 1-hour test in boundary lubrication steady condition; $p=1.68$ GPa, $T=25$ °C, $v=5$ mm/s.

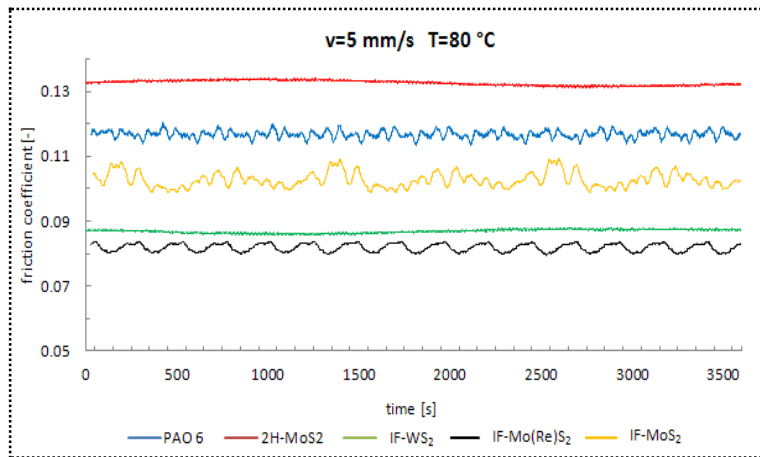


Fig. 2.20b-Evolution of friction coefficient; 1-hour test in boundary lubrication steady condition; $p=1.68$ GPa, $T=80$ °C, $v=5$ mm/s.

The results show a generally low dispersion of the data around the average CoF during each steady test for given sample, temperature, sliding speed and load. Also in the case of the steady-state test, the sample with Re:IF-MoS₂ presents the best frictional results in the two considered lubrication regimes.

The CoF values from the steady-state test are comparable with those obtained in the same tribopair working conditions through the sweep-speed test used for plotting the Stribeck curves discussed in par. 1.6.

This substantiates that the sweep speed test allows friction measurement not influenced by transient effects. The diameters of the wear circle observed on the steel ball specimens after 1-h steady-state test are listed in Tables 2.17-2.18. The entire IF samples induce significant reduction of the wear-scar diameter (WSD). Here again, the smallest WSD value emerges for the sample with Re:IF-MoS₂.

The friction coefficient in the Tables 2.17 and 2.18 are presented with an expanded uncertainty equal to $5.0 \cdot 10^{-3}$.

Sample	Friction coefficient[-] in boundary lubrication at 25°C	Friction coefficient[-] in boundary lubrication at 80°C	Difference
PAO 6	0.103	0.118	<i>Benchmark</i>
PAO 6 with 1 wt% 2H-MoS ₂	0.100	0.132	-3% +11%
PAO 6 with 1 wt% IF-MoS ₂	0.088	0.106	-15% -10%
PAO 6 with 1 wt% IF-WS ₂	0.083	0.087	-19% -26%
PAO 6 with 1 wt% IF-Mo(Re)S ₂	0.063	0.068	-39% -42%

Tab. 2.17-Friction coefficient in boundary lubrication steady condition; sliding speed: 5.0 mm/s.

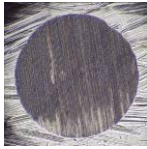
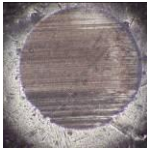
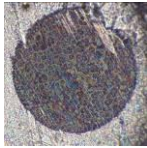
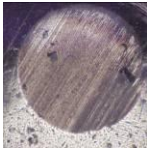
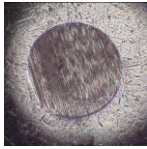
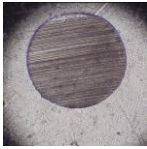
The Table 2.18 shows CoF values in good agreement with those measured with the frictional speed-sweep tests previously described and represented by the Stribeck curves.

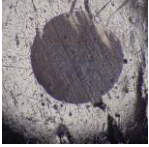
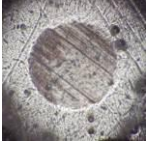
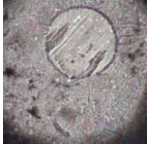
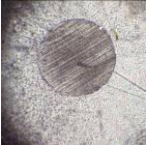
Sample	Friction coefficient [-] in mixed lubrication at 25 °C	Friction coefficient [-] in mixed lubrication at 80 °C	Difference
PAO 6	0.098	0.107	<i>Benchmark</i>
PAO 6 with 1 wt% 2H-MoS ₂	0.095	0.120	-3% +10%

PAO 6 with 1 wt% IF-MoS ₂	0.076	0.085	-22%	-21%
PAO 6 with 1 wt% IF-WS ₂	0.072	0.075	-26%	-30%
PAO 6 with 1 wt% IF-Mo(Re)S ₂	0.060	0.068	-39%	-36%

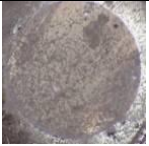
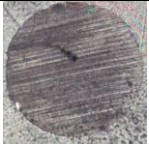
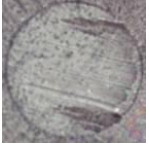

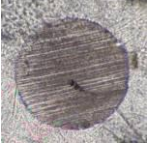

Tab. 2.18-Friction coefficient in mixed lubrication steady condition; sliding speed: 0.50 m/s.

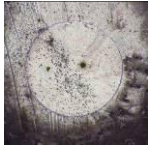
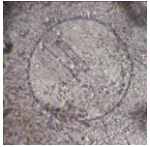
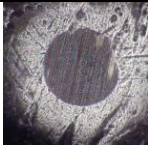
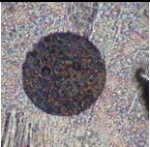
The Tables 2.19 and 2.20 illustrates the optical micrograph and the diameter of the wear circles observed on the steel ball specimens after 1-hour steady conditions wear test.

Sample	Ball wear scar diameter [μm] in boundary lubrication at 25 °C	Ball wear scar diameter [μm] in boundary lubrication at 80 °C	Difference
PAO 6	 700	 720	<i>Benchmark</i>
PAO 6 with 1 wt% 2H-MoS ₂	 700	 710	0% -1%
PAO 6 with 1 wt% IF-MoS ₂	 560	 580	-20% -19%

PAO 6 with 1 wt% IF-WS ₂	 500	 510	-28% -29%
PAO 6 with 1 wt% IF-Mo(Re)S ₂	 420	 440	-40% -39%

Tab. 2.19-Optical micrograph and wear scar diameter (WSD) after boundary lubrication steady condition test; sliding speed: 5.0 mm/s.

Sample	Ball wear scar diameter [μm] in mixed lubrication at 25 °C	Ball wear scar diameter [μm] in mixed lubrication at 80 °C	Difference
PAO 6	 810	 830	<i>Benchmark</i>
PAO 6 with 1 wt% 2H-MoS ₂	 790	 830	-2% 0%
PAO 6 with 1 wt% IF-MoS ₂	 640	 680	-21% -18%

PAO 6 with 1 wt% IF-WS ₂	 580	 600	-28% -28%
PAO 6 with 1 wt% IF-Mo(Re)S ₂	 470	 490	-42% -42%

Tab. 2.20-Optical micrograph and wear scar diameter (WSD) after mixed lubrication steady condition test; sliding speed: 0.50 m/s.

Regarding to the wear test outcomes, they mirror those related to the friction measurements resulting in high Pearson's correlation coefficients: 0.89 on the couples of data CoF-WSD in boundary lubrication tests and 0.95 for the data from mixed-EHL tests.

The best results emerge again for the samples with IF-Mo(Re)S₂ and IF-WS₂. In fact, as for friction results there is a slightly impact of the 2H shaped MoS₂, while the reduction of the wear scar is important for the samples with IF-nanoparticles. For a given lubricant sample, the anti-wear performance based on the WSD reduction is practically the same in both the lubrication regimes.

It is worth noting that all the outcomes of the wear test mirror the respective average CoF values in Figures 2.20 resulting in high Pearson's correlation coefficients: 0.89 for the couples of data CoF-WSD in boundary lubrication conditions and 0.95 for the data from mixed tests.

2.2.4 Surface analysis

SEM, EDS and XRD confirmed that the IF NP, i.e., IF-WS₂, IF-MoS₂ and Re:IF-MoS₂, remain on the surface of the ball after the test (Figures 2.21 and Figures 2.22). In contrast, 2H-MoS₂ platelets are rarely observed on the wear scar (Figure 2.21a). These results could explain the fact that the CoF and WSD for 2H-MoS₂ with PAO-6 are so similar to those of the pure PAO-6 under mixed and boundary lubrication regimes (Figures 2.20 and Table 2.19-2.20). SEM micrographs (Figure 2.21b) reveal that the IF-

WS₂ are somewhat damaged after the sliding wear test. Both, IF-WS₂ and the IF-MoS₂ are found to be agglomerated (Figure 2.21b and d).

In contrast, in the areas of WSD which were covered by Re:IF-MoS₂ it appears that these NP form a type of a discontinuous ordered monolayer tessellation on the surface (Figure 2.21c). Moreover, the Re doped IF exhibits the smallest damage to the tested surface.

It is worth noting that the IF NPs are located not only on the wear scar surface, but also in the little dimples on the WSD (Figures 2.23).

This “mending” of the surface probably also contributes to the reduction of CoF and WSD. The EDS analysis shows large variance between the different tribological surfaces (Table 2.21). For small magnification, i.e., large analyzed surfaces (50 mm spots), the EDS signal of the ball tested with 2H-MoS₂ produces a very weak molybdenum signal, which varies from place to place.

On the contrary, the surface tested with Re-doped NP produces much more uniform Mo signal, indicative of a uniform distribution of the Re-doped NP on the metal surface.

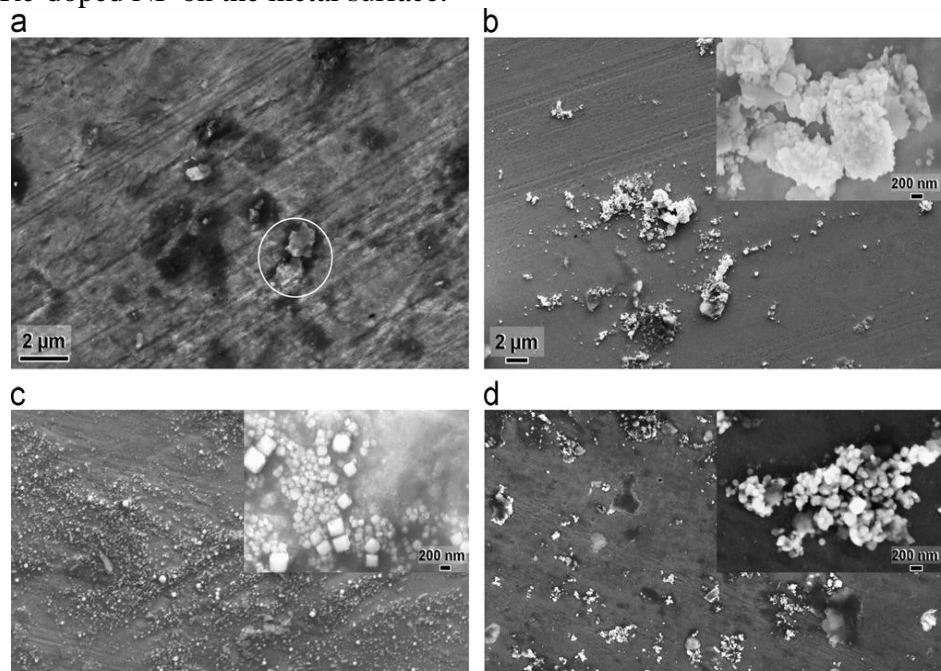


Fig. 2.21- SEM micrographs wear scar of steel ball for each lubricant sample: (a) 2H-MoS₂, (b) IF-WS₂, (c) Re:IF-MoS₂ and (d) IF-MoS₂.

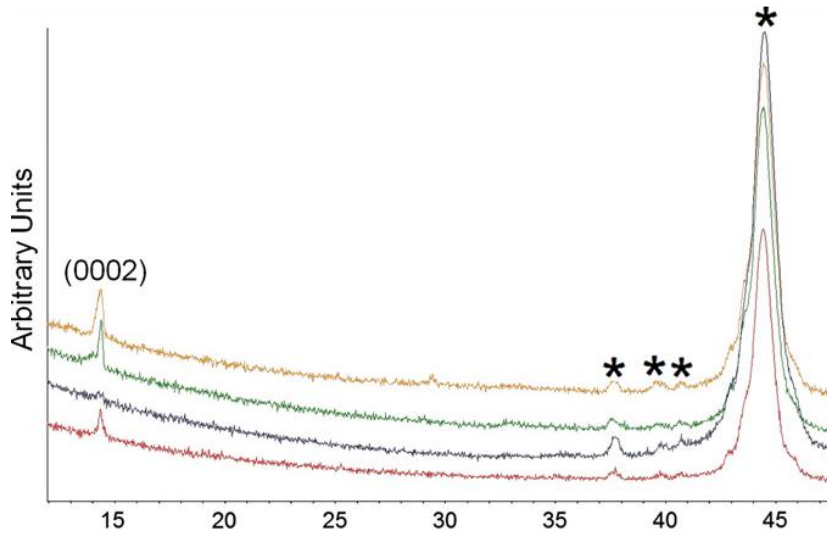


Fig. 2.22- XRD patterns of the wear-scar for all the tested samples. The (0 0 0 2) peak is related to MS_2 (M=Mo,W). The peaks marked with asterisk (*) are related to the steel ball.

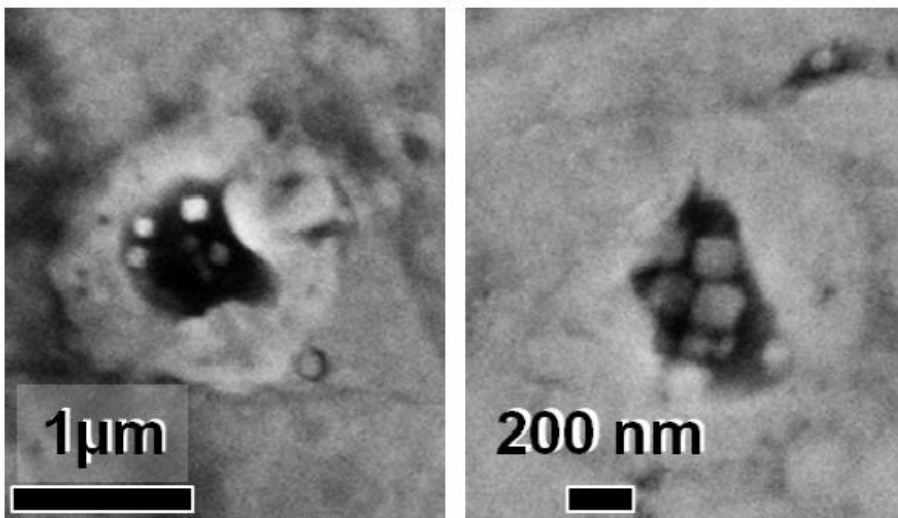


Fig. 2.23- SEM micrograph of a typical dimple on the wear scar of steel ball, filled with the IF.

Sample	Average atomic % per mm
PAO 6 with 1 wt% 2H-MoS ₂	0.0028
PAO 6 with 1 wt% IF-MoS ₂	0.0089
PAO 6 with 1 wt% IF-WS ₂	0.0151
PAO 6 with 1 wt% IF-Mo(Re)S ₂	0.0069

Tab. 2.21- EDS (energy dispersive X-ray spectroscopy) analysis of the wear scar (small magnification). The steel ball for each lubricant sample was prepared by 1-h sliding wear test in steady-state conditions, such that the average hertzian pressure was 1.68 GPa, temperature 25°C and sliding speed 0.50 m/s.

The EDS analysis of the surfaces lubricated with the undoped NP exhibited a scenario in between these two extremes, i.e., the undoped nanoparticles are non-uniformly distributed on the metal surface, but with non-uniformities smaller than those found for the surfaces lubricated with the 2H-MoS₂ platelets. For additional quantification of the NP on the wear scars, XRD analysis was performed (Figure 2.22). From the area below the (0002) peaks, it could be concluded that the apparent amount of the Re:IF-MoS₂ NP on the ball surface is 5 to 10 times smaller than the other IF's. These findings cannot be easily understood given the fact that both SEM and EDS analyses showed quite uniform surface coverage of the Re-doped NP. However, since the size of the probing XRD beam (1mm in diameter) is appreciably larger than the electron beam size used for the EDS analysis, it is not affected so much from non-uniformities of the surface coverage. The XRD analysis also revealed that the (0 0 0 2) peak of the 2H-MoS₂ platelets is higher than that of the Re:IF-MoS₂. It suggests that the platelets have a stronger crystalline orientation and does not necessarily reflect a quantitative difference in the surface coverage. To verify this assumption, thetascan (rocking curve) of all the samples was performed at the fixed 2-theta of the (0 0 0 2) peak. Indeed, high

preferred orientation of the 2H-MoS₂ platelets was observed. Due to the squashed ellipsoid shape of the IF NP, theta-scan of the IF-MoS₂ and IF-WS₂ revealed some preferred orientation [42]. However this orientation was much weaker than that obtained for the 2H platelets. Re-doped sample did not show any peak, which is another indication for the small amount and the uniform distribution of these NP. The XRD analysis did not show any peaks of Mo or W-oxide phases on the wear scar on either the IF or platelets-tested surfaces. Thus, it can be concluded that the particles which were oxidized during the wear tests resulted in amorphous oxide material.

2.2.5 DISCUSSION

The fact that the fullerene-like nanoparticles of WS₂ and MoS₂ outperform their bulk analogues as solid lubricant is known for some time [43,44]. The on-going debate on the friction mechanism of such nanoparticles is also not new. It was argued that the main three tribological mechanisms involved are: rolling, sliding and exfoliation/materials transfer. It was furthermore argued that the reduced wear in this case can be attributed to the robustness and flexibility of such nanostructures which prevent metal to metal contact. The combined post-mortem SEM/EDS/XRD analysis shows that the platelets of MoS₂ are almost absent from the tribological interface, while the IF nanoparticles are clearly seen (see Figure 2.21). This suggests that the nanoparticles can access the tribological interface more easily and they are not consumed as fast as the MoS₂ platelets. The relative chemical inertness of the IF nanoparticles can be attributed to their closed morphology, i.e., absence of reactive dangling bonds which are prone to facile chemical oxidation.

However, since here the size difference between the IF NP is not significant, it did not affect the results. Nevertheless, the small (as compared to the platelets) size of the NP allows them an easy access to the metal contact area, thus substantially lowering the CoF and wear. Two series of experiments with individual nanoparticles were recently reported. In one series of experiments, carried out within high resolution TEM, individual IF nanoparticles were loaded and sheared between two surfaces [45,46]. In the other series, performed in high resolution SEM, similar loading and shearing of individual NP was performed [47]. Both

kinds of experiments, while being far from realistic tribological tests, provided a first-hand evidence for the tribological mechanisms of metal interfaces in the presence of such nanoparticles. Indeed, rolling friction, which provides an extremely low friction, was clearly observed in these two series of experiments. Furthermore, in these studies, exfoliation of the IF nanoparticles was shown to be a predominant lubrication mechanism under boundary lubrication conditions. Finally, the strength of the nanoparticles was found to be between 1 and 3.5 GPa, pending on the size, faceting, and kind of NP with IF-MoS₂ being stronger than IF-WS₂.

This suggests that such nanoparticles can effectively separate two metal surfaces and prevent rapid wear during tribological tests. Another aspect which has been recently discussed in the literature in relation with nanoparticles' additives is the "mending effect", i.e., the healing of the surface during the tribological test. A similar effect was found for surfaces lubricated with the Re-doped nanoparticles. It was shown that the measured surface roughness of the wear trace was reduced from the initial 1.5 mm to about 0.15 mm after the tribological test. [48] The smooth surface produces an effective larger contact area, i.e., a lower average load, which is translated into a reduced friction and wear. In yet another recent report, the mending effect in the presence of (undoped) IF nanoparticles was studied using different substrates [46]. Apparently, the IF nanoparticles which were exfoliated during the tribological work, reacted with the oxidized stainless steel surface. A tribochemical mechanism involving the reaction between the molecular MoS₂ sheet and the iron oxide has been proposed. Notwithstanding this complexity, more work is called for to clarify the functioning of the doped nanoparticles in tribological interfaces. Additional reason for the smoother surface of the surface lubricated with the doped NP could be the "filling" of the little dimples by the doped NP (Figure 2.23). One of the obstacles for the nanoparticles to operate effectively is their accumulation and agglomeration at the tribological interface. The agglomeration prevents their free motion and denies the supply of oil into the rubbed zone. The mutual repulsion between the negatively charged Re-doped nanoparticles [42] seems to alleviate this problem and allow an independent and free action of the NP within the tribological interface. Indeed, the Re-doped nanoparticles were shown to disperse and form stable suspensions with different solvents [43]. SEM analysis of the tribological interfaces (see Figure 2.21c) clearly shows reduced agglomeration of the Re-doped IF

NP. This analysis supports the idea that the reduced agglomeration of the doped NP allows them to operate more effectively, alleviating thereby both friction and wear. Static charge accumulation is inevitable in the tribological interfaces. Thus a clear linkage between the electrical properties of the lubricating NP and the reduction of CoF and WSD, is expected [32-34]. The resistivity of the Re:IF-MoS₂ NP was studied and compared to the undoped IF-MoS₂ NP and 2H-MoS₂ before [22]. It was shown that the doping of the IF NP leads to a remarkable drop in their resistivity as compared to the undoped NP. Thus the considerable decrease in CoF and WSD when Re:IF-MoS₂ NP are used, could be attributed also to the build-up of a film with significant conductivity on the matting metal contact. These results indicate that CoF and WSD are adversely affected by tribocharging of the interface.

2.2.6 Conclusions

The tribological tests confirm the earlier observations that the performance of PAO oils formulated with IF nanoparticles as solid lubricants, lead to significant reduction in both friction and wear in both boundary and mixed lubrication regimes under severe test conditions.

The best results were achieved by the doped Re:IF-MoS₂ NPs. For instance, with average contact pressure of 1.68 GPa and temperature in the range 25–80 °C, the average CoF decreased by more than 40% compared with the base lubricant value. Using IF-WS₂ nanoparticles also resulted in rather low friction and wear, however the tendency for agglomeration and oxidation is an important disadvantage when compared to the Re doped IF.

It is noteworthy to mention that all the particles dispersed in the lubricant in this work did not require chemical activation and show a clear effect already at room temperature. Thus, the effectiveness of the nano-additives appears to be closely related to their precipitation tendency. This assumption is confirmed by the friction results at higher temperatures. For instance, the lubricant samples with Re:IF-MoS₂ reveal the highest stability of the mixture. In contrast, the sample formulated with 2H-MoS₂ show a very high inclination to precipitate and exhibit the same frictional behavior like the base oil.

The IF nanoparticles exhibited improved tribological behavior compared to the 2H-MoS₂ platelets. Their closed structure entails chemical inertness, which makes them less prone to facile chemical oxidation. Their small size and round like configuration facilitates their access to the tribological interface.

Despite the small amount of the Re-doped NP observed on the metal surface after the test, i.e., only one-fifth compared to the other IF, the oil with these NP demonstrated superior tribological behaviour to all other additives. This significant improvement could be attributed to their better dispersion in the oil which endowed the lubricant improved rheological behaviour. Furthermore, the advanced lubricity could be attributed to the low resistivity and the negative charge which led to the formation of highly uniform and conductive IF monolayer on the mating metal contact.

2.3 ORGANIC NANOADDITIVES: GRAPHENE AND GRAPHITE

In the last section of the present chapter the tribological results obtained using organic nanoadditive in oil lubricant will be presented. In particular, the effect of graphite powder and graphene oxide platelets will be shown.

2.3.1 Introduction

Recently, due to high load-bearing capacity, low surface energy, high chemical stability, weak intermolecular, and strong intramolecular bonding, nanocarbon materials, such as graphite [47] and some graphite derivatives [48], have received a great attention by tribology researchers. These materials are characterized by weak interatomic interactions between their layers (Van der Waals forces) and low-strength shearing. In recent years graphene platelets due to their unique structure and remarkable properties have been the focus of interest. Huang et al. [49] investigated the tribological properties of graphite nanosheets (10-20 nm thick), obtained by ball milling of natural flake graphite, in oil. They found that the frictional behaviour and anti-wear ability of the lubricating oil were improved when graphite nanosheets and dispersant were added to the paraffin oil at the optimal concentration. Lin et al. [50] suggested

that functionalizing the graphene platelets with a proper modifier is an effective way to prevent the dispersion of the additive. They demonstrate that stearic acid and oleic acids are the most suitable modifiers for their platelets (10-15 nm thick). Contemporaneously [51], graphene oxide nanosheet, obtained by graphite chemical exfoliation, modified with oleic acid to enhance the dispersability in oil, and further reduced in hydrazine hydrate to improve the carbon order level, were investigated using a four-ball tribometer. Here we report the preparation of graphene oxide (GO) nanosheets (5-6 nm thick) by a very fast modified Hummers method. Due to the preparation method the nanosheets are characterized by a low level of order, while the surfaces result in rich of $-OH$ and $-COOH$ groups giving them a polar behaviour. We chose, at the best of our knowledge for the first time, to use as produced GO, avoiding further chemical reactions and to disperse through a methodology well known to the lubricant industry by the use of a dispersant, that with its polar head can enwrap one nanoparticle to repel another and therefore form a uniform dispersion. On the other hand, amorphous structure are much easier exfoliated than the perfect structure [52] leading to an easier formation of a tribofilm on the worn steel surface. The tribological behaviour of a very low amount of GO mixed with a dispersant in a base mineral (SN150) was investigated under very wide spectrum of conditions, i.e. from boundary and mixed lubrication to the elastohydrodynamic (EHL) regimes. The nanosheets were widely characterized. To explore the performances of the nanosheets in the lubricating fluid, a rotational tribometer with a ball on disc setup has been employed. Raman analysis on the steel ball worn surfaces was performed to investigate the presence of graphitic material on the mating surfaces after tribological tests, in order to verify the formation of a protective film on the rubbing surfaces due to the additive.

2.3.2 Nanosheets preparation and characterization

2.3.2.1 Materials

Graphene Oxide (GO) nanosheets were prepared by a modified Hummer method [53]. The oxidation of graphite particles were obtained from Lonza [54] to graphitic oxide accomplished with a water-free mixture of concentrated sulfuric acid, sodium nitrate and potassium permanganate.

The entire process requires less than two hours for completion at temperatures below 45 °C. With the aid of further sonication step, the oxidized graphite layers were exfoliated from each other. Then 30% H₂O₂ was added to the suspension to eliminate the excess MnO₄⁻. The desired products were rinsed with deionized water. The remaining salt impurities were eliminated with resinous anion and cation exchangers. The dry form of graphitic oxide was obtained by centrifugation followed by dehydration at 40 °C. To provide dispersion stability of the additive a polyisobutyl succinic acid-polyamine ester was sonicated with the GO nanosheet (0,01 w.t.% in base oil), the weight ratio GO/dispersant was 0.35. The dispersant attaches itself to the solid particles with its polar head, and has a very long hydrocarbon tail that keeps it suspended in oil. For the dispersion, a sonication (Hielscher UP 400S) of 30 min in 25 ml mineral oil, followed by a mixing with a Silverson L5M homogenizer for 30 min, were employed. The resulting sample is named GSN150 in the following.

2.3.2.2 Characterization techniques

Scanning electron microscopy (SEM) pictures were obtained with a LEO 1525 microscope. The samples, without any pre-treatment, were covered with a 250 Å thick gold film using a sputter coater (Agar 108 A). Raman spectra were obtained at room temperature with a microRaman spectrometer Renishaw inVia with 514 nm excitation wavelength (laser power 30 mW) in the range 100-3000 cm⁻¹. Optical images were collected with a Leica DMLM optical microscope microscopy connected on line with the Raman instruments. XRD measurements were performed with a Bruker D8 X-ray diffractometer using CuKα radiation. Transmission electron microscopy (TEM) micrographs were obtained with a JEOL JEM 2010 electron microscope operating at 200 keV. Thermogravimetric analysis (TG-DTG) at 20 K/min heating rate in flowing air was performed with a SDTQ 500 Analyzer (TA Instruments).

2.3.2.3 Tribological tests description

As for the test performed for the lubricant samples with the addition of the inorganic nanoparticles showed in the previous section, also for the

organic additive samples, the investigated tribopair was composed by an upper rotating disc and a lower ball specimen completely flooded in a temperature-controlled lubricant bath. The upper element of the tribopair was a X155CrVMo12-1 steel disc, 60 HRC, roughness $R_a = 0.50 \mu\text{m}$ and 105 mm diameter, the lower one was a X45Cr13 steel ball, 52-54 HRC, 8 mm diameter. Speed-sweep tests at constant load and constant sliding speed have been performed at the same contact pressures, temperatures and sliding speeds used in the previous section.

2.3.2.4 Graphite and GO characterization

Graphite chips and GO nanosheets are shown in Figures 2.24a, 2.24b respectively. The images evidence the loss of the chips structure of original graphite to GO transparent and thin flakes.

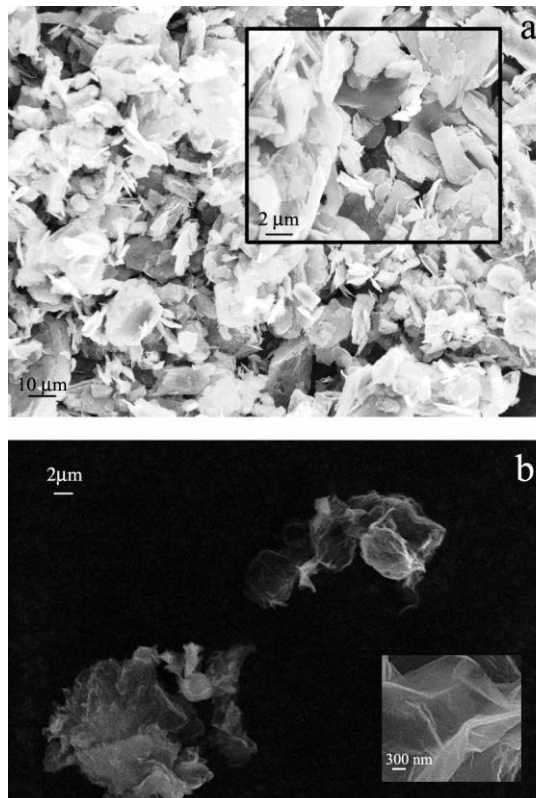


Fig.2.24- SEM images of Graphite (a), GO (b).

The TEM images in Figure 2.25 reveal the thickness of the graphene oxide nanosheets that is in the range 5-6 nm. The high resolution transmission electron image quite permits to measure the number of sheets, characterized by a not so high level of order. X-ray diffraction spectra of original graphite and GO are shown in Figure 2.26, in the 2θ range 20° – 80° . It is clearly evident the loss of the original graphite structure for GO [55,56].

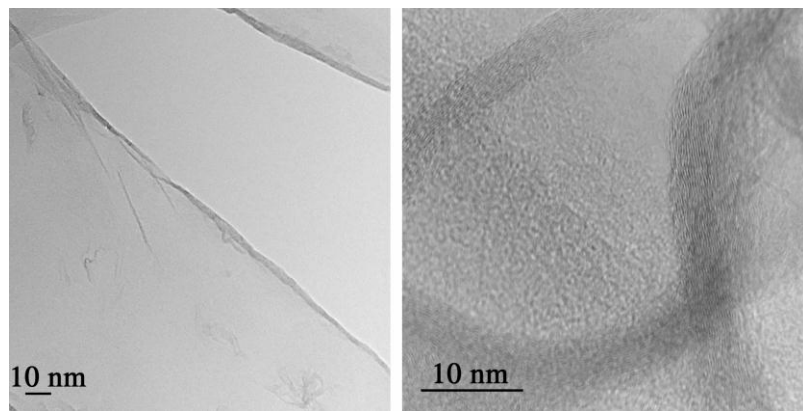


Fig. 2.25-TEM image of GO at different magnification.

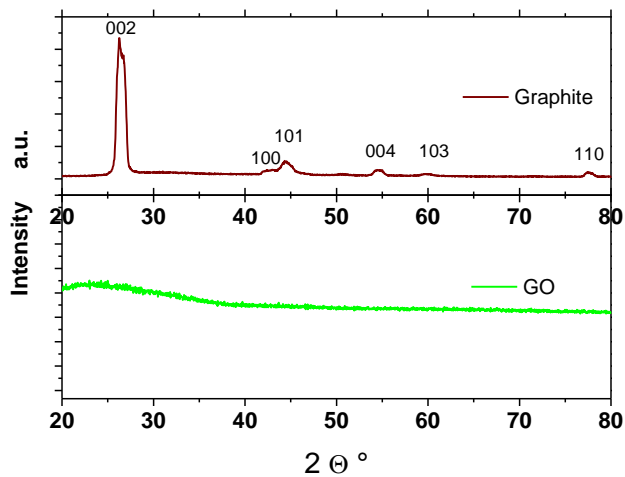


Fig. 2.26- X-ray diffraction patterns of Graphite and GO.

In Figure 2.27 the TG-DTG profiles of the tests performed with graphite and GO, are reported. The oxidation of the GO occurs as a one-step loss, centred at 605 °C, well below the graphite oxidation temperature, likely due to the loss of the graphite original order. The thermal conversion of the dispersant in air flow occurred in two main weight loss steps (Figure 2.28), due to its decomposition (as clearly indicated by the corresponding total ion current (TIC), in particular in the figure the mass fragments peaks: $m/z = 58$, 72, 83 coming from the NH_2 -containing group are shown), and the formation of CO_2 ($m/z = 44$) [57].

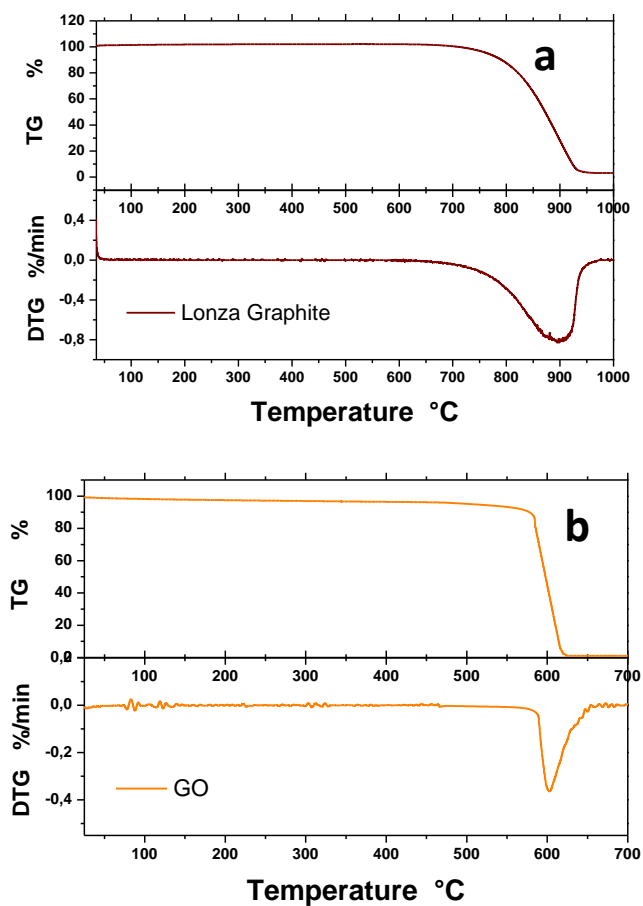


Fig. 2.27- TG-DTG analysis of Graphite (a) and GO (b).

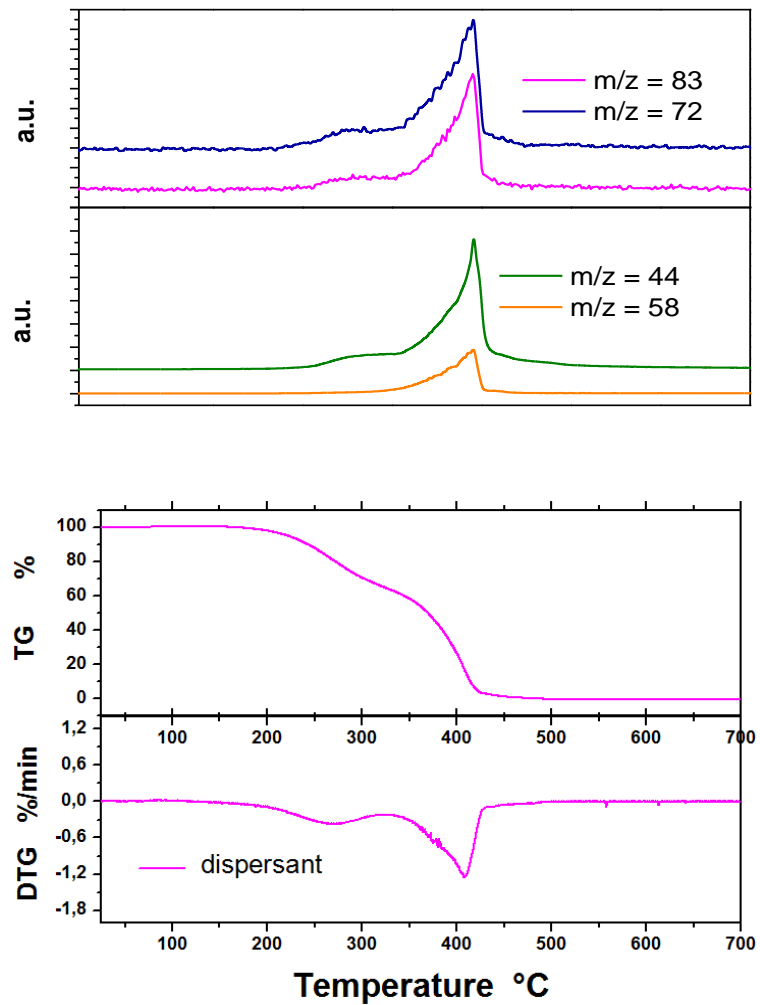


Fig. 2.28- TG-DTG analysis and the MS evaluation of the dispersant.

2.3.3 Friction test—Stribeck curve

The measured data are presented according to the Stribeck curves representation, i.e. friction coefficient vs. sliding speed. Results obtained

for the base oil sample and the sample formulated with GO nanosheets for different level of temperature and average hertzian contact pressure are shown and discussed in this section. The main properties of SN150 base oil were: kinematic viscosity, 29.7 cSt at 40 °C, 5.1 cSt at 100 °C; density at 20 °C, 0.87 kg/dm³. The set of graphs in Figure 2.29 introduces the Stribeck curves exhibited in the sliding tests by the SN 150 oil with 0.01 w.t.% GO nanosheets at different levels of average hertzian contact pressure and lubricant temperature, along with the error bars denoting the standard deviation around the rolling mean.

Those results show the decrease of the friction coefficient for increasing average hertzian contact pressure for the formulated sample; the same behaviour has been observed for the base oil according to a point-contact studied effect: the shear stress increases less in proportion to the contact pressure; this leads to a slight reduction of friction. As expected, for a given sample, the minimum of the Stribeck curve moves right for increasing temperature due to the lower viscosity. Additionally, for each sample, the CoF increased with the temperature at given level of speed and contact pressure. This observation could be mainly addressed to the effect of the lower lubricant viscosity and the ensuing GO precipitation at higher temperature.

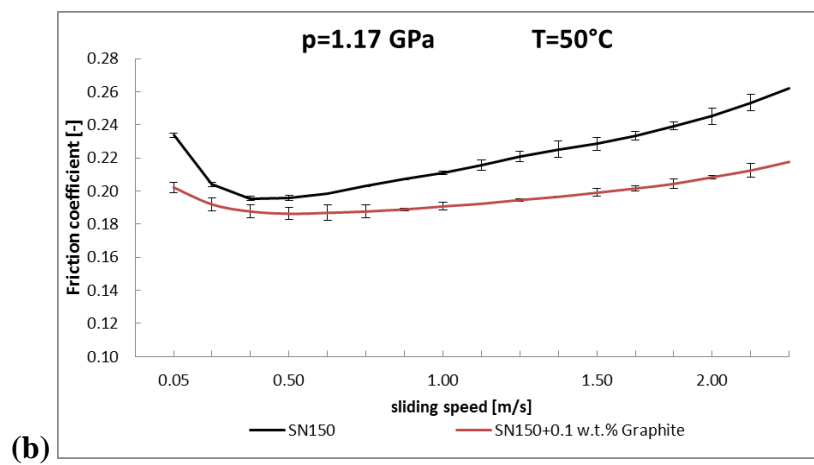
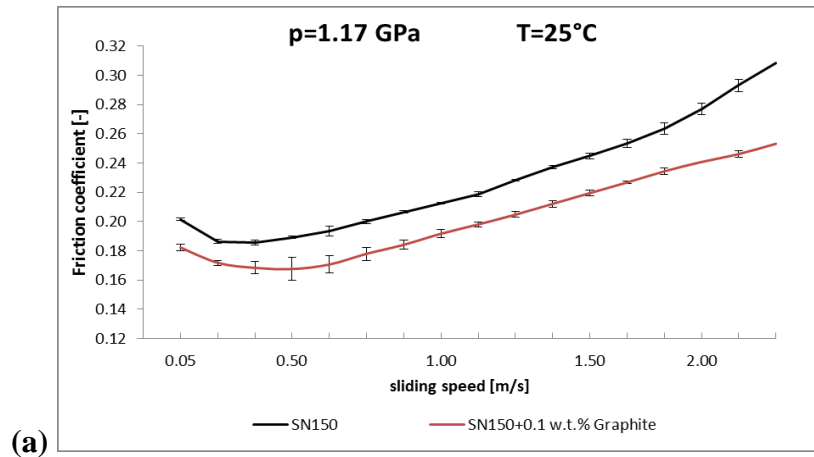
The Stribeck graphs in the Figures 2.29 for average hertzian pressure equal to 1.17 GPa, 1.47 GPa and 1.68 GPa show a shape with a well-developed minimum, that is considered the transition from mixed lubrication regime to EHL regime for increasing speed.

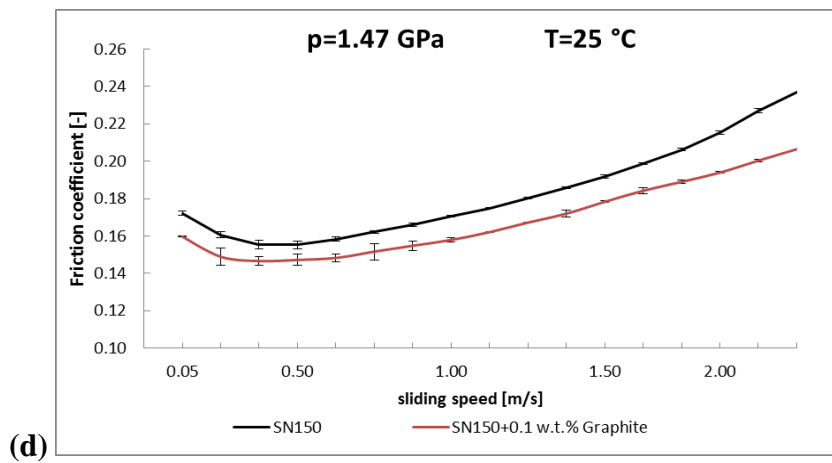
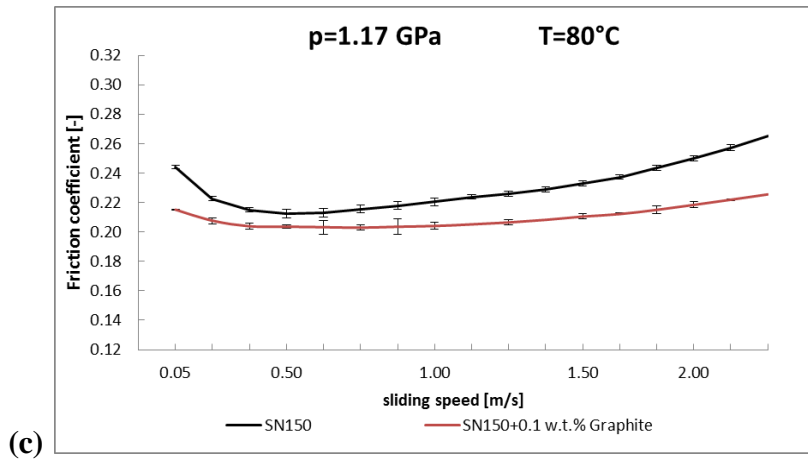
This frontier divides the region with concurrent phenomena of solid-to-solid contacts, adhesion and interaction between friction modifier additives and steel surface (mixed lubrication) from the other with predominant viscous stress and elastic deformation of the tribopair surfaces (EHL). For instance, the transition appears in the speed range 0.30-0.40 m/s for the test at 25 °C and 0.50-0.60 m/s at the higher temperature, 80 °C.

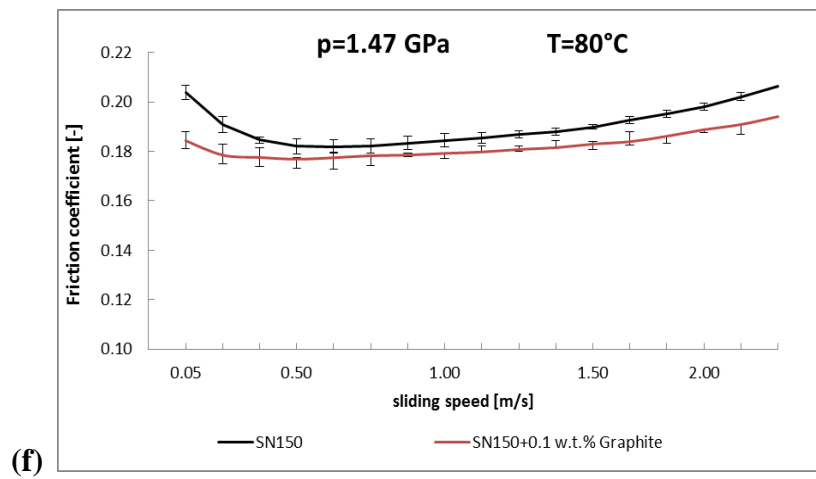
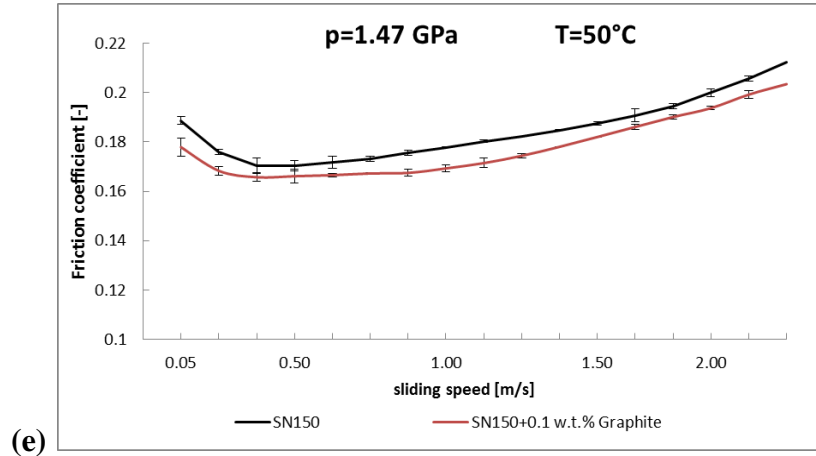
These tests confirm that using graphene nanoparticles in lubricants enhances the friction reduction in boundary, mixed and EHL lubrication regimes. For instance, with contact pressure of 1.17 GPa and temperature in the range 25-80 °C, the average friction coefficient decreased by 20% of the base lubricant value; similar average reduction could be observed for all the combinations of the operating conditions.

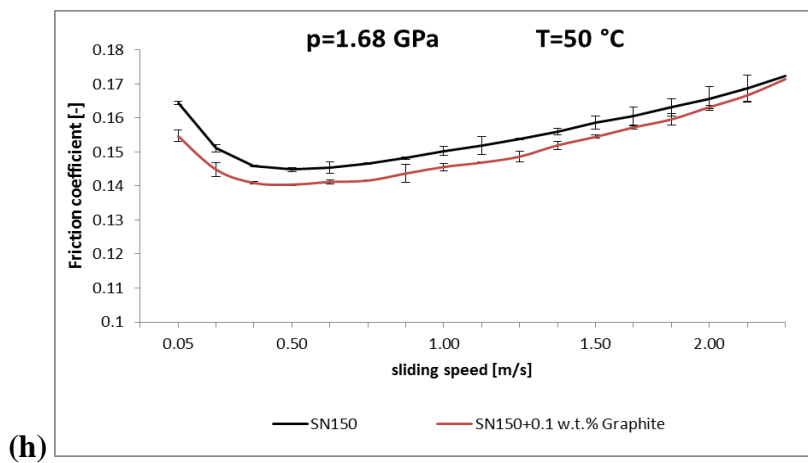
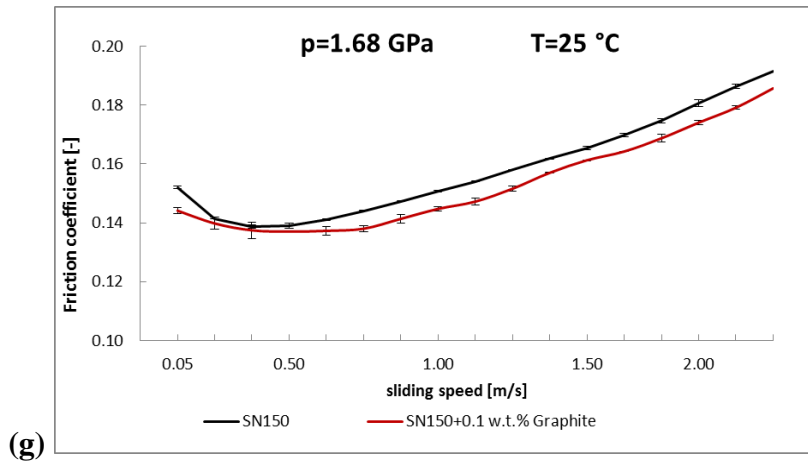
Even in the heaviest test conditions (high pressure and

temperature) and in fully developed EHL regime where the viscous stresses are prevalent, the CoF reduction is greater than 8% (Figure 2.29j).









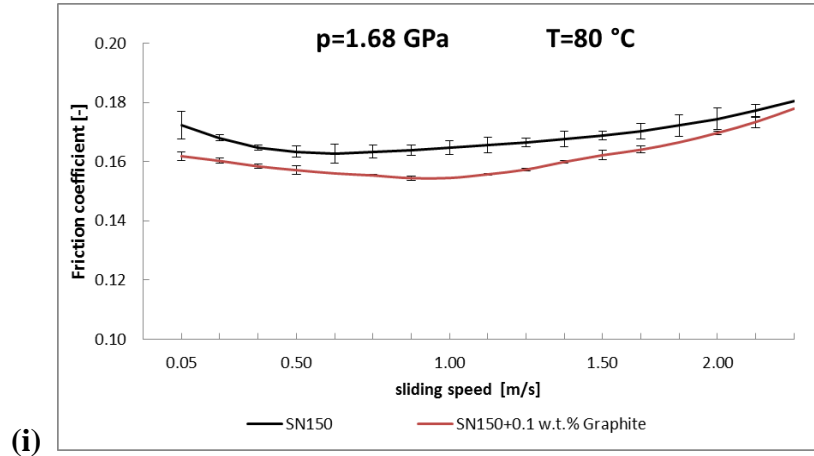
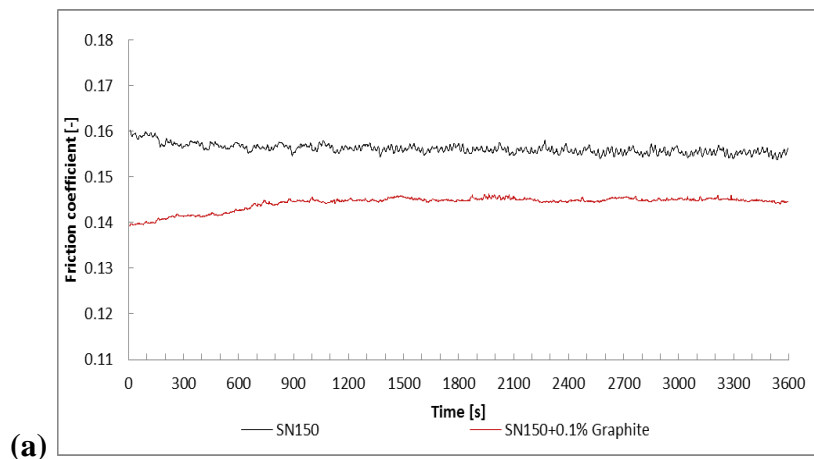
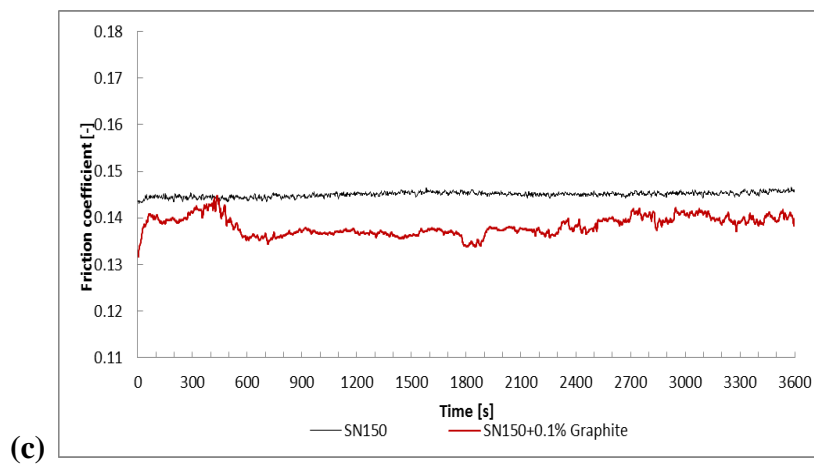
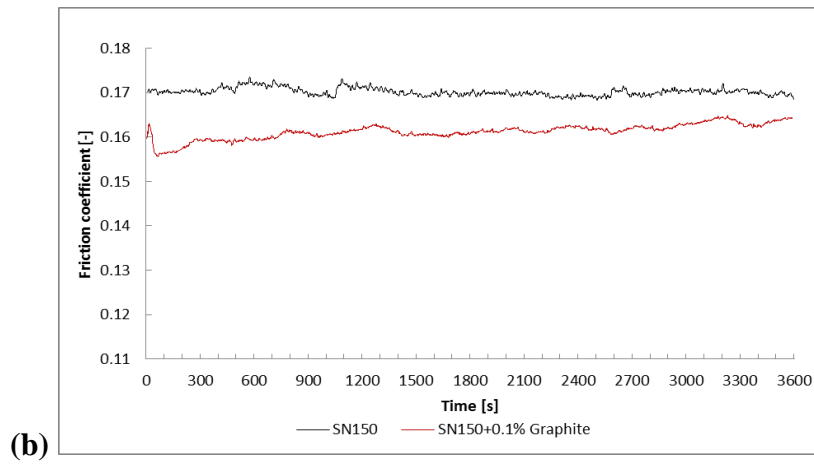


Fig. 2.29- Stribeck curves comparison from the sweep-speed test (SN150 - black, SN150 with 0.1 w.t. % Graphite – red, SN150 with 0.1 w.t. % GO - violet).

2.3.4 Friction and wear in steady-state tests

1-hour sliding tests were also performed to analyse the influence of the progressive wearing of the mating materials on the friction coefficient (Figures 2.30). The average friction coefficients measured during these steady state tests are presented in Tables 2.22 and 2.23.





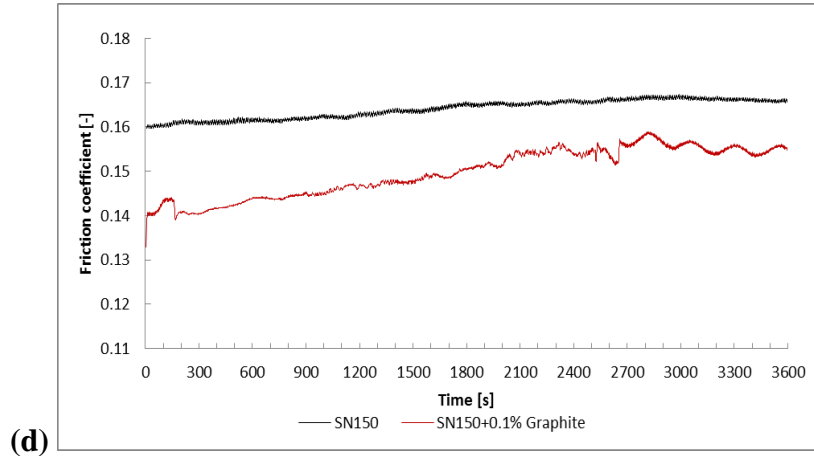


Fig. 2.30- Friction coefficient in 1-hour steady state test with average hertzian contact pressure 1.68 GPa and sliding speed 5.0 mm/s (boundary regime): oil temperature 25° C (a) and 80 °C: (b); sliding speed 0.50 m/s (mixed/EHL regime): oil temperature 25° C (c) and 80 °C: (d); (SN150 - black, SN150 with 0.01 w.t.% GO – red).

Sample	Friction coefficient[-] in boundary lubrication at 25°C	Friction coefficient[-] in boundary lubrication at 80°C	Difference
SN150 – Base oil	0.158	0.173	<i>Benchmark</i>
Graphene oxide in SN150	0.136	0.141	-14% -18%

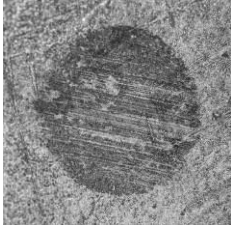
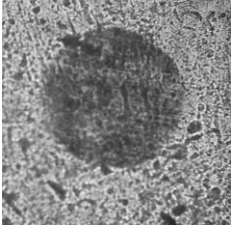
Tab. 2.22-Friction coefficient in boundary lubrication steady condition; sliding speed: 5.0 mm/s. Average hertzian contact pressure: 1.68 GPa

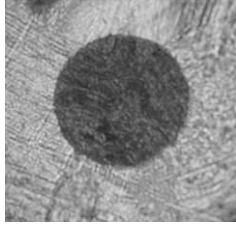
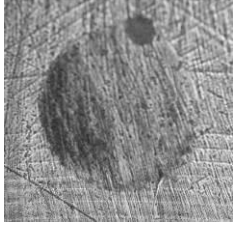
Sample	Friction coefficient[-] in Mixed/EHL lubrication at 25°C	Friction coefficient[-] in Mixed/EHL lubrication at 80°C	Difference
SN150 – Base oil	0.142	0.163	<i>Benchmark</i>
Graphene oxide in SN150	0.118	0.139	-17% -15%

Tab. 2.23-Friction coefficient in Mixed/EHL lubrication steady condition; sliding speed: 0.5 mm/s. Average hertzian contact pressure: 1.68 GPa

The anti-wear property of GO as additive for liquid lubricants has been clearly exhibited in all the lubrication regimes.

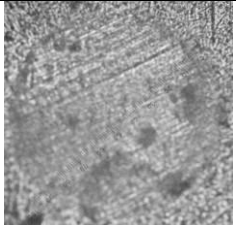
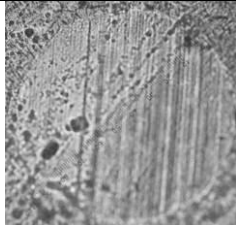
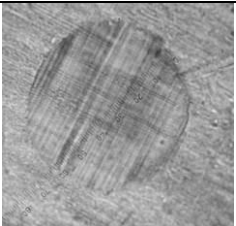
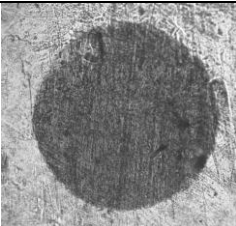
In particular the presence of graphene oxide in the formulated samples, leading to the reduction of the ball wear scar diameter data equal to 12%, 27% and 30% in boundary, mixed and EHL regime, respectively (Tables 2.24-2.25).

Sample	Ball wear scar diameter [μm] in boundary lubrication at 25 °C	Ball wear scar diameter [μm] in boundary lubrication at 80 °C	Difference
SN150 – Base oil	 600	 620	<i>Benchmark</i>

Graphene oxide in SN150			-12% -13%
	530	540	

Pictures not to scale

Tab. 2.24- Optical micrograph and wear scar diameter (WSD) after boundary lubrication steady condition test; sliding speed: 5.00 mm/s.

Sample	Ball wear scar diameter [μm] in Mixed/EHL lubrication at 25 °C	Ball wear scar diameter [μm] in Mixed/EHL lubrication at 80 °C	Difference
SN150 – Base oil	 900	 910	Benchmark
Graphene oxide in SN150	 630	 660	-30% -27%

Pictures not to scale

Tab. 2.25- Optical micrograph and wear scar diameter (WSD) after mixed/EHL lubrication steady condition test; sliding speed: 0.50 m/s.

The obtained results for the sample formulated graphene oxide platelets have been also compared with those obtained formulating the SN150 base oil with a more common graphite powder, widely use as lubricant additive in the last decade.

The differences are depicted in terms of friction coefficient obtained in steady condition (constant speed, contact pressure and temperature, duration 1h), Figures 2.31, and wear scar diameters, Figures 2.32.

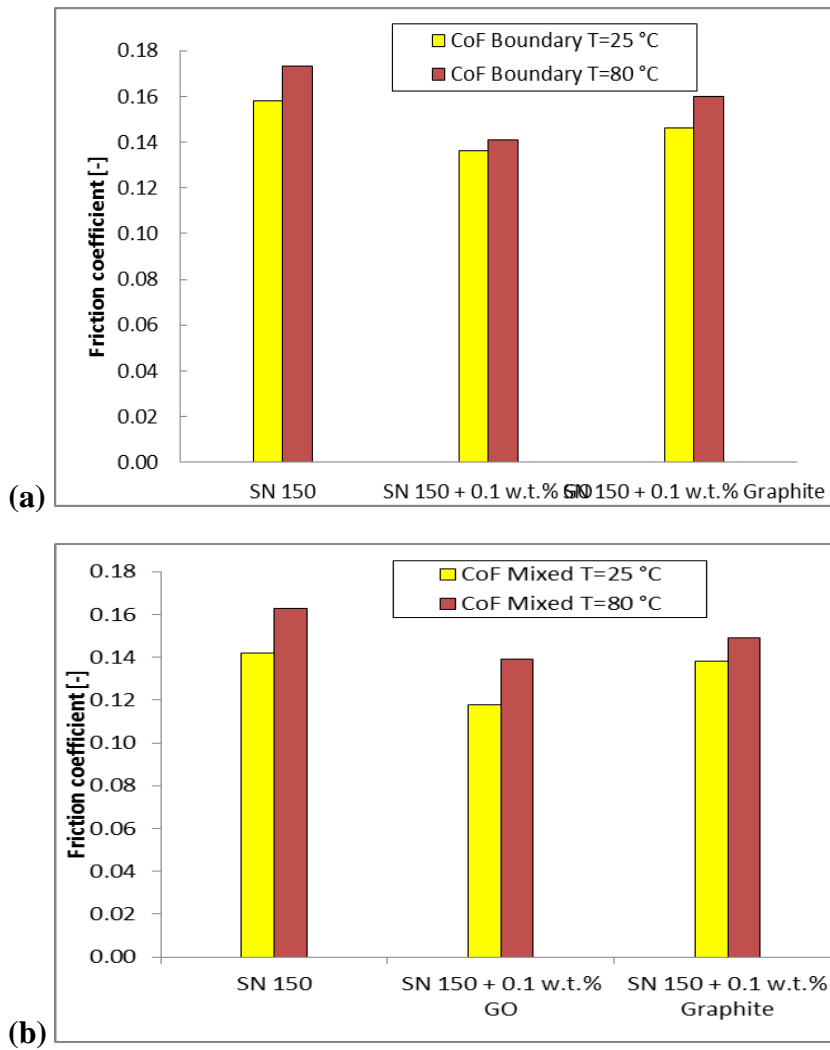


Fig. 2.31- Friction coefficient in steady boundary (a) and EHL (b) lubrication conditions at 25 °C and 80 °C.

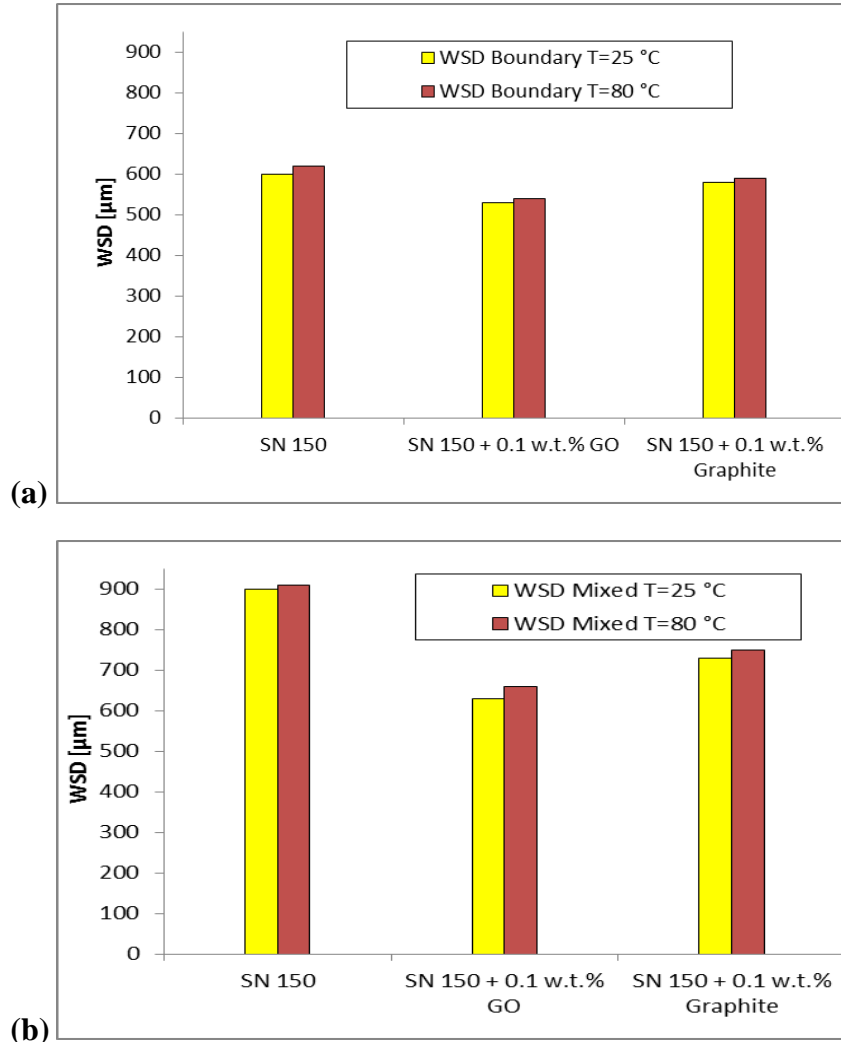


Fig. 2.32- Wear scar diameter (WSD) after 1-hour boundary (a) and EHL (b) regime test at 25 °C and 80 °C.

2.3.5 Surface analysis

2.3.5.1 Raman spectrum of the worn surface

In Figure 2.33, the Raman Spectrum collected on the ball wear after a 1 hour test at $p=1.68$ GPa, $T=25$ °C, $v=0.5$ m/s (in the following GSN150_1h) is also reported (more than 40 measurements have been

collected on the worn surface). A notable fact is that the G band of this spectrum is located almost at the same frequency as that in graphite, while the G' band exhibits a single Lorentzian feature and D-band results reduced, evidencing a further exfoliation of the GO and the formation of a thin carbon film (“tribo-film”) on the wear scar surface. In Figure 2.34 the Raman spectra of GO, SN150, GSN150_1h and GO on the ball wear scar after the 1 hour test at $p=1.68$ GPa, $T=25$ °C, $v=0.5$ m/s, are also reported for comparison.

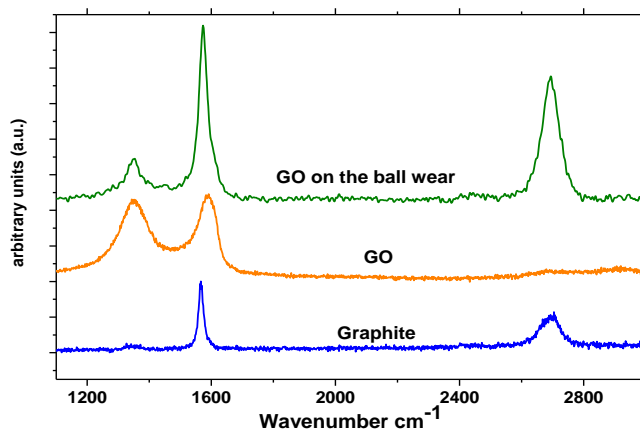


Fig. 2.33-Raman spectra of graphite, GO and further exfoliated GO on the ball wear after 1 hour test at $p=1.68$ GPa, $T=25$ °C, $v=0.5$ m/s.

For the Raman measurement, of the oil and GSN150_1h, a drop was casted on a glass slide. All the typical D, G, and 2D of carbon can be observed (green arrow in the Figure 2.34) in the spectrum of GSN150_1h, indicating that inside the oil at the end of the 1h test, GO further exfoliated as that found on the ball wear scar (see in particular the presence of the 2D band as shown in the insert of Figure 2.34), is also present.

Finally, in Figure 2.35 two typical Raman spectra of original graphite powder and two profiles obtained on the wear scar after the tribological test, collected on the ball wear after a 2 hours test at $p=1.68$ GPa, $T=25$ °C, $v=0.5$ m/s, are reported. In particular, in the spectrum of graphite, the most prominent features [58], the so-called G band appearing at 1582 cm⁻¹ and the G' or 2D band at about 2700 cm⁻¹, using

514 nm excitation wavelength, are collected. The G' band at room temperature can be fitted with two Lorentzian lines.

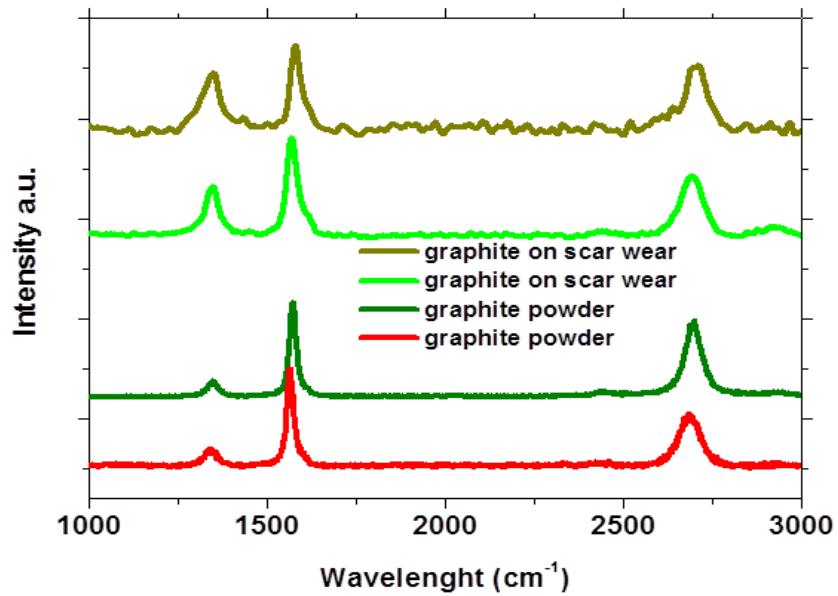


Fig. 2.34- Raman spectra of GO, SN150, GSN150_1h and GO on the ball wear scar after 1 hour test at $p=1.68$ GPa, $T=25$ °C, $v=0.5$ m/s.

A non-homogeneity of the original graphite is suggested by the differences in the relative spectra. The graphite spectra after the tribological test show an improved D band intensity, probably due to an increased border edge effects.

Interestingly, the G and 2D Raman bands obtained in different areas of the wear scar can be overlapped, indicating that the thickness of the exfoliated graphite on the ball wear scar is determined by the tribological test conditions.

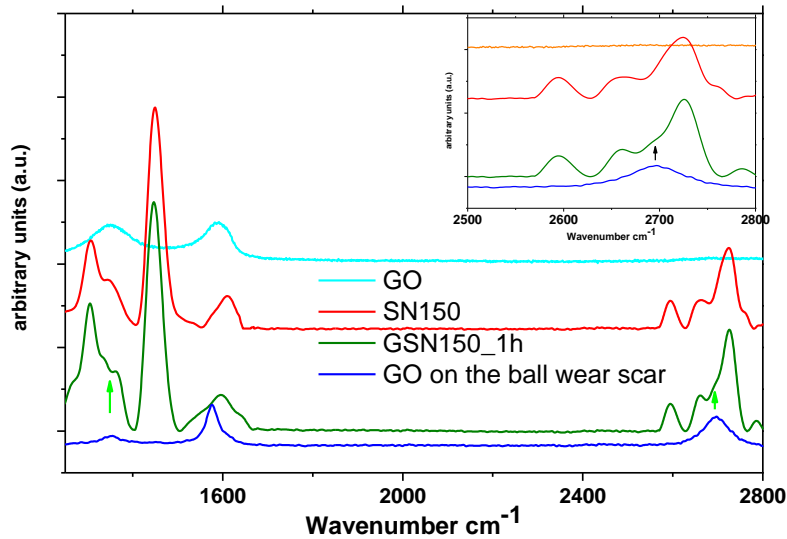


Fig. 2.35- Raman spectra of original graphite and graphite on the ball wear scar.

2.3.5.2 Optical profiler of the rubbed surfaces

Figures 2.36 shows the 3D surface morphologies, obtained by means of an optical profiler with confocal technology, of the rubbed surfaces, tested with pure SN150 (a) and GSN150 (b), after 1 hour test in boundary lubrication regime: $p=1.68$ GPa, $T=25$ °C, $v=5.0$ mm/s. As shown, the rubbed surface after the test with the pure oil is rough with wide and deep furrows together with large and tall ridges.

Addition of 0.01% of GO results in a reduced roughness from 552 nm to 424 nm. On the other hand, not only the roughness is decreased, but the morphology of the wear scar surface has changed, on which it is possible to observe a succession of ridges and valleys of about 15 μm wide.

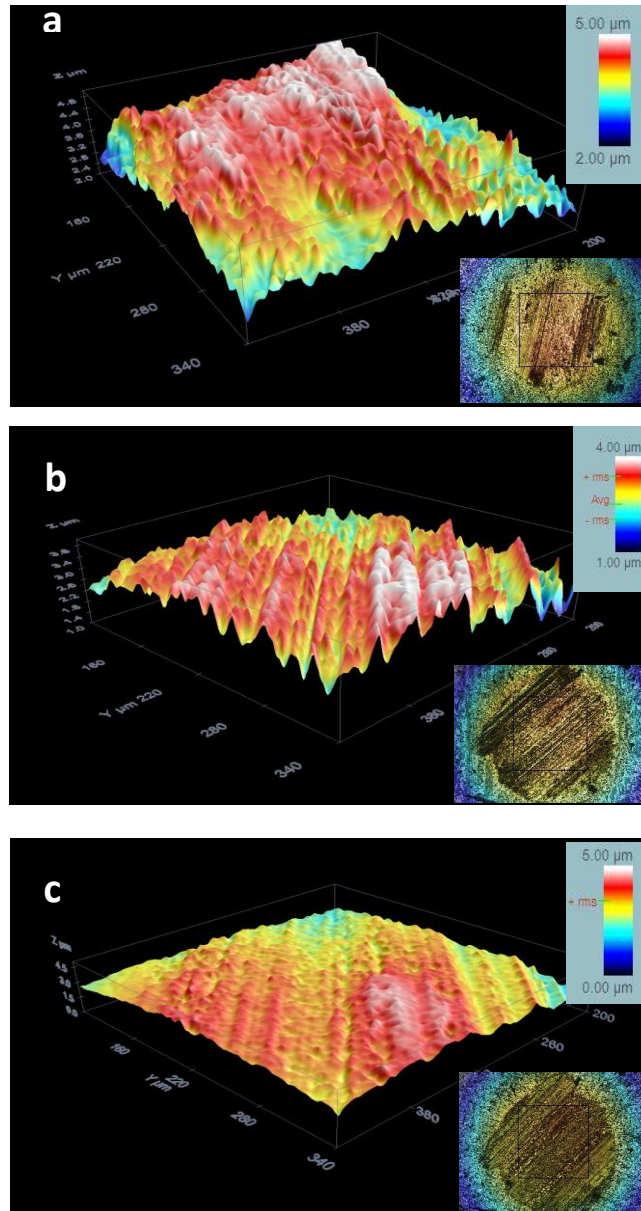


Fig. 2.36- 3D surface morphologies of the wear scars: (a) after 1 hour test at $p=1.68$ GPa, $T=25$ °C, $v=0.5$ m/s with base oil SN150; (b) after 1 hour test at $p=1.68$ GPa, $T=25$ °C, $v=0.5$ m/s with GSN150; (c) on the wear

scar in (b) after a thermal oxidation to remove GO.

The roughness so measured is 500 nm, which suggests a GO filling of the deeper valleys and the formation of a thinner film on the asperities, since if the entire surface had been covered with a uniform exfoliated GO thickness, the same roughness would be measured before and after the oxidation. On the other hand, the surface morphology in Figure 2.36b and 2.36c are quite close.

2.3.6 Discussion

The incessant literature dispute on the friction reduction mechanism introduced by nanoparticles as lubricant additives finds in the following list the more convincing physical explanations: rolling-sliding “rigid” motions together with flexibility properties [59], nanoadditive exfoliation and material transfer to metal surface to form the so called “tribofilm” or “tribolayer” [60], electronic effects in tribological interfaces [61], surface roughness improvement effect or “mending” [62]; along with the more classical hypothesis of surface sliding on lower shear stress layers due to weak interatomic forces, valid also for micro-scale additives used from decades. Our observation of the surface morphologies indicate that the addition of GO considerably leads to smoother surface, by reducing the surface r.m.s. roughness: the tribopair surface sliding on lower shear stress layers due to weak interatomic forces of GO sheets allows modified interaction between the asperities of the tribopair steel parts even from the qualitatively point of view. Exfoliated GO fills the deeper scratches and covers with a thinner film the surface peaks.

Firstly, the experimental evidences of the obtained results represent a proof of the presence of a tribological film of reduced graphene oxide which covers the whole worn surface of the steel ball, together with a mending effect [62]. The since-start reduction of friction coefficient can be addressed to the surface rubbing through the low shear stress GO layers. The GO 0.01 w.t.% concentration is quite lower than the usual one for inorganic nanoadditives [63] and carbon nanotubes and in line with previous studies in which oleic acid-modified graphene was used [64]. This feature is welcomed in the preparation of fully formulated engine or gearbox lubricants since the GO addition could only slightly

modify the delicate equilibrium achieved by oil manufacturers between the essential and ubiquitous additives as antioxidant, viscosity modifier, pour-point depressant and other minors.

Furthermore, the experimental results underline that the sample of graphite powder was initially inhomogeneous featuring stacks of planes with different thickness, according to TEM/Raman results. The compression/shear stresses of the tribological test result in further in-plane exfoliation of the stacks, along with damaging and 2D size reduction. The exfoliated graphite material on the ball worn surface has uniform thickness and structure, both controlled by the tribological test conditions (temperature, pressure, sliding speed). This lower limit about the thickness during exfoliation would result in a frontier for the graphite powder to effectively contribute to the reduction of the friction coefficient over a given amount. Moreover, the graphene oxide with definitely lower initial thickness allows better frictional performance and a further exfoliation during the tribological test due to its low-order structure [65].

Secondly, the tribological tests confirm good reduction of friction and wear parameters in boundary lubrication, mixed lubrication and EHL regimes achieved with mineral oils formulated with Graphene Oxide (GO) nanosheets. For instance, with average contact pressure of 1.17 GPa and temperature in the range 25-80 °C, the average CoF decreased by more than 20% compared with the base lubricant value. The sliding tests in steady state conditions have shown an average reduction of CoF equal to 16%. The frictional reduction benefit has been proven at any level of oil temperature, contact pressure and sliding speed. The best anti-wear result has been observed on the ball surface in the mixed lubrication and EHL regime, with a marked average decreasing around 30%.

The good friction and anti-wear properties of graphene sheets may possibly be attributed to their small structure and extremely thin laminated structure, which offer lower shear stress and prevent interaction between metal interfaces. The results clearly prove that graphene platelets in oil easily form protective deposited films to prevent the rubbing surfaces from coming into direct contact and, thereby, improve the entirely tribological behaviour of the oil. Future works will be addressed toward: methods for dispersion improvement of GO in oil, addition to other bases and fully formulated oils, search of optimal concentration and testing at lower contact pressure to verify the existence of activation threshold related to nanoparticles structure modification.

REFERENCES

- [60] Ohmae, N., Mori, S., Martin, J.M., Micro and nanotribology, Amer Society of Mechanical, 2005.
- [61] Bhushan, B., Handbook of Micro/Nano Tribology, Second Edition. CRC Press, Technology & Engineering, 1998.
- [62] Lin, J., Wang, L., Chen, G., Modification of Graphene Platelets and their Tribological Properties as a Lubricant Additive. Tribol Lett; 41:209-15, 2011.
- [63] Martin, J. M., Ohmae, N., Nanolubricants, Tribology in Practice Series-Tribology series, Volume 13, Wiley, 2008.
- [64] Tannous, J., Dassenoy, F., Bruhacs, A., W. Tremel, Synthesis and Tribological Performance of Novel $\text{Mo}_x\text{W}_{1-x}\text{S}_2$ ($0 \leq x \leq 1$) Inorganic Fullerenes, Tribology letters, 37, 83-92, 2010.
- [65] M. Chhowalla, G.A.J. Amaratunga, Thin films of fullerene-like MoS_2 nanoparticles with ultralow friction and wear, Nature, 407, 164-167, 2000.
- [66] Wiesel, I., Arbel, H., Albu-Yaron, A., Popovitz-Biro, R., Gordon, J.M., Feuermann, D., Tenne R., Synthesis of WS_2 and MoS_2 Fullerene-Like Nanoparticles from Solid Precursors, Nano Res. 2, 416-424, 2009.
- [67] Enyashin, A.N., Gemming, S., Bar-Sadan, M., Popovitz-Biro, R., Hong, S.Y., Prior, Y., Tenne, R., Seifert, G., Structure and Stability of Molybdenum Sulfide Fullerenes, Angew. Chem. Int. Ed. 46, 623-627, 2007.
- [68] Rapoport, L., Bilik, Y., Feldman, Y., Homyonfer, M., Cohen, S.R., Tenne, R., Hollow nanoparticles of WS_2 as potential solid-state lubricants, Nature, 387, 791-793, 1997.
- [69] H. Huang, J. Tu, T. Zou, L. Zhang, D. He, Friction and Wear Properties of IF- MoS_2 as additive in Paraffin Oil, Tribology letters, 20, 247-250, 2005.
- [70] Rapoport L., Feldman Y., Homyonfer M., Cohen S.R., Sloan J., Hutchison J.L., Tenne R., Inorganic fullerene-like material as additives to lubricants: structure-function relationship, Wear, 225-229, 975-982, 1999.

- [71] Rosentsveig, R., Gorodnev, A., Feuerstein, N., Friedman, H., Zak, A., Fleischer, N., Tannous, J., Dassenoy, F., Tenne, R., Fullerene-like MoS₂ Nanoparticles and Their Tribological Behavior, *Tribology Letters*, 36, 175-182, 2009.
- [72] Greenberg, R., Halperin, G., Etsion, I., Tenne, R., The Effect of WS₂ Nanoparticles on Friction Reduction in Various Lubrication Regimes, *Tribology Letters*, 17 179-186, 2004.
- [73] Rapoport, L., Moshlovich, A., Perfilyev, V., Tenne, R., On the efficacy of IF-WS₂ nanoparticles as solid lubricant: The efficacy of the loading scheme, *Tribol. Lett.*, 2881-87, 2007.
- [74] Rapoport, L., Nepomnyashchy, O., Lapsker, I., Verdyan, A., Moshkovich, A., Feldman, Y., Tenne, R., Behavior of fullerene-like WS₂ nanoparticles under severe contact conditions, *Wear* (2005), 259.
- [75] Drummond, C., Alcantar, N.A., Israelachvili, J., Tenne, R., Golan, Y., Microtribology and Friction-Induced Material Transfer in WS₂ Nanoparticle Additives, *Adv. Funct. Mater.*, 11, 348-354, 2001.
- [76] Nasir, T., Yousif, B.F., Mc William, S., Salih, N.D., Hui, L.T., An artificial neural network for prediction of the friction coefficient of multi-layer polymeric composites in three different orientations. *Proc.I.Mech.E. Part C, J Mech.Eng.Sci*, 225:419–29, 2009.
- [77] Cirovic, V., Aleksendric, D., Development of neural network model of disc brake operation. *FME Trans*, 38:29–38, 2010.
- [78] Fujii, H., Mackay, D.J.C., Bhadeshia, H.K.D.H., Bayesian neural network analysis of fatigue crack growth rate in nickel base superalloys. *ISIJ Int*, 36: 1373–82, 1996.
- [79] Sen, T.K., Oliver, R., Sen, N., Predicting corporate mergers. In: Refenes AP, editor. *Neural networks in the capital markets*. New York, Wiley, p.325–40, 1995.
- [80] Zhang, G.P., Neural networks for classification: a survey. *IEEE Trans. Syst. Man .Cybern.-Part C, Appl.Rev*, 30, 451–62, 2000.
- [81] Hettiarachchi, P., Hall, M.J., Minns, A.W., The extrapolation of artificial neural networks for the modelling of rainfall–runoff relationships. *J Hydroinf* 2005; 7:291–6.
- [82] Khamlichi, A., Bezzazi, M., Optimizing the thermal properties of clutch facings. *J. Mater. Process. Tech.*, 142:634-42, 2003.

- [83] Kogovšek J., Kalin M., Tribological Behaviour of MoS₂ Nanotubes in Oil, presented at 3rd European Conference on Tribology, Ecotrib – Viennano 2011.
- [84] Chinas-Castillo F., Spikes H.A., Mechanism of action of colloidal solid dispersion, *Journal of Tribology*, Vol. 125 pag. 552-557, (2003).
- [85] Joly-Pottuz L., Martin J. M., Dassenoy F., Belin M., Montagnac Reynard G.B., Fleischer N., Pressure-induced exfoliation of inorganic fullerene-like WS₂ particles in a Hertzian contact, *J. of Applied Physics* 99, 2006.
- [86] Kroto, W., Heath, J.R., O'Brein, S.C., Curl, R.F., Smalley R.E., C₆₀: Buckminster fullerene, *Nature* 318, 162, 1985.
- [87] Tenne, R., Remskar, M., Enyashin, A., Seifert, G., *Inorganic Nanotubes and Fullerene-Like Structures (IF)*, 2008.
- [88] Cizaire, L., Vacher, Le Mogne, B. T., Martin, J. M., Rapoport, L., Margolin, A., Tenne, R., Mechanism of ultra-low friction by hollow inorganic fullerene-like MoS₂ nanoparticles, *Surface and Coating Technology*, 160, 2002.
- [89] D.Y. Lee, J. Lee, J. Hwang, S.H. Choa, Effect of relative humidity and disk acceleration on tribocharge build-up at a slider-disk interface, *Tribol. Int.*, 40, 1253-1257, 2007.
- [90] Calin, L., Caliap, L., Neamtu, V., Morar, R., Iuga, A., Samuila, A., Dascalescu, L., Tribocharging of granular plastic mixtures in view of electrostatic separation, *IEEE Trans. on Ind. Appl.*, 44 1045-1051, 2008.
- [91] Takagi, K., Castle, G., Takeuchi, M., Tribocharging mechanism of monocomponent irregular and spherical toners in an electrophotographic development system, *Powder Technol.*, 135, 35-42, 2003.
- [92] Sharma, R., Clark, D.W., Srirama, P.K., M.K., Mazumder, Tribocharging characteristics of the Mars dust simulant (JSC Mars-1), *IEEE Trans. on Ind. Appl.*, 44 32-39, 2008.
- [93] Derjaguin, B., Smilga, V., Electrostatic component of the rolling friction force moment, *Wear*, 7, 270-281, 1964.
- [94] Budakian, R., Putterman, S., Correlation between charge transfer and stick-slip friction at a metal-insulator interface, *Phys. Rev. Lett.*, 85, 1000-1003, 2000.

- [95] Dayo, A., Alnasrallah, W., Krim, J., Superconductivity-dependent sliding friction, *Phys. Rev. Lett.*, 80, 1690-1693, 1998.
- [96] Persson, B., Electronic friction on a superconductor surface, *Solid State Commun.*, 115 145-148, 2000.
- [97] Joly-Pottuz, L., Dassenoy, F., Belin, M., Vacher, B., Martin, J.M., Fleischer, N., Ultralow-friction and wear properties of IF-WS₂ under boundary lubrication, *Tribol. Lett.*, 18, 477-485, 2005.
- [98] Katz, A., Redlich, M., Rapoport, L., Wagner, H., Tenne, R., Self-lubricating coatings containing fullerene-like WS₂ nanoparticles for orthodontic wires and other possible medical applications, *Tribol. Lett.*, 21, 135-139, 2006.
- [99] Hou, X., Shan, C., Choy, K.L., Microstructures and tribological properties of PEEK-based nanocomposite coatings incorporating inorganic fullerene-like nanoparticles, *Surf. Coat. Technol.*, 202 2287-2291, 2008.
- [100] Naffakh, M., Martin, Z., Fanegas, N., Gomez, C., Jimenez, M., Influence of inorganic fullerene-like WS₂ nanoparticles on the thermal behavior of isotactic polypropylene, *J. Polym. Sci., Part B: Polym. Phys.*, 45 2309-2321, 2007.
- [101] Wildervanck, J.C., Jellinek, F., The Dichalcogenides of Technetium and Rhenium, *J. Less Common Metals.* 24, 73, 1971.
- [102] Enyashin, A.N., Popov I., Seifert G., Stability and electronic properties of rhenium sulfide nanotubes, *Phys. Status Solidi B* 246, 114-118, 2009.
- [103] Virsek, M., Krause, M., Kolitsch A., Remskar M., Raman characterization of MoS₂ microtube, *Phys. Status Solidi B* 246, 2782-2785, 2009.
- [104] Kopnov, F., Yoffe, A., Leitius, G., Tenne, R., Transport properties of fullerene-like WS₂ nanoparticles, *Phys. Stat. Solidi B*, 243, 1229-1240, 2006.
- [105] Doerr, M., Feller, J., Oppermann, H., Coexistent phases and their electrical and structural behaviour in the ternary Re/Mo/O system, *Cryst. Res. Technol.* 31, 231-241, 1996.
- [106] Winterlin, J., Bocquet, M.L., Graphene on metal surfaces. *Surf Sci*, 603(10-12): 1841-52, 2009.
- [107] Ramanathan, T., Abdala, A.A., Stankovich, S., Dikin, D.A., Herrera-Alonso, M., Piner, R.D., Functionalized graphene sheets for polymer nanocomposites. *Nat Nanotechnol*, 3:327-31, 2008.

- [108] Wei, D., Liu, Y., Wang, Y., Zhang, H., Huang, L., & Yu, G., Synthesis of N-doped graphene by chemical vapor deposition and its electrical properties, *Nano letters*, 9(5), 1752-1758, 2009.
- [109] Lin, J., Wang, L., Chen, G., Modification of Graphene Platelets and their Tribological Properties as a Lubricant Additive. *Tribol Lett*, 41:209-15, 2011.
- [110] Bryant, P.J., Gutshall, P.L., Taylor, L.H., A study of mechanisms of graphite friction and wear. *Wear*, 7(1):118-26, 1964.
- [111] Bernan, D., Erdemir, A., Sumant, A.V., Few layer graphene to reduce wear and friction on sliding steel surfaces, *Carbon*, 54:454-9, 2013.
- [112] Hummers W., Offeman R., Preparation of graphitic oxide, *J. Am. Chem. Soc.*, 80, 1339-1342, 1958.
- [113] The history of Lonza's graphite powders. *Industrial Lubrication and Tribolog.*, 27, 59-69, 1948.
- [114] Fusaro, R.L., Mechanisms of graphite fluoride [(CF_x)_n] lubrication, *Wear*, 53(2):303-23, 1979.
- [115] Tian, J., Xue, Q.J., The deintercalation effect of FeCl₃-graphite intercalation compound in paraffin liquid lubrication, *Tribol Int*, 30(8):571-4, 1997.
- [116] Hilton, M.R., Bauer, R., Didziulis, S.V., Dugger, M.T., Keem, J.M., Scholhamer, J., Structural and tribological studies of MoS₂ solid lubricant films having tailored metal-multilayer nanostructures, *Surf Coat Technol*, 53:13-23, 1992.
- [117] Wei, Z., Ming, Z., Hongwei, Z., Yu, T., Kunlin, W., Jinqian, W., Tribological properties of oleic acid-modified graphene as lubricant oil additives. *J Phys D Appl Phys*, 44(20):205303, 2011.
- [118] Sarno, M., Cirillo, C., Piscitelli, R., Ciambelli, P., A study of the key parameters, including the crucial role of H₂ for uniform graphene growth on Ni foil. *J Mol Cat A Chem*, 473:5-6, 2013.
- [119] Kudin, K.N., Ozbas, B., Schniepp, H.C., Prud'homme, R.K., Aksay, I.A., Car, R., Raman Spectra of Graphite Oxide and Functionalized Graphene Sheets. *Nano Lett*, 8(1):36-41, 2008.
- [120] Wintterlin, J., Bocquet, M.L., Graphene on metal surfaces, *Surf. Sci.*, 603, 1841–1852, 2009.
- [121] Ramanathan, T., Abdala, A.A., Stankovich, S., Dikin, D.A., Herrera-Alonso, M., Piner, R.D., Adamson, D.H., Schniepp, H.C.,

- Chen, X., Ruoff, R.S.: Functionalized graphene sheets for polymer nanocomposites, *Nat. Nanotechnol.*, 3, 327–331, 2008.
- [122] Bryant P.J., Gutshall P.L., Taylor L.H., A study of mechanisms of graphite friction and wear, *Wear*, 7, 118–126, 1964.
- [123] Ferrari A.C., Raman spectroscopy of graphene and graphite: Disorder, electron-phonon coupling, doping and nonadiabatic effects, *Solid State Communication*, 143, 47-57, 2007.
- [124] Pimenta M.A., Dresselhaus G., Dresselhaus M.S., Cançado L.G., Jorio A., Saito R., Studying disorder in graphite-based systems by Raman spectroscopy, *Physical Chemistry Chemical Physics*, 9, 1276-1291, 2007.

CHAPTER 3

Nanoparticles in lubricating greases

3.1 Introduction

Lubricating greases are widely used in several heavily loaded tribopairs such as rolling element bearings, gears, chains, etc. Each application represents its own unique load/speed/temperature operating condition that the grease needs to be designed to. As it is well known, grease is a semisolid lubricating material whose main function is to remain in contact with the surfaces. The lubricating grease has been defined in many ways; one of the most frequently used is the ASTM definition, provided in ASTM Standard D288 that defines grease in terms of its physical appearance and composition. This definition characterizes the lubricating grease as “a solid-to-semifluid product of dispersion of a thickening agent in a liquid lubricant” [1-4]. Other ingredients imparting special properties may be included, so that, lubricating greases are composed of three components: thickener, base fluid, and additives, which are used to enhance grease properties and performance. While the amount of each differs from grease to grease, as a general guideline the lubricating grease contains 70–90% base fluid, which can be mineral, synthetic, or natural in origin; about 5–25 % thickener; and the additives make up the difference. It is the base fluid and the additives that perform the lubrication function and impart various desirable performance properties to the lubricating grease. Soap’s or thickener’s function is to provide structure to the grease, in fact, thickener is the component that is primarily responsible for the gel-like structure of the lubricating grease. There are a number of ways in which the lubricating greases are classified, as, for example:

- Application: industrial or automotive;
- Soap Type: soap-free or nonsoap grease and soap containing grease and soap-containing greases are classified based on the metal ion of the soap or the thickener, for example, lithium, sodium, calcium, barium, aluminum soap greases;
- Base Oil: mineral oil-based grease or synthetic fluid based grease;

- Consistency. Consistency is the resistance of the lubricating grease to deform under load, or in other words it measures the degree of hardness of the grease. Consistency is usually measured by the ASTM Cone Penetration Test, ASTM D217. Various classes of lubricating greases based on consistency are provided in the National Lubricating Grease Institute's (NLGI) classification system. Under this system, the lubricating greases are classified into nine classes, which are provided in Table 3.1, along with potential applications [5].

NLGI Consistency (Grade number)	ASTM Worked Penetration at 25°C (penetration in 0.1 mm)	Appearance
000	445 – 475	Fluid
00	400 – 430	semi-fluid
0	355 – 385	very soft
1	310 – 340	Soft
2	265 – 295	"normal" grease
3	220 – 250	Firm
4	175 – 205	very firm
5	130 – 160	Hard
6	85 – 115	very hard

Tab. 3.1 – NLGI Grease classification for lubricating greases

Lubricating greases have their own set of property tests that may need to be considered when screening greases in wear and friction tests. Some of the tests are for determining tribological properties as opposed to physical properties (D 2596, D 2266, D 4170, D 3704, D 5707).

Lubricating grease shows conspicuous non-Newtonian characteristics. Actually, grease has a yield stress and hence will not easily flow back to replenish the track when it is pushed aside by a rolling ball. This implies that bearing contacts are starved of bulk grease.

Also, grease is shear-thinning which makes the film thickness speed sensitive and time-dependent.

Several experimental studies have shown that in a fully flooded situation for the same basic composition, the greater the percentage in volume of the thickener, the greater is the film thickness [6,7]. Also, when the resistance to

structural degradation is higher, the behaviour of the grease in the contact will be more stable and the film thickness will be greater.

These results confirm the practical ones: the tested greases that give a higher regularity of film thickness and a greater film thickness are those that provide a higher life in mechanisms [8].

In this chapter, the performances of nano-formulated grease through organic and inorganic based additives have been tested and discussed.

3.2 GREASES WITH NANOSIZED INORGANIC BASED ADDITIVES

The influence of WS_2 and MoS_2 nanoparticles has been investigated on two different commercial greases of one with Lithium thickener and another with Calcium.

The base lubricant greases used can be classified in the NLGI system mentioned above. The Lithium based grease NLGI 3 properties are given as follows (Table 3.2):

Colour	Amber
Oil type	Mineral
Soap type	Lithium
Drop point (ASTM D 566)	> 190 °C
Penetration at 25 °C (ASTM D 217)	220/250 1/10 mm
NLGI grade (DIN 51818)	3

Tab. 3.2 – Lithium grease properties

The Calcium based grease NLGI 2 properties are given as follows (Table 3.3):

Colour	Green
Oil type	Mineral
Soap type	Calcium
Drop point (ASTM D 566)	> 140 °C
Penetration at 25 °C (ASTM D 217)	260/290 1/10 mm
NLGI grade (DIN 51818)	2

Tab. 3.3 – Calcium grease properties

For the preparation of the samples, one-pot syntheses were used to obtain free-floating nanosheets of tungsten and/or molybdenum disulphide functionalized by long chain amines in the form of fluid suspension or

solid paste.

The nanosheets obtained are constituted by one or few layers of crystalline metal chalcogenides completely covered by an organic coating. With respect to similar inorganic materials, the presence of coating stabilizes the suspension, avoids aggregation and oxidation phenomena [9]. The nano-materials, successfully tested in base lubricating oils [10-13], were dispersed in the lubricating greases and compared by rheological and tribological tests to the conventional lubricating greases.

3.2.1 Synthesis of 2D MS_2 @oleylamine nanosheets crystals

Stable free standing nanosheets of MS_2 ($M=Mo,W$), coated by long chain amine were obtained by new wet chemistry approach based on low temperature ($360\text{ }^\circ\text{C}$) decomposition in oleylamine of a single-source precursor containing both metal and sulfur [14-15]. In particular the precursor was dissolved under inert atmosphere and vigorous stirring in oleylamine for 15 min at $100\text{ }^\circ\text{C}$ to promote the formation of oleylamine-thio-tungstate complex Figure 3.1. The temperature was increased to $360\text{ }^\circ\text{C}$ and after 90 min of reaction the reactor was cooled down to room temperature. The product was a dense black oil Ethanol was added to the mixture and the precipitate was separated by centrifuge and washed several time to remove the excess of oleylamine

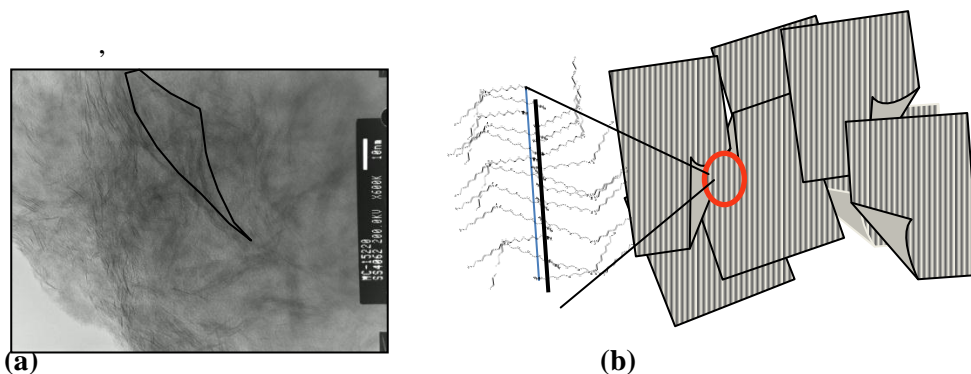


Fig. 3.1 – (a) WS_2 @oleylamine nanosheet highlighted in a TEM image, (b) schematic representation of WS_2 nanosheets covered by a “brush of oleylamine”

The results is a paste of $MS_2@$ oleylamine with a 20% of MS_2 (M=Mo, W), Figure 3.2. The paste was mechanically mixed (10 min, 50 rpm) with Calcium based grease – NLGI 2 and Lithium Based grease – NLGI 3 to obtain respectively Calcium based grease – NLGI 2 with 2 w.t.% and 4% w.t. of MS_2 nanosheets and Lithium Based grease – NLGI 3 with 2 w.t.% and 4% w.t. of MS_2 nanosheets.

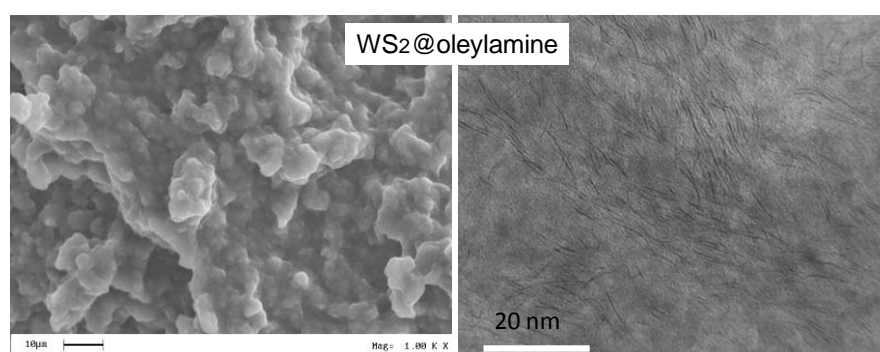


Fig. 3.2 - SEM and TEM images of WS_2 nanosheets synthesized in oleylamine

Moreover, other test have been performed on lubricating greases samples obtained with the addition of nanoparticles synthesized at the Weizmann Institute of Tel Aviv in Israel, a leader in the field of chemistry of nanoparticles, and the results have been compared to those obtained with the samples containing the nanoparticles synthesized at the Industrial Chemistry laboratories of the University of Salerno. Accordingly, the tested samples are reported as follows, reported in Figures. 3.3 and 3.4:

1. Calcium based grease formulated with 4% NanoLub GH paste (Weizmann Institute Sample)
2. Calcium based grease formulated with 2% w.t. MoS_2 nanoparticles (Nanomates Sample)
3. Lithium based grease formulated with 4% w.t. WS_2 nanoparticles (Nanomates Sample NM27O16W4 - NLGI2)
4. Lithium Based grease – NLGI 3
5. Lithium based grease formulated with 4% NanoLub GH paste (Weizmann Institute Sample)
6. Lithium based grease formulated with 4% w.t. WS_2 nanoparticles (Nanomates Sample NM28O16W4 - NLGI3)

7. Lithium based grease formulated with 4% w.t. MoS₂ nanoparticles (Nanomates Sample NM26O16Mo4 - NLGI3)
8. Lithium based grease formulated with 2% w.t. MoS₂ nanoparticles (Nanomates Sample)
9. Calcium based grease – NLGI 2

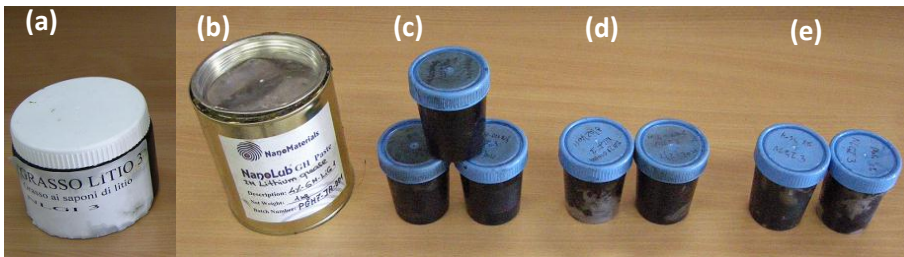


Fig. 3.3 – Grease samples Lithium based: (a) Lithium based grease NLGI 3, (b) Lithium based grease formulated with 4% NanoLub GH paste, (c) Lithium based grease formulated with 4% w.t. MoS₂ nanoparticles (NM26O16Mo4-NLGI3), (d) Lithium based grease formulated with 4% w.t. WS₂ nanoparticles (NM28O16W4-NLGI3), (e) Lithium based grease formulated with 2% w.t. MoS₂ nano-particles.

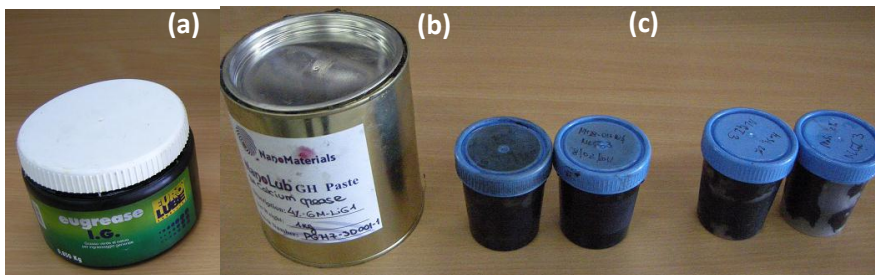


Fig. 3.4 – Grease samples Calcium based: (a) Calcium based grease NLGI 2, (b) Calcium based grease formulated with 4% NanoLub GH paste, (c) Calcium based grease formulated with 4% w.t. WS₂ nanoparticles (NM27O16W4-NLGI2), (d) Calcium based grease formulated with 2% w.t. MoS₂ nanoparticles.

3.2.2 Rheological characterization

The rheological measurements were carried out in a Physica MCR 301 (Anton Paar) rotational rheometer, equipped with a parallel plate geometry (25 mm diameter, 1 mm gap), Figure 3.5. The Calcium based grease NLGI 2 and the Lithium based grease NLGI 3 have been tested, as

well as the corresponding nanocomposites containing 4 wt % WS₂ nanosheets.

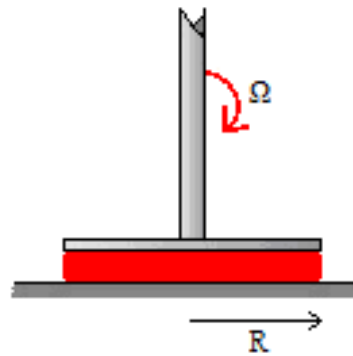
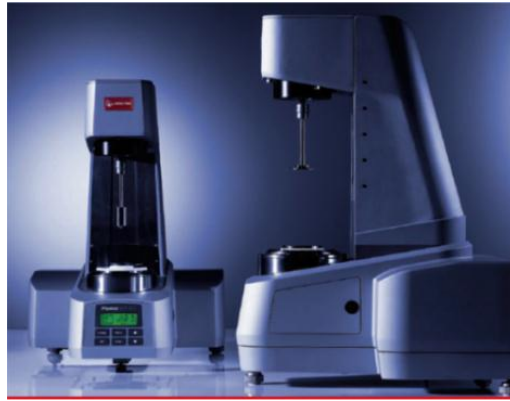


Fig. 3.5 - PHYSICA MCR 301 Anton Paar for the rheological characterization

Strain sweep tests, at the frequency of 1 rad/s, were performed on each sample at the temperatures of 25, 50, 75 and 100 °C to determine the linear viscoelastic region. Small amplitude oscillatory shear measurements, inside the linear viscoelasticity regime, were performed in the frequency range comprised between 10^{-2} and 10^2 rad/s at 25, 50, 75 and 100 °C.

The results for the Lithium based grease, NLGI 3, in terms of the storage (G') and loss (G'') moduli as a function of frequency, are reported in Figure 3.6 at the different temperatures tested. As it can be

observed, the values of the storage modulus are always significantly higher than those found for the loss modulus, in the whole frequency range studied.

The G' profiles are characterized by a slight increase with frequency with a tendency to reach a plateau modulus in the so called “plateau region”, where G'' shows a clear minimum.

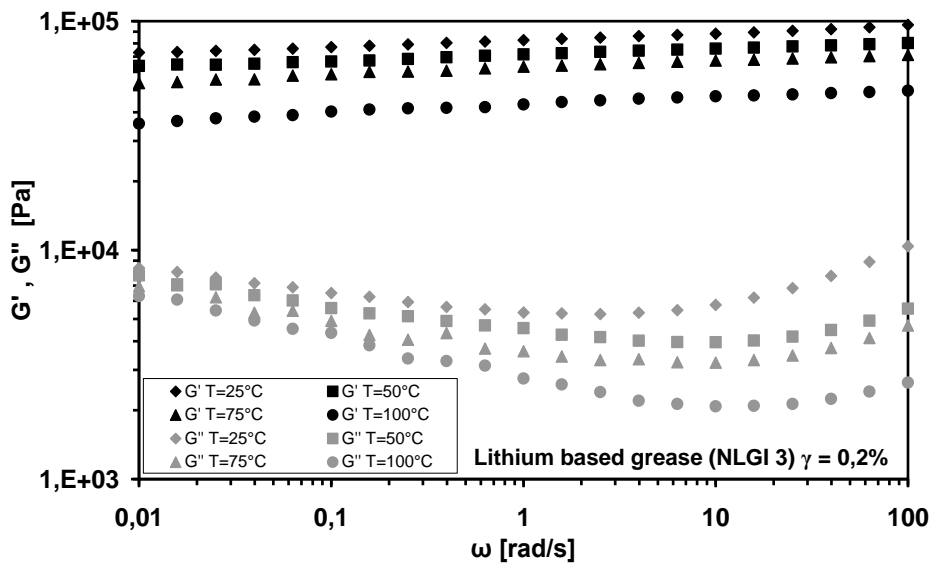


Fig. 3.6 - Storage Modulus (G') and Loss Modulus G'' vs frequency for the Lithium based grease

The viscoelastic behaviour of the Lithium based grease supports, then, the hypothesis that lubricating greases are highly structured systems with the thickener forming a three-dimensional network, in agreement with literature results [16-19]. Similar results have been also obtained for the Calcium based grease, NLGI 2.

The viscoelastic response of the both the Lithium and the Calcium greases nanocomposites containing 4 wt% WS_2 nanosheets has been tested and compared to the behaviour of the corresponding base grease. In particular, in Figures 3.7 and 3.8 the storage and loss moduli, as well as the complex viscosity, are reported for the Calcium grease and the nanocomposite at 25 and 100 °C respectively.

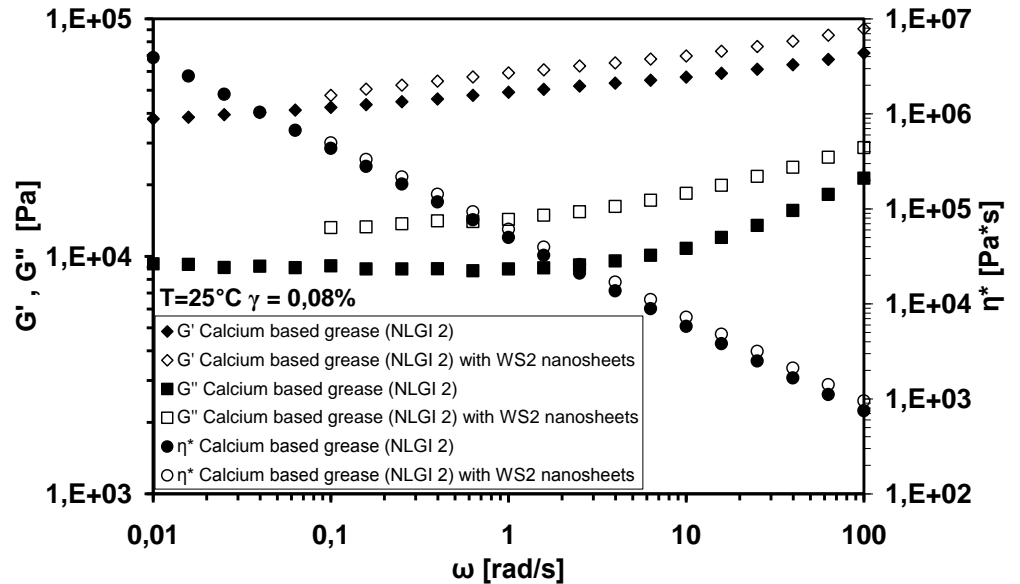


Fig. 3.7 - Storage Modulus (G'), Loss Modulus G'' and Complex Viscosity (η^*) vs frequency for the Calcium based grease NLGI 2 and the Calcium based grease – NLGI 2 with 4 wt % WS_2 nanosheets. $T= 25\text{ }^\circ\text{C}$.

The elastic response of the nanocomposite is characterized by G' values slightly higher than those of the Calcium grease NLGI 2 at $T= 25\text{ }^\circ\text{C}$, while the G' moduli become significantly lower than those of the lubricating grease at $100\text{ }^\circ\text{C}$.

The complex viscosity is strongly shear thinning in the whole frequency range tested.

The inclusion of the WS_2 nanosheets determines slight higher values for η^* compared to those of the lubricating grease at $25\text{ }^\circ\text{C}$, while at $100\text{ }^\circ\text{C}$ the complex viscosity of the nanocomposite is always lower than that of the lubricating Calcium grease NLGI 2 grease, Figure 3.8.

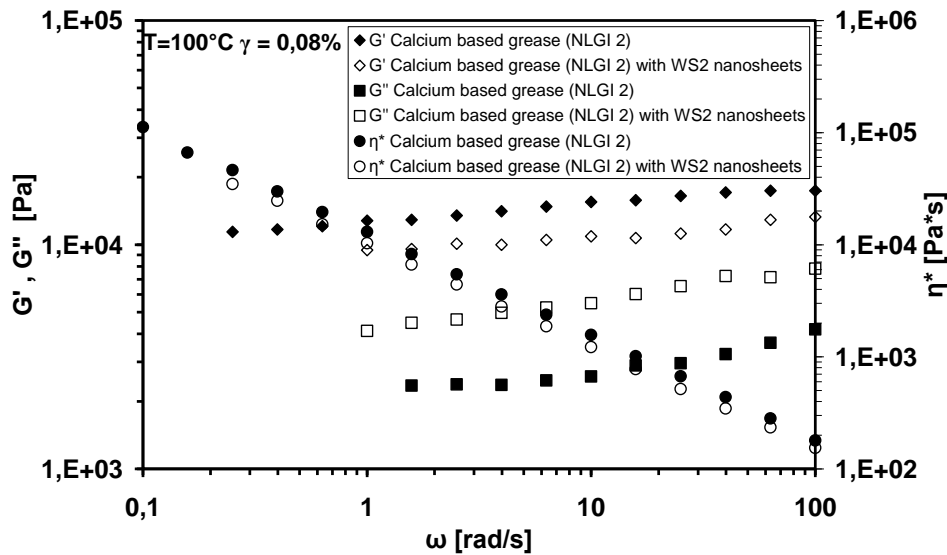


Fig. 3.8 - Storage Modulus (G'), Loss Modulus G'' and Complex Viscosity (η^*) vs frequency for the Calcium based grease NLGI 2 and the Calcium based grease – NLGI 2 with 4 wt % WS_2 nanosheets. $T=100^\circ C$.

The rheological tests performed on the greases formulated with the molybdenum disulphide additive showed the same results for those obtained for the samples with the tungsten nanosheets. Actually, the results obtained for the grease samples with 2 w.t.% nanoparticles showing no difference with those obtained for the grease samples formulated with 4 w.t.% of MS_2 . The obtained results highlight that the different types of inorganic nanoparticles, with the concentrations in weight used in this work, does not affect the rheological behaviour of the lubricating grease.

3.2.3 Tribological test

As for the tribological test on the formulated lubricants presented in Chapter 2, the Wazau rotational tribometer has been also used for the tribological grease characterization tests. The mating materials are: steel X40Cr14 ball, hardness: HRC 52-54, diameter: 8 mm; steel X155CrVMo12 disc, hardness: HRC 60, diameter: 105 mm. The experimental outcomes mentioned in this chapter are referred to steady

state operations opportunely chosen to investigate two different lubrication regimes. A normal load equal to 90 N has been applied, on the same tribological setup described in the chapter 2, in order to achieve the average hertzian contact pressure equal to 1.68 GPa. The grease temperature has been kept constant at room level. The relative motion between steel ball and disc was pure sliding at two speed levels: 5 mm/s for the test in boundary regime; 500 mm/s for the mixed regime. The test length was 60 minutes for friction/wear test with following scar diameter measurements on optical micrographs. The results of the friction tests in both the lubrication regimes and for both the additives investigated are summarized in the Tables. 3.4-3.5 and Figures 3.9-3.10, below:

Sample	Friction coefficient in boundary lubrication [-]	Friction coefficient in mixed-EHL lubrication [-]	Difference
Calcium based grease – NLGI 2	0.110	0.100	Benchmark
Calcium based grease formulated with 4% NanoLub GH paste	0.100	0.100	-9% 0%
Calcium based grease formulated with 2% MoS ₂	0.061	0.072	-44% 28%
Calcium based grease formulated with 4% WS ₂ (NM27O16W4 – NLGI2)	0.080	0.080	-27% 20%

Tab. 3.4 - Friction coefficient values for Calcium based grease and Calcium grease samples formulated with nanoparticles in boundary and mixed/EHL lubrication regimes

Sample	Friction coefficient in boundary lubrication [-]	Friction coefficient in mixed-EHL [-]	Difference
Lithium Based grease – NLGI 3	0.090	0.090	Benchmark
Lithium based grease formulated with 4% NanoLub GH paste	0.050	0.080	-44% 11%
Lithium based grease formulated with 2% MoS2	0.053	0.065	-40% 28%
Lithium based grease formulated with 4% MoS2 (NM26O16Mo4 - NLGI3)	0.060	0.070	-33% -22%
Lithium based grease formulated with 4% WS2 (NM28O16W4 - NLGI3)	0.070	0.070	-22% -22%

Tab. 3.5 - Friction coefficient values for Lithium based grease and Lithium grease samples formulated with nanoparticles in boundary and mixed/EHL lubrication regimes

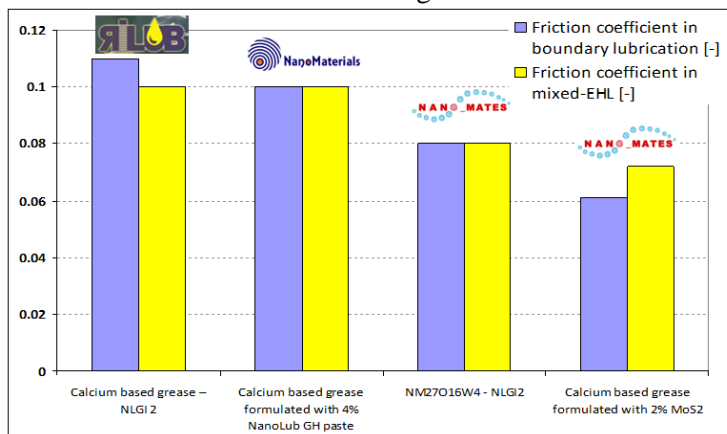


Fig. 3.9 - Calcium based grease and calcium formulated samples comparison

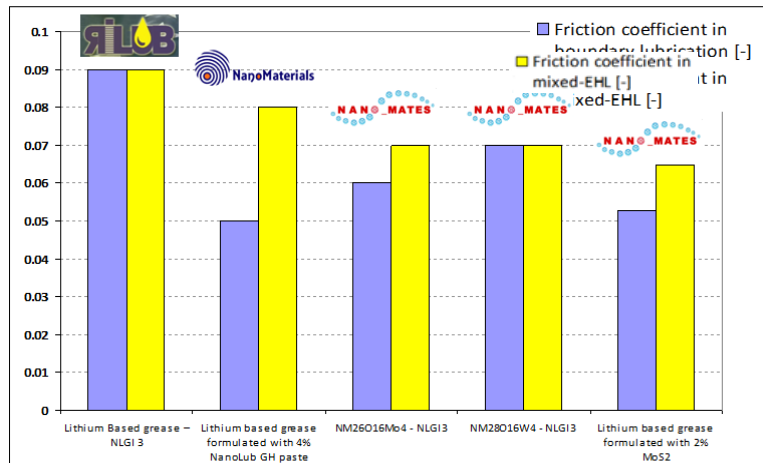


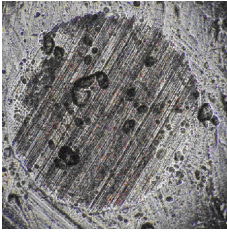
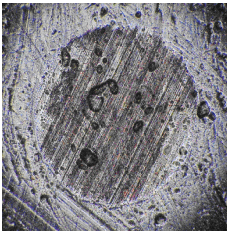
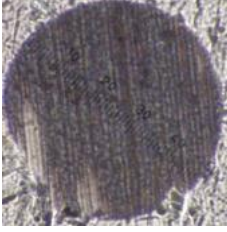
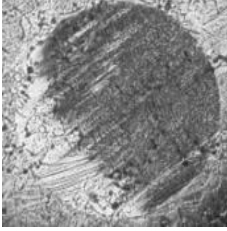
Fig. 3.10 – Lithium based grease and calcium formulated samples comparison

The better performance in terms of frictional behaviour is offered by Lithium Based grease – NLGI 3, compared to Calcium based grease – NLGI 2. There is a good improvement in terms of reduction of the friction coefficient especially for the Calcium based grease formulated with 4% w.t. WS₂ nanosheets and for the Lithium based grease formulated with 4 w.t.% NanoLub GH paste for both the lubrication regimes.

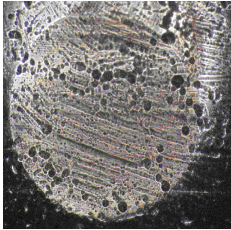
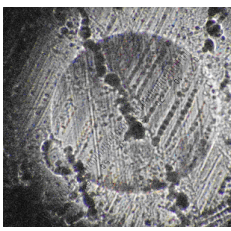
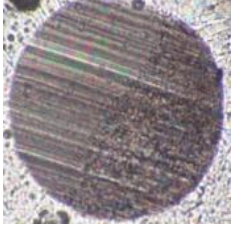
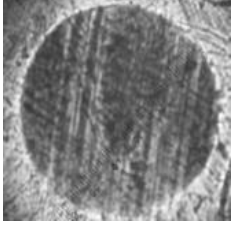
Furthermore, the tribological results show a marked decreasing in friction coefficient in both the boundary and mixed lubrication regimes achievable through MoS₂ nanosheets dispersion, with 36% average reduction for Calcium grease and 34% for Lithium one. Accordingly, the worn surface of the steel ball has been also analysed by means of an optical microscope to measure the diameters of the wear circle.

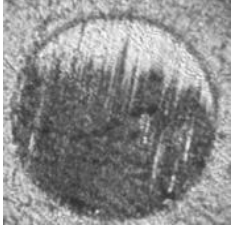
The anti-wear property of nanosheets as additive for Calcium and Lithium greases has been clearly exhibited in both the above lubrication regimes. Actually, these tests confirm the enhanced anti-wear property allowed by the nanosheets of tungsten and molybdenum disulphide for both Calcium and Lithium greases.

The values of the wear scar diameter and the optical micrographs of the wear circle collected on the steel ball after 1-hour test are given in the Tables. 3.6 and 3.7.

Sample	Ball wear scar diameter [μm] Boundary lubrication	Difference
Calcium based grease – NLGI 2	 820	<i>Benchmark</i>
Calcium based grease formulated with 4 wt% NanoLub GH paste	 610	-26%
Calcium based grease formulated with 2 wt% MoS ₂	 520	-36%
Calcium based grease formulated with 4 wt% WS ₂ (NM27O16W4 – NLGI2)	 590	-28%

Tab. 3.6 – Values of the Wear scar diameter and the optical micrographs of the wear circle collected on the steel ball after 1-hour test for Calcium based grease and Calcium grease samples formulated with nanoparticles in boundary lubrication regime

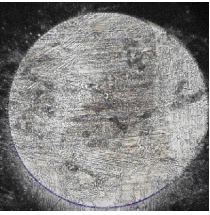
Sample	Ball wear scar diameter [μm] Boundary lubrication	Difference
Lithium based grease – NLGI 2	 800	<i>Benchmark</i>
Lithium based grease formulated with 4 wt% NanoLub GH paste	 570	-29%
Lithium based grease formulated with 2 wt% MoS ₂	 530	-34%
Lithium based grease formulated with 4 wt% MoS ₂ (NM26O16Mo4 - NLGI3)	 580	-27%

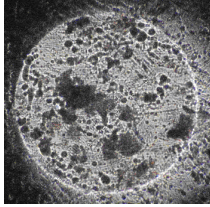
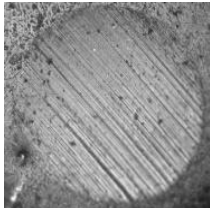
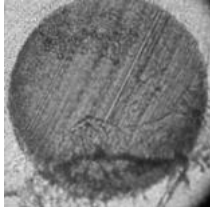
<p>Lithium based grease formulated with 4 wt% WS₂ (NM28O16W4 - NLGI3)</p>	 <p>600</p>	<p>-25%</p>
---	--	-------------

Tab. 3.7 – Values of the Wear scar diameter and the optical micrographs of the wear circle collected on the steel ball after 1-hour test for Lithium based grease and Lithium grease samples formulated with nanoparticles in boundary lubrication regime

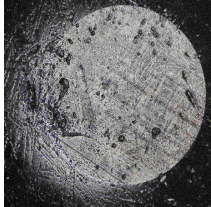
The anti-wear property of MoS₂ and WS₂ nanosheets as additive for Calcium and Lithium greases has been clearly exhibited in both the above lubrication regimes, leading to 24% of average reduction in wear scar diameter.

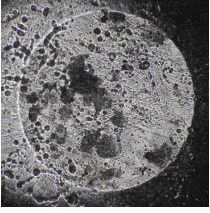
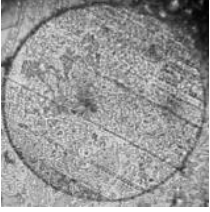
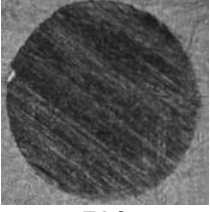
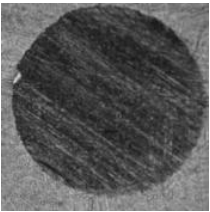
In boundary regime, for example, Calcium based grease formulated with 4 w.t. % WS₂ and Lithium based grease formulated with 4 w.t. % WS₂ exhibit a very similar performance in terms of reduced wear with a reduction of about 25-28% of the scar diameter with respect to the base grease. Another test pattern has been carried out in the same loading conditions at higher sliding speed (0.50 m/s), where Mixed/EHL regime is assumed to appear. The values of the wear scar diameter and the optical micrographs of the wear circle collected on the steel ball after 1-hour test are given in the Tables. 3.8 and 3.9.

Sample	Ball wear scar diameter [μm] Mixed-EHL lubrication	Difference
<p>Calcium based grease – NLGI 2</p>	 <p>1200</p>	<p><i>Benchmark</i></p>

<p>Calcium based grease formulated with 4 wt% NanoLub GH paste</p>	 <p>830</p>	<p>-31%</p>
<p>Calcium based grease formulated with 2 wt% MoS₂</p>	 <p>770</p>	<p>-36%</p>
<p>Calcium based grease formulated with 4 wt% WS₂ (NM27O16W4 – NLGI2)</p>	 <p>820</p>	<p>-32%</p>

Tab. 3.8 – Values of the Wear scar diameter and the optical micrographs of the wear circle collected on the steel ball after 1-hour test for Calcium based grease and Calcium grease samples formulated with nanoparticles in Mixed/EHL lubrication regime

Sample	Ball wear scar diameter [μm] Mixed-EHL lubrication	Difference
<p>Lithium based grease – NLGI 2</p>	 <p>920</p>	<p><i>Benchmark</i></p>

Lithium based grease formulated with 4 wt% NanoLub GH paste	 <p style="text-align: center;">810</p>	-31%
Lithium based grease formulated with 2% MoS ₂	 <p style="text-align: center;">750</p>	-36%
Lithium based grease formulated with 4% MoS ₂ (NM26O16Mo4 - NLGI3)	 <p style="text-align: center;">790</p>	-14%
Lithium based grease formulated with 4% WS ₂ (NM28O16W4 - NLGI3)	 <p style="text-align: center;">800</p>	-13%

Tab. 3.9 – Values of the WSD and the optical micrographs of the wear circle collected on the steel ball after 1-hour test for Lithium based grease and Lithium grease samples formulated with nanoparticles in Mixed/EHL lubrication regimes

For these tests in Mixed/EHL regime, Calcium based grease formulated with 2 w.t. % MoS₂ and Lithium based grease formulated with 2 w.t.% MoS₂ reveal two unlike performance in terms of wear.

Actually, the Calcium formulated samples gains a better improvement than Lithium sample, with 36% reduction of the wear circle diameter, while the latter exhibits a reduction equal to 18%. In the same

way, Calcium based grease formulated with 4 w.t. % WS_2 gains a better improvement than Lithium sample with 4 w.t. % WS_2 . Furthermore, Calcium samples show an average reduction of the wear circle diameter up to 32%, while the Lithium additive samples exhibit a reduction of 15%. Accordingly, the most evident benefit of MoS_2 nanosheets addition has been exhibited by the Calcium based grease.

This result is even more remarkable considering the initial lower NLGI grade of the Calcium base. At the same way the samples formulated with WS_2 show a similar behaviour in terms of reduction of the wear diameter in the boundary lubrication regime, whereas under mixed-EHL the formulation with molybdenum disulphide shows better results.

3.2.4 Tribological tests at Nanomaterials facilities on Rilub greases with 2 wt% MoS_2 nanoparticles synthesized by Nano_Mates

The 4 balls anti wear properties measurements are performed by following ASTM D2596 - 10 Standard Test Method for Measurement of Extreme-Pressure Properties of Lubricating Grease (Four-Ball Method). While the Brugger test, according to DIN 51834, was developed by Mueller Weingarten for testing the high load carrying capacity of lubricants and greases. Depending on the lubricating properties the rotating roller produces different wear scars onto the fixed cylinder. The scar has the shape of an ellipse. The main axes of the ellipse are measured with a magnifier. Thus the projection surface of the wear scar is calculated. The quotient of the pressure force and projected wear scar is the load-carrying capacity of the lubricant according to Brugger (N/mm^2). At present the test method according to Brugger is the only basis for finding the optimal lubricant with regard to the load-carrying capacity. A great number of measurements showed a good reproducibility of the results. The deviations from the measured values are $\pm 10\%$, Figure 3.11.

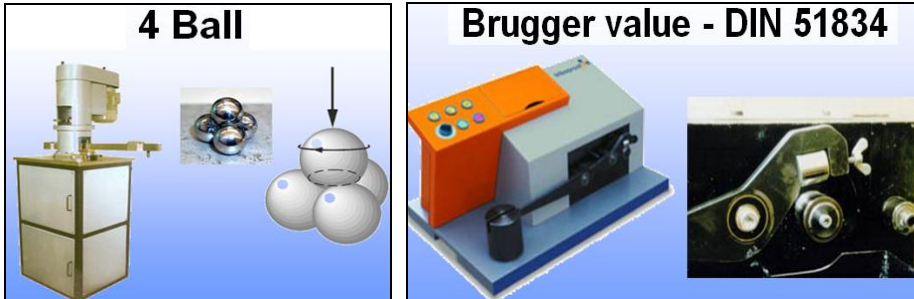


Fig. 3.11 - Four balls and DIN 51834 test setups

After testing, scar diameters are measured on each of the three clamped balls. The mean value of the three scar diameters is reported and gives the anti-wear characteristic of the tested fluid as described in ASTM D 4172. Because of repeatability questions, each fluid is tested twice following the same procedure. The results of the friction and wear tests performed by Nanomaterials (NanoMaterials, Ltd. –Israel) are summarized in the Figures 3.12, 3.13 and 3.14, below:

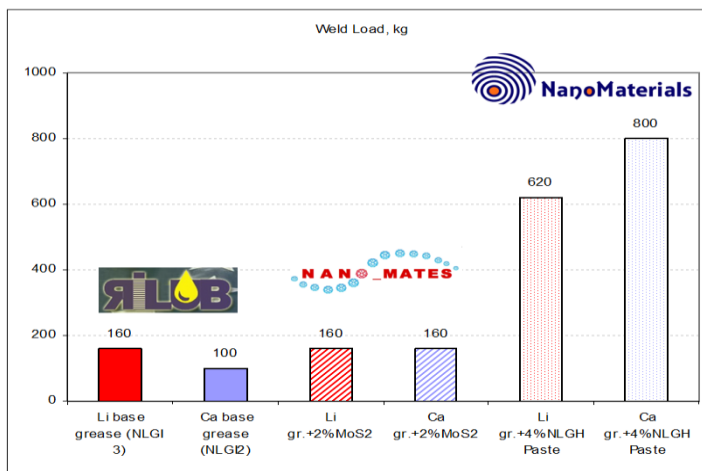


Fig. 3.12 - Weld load test result using 4 Ball test

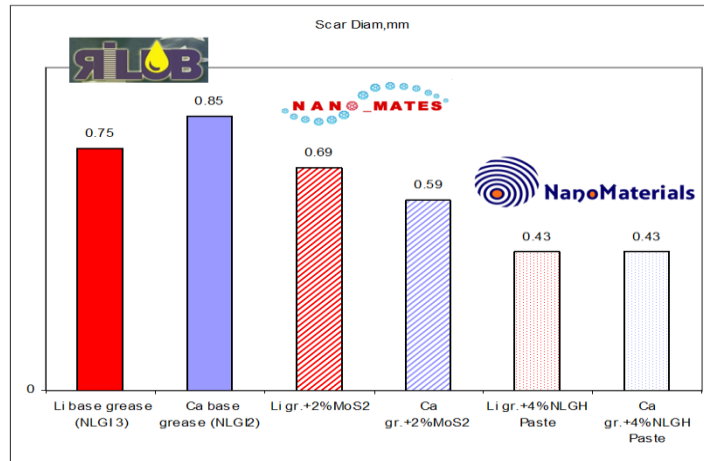


Fig. 3.13 - Scar Diameter test result using 4 Ball test

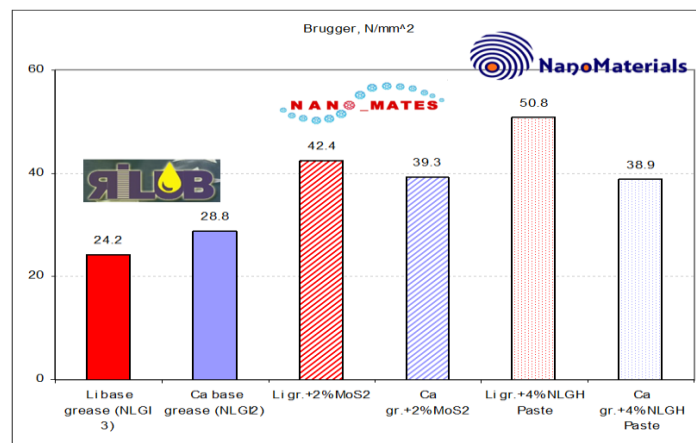


Fig. 3.14 - The Bruggen value test result using 4 Ball test

3.2.5 FRETING TEST

Finally, fretting tests were performed on steel ball for the samples formulated with the tungsten disulphide nanoadditives. Fretting refers to wear and sometimes corrosion damage at the asperities of contact surfaces. This damage is induced under load and in the presence of repeated relative surface motion, as induced for example by vibration, Figure 3.15.

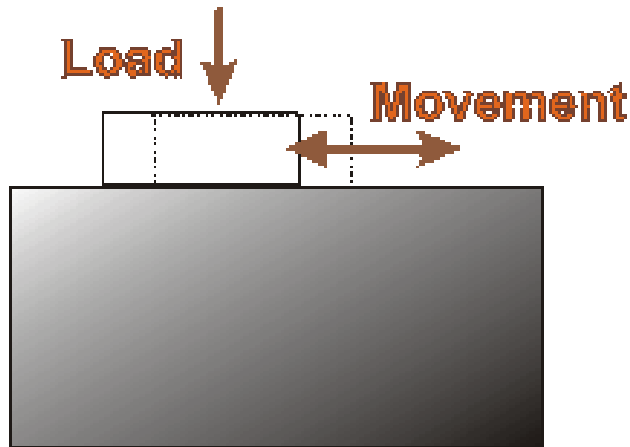


Fig. 3.15 – Fretting wear process

The ASM Handbook on Fatigue and Fracture defines fretting as: "A special wear process that occurs at the contact area between two materials under load and subject to minute relative motion by vibration or some other force" [3].

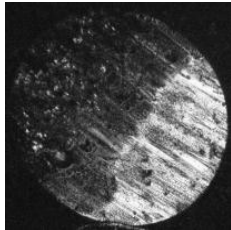
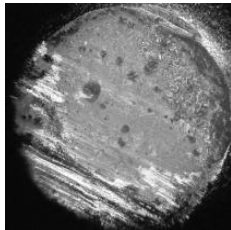
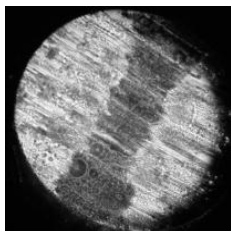

The testing conditions of the performed fretting test are reported in Table 3.10, below:

Average hertzian contact pressure	1.68 GPa (90 N)
Frequency	3 Hz
Angle	$\pm 85^\circ$
Grease feeding to contact surface	Ambient air
Grease temperature	Room temperature
Test duration	2 hours

Tab. 3.10 – Operating conditions used for the fretting test

The tests performed in order to evaluate the wear damage due to an oscillatory motion at high frequency (fretting wear) have been performed only on the samples formulated with tungsten disulphide nanosheets.

Accordingly, the values of the wear scar diameter and the optical micrographs of the wear circle collected on the steel ball after 2-hour test are given in the Tables 3.11:

Sample	Ball wear scar diameter [μm]	Difference
Calcium based grease – NLGI 2	 1450	<i>Benchmark</i>
Calcium based grease formulated with 4 wt% WS_2	 1250	-14%
Lithium Based grease – NLGI 3	 1290	<i>Benchmark</i>
Lithium based grease formulated with 4 wt% WS_2	 1180	-9%

Tab. 3.11 – Values of the wear scar diameter and the optical micrographs of the wear circle collected on the steel ball after 2-hour test for Lithium and Calcium grease samples formulated with tungsten disulphide

The pictures also show in some cases a deeper track in the center of the rim diameter of the wear scar circle due to the continuous change of the rotation direction.

3.2.6 Discussion on the greases formulated with nanosized inorganic based additives

In the light of the results presented in the first section of this chapter some important conclusion can be made. First of all, Nanomaterials Nanolub GH Paste and MS_2 nanoparticles synthesized at Nano_mates laboratories improve the tribological performance of Rilub Calcium (NLGI 2) and Lithium (NLGI 3) based greases. Moreover, the best frictional results have been achieved by Calcium based grease formulated with 2 wt% MoS_2 (Nano_mates) and Lithium based grease formulated with 4 wt% NanoLub GH paste.

Actually, the tribological results show a marked decreasing in friction coefficient both in boundary and mixed lubrication regimes achievable through MoS_2 nanosheets dispersion, with average reduction for Calcium and Lithium grease around 35%. At the same time, the tribological results show a marked decreasing in friction coefficient both in boundary and mixed lubrication regimes achievable through WS_2 nanosheets dispersion, with 22% average reduction for Calcium grease and 11% for Lithium one. Furthermore, the best performance in terms of wear scar diameter (WSD) has been provided by Nano_mates samples (Li and Ca) prepared with 2 w.t.% of MoS_2 .

The anti-wear property of MoS_2 nanosheets as additive for Calcium and Lithium greases has been also clearly exhibited in both the above lubrication regimes, leading to an average level of 30% decreasing on the scar diameter measured on the steel ball worn surface. Accordingly, the most evident benefit of the nanoparticles addition has been exhibited by the Calcium based grease. Moreover, the Nano_mates sample (Li base) with Molybdenum disulphide at 2 wt% performs better than 4 wt% formulation. Future studies will be carried out to investigate if these results are linked to the different concentration of dispersant and/or oleylamine.

As for the MoS_2 additives, the grease samples formulated with the tungsten disulphide nanosheets clearly exhibits good anti-wear property

in both the above mentioned lubrication regimes, leading to 24% of average reduction in wear scar diameter.

Actually, in boundary regime, Calcium based grease formulated with 4 w.t.% WS₂ and Lithium based grease formulated with 4 w.t. % WS₂ exhibit a very similar performance in terms of reduced wear with a reduction of about 25-28% of the scar diameter with respect to the base grease measure.

Unlikely, for these tests in Mixed/EHL regime, Calcium based grease formulated with 4 w.t. % WS₂ and Lithium based grease formulated with 4% w.t. WS₂ reveal two unlike performance in terms wear. In fact, the Calcium formulated samples gains a better improvement than Lithium sample, with 32% reduction of the wear circle diameter, while the latter exhibits a reduction equal to 15%.

It is also important to highlight that MS₂@oleylamine nanosheets were successfully synthesized by means of a novel wet chemistry approach and the rheological results show that the inclusion of the MS₂ nanosheets determines slight higher values for the Calcium grease complex viscosity η^* at 25°C, and lower values at 100 °C.

3.3 GREASES WITH HYBRID NANOSHEETS OF MOS₂ ON CNT

This section of the chapter shows the tribological experimental investigation performed on grease samples formulated with hybrid additives made up by nanosheets of MoS₂ and carbon nanotube synthesized at NanoMates centre (University of Salerno). Actually, in order to conjugate and to enhance, through a unique synergy, the performances of these extraordinary materials at the nanoscale, the synthesis of hybrid-nanostructures made by CNT and nanochalcogenides, has become an important goal and not only in lubrication [20-29].

Furthermore, in literature is possible to find, binary systems such as MoS₂-coated carbon nanotubes have been recently synthesized by hydrothermal route [30-34], impregnation and annealing [35-38], electrodeposition [39]. In this section a new synthetic strategy to obtain hybrid organic-inorganic oleylamine@MoS₂-CNT nanocomposites with different compositions will be described and their use as anti- friction and

anti-wear additives for grease lubricants will be reported. The schematic representation of such hybrid nanocomposite is reported in Figure 3.16.

Using an analogous synthetic approach, previously reported for the synthesis of MoS_2 and WS_2 nanosheets coated by oleylamine (OA)[40,41], nano MoS_2 @OA were synthesized in the presence of high quality CNT nanotubes, produced by a CCVD technique developed in our lab[42-44]. The MoS_2 precursor and MWCNTs, in different concentration ratios, were sonicated in oleylamine. The mixture was heated to 360°C under inert atmosphere to produce a hybrid nanocomposite in which MoS_2 , CNT and oleylamine are intimately bonded and their composition can be easily modulated.

The organic coating enhances the compatibility of the inorganic core for the lubricant base and promotes the mixing process. The products were characterized by X-ray diffraction (XRD), transmission (TEM) and scanning electron microscopy (SEM), Raman spectroscopy and thermo gravimetric analysis coupled with mass spectrometry (TG-MS). The nanohybrid composites were then used as additives for commercial grease lubricant and their tribological performances were tested.

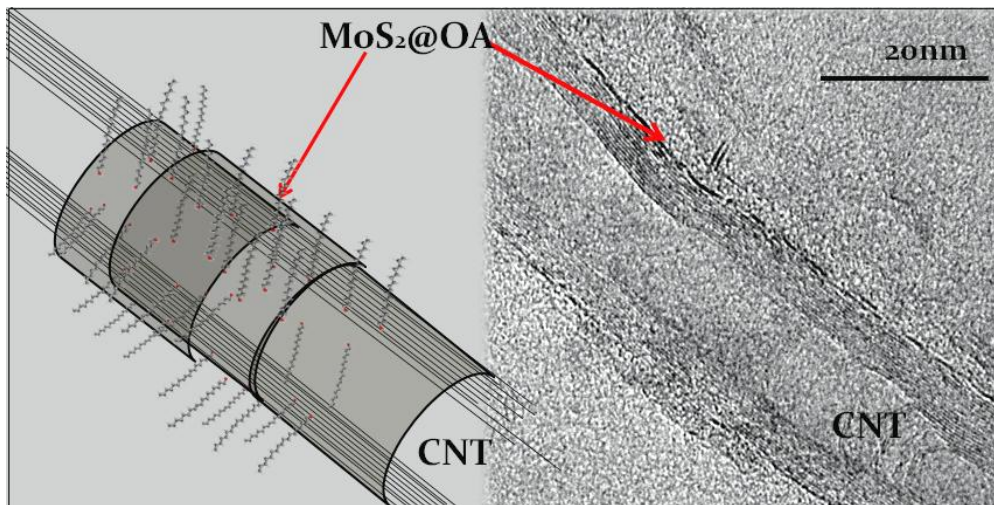


Fig. 3.16 - Schematic representation of hybrid MoS_2 /CNT coaxial nanotubes: carbon nanotubes are externally coated with MoS_2 nanosheets. Oleylamine molecules cover the inorganic core, improving the dispersibility in grease and corresponding TEM image of nano hybrid material.

3.3.1 Experimental Section

Ammonium tetrathiomolybdate (99.97% trace metals basis); oleylamine (technical grade, 70%), hexane (95%) and ethanol (99.8%) were furnished by Aldrich and used without further purification. Calcium based grease NLGI2 and lithium based grease NLGI3 were kindly offered by RILUB Italy.

3.3.1.1 Synthesis of carbon nanotubes

Multiwalled carbon nanotubes (MWNT) were synthesized by ethylene catalytic chemical vapor deposition (CCVD) on Co/Fe- Al_2O_3 catalyst, prepared by wet impregnation of gibbsite ($\gamma\text{-Al}(\text{OH})_3$) powder with cobalt acetate (2.5 wt %) and iron acetate (2.5 wt %) ethanol solution. The catalyst was dried at 393 K for 720 min and preheated before synthesis at 70 K/min up to 973 K under N_2 flow.

For the CNT synthesis a mixture of ethylene 10 % v/v in helium was fed to a continuous flow microreactor at 973 K, with a runtime of 30 min. Gas flow rate and catalyst mass were 120 (stp)cm³/min and 400 mg, respectively.

The CNT synthesis was very effective, yielding more than 95 % conversion of the inlet carbon and about 100% selectivity to CNT. To remove catalyst impurities the samples were treated with HF (46% aqueous solution), and the solid residue was washed with distilled water, centrifuged and finally dried at 353 K for 12 h, resulting in high purity (> 97%) multiwalled carbon nanotubes.

3.3.1.2 Preparation of OA@MoS₂-CNT nanocomposite

Furthermore, 30 mg of CNT were mixed with 0.4 g of $(\text{NH}_4)_2\text{MoS}_4$ in 18 ml of oleylamine and sonicated for 30 minutes. The red homogeneous dispersion was transferred to a three necked spherical flask of 100ml, equipped with a water condenser.

The reaction mixture was gradually (5°C/min) heated to 360°C and maintained at this temperature for 60min under nitrogen atmosphere and magnetic stirring.

The reactor was cooled to room temperature by removing the heating mantle and the product was collected by centrifugation after washing with ethanol.

3.3.1.3 Preparation of OA@CNT-MoS₂ nanocomposite

Analogous procedure was used to produce CNT@MoS₂ nanocomposite with CNT in excess with respect to MoS₂. In this case 0.18g of CNT were mixed with 0.06 g of (NH₄)₂MoS₄ in 18 ml of oleylamine.

3.3.1.4 Preparation of nanoadditivated lubricant grease

Different amounts of oleylamine@CNT-MoS₂ or oleylamine@MoS₂-CNT nanocomposite were added to calcium based grease NLGI2 (Ca NLG2) and lithium based grease NLGI3 (Li NLGI3) and their anti-friction and anti-wear performance have been tested. The compositions of samples are reported in the Table 1. The experimental details for the synthesis of OA@MoS₂ used as reference nanoadditive, have been reported in a previous work [39,40].

3.3.1.5 Physico-chemical characterization

TEM micrographs were obtained with a FEI Tecnai electron microscope operating at 200 KeV. Scanning electron microscopy images were collected with a SEM LEO 125 VP microscope. XRD patterns (Cu K α radiation) were acquired by a Bruker D8 diffractometer. The thermal decomposition of the nanosheet organic coating was investigated with a TG-DTG-DSC simultaneous thermo-analyzer (Q600, TA Instruments) online connected to a quadrupole-mass detector (Quadstar 422, Pfeiffer Vacuum). Raman spectra were obtained with a micro Raman spectrometer Renishaw inVia (514 nm excitation wavelength).

The tested grease samples and their composition are reported in the Table

3.12, below:

Grease	nanoadditive	wt.% of nanoadditive
Ca NLG2	OA@MoS ₂	0.1
Ca NLG2	OA@MoS ₂ -CNT	0.1
Ca NLG2	OA@CNT-MoS ₂	0.1
Li NLGI3	OA@MoS ₂	0.1
Li NLGI3	OA@MoS ₂ -CNT	0.1
Li NLGI3	OA@CNT-MoS ₂	0.1

Tab. 3.12 - Composition of grease samples tested (Ca= Calcium, Li=Lithium)

3.3.2 Results and discussion

3.3.2.1 X-ray diffraction analysis

The XRD patterns of CNT, OA@CNT-MoS₂, OA@MoS₂-CNT, OA@MoS₂ are reported in the Figure 3.17.

The patterns of CNT (black line), typical of well-crystallized material, revealed the presence of 3 peaks, at 26.3°, 42.7° and 44.8°, corresponding to the inter-graphitic interlayer spacing of the nanotubes *d* (002) and to the *d*-spacing of the family planes (100) and (101)[51], respectively. In the XRD patterns of OA@MoS₂ (green line) the (101) and (110) peaks for the *ab* plane are visible, while the (002) peak cannot be seen because of the presence of a large band in the region 10°-30° 2θ, due to the oleylamine.

The XRD pattern of an analogous sample repeatedly washed and centrifuged with ethanol, reported in a previous work [39,40], does not exhibit the large band of oleylamine and presents a very low intense (002) reflection corresponding to the *c* axis typical of the predominant formation of single layer-MoS₂@oleylamine [52-54].

Both nanocomposites OA@MoS₂-CNT (red line) and OA@CNT-MoS₂ (blue line) present the wide band in the region 10°-30° 2θ, due to OA that was difficult to remove completely with washing, suggesting a strong interaction of OA with the inorganic core of the nanocomposite, as reported in previous works [55-58], where carbon materials were treated

with OA to promote their dispersibility in organic solvents or the adsorption of nanoparticles.

In the XRD pattern of OA@MoS₂-CNT, where the weight ratio CNT/MoS₂ is 1/10, the (101) (110) peaks for the ab plane of MoS₂ are clearly visible and the CNT (002) reflection appears as a low intense asymmetry, centered at 26.2°, of the OA band. On the contrary, for OA@CNT-MoS₂, whose weight ratio CNT/MoS₂ is 5/1, only the inter-graphitic interlayer spacing of the nanotubes, corresponding to the (002) peak, can be clearly seen.

It is similar to that of bare carbon nanotubes, indicating that the MoS₂ coating does not lead to much distortion of the carbon nanotubes [25].

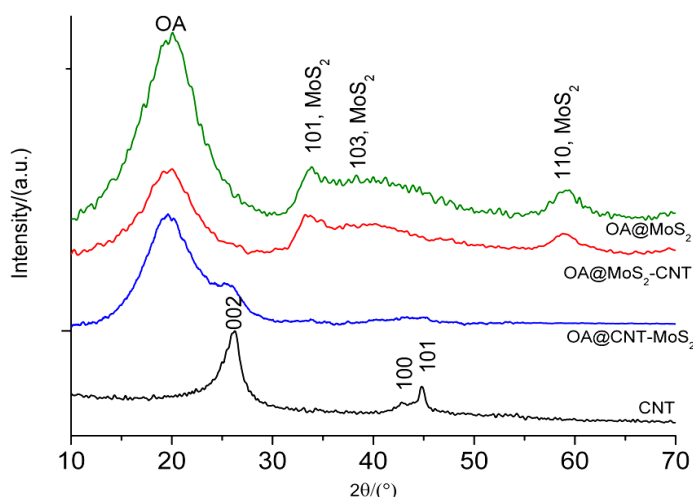


Fig. 3.17 - XRD patterns of CNT (black) , OA@CNT-MoS₂ (blue), OA@MoS₂-CNT (red), OA@MoS₂ (green)

3.3.2.2 Scanning electron microscopy analysis

The SEM images of OA@MoS₂-CNT collected at different magnifications are reported in the Figure 3.18. In this sample the presence of little aggregates embedded in oleylamine matrix strictly resemble the typical morphology of MoS₂@oleylamine[59,60] and is consistent with the nanocomposite weight ratio MoS₂/CNT of 10:1. The CNTs are embedded in the MoS₂@oleylamine matrix and also at higher

magnification they cannot be distinguished. This conclusion agrees with the XRD results showing that the MoS₂ structure and oleylamine patterns are predominant (see Figure 3.17, red line). On the contrary, the SEM images of OA@CNT-MoS₂, reported at different magnifications in the Figure 3.19, show a completely different morphology with respect to the previous one.

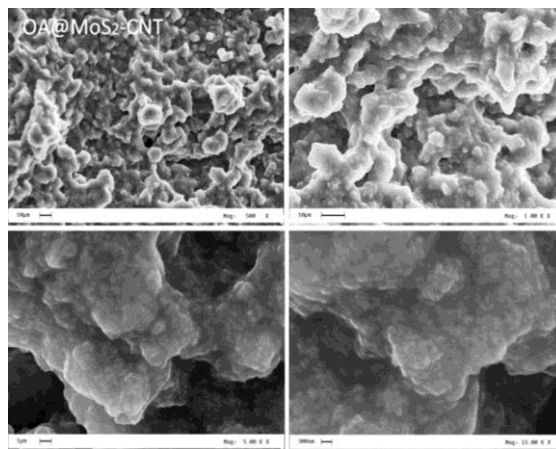


Fig. 3.18 - SEM images at different magnification (500x, 1000x, 5000x and 15000x) of OA@MoS₂-CNT nanocomposite.

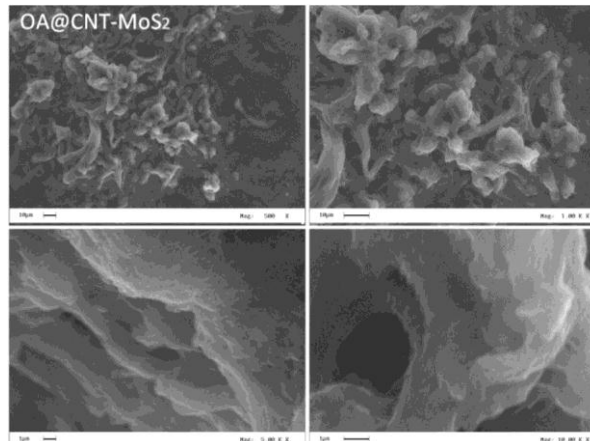


Fig. 3.19 - SEM images of OA@CNT-MoS₂ nanocomposites at different magnification (500x, 1000x, 5000x and 10000x)

In fact, the structure morphology seems to be consistent with bundles of CNT embedded in oleylamine, according to XRD data where only the (002) peak of CNT and the oleylamine band are visible (see figure 3 blue line) and in agreement with the composition of nanocomposite, whose weight ratio CNT/MoS₂ is 5/1.

3.3.2.3 Transmission electron microscopy analysis

In Figs. 3.20 and 3.21, TEM images of OA@MoS₂-CNT and OA@CNT-MoS₂ are reported. Since both molybdenum and sulphur atoms have larger weight than the carbon atom, the MoS₂ results highly contrasted. In panels (a) and (b) of figure 6, nanosheets (1 to 3) of MoS₂ dispersed in oleylamine are clearly visible. They have an average d space (002) of $6.7 \pm 2 \text{ \AA}$ [61].

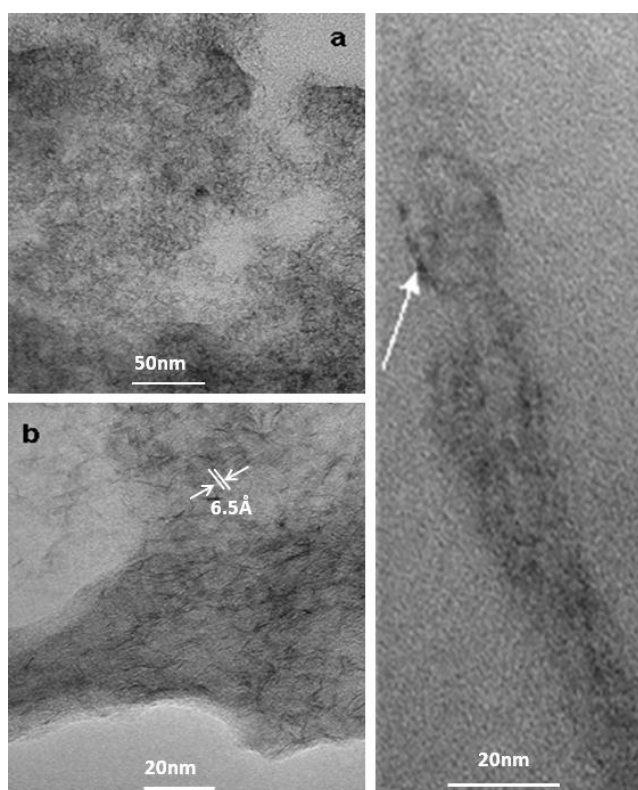


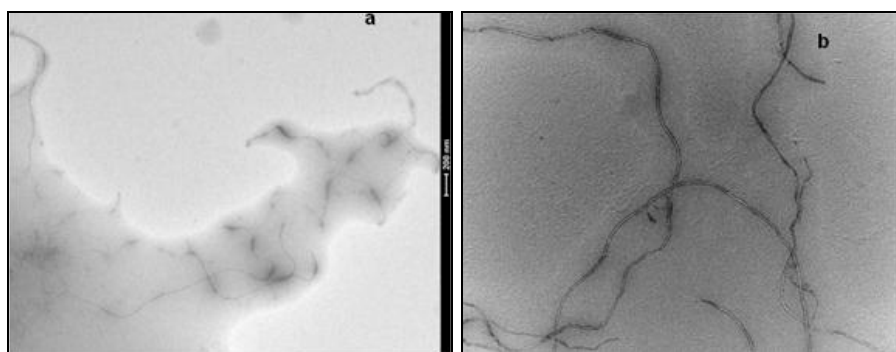
Fig. 3.20 - TEM images of OA@MoS₂-CNT at different magnification

On the other hand, it is very difficult to focus on CNT in this sample, as evidenced in the image of panel (c), where nanosheets of MoS₂ can be observed on the nanotubes external surface. CNTs dipped in an oleylamine matrix covered by MoS₂ nanosheets are clearly visible in Figure 3.21 for OA@CNT-MoS₂.

MoS₂ can deposit easily on the outer surface of the carbon nanotube matrix owing to the nearly identical crystal structure of graphite and layered MoS₂. CNTs have 10-20 nm outer diameter and 4-12 carbon walls (Figure 3.21d) partially sheathed with 1-3 layer MoS₂ nanosheets (Figure 3.21c and Figure 3.17)[62].

3.3.2.4 TG-DTG-DSC-MS analysis

The thermal conversion of OA@MoS₂-CNT and OA@CNT-MoS₂ in air flow occurred as three main weight loss steps at 200-320°C, 320-390°C and 390-570°C (Figure 3.22a, b). All the steps are exothermic and characterized by CO₂ release (see m/z=44). In particular, in the range 200-320°C, oxidation of sulfur impurities to SO₂ (see the SO₂ total ion current (TIC) of m/z =48, 64 in the same temperature range of the weight loss), and decomposition of physisorbed oleylamine (as clearly indicated by the corresponding TIC of the most intense mass fragments peaks: m/z =41, 55) occurred.



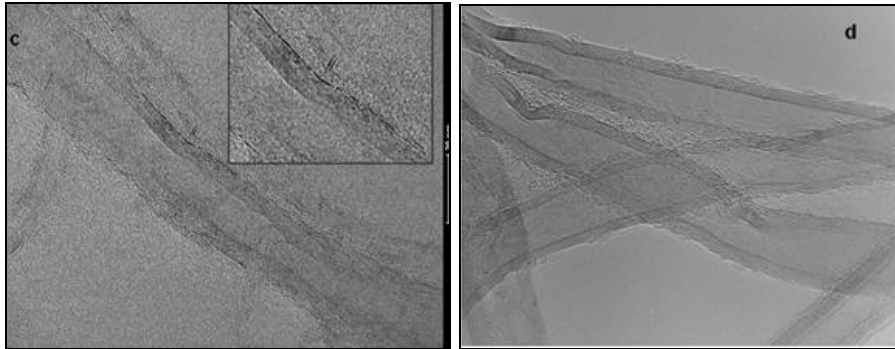
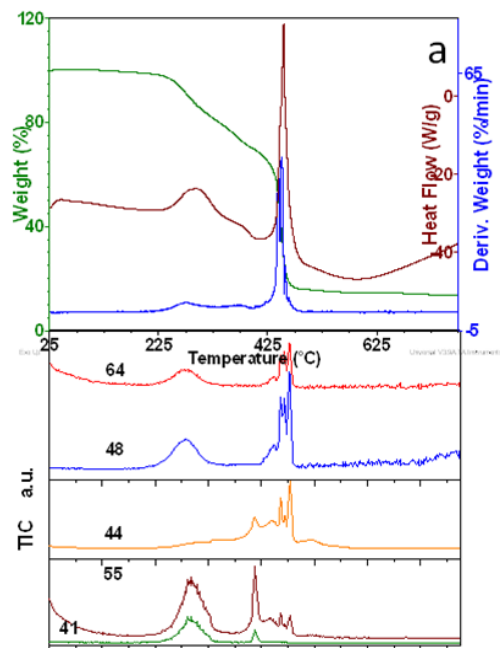


Fig. 3.21 - TEM images of OA@CNT-MoS₂ (a, b, c) and CNT (d).at different magnification



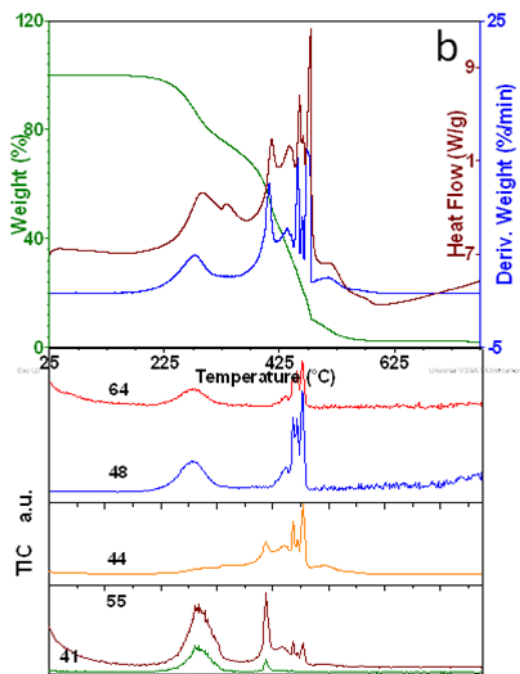


Fig. 3.22 - TG-DTG-DSC and relevant total ion current signals of OA@MoS₂-CNT (a) and OA@CNT-MoS₂ (b)

The multi-peak last step begins with a small weight loss in the range 390-420°C, likely due to oleylamine physisorbed on the CNTs surface and inside the CNT hollow core; this peak is more visible for OA@CNT-MoS₂ that has a higher CNT content. The temperature of 420°C is the onset of the last five DTG peaks for OA@MoS₂-CNT (centred at 445°, 450°, 456°, 460°C and a weaker one at 500 °C, respectively) corresponding to the oxidation of the MoS₂/CNT/oleylamine system.

The first four peaks correspond in pairs to the thermal decomposition of the chemisorbed oleylamine, followed by a more pronounced oxidation of S and Mo (now accessible to air oxygen) to SO₂ and MoO₃, and of decomposed oleylamine carbon to CO₂. For OA@MoS₂-CNT, the first two peaks are much more intense, the opposite for OA@CNT-MoS₂.

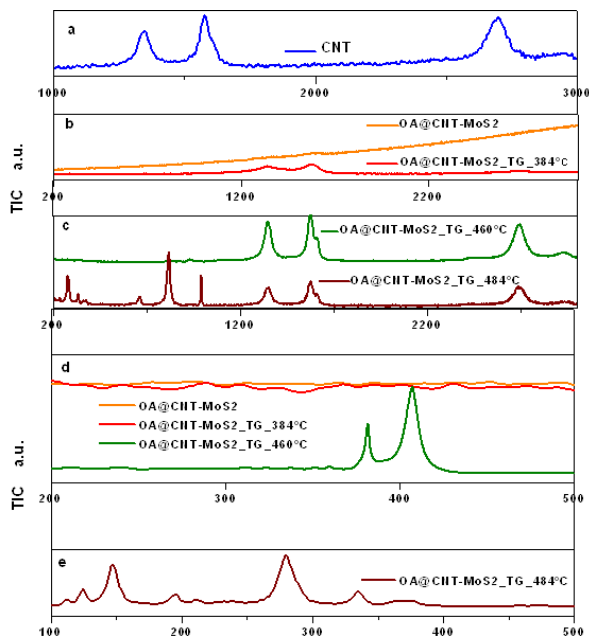


Fig. 3.24 - Raman spectra of OA@CNT-MoS₂, OA@CNT-MoS₂_TG_384, OA@CNT-MoS₂_TG_460, OA@CNT-MoS₂_TG_4

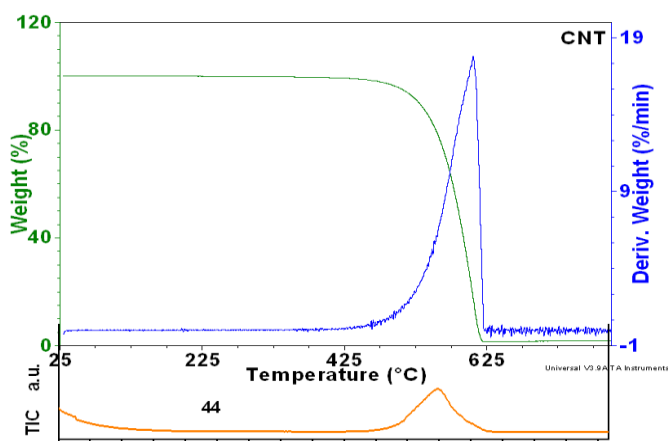


Fig. 3.23 - TG-DTG of CNT and the relevant total ion current signal showing the formation of CO₂ from carbon oxidation

In particular, in the range 470°C-570°C, the MoS₂ coated by oleylamine inside the tubes, now exposed to air (this peak is more visible for

OA@CNT-MoS₂ that has a higher CNT content), decomposes and oxidizes (see the DTG centred at 525 °C and the corresponding TIC). The TG residue is consistent with the amount of MoO₃ formed by MoS₂ oxidation

3.3.2.5 Raman spectroscopy analysis

For a better explanation of the thermogravimetric results three samples, obtained after three different thermogravimetric tests of OA@CNT-MoS₂, stopped respectively at 384°, 460° and 484 °C, were investigated by Raman analysis.

The samples were respectively named OA@CNT-MoS₂_TG_384, OA@CNT-MoS₂_TG_460, OA@CNT-MoS₂_TG_484. In Figure 3.24 the Raman spectra of these three samples, of CNT and the untreated OA@CNT-MoS₂, are reported for comparison.

The Raman spectrum of OA@CNT-MoS₂ (Figure 3.24 b, orange pattern) indicates that the bands of CNTs and MoS₂ are covered by those of oleylamine. This is also confirmed by the Raman spectrum of OA@CNT-MoS₂_TG_384, where the bands of CNT become visible (Figure 3.24 b, red pattern), likely due to physisorbed oleylamine removal caused by the first thermal treatment to 384°C. The bands are much more evident in the Raman spectrum of OA@CNT-MoS₂_TG_460 (Figure 3.24 c, green pattern).

A very slow scanning at very narrow pass of OA@CNT-MoS₂_TG_460, in the range 200-500°C, allows to clearly observe (Figure 3.24 d, green pattern) the Raman bands at 383 and 408 cm⁻¹, which correspond to the typical E_{12g} and A_{1g} modes of MoS₂, respectively [63-65]. E_{12g} and A_{1g} modes involve, respectively, in-layer displacements of molybdenum and sulfur atoms and out-of-layer symmetric displacements of sulphur atoms along the c axis [66-68].

After thermal treatment up to 484°C the bands of MoO₃ become prevalent [69,70], while the bands of sulfide are only just visible (Figure 3.24e, brown pattern).

3.3.2.6 Tribological characterization

As for the previous section of this chapter about the test results obtained

with inorganic nanoadditives, also for this test campaign the experimental data are referred to steady sliding tests aimed at investigating two different lubrication regimes. A normal load level of 90 N has been applied to attain an average hertzian contact pressure of 1.68 GPa.

The grease temperature has been kept constant at room level in each test. The relative motion between steel ball and disc was pure sliding at two speed levels: 5.0 mm/s and 0.50 m/s.

For each experiment, both the ball and the disk were pre-cleaned and the grease was then evenly pasted on the disk sliding path forming a layer with thickness of 2 mm at least. The test length was 60 minutes; thus, the actual sliding distances were 18 m and 1800 m for the speed of 5.0 mm/s and 0.50 m/s, respectively.

3.3.2.7 Tribological results

The results of the friction tests, performed under the operating conditions previously described in the first section of this chapter (cfr. 3.2.3) in both the investigated lubrication regimes are summarized in the Tabs. 3.13 and 3.14.

Tests were also performed to analyse the behaviour of the lubricating grease samples with regard to the wear damage of the steel ball surface. In particular, the worn surface of the steel ball has been analysed by means of an optical microscope to measure the wear scar diameter (WSD).

Both in lithium and calcium greases, the addition of OA@MoS₂-CNT (constituted essentially of MoS₂ nanosheets and few coaxial CNT-MoS₂ nanotubes coated by oleylamine) determines a reduction of friction and wear at ball-disc interface with respect to OA@Mo.

Sample	Friction coefficient in boundary lubrication [-]	Friction coefficient in mixed-EHL lubrication [-]	Difference
Ca NLGI 2	0.110	0.100	Benchmark
Ca NLGI2 at 0.1 w.t.% of OA@MoS ₂	0.094	0.092	-15% -8%
Ca NLGI2 at 0.1 w.t.% of OA@MoS ₂ -CNT	0.090	0.081	-18% -19%
Ca NLGI2 at 0.1 w.t.% of OA@CNT-MoS ₂	0.083	0.080	-25 -20%
Li NLGI 3	0.090	0.090	Benchmark
Li NLGI3 at 0.1 w.t.% of OA@MoS ₂	0.081	0.080	-10% -11%
Li NLGI3 at 0.1 w.t.% of OA@MoS ₂ -CNT	0.077	0.073	-14% -19%
Li NLGI3 at 0.1 w.t.% of OA@CNT-MoS ₂	0.071	0.069	-21% -23%

Tab. 3.13 - Friction tests results in both boundary and mixed regimes

Sample	Ball wear scar diameter [μm] Boundary Lubrication	Ball wear scar diameter [μm] Mixed-EHL test	Difference
Ca NLGI 2	820	1200	Benchmark
Ca NLGI2 at 0.1 w.t.% of OA@MoS ₂	730	940	-11% -22%
Ca NLGI2 at 0.1 w.t.% of OA@MoS ₂ -CNT	710	900	-13% -25%
Ca NLGI2 at 0.1 w.t.% of OA@CNT-MoS ₂	660	820	-20% -32%
Li NLGI 3	800	920	Benchmark
Li NLGI3 at 0.1 w.t.% of OA@MoS ₂	700	820	-13% -11%
Li NLGI3 at 0.1 w.t.% of OA@MoS ₂ -CNT	690	800	-14% -13%
Li NLGI3 at 0.1 w.t.% of OA@CNT-MoS ₂	640	720	-20% -22%

Tab. 3.14 - Wear tests results in both boundary and mixed regimes

S₂. The better performances with regard to the frictional and wear reduction are offered by the samples with 0.1 w.t. % concentration of OA@CNT-MoS₂ in both calcium and lithium base greases.

This finding clearly shows an active role of the hybrid nanoadditive OA@CNT-MoS₂, in which the inorganic core is made of coaxial CNT-MoS₂ coated by oleylamine, in the decreasing of mechanical energy loss due to the shearing motion of the grease layers and in the interaction of the nanoadditive with the tribopair rough surfaces as well. The enhanced tribological properties are probably due to the high resilience and elasticity of coaxial CNT-MoS₂ nanotubes combined with the higher volume/weight ratio of the CNTs and to the so called “mending effect”, i.e. the decreasing of the tribopair average roughness during the rubbing motion as outcome of enhanced filling of the grooves and scars of the frictional surfaces with nanoscale additives [71]. Moreover, the lithium based grease classified as NLGI3 according to the standard ASTM D 217 provides better tribological behaviour on the whole testing spectrum than the calcium based grease, NLGI2, as expected. The improved values of the frictional coefficient and wear parameter due to the addition of the nanoadditives seem to replicate the differences found by testing the original commercial samples.

REFERENCES

- [1] Aihara, S., Dowson, D., A Study of Film Thickness in Grease Lubricated EHL Contacts. Proc. of the 5th Leeds-Lyon Symposium on Tribology, ed. D. Dowson, pp. 104-115, 1979.
- [2] Poon, S., An Experimental Study of Grease in EHL. ASME, J. of Lub. Tech., vol. 94, pp. 27-34, 1972.
- [3] Boehringer, R. H., Grease, American Society of Metals Handbook, Friction, Lubrication, and Wear Technology, Scott D. Henry, Ed., ASM International, 18, 123–131, 1992.
- [4] Wilson, B., Lubricants and functional fluids from renewable sources. Industrial Lubrication and Tribology 50, 6-15, 1998.
- [5] NLGI, Lubricating Greases Guide. "National Lubricating Grease Institute." Kansas City, MO (1994).
- [6] Dyson, A., Wilson, A., Film Thickness in EHL of Roller by Greases. Proc. of the I. Mech. E, Pt 3F, vol. 184, pp. 1969-70, 1969.

-
- [7] Andrade-Ferreira, L., Grease lubrication of elastohydrodynamic contacts: a critical review, Proc. of the AITC 2002 Conference in Tribology, Salerno, Italy, CD ISBN 88-900908-0-4, 2002
- [8] Franke, E., On the influence of lubricating grease composition on the tribological behaviour of high-speed rolling bearings, thesis, University of Hanover, 1999.
- [9] Black, A.L.; Dunster, R.W.; Sanders, J.V., Comparative study of surface deposits and behaviour of MoS₂ particles and molybdenum dialkyl-dithio-phosphate, *Wear*, 1969, 13, 119.
- [10] Gansheimerand, J.; Holinsky R., A study of solid lubricants in oils and greases under boundary conditions, *Wear*, 1972, 19, 439.
- [11] Bowden, F.P.; Tabor, D., *The Friction and Lubrication of Solids*, Part II, Oxford Univ. Press, London, 1964.
- [12] Bhushan, B.; Gupta, B.K. *Handbook of Tribology*, McGraw-Hill, New York, 1991.
- [13] Watanabe, S.; Noshiro, J.; Miyake, S., Tribological characteristics of WS₂/MoS₂ solid lubricating multilayer films, *Surf. Coat. Tech.* 2004, 188–189, 644.
- [14] Joly-Pottuz, L.; Vacher, B.; Ohmae, N.; Martin, J.M.; Epicier, T., Anti-wear and friction reducing mechanisms of carbon nano-onions as lubricant additives, *Trib. Lett.* 2008, 30, 69.
- [15] Yao, Y.; Wang, X.; Guo, J.; Yang, X.; Xu, B, Effect of MoS₂ Content on Microstructures and Performances of the Self-Lubricant Coating, *Mat. Lett.* 2008, 62, 2524.
- [16] Zhao, W.; Tang, J.; Puri, A.; Sweany, R. L.; Li, Y., Tribological properties of fullerenes C₆₀ and C₇₀ microparticles, *Chen, L. J. Mat. Res.* 1996, 11, 2749.
- [17] Rosentsveig, R.; Gorodnev, A.; Feuerstein, N.; Friedman, H.; Zak, A.; Fleischer, N.; Tannous, J.; Dassenoy, F.; Tenne, R., Fullerene-like MoS₂ nanoparticles and their tribological behavior *Trib. Lett.* 2009, 36, 175.
- [18] Brown, S.; Musfeldt, J. L.; Mihut, I.; Betts, J.B.; Migliori, A.; Zak, A.; Tenne, R., Bulk vs nanoscale WS₂: finite size effects and solid-state lubrication, *Nano Lett.* 2007, 7, 2365.
- [19] Perfiliev, V.; Moshkovith, A.; Verdyan, A.; Tenne, R.; Rapoport, L.; Sedimentation of IF-WS₂ aggregates and a reproducibility of the tribological data, *Trib. Lett.* 2006, 21, 89.

- [20] Haiping, H.; Dustin, T.;Waynick, A.; Yu ,W.; Smith, P.; Roy W., Carbon nanotube grease with enhanced thermal and electrical conductivities, *J Nanopart Res* 2010 12,529.
- [21] Song, X. C.; Zheng, Y. F.; Zhao, Y.; Yin, H. Y.; Hydrothermal synthesis and characterization of CNT@ MoS₂ nanotubes, *Mat. Lett.* 2006, 60, 2346.
- [22] Bar-Sadan, M.; Tenne, R., *Inorganic Nanoparticles:Synthesis, Applications and Perspectives* (Eds C. Altavilla, E. Ciliberto) CRC press, 2011, Ch 17.
- [23] K. H.; Hu, X. G.; Xu, Y.F; Huang, F.; Liu, J.S., The effect of morphology on the tribological properties of MoS₂ in liquid paraffin, *Tribol. Lett.* 2010 , 40,155.
- [24] Ciambelli, P.; Altavilla, C.; Sarno, M.; Siraw, Y.; Petrone, V.; Senatore, A.; Nobile, M. R.; Somma, E.; Gnerre C. *NanotechItaly 2010, Int. Conference on Nanotechnology and Nanomaterials . Veneto Nanotech, Venezia, 2010, 177.*
- [25] Altavilla, C.; Ciambelli, P.; Sarno, M.; Nobile, MR.; Gnerre, C.; Somma, E.; D'Agostino, V.; Senatore, A.;V. Petrone In: *Proceedings of the 3rd European Conference on Tribology ECOTRIB 2011 and 4th Vienna Inter.Conf. on Nano-Technology VIENNANO 2011 , The Austrian Tribology Society, Vienna 2011, 903.*
- [26] Eswaraiah, V.; Sankaranarayanan, V.; Ramaprabhu, S., Functionalized Graphene–PVDF Foam Composites for EMI Shielding , *ACS Appl. Mat. & Int.* 2011, 3, 4221.
- [27] Jinshan, L.; Liwei,W.; Guohua, C., Modification of graphene platelets and their tribological properties as a lubricant additive , *Trib. Lett.* 2011, 41, 209;
- [28] Zhang et al., Synthesis and gas sensing characteristics of highly crystalline ZnO–SnO₂ core–shell nanowires *J. Phys. D: Appl. Phys.* 44, 2011,205303
- [29] Church, A.H.; Zhang, X.F.; Sirota, B.; Kohli, P.; Aouadi, S.M.; Talapatra, S., Carbon Nanotube-Based Adaptive Solid Lubricant Composites, *Adv. Sci. Lett.* 2012,5,188.
- [30] Shu, L.; Feng, Y.; Yang, X., Influence of adding carbon nanotubes and graphite to Ag-MoS₂ composites on the electrical sliding wear properties, *Acta Metall. Sin.* 2010, 23,27.

- [31] Zhang, X.; Luster, B.; Church, A.; Muratore, C.; Voevodin, A. A.; Kohli, P.; Aouadi, S.; Talapatra S., Carbon Nanotube– MoS₂ Composites as Solid Lubricants, *ACS Appl. Mater. Interfaces*, 2009, 1, 735.
- [32] Miura, K., Nanomechanics of Superlubricity, in *Encyclopedia of Nanoscience and Nanotechnology* Ed. Nalwa, Hari Singh 2004, 9, 947.
- [33] Q.; Li, J.; Synthesis and Electrochemical Performance of Graphene-like WS₂, *J. Phys. Chem. C* 2007, 111, 1675.
- [34] Shujiang, D. ; Song, C. J. ; Wen, L. X., PVP-assisted synthesis of MoS₂ nanosheets with improved lithium storage properties, *Chem.-A Eu. J.* 2011, 17, 13142.
- [35] Jeong-Hui, K. ; Hyo-Jun, A. ; Min-Sang, J. ; Ki-Won, K. ; In-Shup, A.; Jou-Hyeon, A.; Guoxiu, W. ; Ho-Suk R., The electrochemical properties of Li/TEGDME/MoS₂ cells using multi-wall carbon nanotubes as a conducting agent, *Res. Chem. Inter.* 2010, 36 749.
- [36] Laursen , A.B. ; Kegnæs ,S.; Dahl, S.; Chorkendorff , I., Molybdenum sulfides—efficient and viable materials for electro- and photoelectrocatalytic hydrogen evolution , *Energy Environ. Sci.* 2012, 5, 5577
- [37] Li, J.; Bai, T., The effect of CNT modification on the mechanical properties of polyimide composites with and without MoS₂, *Mech. Comp. Mat.*, 2011, 47, 597.
- [38] Levy, M.; Albu-Yaron, A.; Tenne, R.; Feuermann, D.; Katz, E.A.; Babai, D.; Gordon, J., Synthesis of Inorganic Fullerene-like Nanostructures by Concentrated Solar and Artificial Light/Synthesis and Characterization of Nanoparticles, Nanotubes, Nanopans, and Graphene-like Structures of Boron Nitride, *Israel J.Chem.* 2010, 50, 417.
- [39] Song, X.C.; Zheng, Y. F.; Zhao, Y.; Yin, H. Y.; "Hydrothermal synthesis and characterization of CNT@ MoS₂ nanotubes *Mat. Lett.* 2006, 60, 2346.
- [40] Ma, L.; Chen, W.-X.; Xu, Z.-D.; Xia, J.B.; Li, X.; Carbon nanotubes coated with tubular MoS₂ layers prepared by hydrothermal reaction, *Nanotechnology*, 2006, 17, 571.
- [41] Koroteev, V.O.; Okotrub, A.; Yu., V.; Mironov, V.; Abrosimov, O.G. ; Shubin, Yu., V. Bulusheva, L.G., Growth of MoS₂ layers on the

- surface of multiwalled carbon nanotubes, *Inorganic Materials*, 2007, 43, 236
- [42] Altavilla, C.; Sarno, M.; Ciambelli, P., A Novel Wet Chemistry Approach for the Synthesis of Hybrid 2D Free-Floating Single or Multilayer Nanosheets of MS2@ oleylamine (M□ Mo, W), *Chem. Mat.* 2011, 23, 3879.
- [43] Altavilla, C.; Sarno, M.; Ciambelli, P. *PCT Int. Appl.*, " one pot" synthesis of 2d, 1d, and 0d nano crystals of tungsten and molybdenum chalcogenides (ws2, mos2) functionalized with long chain amine and/or carboxylic acid and/or thiol, WO 2012042511A1 20120405, 2012.
- [44] Sarno, M.; Sannino, D.; Leone, C.; Ciambelli, P., Evaluating the effects of operating conditions on the quantity, quality and catalyzed growth mechanisms of CNTs, *J. Mol. Catalysis A: Chem.* 2012, 357, 26.
- [45] Sarno, M.; Cirillo, C.; Piscitelli, R.; Ciambelli, P., A study of the key parameters, including the crucial role of H2 for uniform graphene growth on Ni foil, *J. Mol. Catalysis A: Chem.* 2013, 366, 303.
- [46] Altavilla, C.; Sarno, M.; Ciambelli, P., A Novel Wet Chemistry Approach for the Synthesis of Hybrid 2D Free-Floating Single or Multilayer Nanosheets of MS2@ oleylamine (M□ Mo, W), *Chem. Mat.* 2009, 21, 4851.
- [47] Ciambelli, P.; Sannino, D.; Sarno, M.; Leone, C., Wide characterisation to compare conventional and highly effective microwave purification and functionalization of multi-wall carbon nanotubes, *Thin Sol. Films* 2011, 519, 2121.
- [48] Di Bartolomeo, A.; Sarno, M.; Giubileo, F.; Altavilla, C.; Iemmo, L. ; Piano, S.; Bobba, F. ; Longobardi, M.; Scarfato, A.; Sannino, D.; Cucolo, A. M.; Ciambelli, P., Multiwalled carbon nanotube films as small-sized temperature sensors, *J. Appl. Phys.* 2009, 105, 064518/1.
- [49] Ciambelli, P.; Sannino, D.; Sarno, M. ; Fonseca, A.; Nagy, J.B.; Selective formation of carbon nanotubes over Co-modified beta zeolite by CCVD, *Carbon* 2005, 43, 631.
- [50] Altavilla, C.; Bobba, F.; Ciambelli, P.; Cucolo, A.M.; Di Bartolomeo, A.; Giubileo, F.; Piano, S.; Sannino, D.; Sarno, M.; Scarfato, A. , Multiwalled carbon nanotube films as small-sized temperature sensors, *PCT Int. Appl.* (2010), WO 2010016024 A1 20100211.

- [51] Di Bartolomeo, A.; Sarno, M.; Giubileo, F.; Altavilla, C.; Iemmo, L. ; Piano, S.; Bobba, F. ; Longobardi, M.; Scarfato, A.; Sannino, D.; Cucolo, A. M.; Field emission properties of as-grown multiwalled carbon nanotube films, Ciambelli, in NSTI Nanotech, Nanotechnology Conference and Trade Show, Technical Proceedings, Boston, MA, USA, June 1-5, 2008, 1, 112.
- [52] Greenberg, R.; Halperin, G.; Etsion, I.; Tenne, R., Friction mechanism of individual multilayered nanoparticles, *Tribol. Lett.* 2004, 17, 179.
- [53] Kalin, M.; Velkavrh, I.; Vizintin, J., The Stribeck curve and lubrication design for non-fully wetted surfaces, *Wear* 2009, 267, 1232.
- [54] Rao, C. N. R., Nag, A., Inorganic analogues of graphene, *Eur. J. Inorg. Chem.* 2010, 27, 4244.
- [55] Matte, H. S. S. R.; Gomathi, A.; Manna A. K.; Late, D.; Datta, R.; Pati, S.K.; Rao, C. N., Unusual magnetic properties of graphene and related materials, *Chem.* 2010, 122, 4153.
- [56] , E.; Santa Ana ; Mendizabal, F.; Gonzalez, G. Intercalation chemistry of molybdenum disulfide, *Coord. Chem. Rev.* 2002, 224, 87.
- [57] Tzitziosa, V.; Georgakilas, V.; Oikonomou, E.; Karakassides, M.; Petridis, D., Synthesis and characterization of carbon nanotube/metal nanoparticle composites well dispersed in organic media, *Carbon* 2006, 44, 848.
- [58] Li, X.; Thompson, J. D.; Zhang, Y.; Brady, C. I.; Zou, G.; Williams, D.; Duque, J. G.; Jia, Q.; Doorn S.K., Efficient synthesis of tailored magnetic carbon nanotubes via a noncovalent chemical route, *Nanoscale*, 2011, 3, 668.
- [59] Vermisoglou, E.C.; Georgakilas, V.; Kouvelos, E.; Pilatos, G.; Viras, K.; Romanos, G.; Kanellopoulos, N.K., Sorption properties of modified single-walled carbon nanotubes , *Microp. Mes. Mat.* 2007, 99, 98.
- [60] Yu,W. ; Huaqing, X. ; Xinwei,W. ; Xiaoping,W. Highly efficient method for preparing homogeneous and stable colloids containing graphene oxide , *Nanoscale Res Lett* 2011, 6, 47.
- [61] Frey, G. L.; Tenne, R.; Matthews, M. J.; Dresselhaus, M. S.; Dresselhaus, G., Raman and resonance Raman investigation of MoS₂ nanoparticles *Physical Rev B* 1999, 60, 2883.

- [62] Lee, C.; Yan, H.; Brus, L. E.; Heinz, T. F.; Hone, J.; Ryu, S., Anomalous lattice vibrations of single-and few-layer MoS₂, *ACS Nano* 2010, 4, 2695.
- [63] Yan, B.; Zheng, Z.; Zhang, J.; Gong, H.; Shen, Z.; Huang, W.; Yu, T., Orientation Controllable Growth of MoO₃ Nanoflakes: Micro-Raman, Field Emission, and Birefringence Properties, *J. Phys. Chem. C* 2009, 113, 20259.
- [64] Liu, G.; Li, X.; Qin, B.; Xing, D.; Guo, Y.; Fan, R., WS₂ nanorods prepared by self-transformation process and their tribological properties as additive in base oil, *Tribol. Lett.* 2004, 17, 961.
- [65] Joly-Pottuz L., Bucholz E. W., Matsumoto N., Phillipot S. R., Sinnott S. B., Ohmae N., Martin J. M., Friction Properties of Carbon Nano-Onions from Experiment and Computer Simulations, *Tribology Letters*, 37(1), 75-81, 2010.
- [66] Tevet O., Goldbart O., Cohen S., Rosentsveig R., Popovitz-Biro R., Wagner H., Tenne R., Nanocompression of individual multilayered polyhedral nanoparticles, *Nanotechnology*, 21, 365705, 2010.
- [67] O. Tevet, P. Von-Huth, R. Popovitz-Biro, R. Rosentsveig, H.D. Wagner, R. Tenne, Friction mechanism of individual multilayered nanoparticles, *Proceedings of the National Academy of Sciences*, 108, 19901-19906, 2011.
- [68] Pottuz L.J., Dassenoy F., Belin M., Vacher B., Martina J.M., Fleischer N., Ultralow-friction and wear properties of IF-WS₂ under boundary lubrication, *Tribol. Lett.* 18, 477-485, 2005.
- [69] Yadgarov L., Petrone V., Rosentsveig R., Feldman Y., Tenne R., Senatore A., Tribological studies of rhenium doped fullerene-like MoS₂ nanoparticles in boundary, mixed and elasto-hydrodynamic lubrication conditions, 297, 1-2, 15, 1103-1110, *Wear*, 2013.
- [70] Seifert G., Terrones H., Terrones M., Jungnickel G., Frauenheim T., Structure and Electronic Properties of MoS₂ Nanotubes, *Phys. Rev. Lett.*, 85, 146-149, 2000.
- [71] Derjaguin B., Smilga V., Electrostatic component of the rolling friction force moment, *Wear*, 7, 270-281, 1964.

CHAPTER 4

Modeling Elastohydrodynamic lubrication: Piezoviscosity and surface roughness

4.1 Introduction

Elastohydrodynamic Lubrication, hereinafter referred to as EHL, is a topic which is concerned with understanding and modeling lubrication problems in which solid metal surfaces deform under large loads. The range of scales in EHL problems is great. Applied loads cause pressure distributions across the contact of the order of Giga-Pascals, minimum film thickness are in the micrometer range, and lubricant molecules pass through the contact in a hundredth of a second. This illustrates how difficult it is to conduct physical experiments into the behavior of EHL contacts.

It is now the case that research into EHL problems involves a combination of experiments and numerical simulations.

In this chapter, a model for the characterization of the elastohydrodynamic lubrication is proposed. The aim of this numerical approach is to investigate the effects of different piezoviscous lubricant behavior on the EHL results. In particular, the application of the free-volume viscosity model in a Newtonian elastohydrodynamic line and point contact simulation is presented. According to recent experimental studies using high pressure viscometers, the free volume-based pressure-viscosity relationship closely represents the realistic piezo-viscous behavior for the high pressure typically encountered in elastohydrodynamic applications [1]. The effects of different pressure-viscosity relationships, including the exponential model, the Roelands

model, and the free-volume model are investigated through simulations with poly-alpha-olefin lubricant.

To solve the problem, a full multigrid approach, showed in Venner et al. [2] has been used upon the assumptions of isothermal condition for the EHL point contact problem. Multigrid is more effective because it uses coarser grid levels to remove errors of different frequencies, which could be more quickly smoothed away than those on simply the fine grid alone. Moreover, in the second section of this chapter the numerical solution of elastohydrodynamic lubrication (EHL) contact between two rough surface cylinders is presented. Random rough surfaces with Gaussian and exponential statistics have been generated using a method outlined by Garcia and Stoll [3], where an uncorrelated distribution of surface points using a random number generator is convolved with a Gaussian filter to achieve correlation. This convolution is most efficiently performed using the discrete Fast Fourier Transform (FFT) algorithm, which in MATLAB is based on the FFTW library [4]. The maximum pressure and average film thickness are studied at different values of RMS, skewness, kurtosis, autocorrelation function and correlation length.

4.2 HISTORY OF EHL RESEARCH

All work in fluid film lubrication can be traced back to the 1880s, when a combination of experiments was followed by a unifying mathematical theory. In 1886 Osborne Reynolds [5] formulated equations derived from the Navier-Stokes equations, to describe the pressure distribution for an applied load on a given geometry, relating the pressure to the speed of the moving surfaces. This work was itself an attempt to explain the results of the experimental work of Beauchamp Tower [6,7] which was the first to detect high pressures in the lubricant film. This pressure variation was also the conclusion of Nicoli Petrov [8], after he had conducted friction experiments on railway axle bearings, at about the same time.

Despite initial success in the application of the Reynolds Equation to the design of journal bearings, e.g. [9], the case of trying to model lubrication in gears caused problems. Martin [10] considered an isoviscous lubricant between two smooth rigid cylinders, representing the gear teeth. A relationship between the operating conditions and the minimum lubricant film thickness was obtained. However, applying

known physical values into the formula, a film thickness of $0.01 \mu\text{m}$ was predicted, which was significantly less than the known surface roughness of gears at around $0.4\text{--}0.8 \mu\text{m}$. This, therefore, meant that there must have been other factors involved in the near wearless operation of gears than simply the model developed thus far.

This impasse was not resolved quickly. For over 30 years, two possible themes were investigated into what the missing link could be. It was assumed to be either due to the elastic deformation of the solids, or due to the viscosity-pressure characteristics of the lubricant. Work was carried out independently on each of these ideas. Deformation was shown to have some effect, e.g. [11], but the simultaneous calculation of both elasticity and hydrodynamic equations was too complex for a numerical problem at that time. The viscosity-pressure work, e.g. [12] also produced larger film thickness values than those predicted by Martin, but still not nearly enough to obtain numerical results consistent with experiments. The work of Ertel [13] and Grubin [14,15] combined the analytical solution of the deformation of a dry contact [16] with the viscosity-pressure effects calculated using the exponential viscosity-pressure relation of Barus [17], Figures 4.1 a and b.

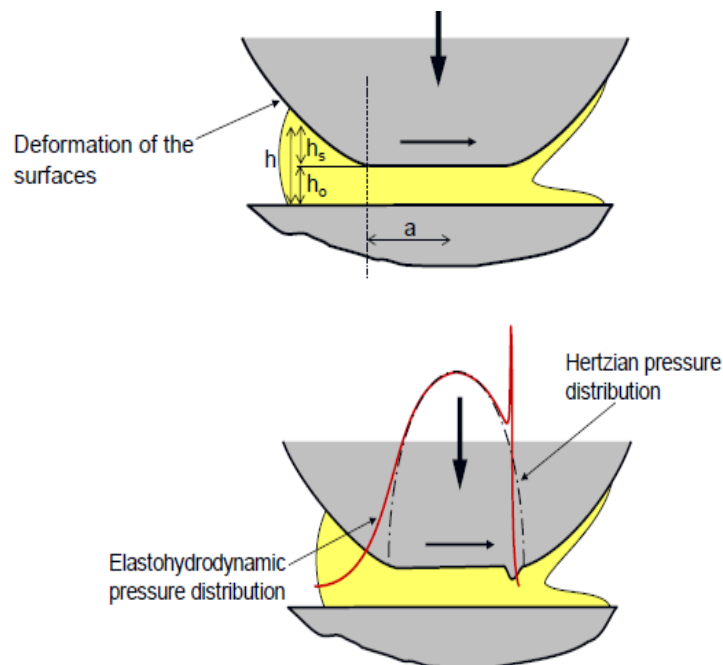


Fig. 4.1- (a) Elastohydrodynamic contact and (b) pressure distribution in the meatus

The minimum film thickness formula obtained was only valid in a very limited parameter region, but this was the most major advance since the formulation of the Reynolds equation.

The first solution of the full numerical line contact elastohydrodynamic lubrication problem was presented by Petrusevich in 1951 [18]. This work also used the Barus viscosity-pressure relation, although only three solutions were obtained. It was also the first to show what has since become known as the *Petrusevich pressure spike*, itself an important factor in the development of subsurface stresses and on the life of rolling contacts [19]. The Petrusevich spike is shown in Figures 4.2 and 4.3 where the typical features of an EHL contact are shown. Lubricant entrainment is from left to right, and the inlet is assumed to be fully flooded.

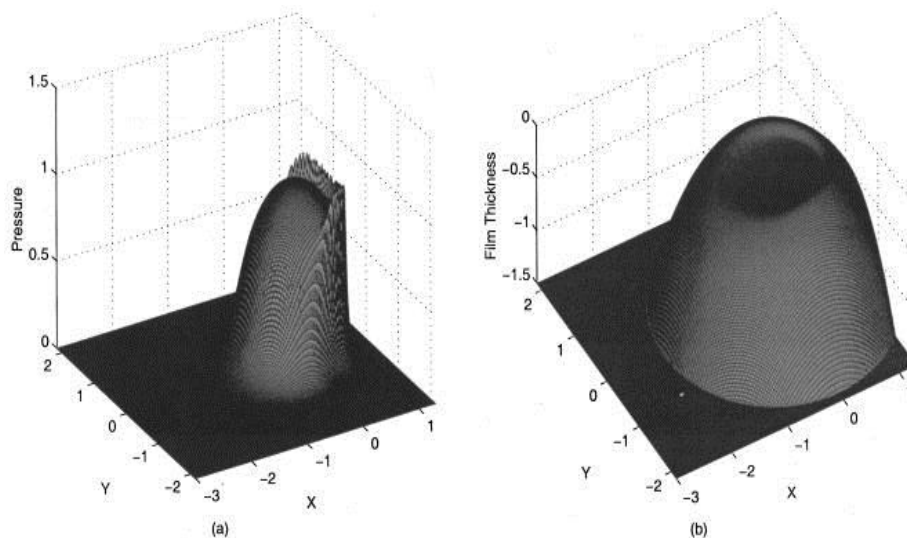


Fig. 4.2 – (a) Pressure profile and (b) Film thickness profile in the case of pure rolling for an EHL point contact problem. [Y.S. Kang, X. Ai, F. Sadeghi, “Debris Effects on EHL Contact”, *J. Tribol.*, vol. 122, 4, pp. 711-720, 2000]

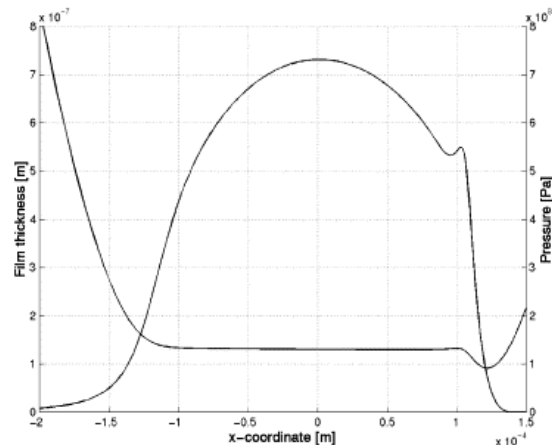


Fig. 4.3 - Film thickness and pressure distribution along the contact in the case of pure rolling for an EHL line contact problem. [T. Almqvist, R. Larsson, “*The Navier–Stokes approach for thermal EHL line contact solutions*”, *Tribol. Int.*, vol.35, 3, pp. 163–170, 2002]

In the center of the contact, known as the *contact region*, there is a near Hertzian pressure profile, with the pressure spike towards the outflow. From the end of the contact region the pressure solution is zero in what is known as the *cavitation region*. This is where the lubricant film is no longer contiguous; bubbles of air at (near) ambient pressure are present in the oil film, as can be seen in the experimental results shown in Figure 4.3. In terms of the geometry of the surfaces, it can be clearly seen that in the elastohydrodynamically lubricated case the parabolic shape on the contact has been deformed. The roller has flattened out across the contact area, with a constriction present in the outflow where the pressure drops steeply.

With the computing power available at that time, obtaining numerical solutions to the two dimensional point contact EHL problem was simply not possible due to the added mathematical difficulties involved. In the mid-1960s two attempts had been made using the Grubin approach [14,20], but full solutions did not appear until the 1970s. Ranger *et al.* concluded their 1975 solution paper [21] by indicating that the two limitations on obtaining solutions were the “computer capacity” available, and the “ignorance of the relationship between pressure, viscosity and density”. The effect of ellipticity in the point contact was investigated by Hamrock and Dowson [22–24], in which expressions for central and

minimum film thickness were developed. These were found to be in reasonable agreement with experimental results.

In point contacts the minimum film thickness is not found on the centerline but on each of the two *sidelobes* which develop to form a horseshoe shape, as showed in Figure 4.1b. This is characteristic of point contact EHL problems. It can be seen that away from the center of the contact the film shape is undeformed from the original parabolic profile. Inside the center of the contact, the large flat central region is again visible, with the horseshoe replacing the film thickness dip of the line contact case. Once the ability to solve two dimensional EHL problems had been established, attention returned to the models of the lubricant used.

As the EHL is a typical regime of lubrication characterized by high contact pressures, a good and accurate prediction of the EHL behavior, in several applications, requires consideration of the constitutive equation for the lubricant, [25–26]. Actually, the EHL has two primary aspects: the increase of viscosity with pressure, and the elastic deformation, caused by high pressure, which is comparable to that of the film thickness. Due to the high pressure and the limited contact area, elastic deformation of the surfaces will occur, which is not negligible; the pressure dependence of viscosity as well plays a crucial role in EHL simulation because the viscosity at the inlet has crucial influence on film formation. For this reason, an accurate prediction of the EHL parameters under a given set of operating conditions requires knowledge in lubricant rheology.

The rheology of liquid lubricants in the Hertzian zone of concentrated contacts has been of principal interest to tribologists in the past few years. In particular, for applications involving lubricants that exhibit shear-thinning behavior, the use of an appropriate pressure–viscosity relationship for the lubricant is required to predict the EHL behavior more accurately. In the light of the above facts, while conducting an EHL simulation, the real pressure–viscosity behavior of the lubricants should not be overlooked.

Nowadays, probably the most established viscosity model used is that of Roelands [27], a more complicated version of the Barus equation. All models used must only be expected to be accurate within certain parameter ranges, because the number of variables required for modeling real life lubricants is far too large to try to model all fluids with one

simple equation. This is especially true when using non-Newtonian lubricant models.

This subject is considered in detail by Petrie [28]. Fluid memory is the idea that a fluid's behavior at any moment is not just related to the conditions it is experiencing at that moment, but also to its previous states. The choice of rheological model to use is very much fluid dependent. Many fluids are Newtonian in their characteristics, whilst the behavior of others varies dramatically with the operating conditions. The simplest elastic non-Newtonian models include those of Maxwell [29] and Oldroyd [30], the latter of which includes shear thinning.

Actually, neither Roelands nor Barus relationship successfully models the piezo-viscous behavior of the lubricant at typical EHL pressures. For this reason, the Doolittle model has been introduced. Doolittle [31] developed the first free-volume model based on a physical meaning which holds that the resistance to flow in a liquid depends upon the relative volume of molecules present per unit of free volume in order to obtain a better modeling of the lubricant rheology. Using an exponential function, Doolittle related viscosity to the fractional free volume [32–34].

Furthermore, in the second part of the chapter, the effect of surface roughness has been investigated. Actually, the components used in engines and machinery are real surfaces which have not been specially prepared before each use, and therefore are not perfectly smooth. This may not be a great revelation, knowing that the roughness of the gears in Martin's work [10] was known to be larger than the minimum hydrodynamic film thickness predicted, however the ability to model rough contacts is now growing in importance. Applications, such as computer hard drives, are continuously reducing the lubricant film width, and hence the effect of surface asperities is becoming more important in estimating the life of components.

In cases where the surface roughness is of at least the same magnitude as the elastohydrodynamic film thickness, then it is well known that the components may operate as though lubricated with a fluid film. This is because the surface roughness will generate pressures great enough to flatten the asperities to leaving only smooth ripples on the surface. This is known as *micro-elastohydrodynamic lubrication*. Accurately measuring surface roughness is a topic which is both limited and defined by the accuracy of the measuring equipment. Today, it is the

effective roughness that is being investigated. Work by Venner *et al.* [35-37], Chang *et al.* [38,39], Ai and Cheng [40] and Hooke [41], investigated line contact problems with either ridges or waviness patterns passing through the contact. The effect of different slide to roll ratios was also investigated. Point contact cases with dents, ridges, and/or waviness patterns, were solved initially in steady state by Lubrecht *et al.* [42], but more importantly for transient analyses by Venner and Lubrecht [43] and Ehret *et al.* [44]. As with all simulations of real life phenomena it is important to ensure that the assumptions made in the models are valid when compared to experimental results. Comparisons against the experimental work of Kaneta *et al.* [45-47] have been done in some of the work mentioned above.

4.3 THEORETICAL MODEL

The EHL lubrication theory is based mainly on three equations: the Reynolds equation [5], the film thickness equation and the load balance equation. The Reynolds equation describes the relation between the pressure in the lubricant film as a function of the geometry of the gap and the velocities of the running surfaces. The film thickness equation presents the elastic deformation of the surfaces caused by the pressure, which describes the deformed geometry of the gap. Finally, the force balance equation states that the integral of the pressure in the film should be such that it balances the applied load.

The equations described above will be presented in the first few sections of this chapter. They will be non-dimensionalised, using Hertzian [48] parameters. Before any numerical results of EHL problems can be calculated, it is necessary to discretize the equations.

4.3.1 Solution Domain

The circular point contact EHL problem can be considered as that of a spherical bearing on a plane, as shown in Figure 4.4. Coordinate axes directions are taken as shown, with the origin taken to be the point on the plane closest to the center of the ball. The convention taken throughout this work will be that surface 1 refers to the ball, and surface 2 to the plane. This is only important in cases of sliding. This is when the speeds

of the two surfaces differ. Lubricant entrainment is taken as parallel to the x -axis in the x - y plane. The z -direction is one of the primary variables in the calculation, since it represents the geometry of the contact, h . There is assumed to be no variation of lubricant properties in this direction for the cases considered here. This is because the pressure gradient across the film in the z direction can be shown to be of the order of h/l and $h \ll l$, where l is the representative length of the contact [49]. If a viscoelastic model was employed then these gradients could be significant and would also have to be taken into account, hence a modified Reynolds Equation would have to be used. The contact being represented need not necessarily be a ball and plate, however it is possible to reduce the real geometry to this arrangement. Throughout the rest of this chapter the word *reduced* will be taken to mean ‘the quantity obtained when the geometry is transformed to the ball and plane scenario’. This will be applied to both the ‘reduced radius’ of the ball considered as well as the combined physical properties of the surfaces and loading conditions. Inside the contact area the undeformed geometry of the ball will be taken as parabolic in both x and y directions. Since only circular, rather than elliptical, contacts are being considered then this geometry will be axially symmetric about the z -axis. The EHL line contact problem can be treated almost in the same way of the point contact, but considering a cylinder rolling on a plane, i.e. a one dimension problem.

4.3.2 The Reynolds Equation

The differential equation governing pressure distribution in a Newtonian lubricant film was first obtained by Reynolds [5] and it can be derived from the Navier-Stokes equations by taking into account some simplifying assumptions at appropriate points in the analysis. These are [50]:

1. Body forces are negligible
2. Pressure is constant through the film in z direction
3. No slip at the boundary surfaces
4. Lubricant flow is laminar
5. Inertia and surface tension forces are negligible compared with viscous forces

- 6. Shear stress and velocity gradients are only significant across the lubricant film (z direction)
- 7. Lubricant is Newtonian
- 8. The lubricant viscosity and the fluid density are constant across the film (z direction)
- 9. The lubricant boundary surfaces are parallel or at small angle with respect to each other

Consider a fluid between two parallel plates where h is the surface separation, $p = f(x, y, h, \mu, u_1, u_2, v_1, v_2, w_1, w_2)$ is the fluid pressure, μ is the dynamic viscosity of the lubricant film and u, v, w are the velocities of the surfaces in the x, y and z -directions. Figure 4.4 illustrates two generalized surfaces in relative motion.

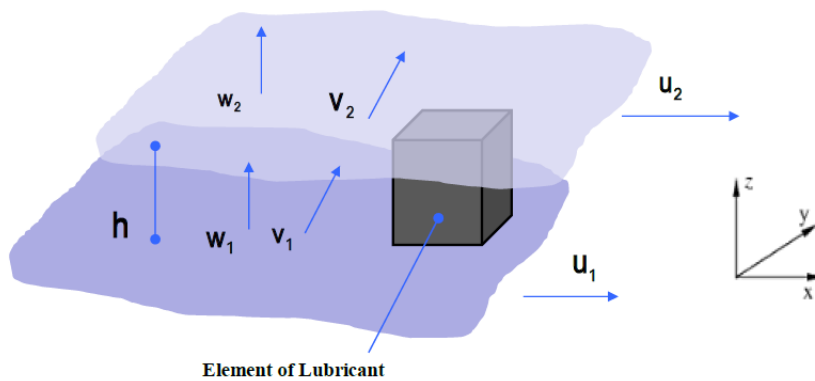


Fig. 4.4 - Two surfaces in relative motion

The derivations of Reynolds equation can start either by applying the above stated simplifying assumptions to Navier-Stokes equations, or by writing the dynamic equilibrium of an element of volume from the fluid.

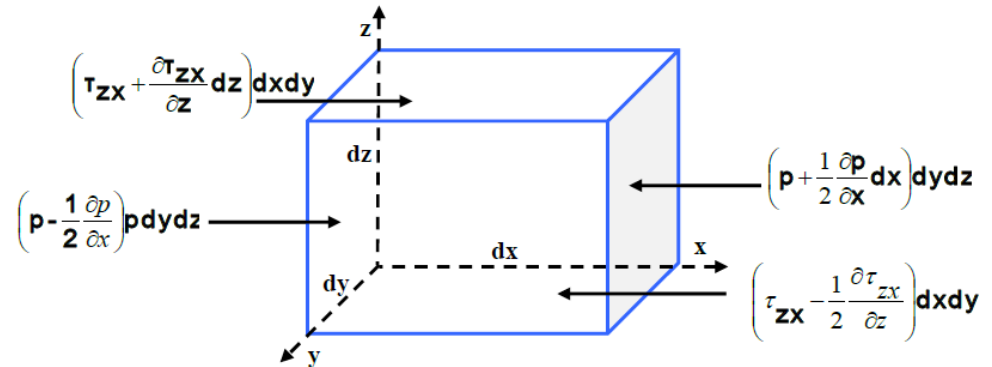


Fig. 4.5 - Forces on an element

Consider a small element of fluid from a hydrodynamic film (Figure 4.5). In this case the forces of the element are acting only in the x direction. The balance of forces in x direction yields:

$$\frac{\partial \tau_{zx}}{\partial z} = \frac{\partial p}{\partial x} \quad (4.1)$$

Similarly in the y direction,

$$\frac{\partial \tau_{zy}}{\partial z} = \frac{\partial p}{\partial y} \quad (4.2)$$

According to the second assumption, since the pressure is constant through the film in the z direction the pressure gradient is equal to zero

$$\frac{\partial p}{\partial z} = 0 \quad (4.3)$$

Considering the fluid as Newton's the shear stress is directly proportional to the shear strain with the factor of proportionality the viscosity μ :

$$\tau_{zx} = \mu \frac{u}{h} = \mu \frac{\partial u}{\partial z} \quad (4.4)$$

where: τ_{zx} is the shear stress acting in the 'x' direction [Pa]

Furthermore the velocity in the y direction is different and consequently the shear stress is different:

$$\tau_{zy} = \mu \frac{v}{h} = \mu \frac{\partial v}{\partial z} \quad (4.5)$$

where: τ_{zy} is the shear stress acting in the 'y' direction [Pa] and v : is the sliding velocity in the 'y' direction [m/s].

Combine equations (4.1) and (4.4) and equations (4.3) and (4.5), the equilibrium conditions for the forces acting in the 'x' and 'y' directions can be obtained:

$$\frac{\partial p}{\partial x} = \frac{\partial}{\partial z} \left(\mu \frac{\partial u}{\partial z} \right) \quad (4.6)$$

$$\frac{\partial p}{\partial y} = \frac{\partial}{\partial z} \left(\mu \frac{\partial v}{\partial z} \right)$$

Now by integrating the above formulas (4.6) twice and taking into account assumption 3, the velocities through the film thickness, for both x and y direction become:

$$u = \left(\frac{z^2 - zh}{2\mu} \right) \frac{\partial p}{\partial x} + (U_1 - U_2) \frac{z}{h} + U_2 \quad (4.7)$$

$$v = \left(\frac{z^2 - zh}{2\mu} \right) \frac{\partial p}{\partial y} + (V_1 - V_2) \frac{z}{h} + V_2$$

If we apply the condition of continuity of flow to a column h , Figure 4.6, and following assumption 3, the volume flow rates per unit width in the x and y direction can be defined as:

$$q_x = \rho \int_0^h u dz \quad \text{and} \quad q_y = \rho \int_0^h v dz \quad (4.8)$$

where ρ denotes the density.

Choosing lubricant flow parallel to the x -axis, assuming no flow velocity variation across the contact for the steady state case, the Equation (4.10) may be rewritten as:

$$\frac{\partial}{\partial x} \left(\frac{\rho h^3}{12\eta} \frac{\partial p}{\partial x} \right) + \frac{\partial}{\partial y} \left(\frac{\rho h^3}{12\eta} \frac{\partial p}{\partial y} \right) - 6u_s \frac{\partial(\rho h)}{\partial x} = 0 \quad (4.10)$$

where the entrainment velocity, u_s is defined by $u_s = u_1 + u_2$.

This equation is referred to as having three different parts. The first two terms involving the second derivatives of pressure are called the *Poiseuille* terms. The *wedge* term is the other spatial derivative whilst the *squeeze* term is the temporal derivative. The Reynolds Equation has no in-built concept of giving physical solutions for pressure, and hence in much of the region beyond the center of the contact, it will be satisfied by negative solutions of pressure. In actuality, at the point of the outflow where this occurs, air pockets will have been formed in the lubricant.

4.3.3 The Film Thickness Equation

The Reynolds equation can be used to solve the pressure in the gap when its geometry is known. In order to determine the shape of the film gap, a relation describing the elastic deformation of the surface by the pressure is required. The film thickness equation, describing the distance between the two contacting surfaces, consists of two components, the gap between the undeformed surfaces and the elastic deformation of the surfaces.

This deformation is therefore dependent on the pressure applied; more particularly, the pressure distribution across the whole contact. This, therefore, is very dependent on the type of contact being modeled.

4.3.3.1 Line contact

The equation describing the film shape in a line contact situation reads:

$$h(x) = h_0 + \frac{x^2}{2R} + d(x) \quad (4.11)$$

where:

R: the reduced radius of curvature: $1/R = 1/R_1 + 1/R_2$

h_0 : constant

$d(x)$: elastic deformation

The elastic deformation $d(x)$ can be calculated according to Timoshenko and Goodier [51] as:

$$d(x) = -\frac{4}{\pi E'} \int_{-\infty}^{\infty} \ln \left| \frac{x-x'}{x_0} \right| p(x') dx' \quad (4.12)$$

where E' is the reduced elastic modulus.

The reduced elastic modulus is defined as:

$$\frac{2}{E'} = \frac{1-\nu_1^2}{E_1} + \frac{1-\nu_2^2}{E_2} \quad (4.13)$$

where E_1 and E_2 are the elastic moduli and ν_1 and ν_2 the Poisson's ratio of surfaces 1 and 2, respectively.

4.3.3.2 Point contact

The film thickness equation for point contact can be written as:

$$h(x, y) = h_0 + \frac{x^2}{2R_x} + \frac{y^2}{2R_y} + d(x, y) \quad (4.14)$$

where:

R_x is the reduced radius of curvature in the x-direction:

$$\frac{1}{R_x} = \frac{1}{R_{1x}} + \frac{1}{R_{2x}} \quad (4.15)$$

R_y is the reduced radius of curvature in the y-direction:

$$\frac{1}{R_y} = \frac{1}{R_{1y}} + \frac{1}{R_{2y}} \quad (4.16)$$

h_0 is a constant and $d(x,y)$ is the elastic deformation, Figure 4.7, which can be calculated according to Love [47] as:

$$d(x, y) = \frac{2}{\pi E'} \int_{-\infty}^{\infty} \int_{-\infty}^{\infty} \frac{p(x', y') dx' dy'}{\sqrt{((x-x')^2 + (y-y')^2)}} \quad (4.17)$$

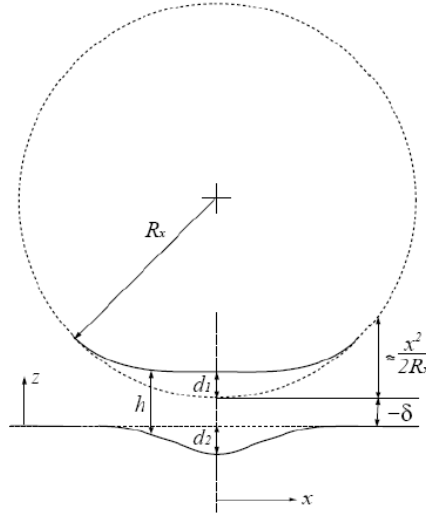


Fig. 4.7 - Geometry of the gap in an EHL point contact for $y=0$

4.3.4 The load balance equation

An equation is also needed to make sure that the load and the pressure in the contact are in equilibrium. This equation is usually called the force balance equation. Hence, the integral over the pressure in the film will give the applied load. For 1D problem, it reads:

$$\int_{\Omega} p(x) dx = w \quad (4.18)$$

For the point contact we have:

$$\iint_{\Omega} p(x, y) dx dy = P \quad (4.19)$$

4.3.5 Dimensionless Equations

For isothermal EHL problems the system of dimensional equations to be solved is defined by equations (4.10), (4.11 or 4.14), (4.18 or 4.19). The orders of numbers in these equations vary from $O(10^9)$ for the pressure, down to $O(10^{-8})$ for the minimum film thickness.

To numerically compute solutions, without incurring artifacts from the floating point arithmetic of the computer used, non-dimensionalisation is highly advisable.

In the process of non-dimensionalisation, dimensionless quantities may also be computed. These values are commonly used to characterize the individual case being studied.

The first parameters to be introduced are the *maximum Hertzian pressure*, and the *Hertzian radius*, which are derived from Hertz's theory for dry contacts [52]. This assumes a pressure distribution, for the line contact EHL problem, of:

$$p(x, y) = \begin{cases} p_h \sqrt{1 - \frac{x^2}{a}} & -a < x < a. \\ 0 & \text{otherwise.} \end{cases} \quad (4.20)$$

While for the point contact formulation the pressure distribution is given by

$$p(x, y) = \begin{cases} p_h \sqrt{1 - \frac{x^2}{a} - \frac{y^2}{a}} & |x^2 + y^2| < a. \\ 0 & \text{otherwise.} \end{cases} \quad (4.21)$$

The contact has been assumed to be circular rather than generally elliptical, i.e. $R_x = R_y$.

The maximum Hertzian pressure is given by:

$$p_h = \begin{cases} \text{Point contact} & \left\{ \frac{3W}{2\pi a^2} \right. \\ \text{Line contact} & \left. 1.27 \frac{W}{2aB} \right\} \quad (4.22)$$

and the Hertzian radius, a , by (if the materials are the same for both the surfaces)

$$\begin{array}{l}
 \text{Point contact} \\
 \text{Line contact}
 \end{array}
 a = \begin{cases} 1.1093 \sqrt{\frac{WR_x}{E'}} \\ 0.797 \sqrt{\frac{WR_x}{E'B}} \end{cases} \quad (4.23)$$

Assuming that a viscosity-pressure and density-pressure equations are used the dimensional equations given above feature 8 parameters, u_m , $\rho_0, \alpha, R_x, R_y, E'$ and w . This implies that the minimum film thickness or the central film thickness are a function of these 8 parameters. However, these parameters are not all independent. To reduce the number of independent parameters, dimensionless variables can be introduced. An optimal choice is the set of dimensionless variables that reduces the number of parameters to a minimum. This is for example the case if the equations are made dimensionless using the Hertzian dry contact parameters, and the viscosity and density at ambient pressure. For the circular contact ($R_x=R_y$) the dimensionless variables are defined as:

$$\begin{array}{ll}
 X = \frac{x}{a} & Y = \frac{y}{a} \\
 P = \frac{p}{p_h} & H = hR_x/a^2 \\
 \bar{\eta} = \frac{\eta}{\eta_0} & \bar{\rho} = \rho/\rho_0
 \end{array} \quad (4.24)$$

Substitution in Equation (4.11) gives:

$$\frac{\partial}{\partial X} \left(\xi \frac{\partial P}{\partial X} \right) + \frac{\partial}{\partial Y} \left(\xi \frac{\partial P}{\partial Y} \right) - \frac{\partial}{\partial X} (\bar{\rho} H) = 0 \quad (4.25)$$

For $X \in [X_a, X_b]$ and $Y \in [-Y_a, Y_a]$

where:

$$\xi = \frac{\bar{\rho} H^3}{\eta \lambda} \quad (4.26)$$

and

$$\bar{\lambda} = \frac{12u_m \eta_0 R_x^2}{a^3 p_h} \quad (4.19)$$

The boundary conditions are $P(X_a, Y) = P(X_b, Y) = P(X, Y_a) = P(X, Y_b) = 0, \forall X, Y$ where X_a, X_b, Y_a, Y_b denote the boundaries of the domain. Furthermore, the cavitation condition $P(X, Y) \geq 0, \forall X, Y$ must be satisfied throughout the domain.

In the line contact formulation the Y coordinate does not appear in the (4.11) and (4.25).

The dimensionless film thickness is given by:

$$H(X, Y) = H_0 + \frac{X^2}{2} + \frac{Y^2}{2} + \frac{2}{\pi^2} \iint_{\Omega} \frac{P(X', Y') dX' dY'}{\sqrt{(X - X')^2 + (Y - Y')^2}} \quad (4.27)$$

with H_0 determined by the dimensionless force balance condition:

$$\iint_{\Omega} P(X, Y) dX dY = \frac{2\pi}{3} \quad (4.28)$$

while for the 1D EHL dimensionless force balance condition is:

$$\int_{\Omega} P(X) dX = \frac{\pi}{2} \quad (4.29)$$

The EHL has two primary aspects: the strong increase of viscosity with pressure, and the magnitude of the elastic deformation caused by high pressure which is comparable to that of the film thickness. Due to the high pressure and the limited contact area elastic deformation of the surfaces will occur and it is not negligible, as well as the pressure dependence of viscosity play a crucial role in EHL simulation because the viscosity at the inlet has crucial influence on film formation.

The core element that protects the surfaces is a thin film of lubricant, for this reason, it is important to be able to predict the lubricant film thickness under a given set of operating conditions. The accurate prediction of the EHL parameters under a given set of operating conditions requires the knowledge lubricant rheology.

However, the real responses of most lubricants are often non-linear [9]. It is usually difficult to predict the non-linearity accurately by the exponential equation, and the value is likely to be underestimated by the Roelands equation [28].

In the light of the above facts, in order to a better modelling of the lubricant rheology Doolittle [32] developed the first free-volume model

based on a physical meaning, that the resistance to flow in a liquid depends upon the relative volume of molecules present per unit of free volume. Using an exponential function, Doolittle related viscosity to the fractional free volume [33-35].

4.3.6 Piezoviscous lubricant models

The majority of available studies on EHL contacts often use one of the two well-known pressure-viscosity equations, i.e. the Barus equation [17] and Roelands relation [28].

4.3.6.1 Barus model

The exponential or Barus model is widely used in the literature as it is a simple equation and thus easy to apply in analytical derivations. However, this equation is valid only for rather low pressures since for high pressures the predicted viscosities are far too high.

$$\bar{\mu} = \exp(\bar{\alpha} \cdot P) \quad (4.30)$$

4.3.6.2 Roelands model

This model is a more accurate viscosity pressure relation, often used also for high and the equation reads:

$$\bar{\mu} = \exp[(\ln \mu_0 + 9.67)(-1 + (1 + 5.1 \cdot 10^{-9} p_h P)^z)] \quad (4.31)$$

with $z=0.6$.

But neither of these two relations successfully models the piezoviscous behavior of the lubricant at typical EHL pressures. For this reason the Doolittle model has been introduced.

4.3.6.3 Free-volume model

Based on Doolittle model, the viscosity–pressure relationship is represented by:

$$\bar{\mu} = \exp \left(B \frac{V_{\infty}}{V_0} \left[\frac{1}{\frac{V}{V_0} - \frac{V_{\infty}}{V_0}} - \frac{1}{1 - \frac{V_{\infty}}{V_0}} \right] \right) \quad (4.32)$$

Where B and V_{∞}/V_0 are constants and V/V_0 can be calculated using the Tait equation of state [1,53]:

$$\frac{V}{V_0} = 1 - \frac{1}{1 + K'_0} \ln \left[1 + \frac{P}{K_0} (1 + K'_0) \right] \quad (4.33)$$

At the same time, while an equation of state is required for a compressible solution to the EHL problem, this is not always available even when viscosities are. A correlation which does not require the equation of state was derived from the Doolittle free volume theory by Yasutomi and coworkers [34] and it is a pressure modified version of the Williams–Landel–Ferry equation. For a complete derivation see Bair [53,54]. The pressure effects on viscosity are given in terms of the pressure dependence of the glass transition temperature, T_g , and of thermal expansivity of free volume, α_f . In this way the viscosity–pressure relationship is represented by:

$$\mu = \mu_g \exp \left(\frac{-2.303 C_1 (T - T_g) F}{C_2 + (T - T_g) F} \right) \quad (4.33)$$

$T_g(p)$ is the glass transition temperature which varies with pressure as:

$$T_g = T_{g0} + A_1 \ln[1 + A_2 p(x)] \quad (4.34)$$

The dimensionless relative thermal expansivity of the free volume, $F(p)$, is given by an empirical expression from Breuer and Rehage [22] for the total thermal expansivity of the liquid, assuming that the temperature dependences of the free volume and total volume change with pressure in the same way.

$$F = 1 - B_1 \ln[1 + B_2 p(x)] \quad (4.35)$$

At the same time, the original Yasutomi correlation suffers from the appearance of a zero in the function describing the pressure dependence of the relative free volume thermal expansivity. For this reason in this

work an improved Yasutomi correlation for viscosity at high pressure showed in Bair et al. [55] was used in order to model the pressure-viscosity lubricant relation.

The obvious requirements for $F'(p)$ are that it should approximate $F(p)$ at low pressures and remain greater than zero for all reasonable positive pressures. A function with these properties is:

$$F' = [1 + b_1 p(x)]^{b_2} \quad (4.36)$$

The lubricant considered in these simulations, for both piezo-viscous models, is poly-alpha-olefin (or poly- α -olefin, sometimes abbreviated as PAO).

The Roelands and Doolittle-Tait parameters for PAO 650 at 75 °C regressed from the measured data presented in literature [1,54] are: $\mu_0=1.42$ Pa·s; $B=4.422$; $V_\infty/V_0=0.6694$; $K'_0=12.83$, $K_0 =1.4252$ GPa. Figure 4.8 illustrates the comparison between the values predicted from the Yasutomi free-volume model and measured from viscometer showing a good agreement.

Furthermore, a better agreement with the measured data of the Yasutomi results compared to the Roelands law is observed [5,56].

Since the Roelands model was not intended to be accurate at high pressures [56] comparisons at EHL pressures are not really sensible. However, because Roelands is the most used model in EHL some comparison of the Yasutomi free volume prediction and the Roelands extrapolation is in order. Hogenboom et al. [57] applied the free volume approach to the same liquid used by Roelands to parameterize his model.

The two models predict the same viscosities up to 0.15 GPa, as expected, while Roelands underestimates the viscosity at high pressures. For most lubricants, however, the new scaling function should provide a very accurate prediction of the temperature and pressure dependence of the low-shear viscosity while requiring no more parameters than free volume. Based on the high pressure viscometer results, the use of free-volume viscosity model for EHL is confirmed and recommended [58].

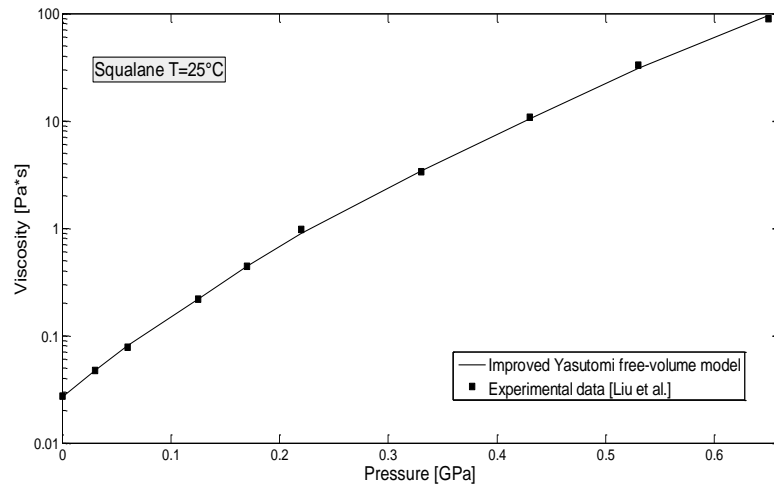


Fig. 4.8 – Comparison between the improved Yasutomi free-volume model and experimental data for a squalane at $T=25^{\circ}\text{C}$.

Because of the high pressures in the film in elastohydrodynamic lubrication, the compressibility of the oil must be taken into account with a separate equation of state when the Roelands or Barus equation are used. The most frequently used density pressure relation was proposed by Dowson & Higginson [59].

$$\bar{\rho}(P) = \frac{5.9 \cdot 10^8 + 1.34 p_h P}{5.9 \cdot 10^8 + p_h P} \quad (4.37)$$

4.4 NUMERICAL DISCRETIZATION

In order to solve for pressures and film thickness under mixed lubrication conditions, the governing equations must first be discretized. All differential schemes are derived from the Taylor series expansion. The first-order backward, second-order central, and second-order backward differentiations are often used for discretizing the Reynolds equation. Because downstream schemes may encounter instability caused by convection, forward schemes are not preferred here.

It is necessary to underline that in this paragraph is just reported the discretization of the EHL point contact problem, while the 1D (line

contact) EHL case can be easily obtained from the 2D case without taking into account the y dimension.

The discretized form of Eq. (4.11) with a uniform grid $\Delta X = \Delta Y$ is given by:

$$\begin{aligned} & \frac{(\bar{\rho}_{i+1/2,j} \bar{H}_{i+1/2,j})^3}{12\bar{\eta}_{i+1/2,j}} \frac{\bar{P}_{i+1,j} - \bar{P}_{i,j}}{\Delta X^2} - \frac{(\bar{\rho}_{i-1/2,j} \bar{H}_{i-1/2,j})^3}{12\bar{\eta}_{i-1/2,j}} \frac{\bar{P}_{i,j} - \bar{P}_{i-1,j}}{\Delta X^2} + \\ & \frac{(\bar{\rho}_{i,j+1/2} \bar{H}_{i,j+1/2})^3}{12\bar{\eta}_{i,j+1/2}} \frac{\bar{P}_{i,j+1} - \bar{P}_{i,j}}{\Delta Y^2} - \frac{(\bar{\rho}_{i,j-1/2} \bar{H}_{i,j-1/2})^3}{12\bar{\eta}_{i,j-1/2}} \frac{\bar{P}_{i,j} - \bar{P}_{i,j-1}}{\Delta Y^2} \\ & U_m \lambda \frac{\bar{\rho}_{i,j} \bar{H}_{i,j} - \bar{\rho}_{i-1,j} \bar{H}_{i-1,j}}{\Delta X} = 0 \end{aligned} \quad (4.38)$$

The discretized form of film thickness equation (4.14) is:

$$H_{i,j} = H_0 + \frac{X_i^2}{2} + \frac{Y_j^2}{2} - \frac{2}{\pi^2} \sum_{k=1}^{n_x} \sum_{l=1}^{n_y} K_{i,k,j,l} P_{k,l} \quad (4.39)$$

where

$$\begin{aligned} K_{i,k,j,l} = & X_p \ln\left(\frac{Y_p + \sqrt{X_p^2 + Y_p^2}}{Y_m + \sqrt{X_p^2 + Y_m^2}}\right) + \\ & Y_m \ln\left(\frac{X_m + \sqrt{X_m^2 + Y_m^2}}{X_p + \sqrt{X_p^2 + Y_m^2}}\right) + X_m \ln\left(\frac{Y_m + \sqrt{X_m^2 + Y_m^2}}{Y_p + \sqrt{X_m^2 + Y_p^2}}\right) + \\ & Y_p \ln\left(\frac{X_p + \sqrt{X_p^2 + Y_p^2}}{X_m + \sqrt{X_m^2 + Y_p^2}}\right) \end{aligned} \quad (4.40)$$

with:

$$\begin{aligned} X_p &= |X_i - X_k| + \frac{\Delta X}{2}, X_m = |X_i - X_l| + \frac{\Delta X}{2} \\ Y_p &= |Y_j - Y_l| + \frac{\Delta Y}{2}, Y_m = |Y_j - Y_k| + \frac{\Delta Y}{2} \end{aligned} \quad (4.41)$$

The discretized force balance equation, (4.19), is given by:

$$\Delta X^2 \sum_{i=1}^{n_x} \sum_{j=1}^{n_y} P_{i,j} = \frac{2\pi}{3} \quad (4.42)$$

Equation (4.31) is solved using the multigrid technique as described in Venner [2]. Multigrid is effective because it uses coarser grid levels to remove errors of different frequencies to those which could be quickly smoothed away on simply the fine grid alone.

The EHL problem is highly non-linear and hence the Full Approximation Scheme (FAS) must be used, see [60,61]. In-depth descriptions of how multigrid is applied to EHL problems can be found in [26]. The effectiveness of these techniques in maintaining the asymptotic convergence rates are shown in both of these works.

In the contact region the distributive Jacobi scheme has to be adopted, because of the non-diagonally dominant nature of the film thickness equation. Essentially, since local changes of pressure produce global changes of deformations, errors would accumulate during the relaxation sweep if a standard scheme was used. The distributive Jacobi scheme is very stable but offers limited smoothing properties, so in the lubricated region it is replaced by the more efficient Gauss-Seidel scheme.

The switch parameter is related to the local current value of the film thickness and has to be tuned. Two main problems have to be correctly addressed: the inter-grid transfer of the cavitation boundary and the cavitation treatment within the line relaxation process. The former is related to the different spatial resolution of grid levels, so restriction and prolongation operators could displace the cavitation boundary leading to a stall of the coarse grid correction cycle.

This can be avoided if, during the inter-grid transfer, the cavitation boundary is determined on the fine grid only and it is not affected by the relaxation on the coarse grid. The second problem consists in the fact that the line relaxation solves changes simultaneously for all points in the line, without any information about cavitation. The remedy is to take into account cavitation just when creating the system of equation for the line, by taking only central terms if at least one point in the neighborhood is cavitated.

The nonlinearity of Reynolds equation is accounted for by means of the Full Approximation Scheme (FAS) in the MultiGrid cycle. This eliminates the need of an additional global loop, as for direct Newton's methods, because only a single linearized local equation for a single unknown has to be solved during the relaxation process.

The developed coarse grid correction cycle proves to be an efficient tool to solve the EHL problem for a wide range of load conditions. However, its performance will depend on the choice of the relaxation factors and on the accuracy of the first approximation of H_0 . The relaxation factors should be small enough to avoid instability.

The Hertzian pressure profile was taken as an initial approximation for P_h . The first approximation for H was obtained by straightforward computation according to Reynolds equation with an initial approximation to H_0 . Throughout the cycle Multilevel Multi-integration is used for the fast evaluation of the elastic deformation integrals. The computing time required by the solver is proportional to $O(N \ln(N))$ if N is the number of nodes on the grid.

4.5 NUMERICAL RESULTS

4.5.1 EHL line contact

In this section the numerical results of the EHL 1D simulations are presented.

In Figure 4.9 the pressure distribution and film thickness profile obtained from a static load EHL analysis with the free-volume model. is shown. The dimensionless load is $W_{1D} = 2.5 \times 10^{-5}$, the dimensionless sliding speed is $U_{1D} = 3.5 \times 10^{-11}$ and the dimensionless material parameter is $G = 4000$.

The maximum Hertzian contact pressure, for these operating conditions, $p_{h, 1D}$, is 1.25 GPa. The dimensionless parameters are reported in the Appendix A at the end of this chapter.

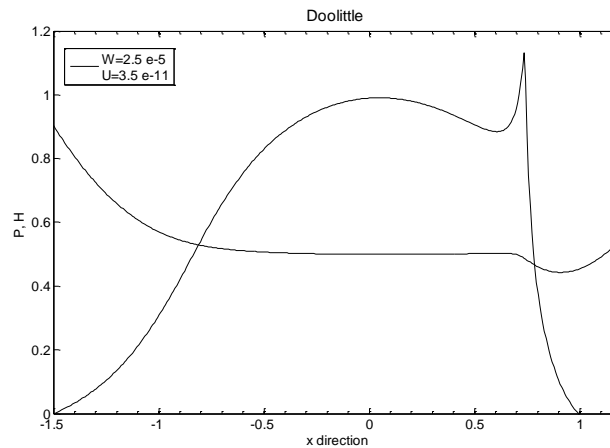


Fig. 4.9 - Film thickness profile and pressure distribution using Doolittle model

Dimensionless pressure profiles and film shapes variations in function of dimensionless load and sliding speed parameters are showed in a domain $-1.5 < X < 1.5$.

The model, using the Doolittle law for the pressure-viscosity relationship, predicts that a pressure spike occurs on the outlet side of the contact, accompanied by a constriction in oil-film thickness.

Increasing speed causes an increase of the pressure spike in height and it is moving from the outlet side of the contact toward the inlet, while increasing the applied load the pressure peak becomes sharper and moves toward the outlet zone.

It could be concluded from these figures that the height of the pressure spike slightly decrease increasing load [26]. The spike is narrower for high loads, because the contact width increases.

On the other side, for the film thickness behaviour, increasing the dimensionless sliding speed, the height of the meatus increases, while for an increase in applied load a reduction of the film thickness is observed (see Figs. 4.10 and 4.11).

Comparing the obtained results, in terms of pressure distribution and film thickness, using the free-volume and the Roelands model for the viscosity-pressure relationship, it could be observed that the pressure spike magnitude is about 20% higher using the model based on the free-

volume theory than those obtained with the Roelands relationship in the same operating conditions (see Figure 4.12).

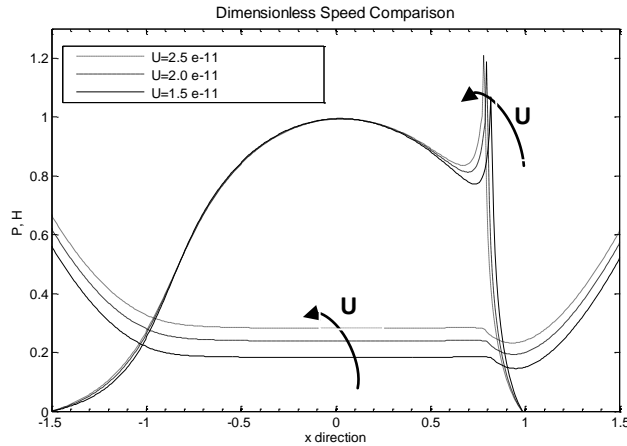


Fig. 4.10 - Film thickness profile and pressure distribution comparison using Doolittle model with $U_{ID}=1.5 \times 10^{-11}$ (solid line); $U_{ID} = 2.0 \times 10^{-11}$ (dashed line), $U_{ID} = 2.5 \times 10^{-11}$ (dot line)

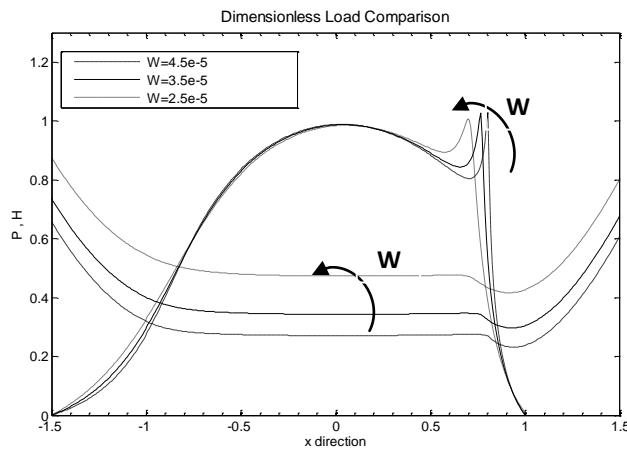


Fig. 4.11 - Film thickness profile and pressure distribution comparison using Doolittle model with $W_{ID} = 2.5 \times 10^{-4}$ (dot line); $W_{ID} = 3.5 \times 10^{-4}$ (solid line), $W_{ID} = 4.5 \times 10^{-4}$ (dashed line)

It is also found that the real pressure–viscosity behaviour predicted by the free-volume model yields a higher viscosity at the low-pressure area which results in a larger central film thickness. The remarkable difference

as regards as the pressure magnitude inside the contact area could also influence the sub surface stresses, for this reason the risk of failure for surface fatigue can be estimated more accurately.

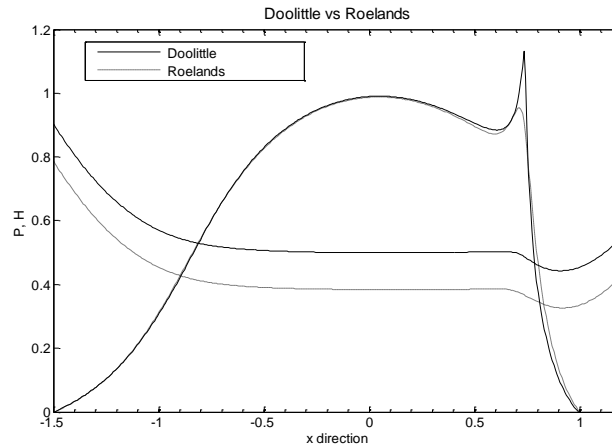


Fig. 4.12 - Film thickness profile and pressure distribution using Doolittle model (solid line) and Roelands law (dashed line) with $W_{1D} = 3.0 \times 10^{-4}$, $U_{1D} = 2.0 \times 10^{-11}$

4.5.2 EHL point contact

For the two dimensional EHL problem the presented solution have been calculated on a domain $-4.5 < X < 1.5$, $-3 < Y < 3$. For pressures as high as typical EHL pressure a larger calculation domain than that usually used at low pressure is essential, in fact if the domain, and particularly the inlet region, is not chosen large enough it results in an underestimation of the film thickness. Because the surfaces, in this section, are assumed to be perfectly smooth, the solutions for the pressure and the film shapes must be symmetric with respect to the centerline of the contact ($Y=0$)

Figs.8-9 show the 3D pressure distribution obtained from a static load EHL 2D analysis with Roeland and Doolittle free-volume model. The dimensionless load is $W = 1.1 \times 10^{-6}$, the dimensionless sliding speed is for $U = 2.6 \times 10^{-11}$ and the dimensionless material parameter is $G = 4000$. The maximum Hertzian contact pressure, for these operating conditions, p_h , is

0.8 GPa. Previously, some scientific works had already compared these different piezo-viscous models, in particular in terms of traction coefficient [27].

In this paragraph, the obtained results using the Doolittle free-volume and the Roelands models for the viscosity-pressure relationship are, instead, presented in terms of pressure distribution and film thickness. As already found in the 1D EHL simulations, it is possible to observe a difference in terms of the pressure magnitude and in terms of the shape of pressure distribution inside the contact area could influence the subsurface stresses of the mating materials (see Figs. 4.13-4.16). Furthermore, the Doolittle model leads to higher pressure spike amplitude of about 1% than that observed using the Roelands model, and similarly it can be seen that the height of the film thickness for the proposed Doolittle model is thicker than that obtained with Roelands relationship (Figs. 4.17-4.18). The fact that film thickness is formed mainly by the entraining action at the inlet area significantly weighs the importance of viscosity variation from different models in this area. The inlet area is a low-pressure area and accordingly the real viscosity of the lubricant predicted by Doolittle model undergoes a rapid increase in a convex function, apparently being larger than the Roelands one. This difference in the viscosity behaviour results in the final difference in film thickness. However, Roelands model always underestimates the low-pressure viscosity and results in a smaller film thickness than the Doolittle one.

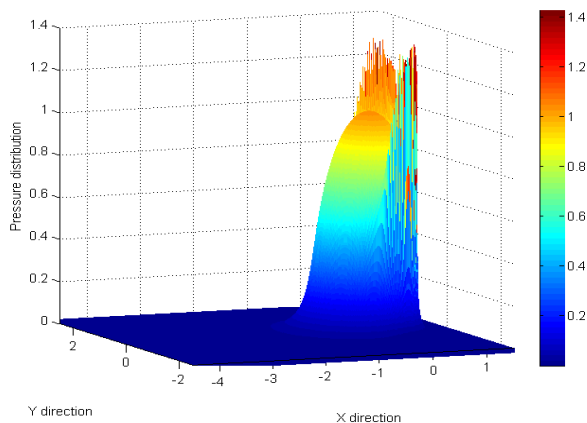


Fig. 4.13 - 3D Pressure distribution for $U=2.6 \times 10^{-11}$ and $W=1.1 \times 10^{-6}$, with Doolittle pressure-viscosity model

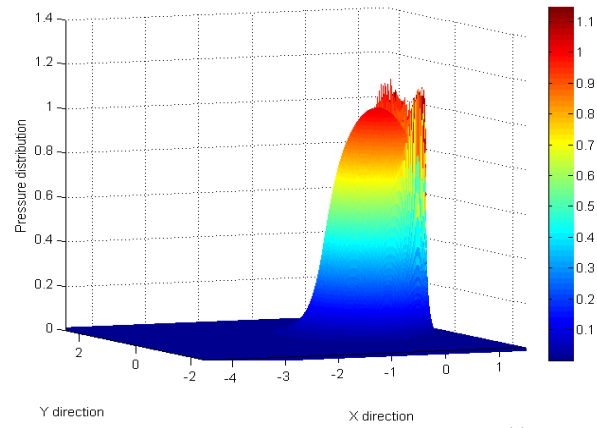


Fig. 4.14 - 3D Pressure distribution for $U=2.6 \times 10^{-11}$ and $W=1.1 \times 10^{-6}$, with Roelands pressure-viscosity model

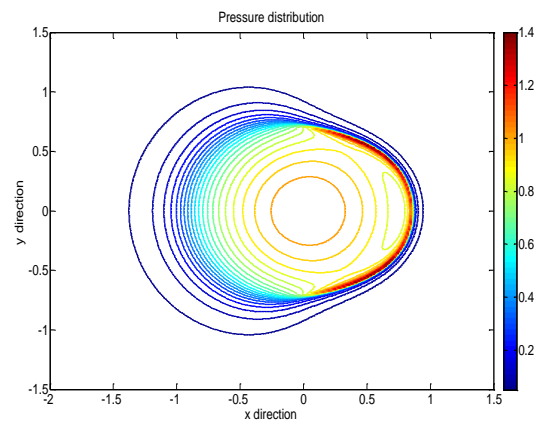


Fig. 4.15 - Pressure distribution level curves for $U=2.6 \times 10^{-11}$ and $W=1.1 \times 10^{-6}$, with Doolittle pressure-viscosity model

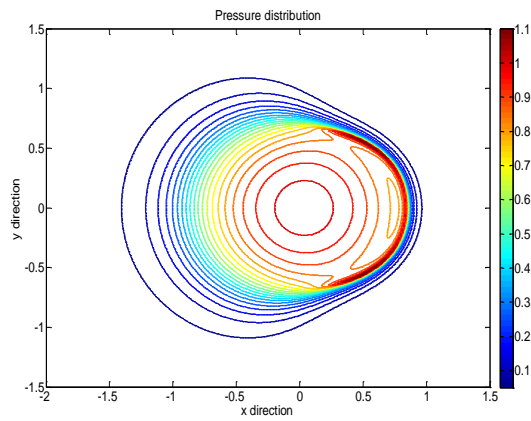


Fig. 4.16- Pressure distribution level curves for $U=2.6 \times 10^{-11}$ and $W=1.1 \times 10^{-6}$, with Roelands pressure-viscosity model

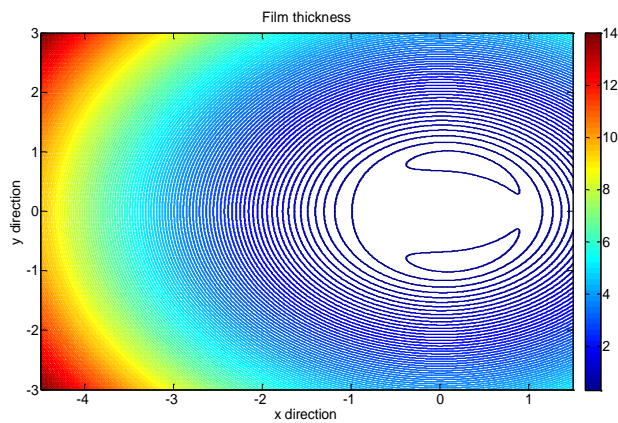


Fig. 4.17 - Film thickness level curves for $U=2.6 \times 10^{-11}$ and $W=1.1 \times 10^{-6}$, with Doolittle pressure-viscosity model

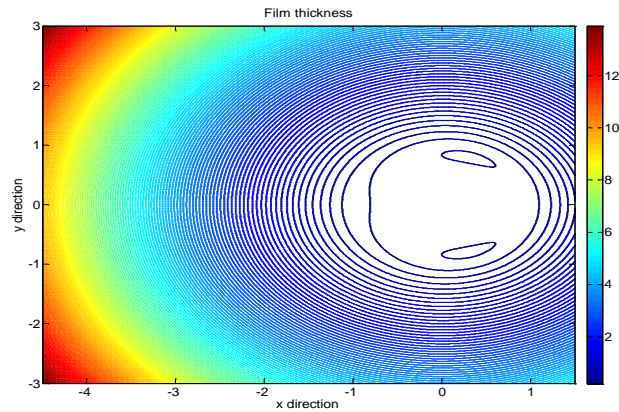


Fig. 4.18 - Film thickness level curves for $U=2.6\times 10^{-11}$ and $W=1.1\times 10^{-6}$, with Roelands pressure-viscosity model

4.5.2.1 Numerical results with Doolittle pressure-viscosity model: Pressure distribution

The numerical results obtained with the Doolittle free-volume viscosity relationship exhibit a tendency similar to those obtained using the Roelands model, in terms of pressure distribution and film shape, in function of the dimensionless applied load and sliding speed.

The magnitude of the pressure spike decreases with increasing in the maximum Hertzian pressure. With increasing load, the pressure profile approximates the Hertzian dry contact pressure and both the inlet region. Increasing speed or applied load it could be also seen a bigger area on the domain subject to the lubricated pressure in the inlet zone (see Figs. 4.19-4.22).

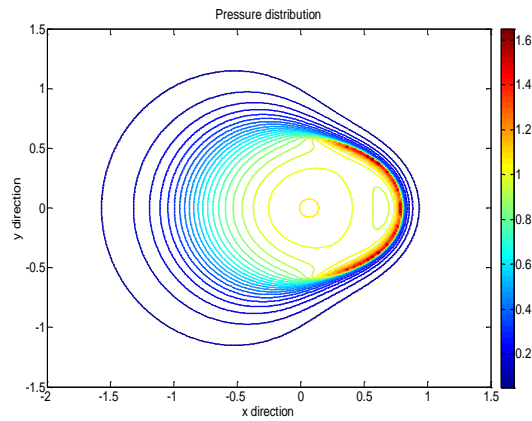


Fig. 4.19 - Pressure distribution level curves for $U=1.1 \times 10^{-11}$ and $W=3.5 \times 10^{-7}$, with Doolittle pressure-viscosity model

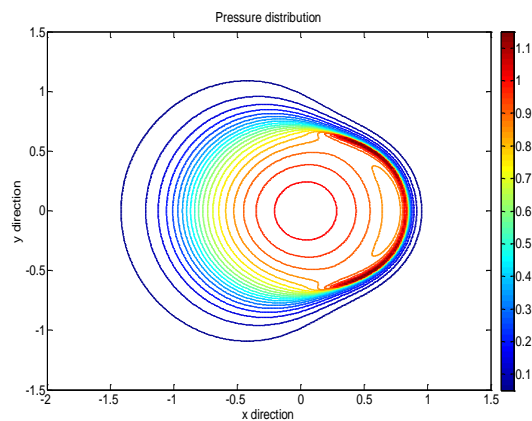


Fig. 4.20 - Pressure distribution level curves for $U=5.3 \times 10^{-12}$ and $W=3.5 \times 10^{-7}$, with Doolittle pressure-viscosity model

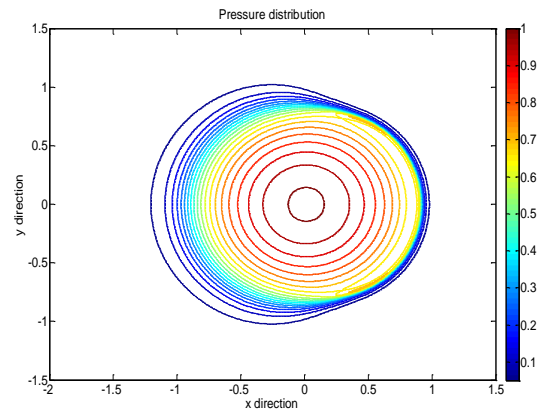


Fig. 4.21 - Pressure distribution level curves for $U=5.3 \times 10^{-12}$ and $W=8.6 \times 10^{-7}$, with Doolittle pressure-viscosity model

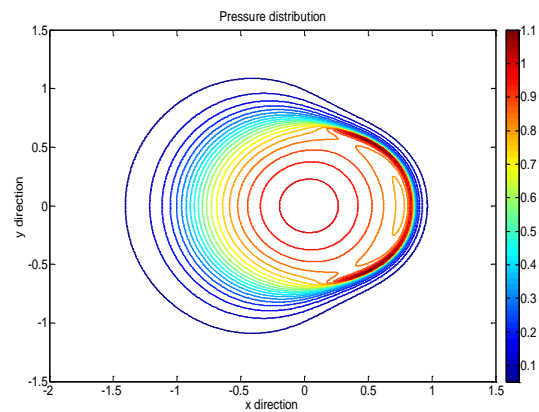


Fig. 4.22 - Pressure distribution level curves for $U=2.6 \times 10^{-11}$ and $W=1.1 \times 10^{-6}$, with Doolittle pressure-viscosity model

4.5.2.2 Numerical results with Doolittle pressure-viscosity model: Film thickness

Due to the elastic deformation the surface is flattened in the central region. This effect decreases towards the outside of the contact as a result of which a horseshoe shape occurs. The overall minimum film thickness occurs in the 'side-lobes' of the horse-shoe. The flattening in the central region is in accordance with the asymptotic behaviour of the Reynolds

equation. For the film thickness behavior, increasing the dimensionless sliding speed, the height of the meatus increases, while for an increase in applied load a reduction of the film thickness is observed (see Figs. 4.23-4.26).

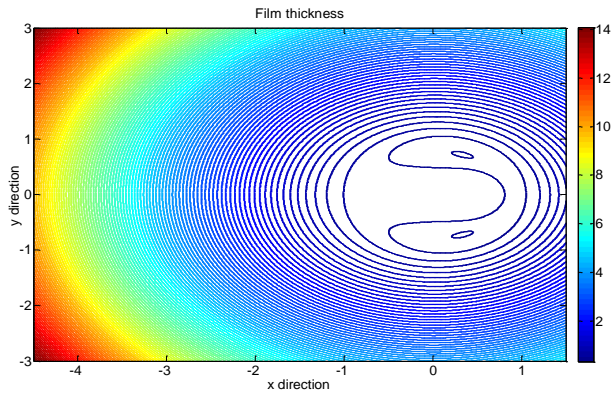


Fig. 4.23 - Film thickness level curves for $U=1.1 \times 10^{-11}$ and $W=3.5 \times 10^{-7}$, with Doolittle pressure-viscosity model

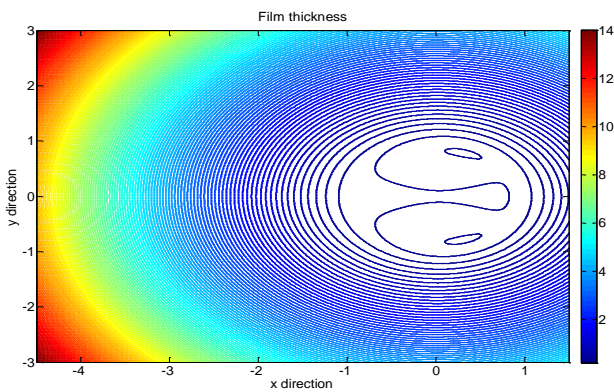


Fig. 4.24 - Film thickness level curves for $U=5.3 \times 10^{-12}$ and $W=3.5 \times 10^{-7}$, with Doolittle pressure-viscosity model

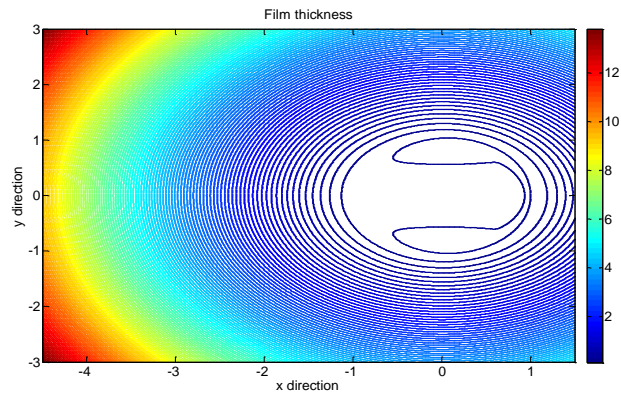


Fig. 4.25 - Film thickness level curves for $U=5.3 \times 10^{-12}$ and $W=8.6 \times 10^{-7}$, with Doolittle pressure-viscosity model

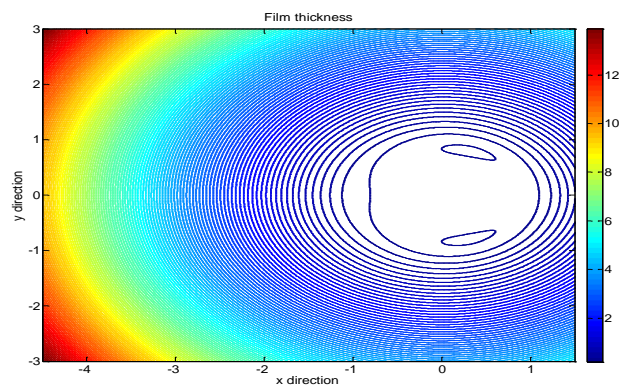


Fig. 4.26 - Film thickness level curves for $U=2.6 \times 10^{-11}$ and $W=1.1 \times 10^{-6}$, with Doolittle pressure-viscosity model

It is necessary to emphasize that a higher resolution results in a much more pronounced pressure spike. Furthermore, this spike forms a shield of high pressure values preceding the drop to the cavitation. Furthermore, to determine how many cycles have been needed to obtain a solution with an error of the magnitude of the discretization several simulations have been also performed. The results show that already using two cycles per grid level an approximation to the minimum and central film thickness is obtained with an error that is very small compared to the discretization error. Finally, through the minimum and central film thickness data presented in Tabs. 4.1 and 4.2, it is possible to observe that these values

converge in a second order manner with decreasing mesh size. The difference between the values of the central and minimum film thickness obtained on two consequent grids decreases with a factor four, when decreasing the mesh size.

Level	H_m	H_c
3 (64x64)	$1.8265 \cdot 10^{-1}$	$2.7683 \cdot 10^{-1}$
4 (128x128)	$1.8759 \cdot 10^{-1}$	$2.9623 \cdot 10^{-1}$
5 (256x256)	$1.9042 \cdot 10^{-1}$	$2.9976 \cdot 10^{-1}$
6 (512x512)	$1.9100 \cdot 10^{-1}$	$3.0083 \cdot 10^{-1}$

Tab. 4.1 - Central and minimum film thickness on four different grids with 2 cycles in FMG algorithm. $U=1.11 \cdot 10^{-11}$ $W=3.46 \cdot 10^{-7}$ with Doolittle model

Level	H_m	H_c
3 (64x64)	$4.9796 \cdot 10^{-2}$	$9.4387 \cdot 10^{-2}$
4 (128x128)	$5.6425 \cdot 10^{-2}$	$1.0815 \cdot 10^{-1}$
5 (256x256)	$5.8073 \cdot 10^{-2}$	$1.0998 \cdot 10^{-1}$
6 (512x512)	$5.8402 \cdot 10^{-2}$	$1.1082 \cdot 10^{-1}$

Tab. 4.2 - Central and minimum film thickness on four different grids with 2 cycles in FMG algorithm. $U=1.11 \cdot 10^{-11}$ $W=1.04 \cdot 10^{-6}$ with Doolittle model

For many years, an important parameter of comparison with regard to the EHL lubrication is the central and the minimum value of the film thickness [22,23]. For the line contact problem the natural choice for a film thickness parameter to be used in overview graphs was the minimum film thickness. In the case of point contact problems the situation is more complex. In this work, the values of the minimum and central film thickness, obtained with the use of the two analyzed piezo-viscous models, have been presented. The numerical results predicted through the use of the two proposed piezoviscous models are compared with values calculated with the well-known Dowson-Higginson formula for the minimum and central film thickness for the point contact problem:

$$H_m^{DH} = 3.63G^{0.49}U^{0.68}W^{-0.073}(1 - e^{-0.68k}) \tag{4.35}$$

$$H_c^{DH} = 2.69G^{0.53}U^{0.67}W^{-0.067}(1 - e^{-0.73k}) \tag{4.36}$$

The calculated simulation results are also compared with the Moes-Venner for the elastic piezoviscous point contact central film thickness predictions (see ref. 28)

$$H_c^M = 1.25M^{-1/12}L^{3/4} \quad (4.37)$$

In order to compare the results obtained from the numerical simulation in term of film thickness with those calculated by the Dowson-Higginson formula, it has been necessary refers to the Hamrock and Dowson parameters [59] and the associated dimensionless film thickness that is defined as $H_D = h/Rx$.

The disadvantage of using these parameters is that it is not the minimum set of parameters, while, on the other hand, one reason mentioned in favor of these parameters is that they represent parameters that one generally varies independently in experiments, i.e. load, speed and lubricant.

For a better comprehension of the range covered in this work with the parameter set U,W,G, are also calculated the often used Moes parameters M, L deeply described in Venner et al. [2]. The results were obtained for different values of dimensionless load (highlighted in soft pink) and speed, Tables 4.3 and 4.4.

U	W	M	L	Hc Doolittle	Hc Roelands	Hc Dowson-Higginson	Hc Moes-Venner
$1.11 \cdot 10^{-12}$	$1.04 \cdot 10^{-6}$	400	4	$4.17 \cdot 10^{-6}$	$3.63 \cdot 10^{-6}$	$3.84 \cdot 10^{-6}$	$3.90 \cdot 10^{-6}$
$1.11 \cdot 10^{-11}$	$3.46 \cdot 10^{-7}$	35	8	$2.04 \cdot 10^{-5}$	$1.68 \cdot 10^{-5}$	$1.93 \cdot 10^{-5}$	$2.08 \cdot 10^{-5}$
$1.11 \cdot 10^{-11}$	$1.04 \cdot 10^{-6}$	100	8	$1.89 \cdot 10^{-5}$	$1.57 \cdot 10^{-5}$	$1.80 \cdot 10^{-5}$	$1.91 \cdot 10^{-5}$
$1.11 \cdot 10^{-11}$	$2.07 \cdot 10^{-6}$	200	8	$1.82 \cdot 10^{-5}$	$1.50 \cdot 10^{-5}$	$1.72 \cdot 10^{-5}$	$1.83 \cdot 10^{-5}$
$2.21 \cdot 10^{-11}$	$3.46 \cdot 10^{-7}$	20	9	$3.28 \cdot 10^{-5}$	$2.81 \cdot 10^{-5}$	$3.08 \cdot 10^{-5}$	$3.31 \cdot 10^{-5}$
$5.53 \cdot 10^{-11}$	$1.21 \cdot 10^{-6}$	35	11	$5.70 \cdot 10^{-5}$	$4.92 \cdot 10^{-5}$	$5.23 \cdot 10^{-5}$	$5.80 \cdot 10^{-5}$

Tab. 4.3 - Doolittle and Roelands predicted central film thickness H_c versus calculated values with Dowson-Higginson equation, for different values of dimensionless speed and applied load

U	W	M	L	Hm Doolittle	Hm Roelands	Hm Dowson- Higginson
$1.11 \cdot 10^{-12}$	$1.04 \cdot 10^{-6}$	400	4	$3.20 \cdot 10^{-6}$	$2.84 \cdot 10^{-6}$	$3.00 \cdot 10^{-6}$
$1.11 \cdot 10^{-11}$	$3.46 \cdot 10^{-7}$	35	8	$1.59 \cdot 10^{-5}$	$1.39 \cdot 10^{-5}$	$1.56 \cdot 10^{-5}$
$1.11 \cdot 10^{-11}$	$1.04 \cdot 10^{-6}$	100	8	$1.49 \cdot 10^{-5}$	$1.24 \cdot 10^{-5}$	$1.44 \cdot 10^{-5}$
$1.11 \cdot 10^{-11}$	$2.07 \cdot 10^{-6}$	200	8	$1.39 \cdot 10^{-5}$	$1.17 \cdot 10^{-5}$	$1.37 \cdot 10^{-5}$
$2.21 \cdot 10^{-11}$	$3.46 \cdot 10^{-7}$	20	9	$2.67 \cdot 10^{-5}$	$2.27 \cdot 10^{-5}$	$2.50 \cdot 10^{-5}$
$5.53 \cdot 10^{-11}$	$1.21 \cdot 10^{-6}$	35	11	$4.50 \cdot 10^{-5}$	$3.95 \cdot 10^{-5}$	$4.25 \cdot 10^{-5}$

Tab. 4.4 - Doolittle and Roelands predicted minimum film thickness H_m versus calculated values with Dowson-Higginson equation, for different values of dimensionless speed and applied load

The minimum height of the film decreases increasing the dimensionless load, while increases increasing the dimensionless speed, for both the piezo-viscous models. By comparing the numerical results obtained using the two proposed viscosity models in this work it could be observed that the use of Roelands model tends to underestimate the height of the minimum and central film thickness in each considered operating conditions.

It could be also observed as the Dowson-Higginson calculated values are bigger than the values obtained by the Roelands model, while both the calculated D-H central and minimum film thickness are slightly smaller than the Doolittle H_c and H_m , highlighting how the accuracy of the nearly 50-year-old numerical solutions is surprising.

Furthermore, the obtained results for the central film thickness using the Moes-Venner formula for the elastic piezoviscous point contact are very close to those calculated through the proposed numerical simulation.

A statistical analysis was performed using the experimental data presented in Liu & al. [1] to quantitatively evaluate the correlation between the simulation data obtained through the use of Doolittle relationship and the above mentioned experimental data.

4.5.3 Discussion

In the simulations presented in the first section of this chapter, the Roelands model, usually used for modelling the pressure-viscosity relationship of the lubricants, has been observed to fail in capturing the

real film thinning behaviour while the more realistic pressure–viscosity relationship described by the Doolittle free-volume model yields results very close to the experimental literature data, with a higher value of viscosity in the low pressure area than those obtained by the Barus and Roelands models.

Higher viscosity in the low-pressure area results in a larger central film thickness. The fact that film thickness is formed mainly by the entraining action at the inlet area significantly weighs the importance of viscosity variation from different models in this area. The inlet area is a low-pressure area and accordingly the real viscosity of the lubricant predicted by Doolittle model undergoes a rapid increase in a convex function, apparently being larger than the Roelands model.

This finding can help explain the inconsistency between experiment data and simulation results encountered in the past, where the computed film thickness was always smaller than the corresponding experimental value.

4.6 THE INFLUENCE OF THE ROUGHNESS PARAMETERS

As mentioned in the introduction of this chapter, surface roughness plays an important role in satisfactory operation of elastohydrodynamic lubrication of rolling/sliding contacts. A number of standard parameters have been used in the simulations presented in this work to describe surface roughness of engineered surfaces [62-67].

Root mean square roughness (R_q) is the square root of the sum of the squares of the individual heights and depths from the mean line.

$$R_q = \sqrt{\frac{1}{n} \sum_{i=1}^n y_i^2} \quad (4.43)$$

Skewness (R_{sk}) is a measure of the average of the first derivative of the surface (the departure of the surface from symmetry). A negative value of R_{sk} indicates that the surface is made up of valleys, whereas a surface with a positive skewness is said to contain mainly peaks and asperities.

$$R_{sk} = \frac{1}{nR_q^3} \sum_{i=1}^n y_i^3 \quad (4.44)$$

Kurtosis (R_{ku}) is a measure of sharpness of profile peaks.

$$R_{sk} = \frac{1}{nR_q^4} \sum_{i=1}^n y_i^4 \quad (4.45)$$

The *autocorrelation function* (ACF) is essentially a measure of the wavelength structure of a surface profile in a given direction. It is defined as:

$$G_x(\lambda) = E[\delta(x)\delta(x + \lambda)] \quad (4.46)$$

here E denotes an expectation, i.e., an average value of $\delta(x)\delta(x + \lambda)$, λ is the correlation length, δ is the height function along the x direction, and $G_x(\lambda)$ is the ACF in the x direction. In the present work exponential and Gaussian ACF were used for rough surfaces simulations [68-70]. FFT technique used in this procedure may speed up the numerical process for generating rough surface, but when correlation length increases, the number of data for FFT should be increased accordingly to guarantee the accuracy.

4.6.1 Numerical results

In this section the numerical results of the EHL 1D simulation are presented for the different analyzed roughness parameters.

Random rough surfaces with Gaussian statistics and prescribed roughness parameters were generated using a method outlined by Garcia and Stoll [3], where an uncorrelated distribution of surface points using a random number generator (i.e. white noise) is convolved with a Gaussian filter to achieve correlation.

By means of the numerical model of EHL lubrication proposed by the present authors, the generated rough surfaces are then used to investigate the effect of RMS, autocorrelation function, correlation length, skewness and kurtosis of rough surface on contact pressure and film thickness using a more realistic free volume model in order to take into account the pressure-viscosity relationship of the lubricant.

The maximum pressure increases with RMS value indicating that higher roughness heights lead to localized thinning of the lubricant film as shown in Figs. 4.27a-c with a remarkable difference on the maximum average contact pressure between the simulation with a root mean square of $1\mu\text{m}$ and $0.1\mu\text{m}$.

Surface roughness produces pressure fluctuations inside the conjunction which tend to increase the maximum stress. These pressure ripples correspond to the asperity peaks. This indicates that surface roughness causes very high local contact pressures which may lead to local thinning of the film. Moreover, the coefficient of friction increases with increases RMS leading to high energy dissipation. This is due to the resistance offered by the surface roughness against the lubricant flow which increases with increasing roughness heights.

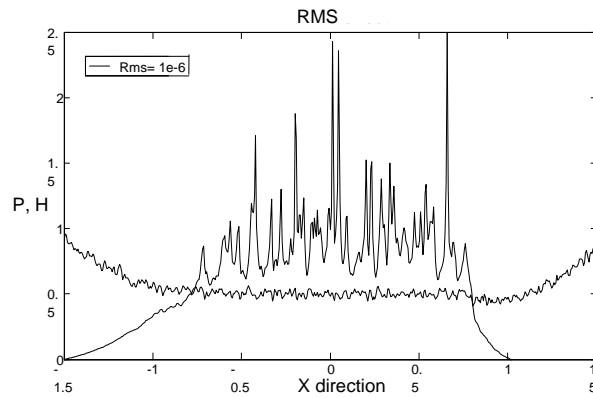


Fig. 4.27a -Pressure distribution and film thickness behavior with a RMS of $1 \mu\text{m}$

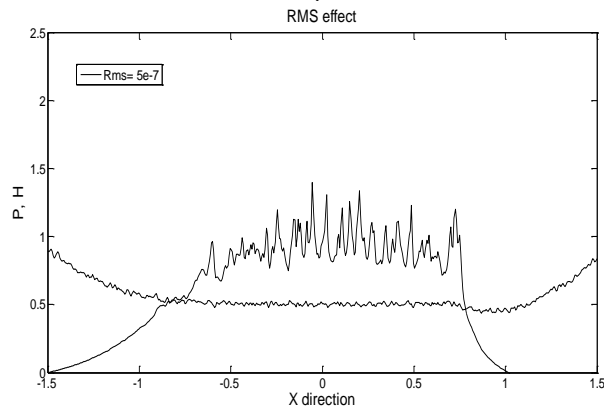


Fig. 4.27b - Pressure distribution and film thickness behavior with a RMS of $0.5 \mu\text{m}$

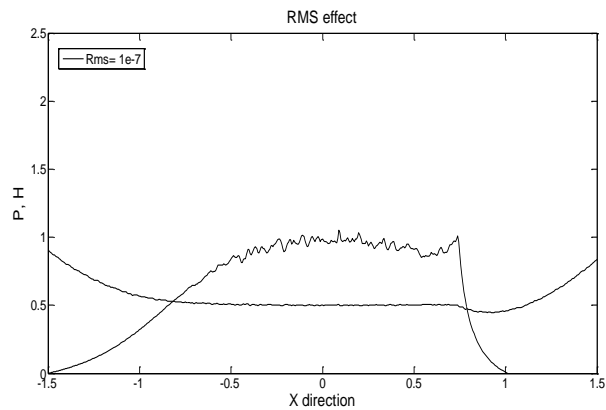


Fig. 4.27c - Pressure distribution and film thickness behavior with a RMS of $0.1 \mu\text{m}$

Furthermore, it was found in the simulations presented by means of the graphs in Figs. 2-3, that skewness and kurtosis have significant influence on the maximum pressure, but weak effect on the film thickness. Accordingly, it can be observed kurtosis increasing produces maximum pressure increase (Figs.4.28a-c).

The correspondence between pressure and kurtosis manifests the effects of roughness characteristic. As is known, with the increase of kurtosis, the rough surface becomes peakier so that pressure spikes become shaper.

On the other hand, the surface with lower kurtosis has better capacity to form lubrication films than the one with higher kurtosis, which also may has an effect on the contact behavior.

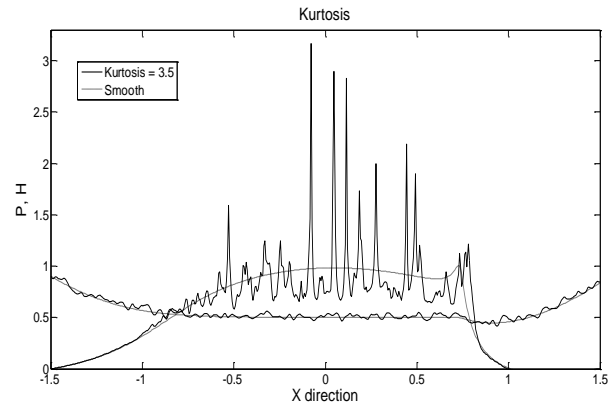


Fig. 4.28a - Pressure distribution and film thickness behavior with a kurtosis of 3.5 (solid line) compared with the results for smooth surfaces (dot line)

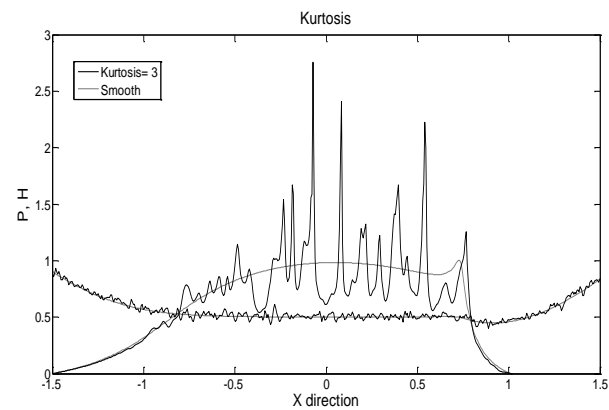


Fig. 4.28b - Pressure distribution and film thickness behavior with a kurtosis of 3 (solid line) compared with the results for smooth surfaces (dot line). The value of RMS is $0.1 \mu\text{m}$

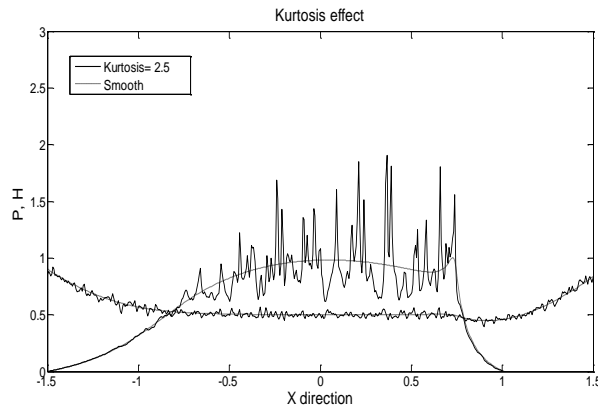


Fig. 4.28b - Pressure distribution and film thickness behavior with a kurtosis of 2.5 (solid line) compared with the results for smooth surfaces (dot line). The value of RMS is 0.1 μm

Finally, Figures 4.29a-b show the pressure distribution and average film thickness as a function of skewness. Similar trends of the Figures. 4.28 are observed. This may also be related to the roughness characteristics. When a smooth surface normally approaches a rough surface, a surface with positive skewness will be much more engaged in contact than negative skewness one.

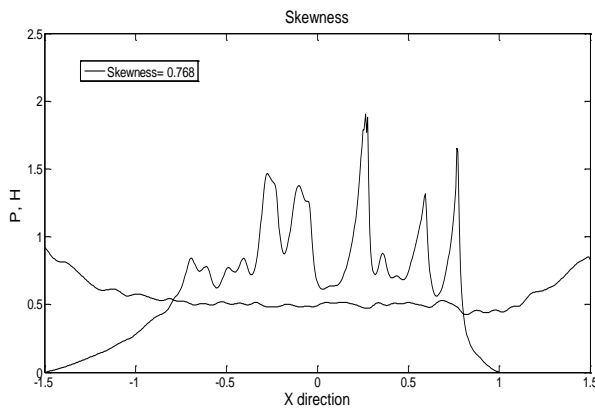


Fig. 4.29a - Pressure distribution and film thickness behavior with a skewness of 0.768. The value of RMS is 0.1 μm

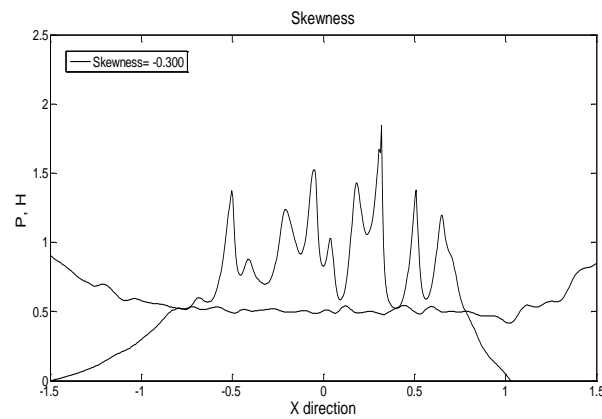


Fig. 4.29b - Pressure distribution and film thickness behavior with a skewness of -0.300 . The value of RMS is $0.1 \mu\text{m}$

Moreover, in Figure 4.30, it is shown the different behavior obtained in terms of pressure distribution and film thickness variations using two different autocorrelation function: Gaussian and exponential.

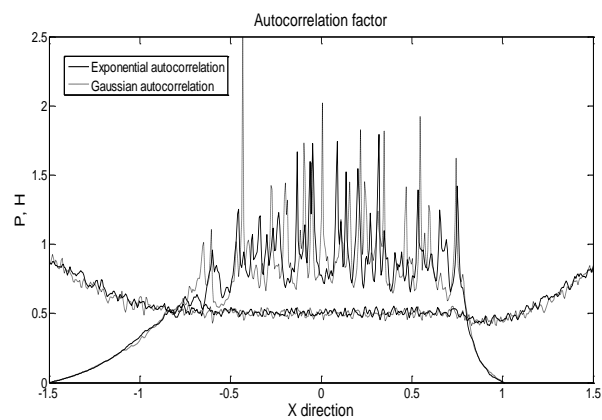


Fig. 4.30 - Pressure distribution and film thickness behavior obtained using an exponential autocorrelation function (solid line) and a Gaussian autocorrelation function (dot line). The value of RMS is $0.1 \mu\text{m}$

The result shows a good agreement for both the film thickness variations while it can be seen some difference in terms of pressure distribution, in particular for the maximum contact pressure, higher for the Gaussian ACF than for the exponential one. Moreover for the Gaussian ACF the

pressure peaks appear sharper than those obtained with an exponential function at the same operating conditions and with the same roughness parameters. The correlation length plays a crucial role on the EHL behavior as it shown in Figures 4.31a-b.

The results show that decreasing the correlation length, from 1 μm to 0.1 μm , the maximum contact pressure increases remarkably and the peaks become greatly sharper.

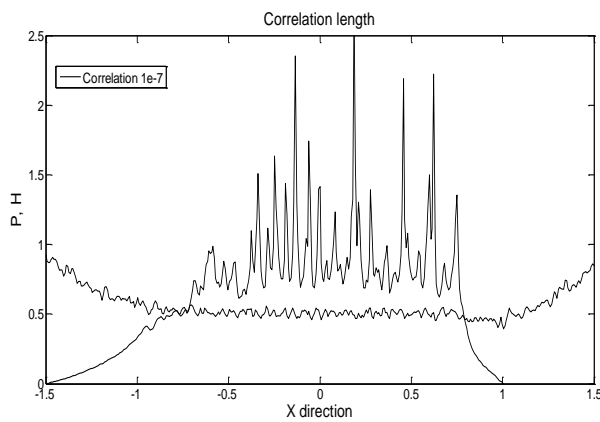


Fig. 4.31a - Pressure distribution and film thickness behavior with correlation length of 0.1 μm and RMS of 0.1 μm

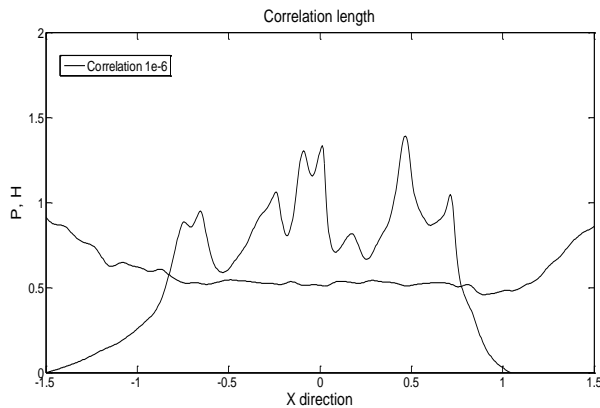


Fig. 4.31b - Pressure distribution and film thickness behavior with correlation length of 1 μm and RMS of 0.1 μm

In previous scientific works[1,55], the comparison between the values predicted from the Doolittle–Tait free-volume model and those measured from viscometer is, also, illustrated. A better agreement with the measured data of the Doolittle results compared to the Roelands law is observed. There has been some discussion regarding the differences in viscosities predicted by free volume and Roelands. Since the Roelands model was not intended to be accurate at high pressures, comparisons at EHL pressures are not really sensible; however, because Roelands is the most frequently used model in EHL, a comparison of the free-volume prediction with the Roelands extrapolation is in order.

Comparing the obtained results, in terms of pressure distribution and film thickness, using the free-volume and the Roelands model for the viscosity-pressure relationship, it could be observed that the average maximum contact amplitude is slightly higher using the model based on the free-volume theory than those obtained with the Roelands relationship in the same operating conditions, Figure 4.32.

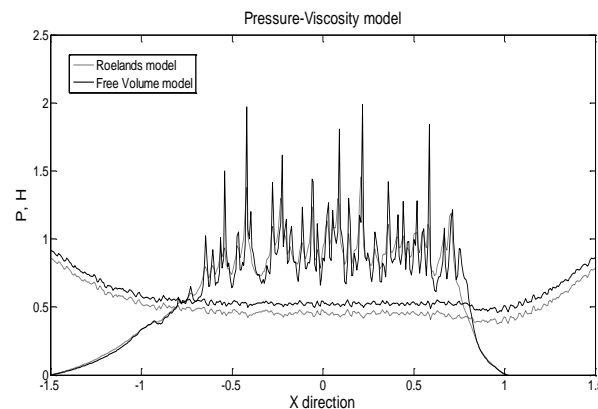


Fig. 4.32 - Pressure distribution and film thickness behavior obtained using the free volume piezoviscosity model (solid line) and the Roelands model (dot line). The value of RMS is 0.1 μm

4.6.2 Discussion

The obtained results indicate that roughness plays a pivotal role in deciding the tribological behavior of the contacting surfaces.

Studying the influence of the roughness parameters on the EHL simulation, the results show that:

- the maximum pressure increases with RMS value indicating that higher roughness heights lead to localized thinning of the lubricant film;
- for lubricated contact kurtosis and skewness were found to be the most important roughness parameters in terms of tribological behavior. In particular, skewness and kurtosis have a significant influence maximum pressure, but little effect on the film thickness. These results indicate that these parameters could be used as design parameters for surface topography modification and texturing aimed to reduce friction;
- the ACF and correlation length also deeply influence the maximum contact pressure and the slope of the pressure spikes. As previously showed, for the Gaussian ACF the pressure peaks appear sharper than those obtained with an exponential function at the same operating conditions and with the same roughness parameters. Moreover, the results show that decreasing the correlation length the maximum contact pressure increases remarkably and the peaks become greatly sharper.

APPENDIX A

Dimensional parameters

b = radius of the Hertzian contact $b = \sqrt[3]{\frac{3wR_x}{2E'}}$ (m)

E' = modulus of elasticity (Pa)

E' = reduced modulus of elasticity (Pa)

h = film thickness (m)

p = pressure (Pa)

p_h = maximum Hertzian pressure $p_h = \frac{3w}{2b^2}$ (Pa)

R_x = reduced radius of curvature in the x direction (m)

R_y = reduced radius of curvature in the y direction (m)

u_m = mean velocity $u_m = (u_1 + u_2)/2$ (m/s)

u_s = sum velocity $u_s = (u_1 + u_2)$ (m/s)

w = applied load per unit length (N/m)

x = coordinate in the x direction (m)

y = coordinate in the y direction (m)

α =piezo-viscous coefficient (Pa^{-1})

Δx =space increment in x direction (m)

Δy =space increment in y direction (m)

μ_o = inlet viscosity of the lubricant (Pa s)

μ = lubricant viscosity at the local pressure (Pa s)

ρ_o = inlet mass density of the lubricant (kg/m^3)

ρ = lubricant mass density at the local pressure (kg/m^3)

λ =correlation length [m]

δ =height function [m]

R_q =Root mean square (RMS) [m]

R_{sk} =Skewness [m]

R_{ku} =kurtosis [m]

Dimensionless parameter for the EHL point contact problem

B =Doolittle parameter

G =dimensionless load parameter $G = \alpha E'$

$G(\lambda)$ =Autocorrelation function

H = dimensionless film thickness $H = \frac{hR_x}{b^2}$

H^{HD} =Hamrock & Dowson dimensionless film thickness $H^{HD} = \frac{h}{R_x}$

K_0 = isotherm bulk modulus at $p=0$ (Pa)

K_0' = pressure rate of change of isothermal bulk modulus at $p=0$

H^M =Moes dimensionless film thickness $H^M = \frac{(h/R_x)}{\sqrt{2U}}$

L =dimensionless material parameter (Moes) $L = \alpha E' \left(\frac{\eta_0 \mu_s}{E' R_x} \right)^{1/4}$

M = dimensionless load parameter (Moes) $M = \frac{w}{E' R_x^2} \left(\frac{\eta_0 \mu_s}{E' R_x} \right)^{-3/4}$

n_x, n_y = number of points in x and y

P = dimensionless pressure $P = \frac{p}{P_h}$

U = dimensionless speed parameter $U = \frac{\mu_0 \mu_m}{E' R_x}$

V_{occ} = occupied volume

V = volume

$V_o =$ volume for $p=0$

$W =$ dimensionless load parameter $W = \frac{w}{E' R_x^2}$

$X =$ dimensionless coordinate in x direction $X = \frac{x}{a}$

$Y =$ dimensionless coordinate in y direction $Y = \frac{y}{b}$

$Z =$ Roelands parameter

$\Delta X =$ dimensionless space increment in x direction (m)

$\Delta Y =$ dimensionless space increment in y direction (m)

$\bar{\mu} =$ dimensionless viscosity $\bar{\mu} = \frac{\mu}{\mu_0}$

$\Omega =$ solution domain

$\bar{\rho} =$ dimensionless mass density $\bar{\rho} = \frac{\rho}{\rho_0}$

Parameters different for the EHL line contact problem

$b_{1D} =$ half width of hertzian contact zone $b_{1D} = 4R \sqrt{\frac{W}{2\pi}}$ (m)

$H_{1D} =$ dimensionless film thickness $H_{1D} = \frac{h}{R_x}$

$p_{h,1D} =$ maximum hertzian pressure $p_{h,1D} = \frac{E' b}{4R}$ (Pa)

$U_{1D} =$ dimensionless speed parameter $U_{1D} = \frac{\mu_0 u_m}{E' R}$

$W_{1D} =$ dimensionless load parameter $W_{1D} = \frac{w}{E' R}$

REFERENCES

- [1] Liu, Y., Wang, Q.J., Wang, W., Hu, Y., Zhu, D., Krupka, I. et al., EHL simulation using the free-volume viscosity model. Tribol Lett 23(1), 27–37 (2006).
- [2] Venner, C. H., Lubrecht, A. A, MultiLevel Methods in Lubrication. Elsevier (2000).
- [3] Garcia, N., Stoll, E., Monte Carlo Calculation of Electromagnetic-Wave Scattering from Random Rough Surfaces, Phys Rev Lett 52, 20, 1798-1801, (1984).

-
- [4] FFTW library - free collection of fast C routines for computing discrete Fast Fourier Transforms. Developed at MIT by Matteo Frigo and Steven G. Johnson.
- [5] Reynolds, O., On the theory of lubrication and its application to Mr. Beauchamp Tower's experiments, including an experimental determination of the viscosity of olive oil. *Phil Trans R Soc* 177, 157-234 (1886).
- [6] Cameron, A., The Beauchamp Tower story, *Industrial Lubrication and Tribology*, Vol. 32 Iss, 1, pp.4 – 10, 1980.
- [7] Petrov, N.P., *Friction in Machines and the Effect of the Lubricant*, *Inzhenerno Zhurnal St. Petersburg*, 1883
- [8] Hamrock, B.J., Schmid, S. R., Jacobson, B.O., *Fundamentals of Fluid Film Lubrication*, Second Edition published by Marcel Dekker, Inc., 2004.
- [9] Martin, H.M., *Lubrication of gear teeth*, Engineering, London, 1916
- [10] Szeri, A. Z., *Fluid Film Lubrication*, Cambridge, 1998, ISBN 0521-48100-7
- [11] Bair, S., Vergne, P., Querry, M., A unified shear-thinning treatment of both film thickness and traction in EHD. *Tribol Lett* 18, 145 – 152 (2005).
- [12] Paredes, X., Fandino, O., Pensado, A. S., Comunas, M. J. P., Fernandez, J., Pressure–Viscosity Coefficients for Polyalkylene Glycol Oils and Other Ester or Ionic Lubricants. *Tribol Lett* 45, 89–100 2012.
- [13] Ertel, A.M., *Hydrodynamic lubrication based on new principles*, *Akad. Nauk SSSR Prikadnaya Mathematic*, 1939.
- [14] Grubin, A.N., *Fundamentals of the hydrodynamic theory of lubrication of heavily loaded cylindrical surfaces*, Investigation of the contact Machine, translation of Russian Book, 1949.
- [15] Morales-Espejel, G.E., Wemekamp, A.W., Ertel—Grubin methods in elastohydrodynamic lubrication – a review, *Proceedings of the Institution of Mechanical Engineers, Part J, Journal of Engineering Tribology* January 1, vol. 222, 1, 15-34, 2008.
- [16] Johnson, K. L., Kendall, K., Roberts, A.D., *Surface Energy and the Contact of Elastic Solids* *Proceedings A of Royal Society*, 1971
- [17] Barus, C., Isotherms, isopiestic and isometrics relative to viscosity. *Am. J Sci* 45, 87-96 (1893).
- [18] Petrusevich, A.I., *Fundamental conclusions from the contact-hydrodynamic theory of lubrication*, *Izv. Akad. Nauk. SSSR (OTN)*, 1951.
- [19] Zhao, J., Sadeghi, F., Hoepflich, M.H., Analysis of EHL circular contact start up, Part I—mixed contact model with pressure and film thickness results. *ASME J Tribol* 123, 67 (2001).
- [20] JA Greenwood, An extension of the Grubin theory of elastohydrodynamic lubrication, *Journal of Physics D, Applied Physics*, 1972.
- [21] Ranger, A.P., The solution of the point contact elasto-hydrodynamic problem, *Proceedings A of Royal society*, 1975.

-
- [22] Hamrock, B.J., Dowson, D., Isothermal elastohydrodynamic lubrication of point contacts, Part I. Theoretical formulation. *J Lubr Technol* 98, 223–229, 1976.
- [23] Hamrock, B.J., Dowson, D., Isothermal elastohydrodynamic lubrication of point contacts, Part II. Ellipticity parameter results. *J Lubr Technol* 98, 375–383, 1976.
- [24] Houpert, L., Hamrock, B.J., Fast approach for calculating film thicknesses and pressures in elastohydrodynamically lubricated contacts at high loads. *ASME J Tribol* 108, 411 – 419 (1986)
- [25] Chapkov, A.D., Bair, S., Cann, P., Lubrecht, A. A., Film thickness in point contacts under generalized Newtonian EHL conditions, Numerical and experimental analysis, *Trib Int* 40, 1474-1478, 2007.
- [26] Goodyear, C.E. Adaptive numerical methods for elastohydrodynamic lubrication. PhD Thesis, University of Leeds, West Yorkshire, 2001.
- [27] Bombard, A. J. F., De Vicente, J., Thin-Film Rheology and Tribology of Magnetorheological Fluids in Isoviscous-EHL Contacts. *Tribol Lett* 47, 149–162, 2012.
- [28] Roelands, C.J.A., Correlational Aspect of Viscosity-Temperature-Pressure Relationships of Lubricating Oils. PhD thesis, Delft University of Technology, The Netherlands (1966).
- [29] Petrie, D., Petroleum, Oxford University Press, 1961
- [30] Meuleman, P.K., Lubrecht, A.A., Traction in elastohydrodynamic lubrication. High contact pressure experiments and a thermal Roelands-Eyring-Maxwell model, Twente University of Technology, 1985, 1985.
- [31] Oldroyd, J.G., Strawbridge, D.J., Toms, B.A., A Coaxial-Cylinder Elastoviscometer, *Proceedings of the Physical Society, Section B*, 64, 1951.
- [32] Doolittle, A.D., Studies in Newtonian Flow. II. The Dependence of the Viscosity of Liquids on Free Space. *J Appl Phys* 22(12), 1471 (1951).
- [33] Williams, M.L., Landel, R.F., Ferry, J.D., The Temperature Dependence of Relaxation Mechanisms in Amorphous Polymers and Other Glass-forming Liquids. *J Am Chem Soc* 77, 3701-3707 (1955).
- [34] Yasutomi, S., Bair, S., Winer, W.O., An Application of a Free Volume Model to Lubricant Rheology I—Dependence of Viscosity on Temperature and Pressure. *J Lubr Techn* 106 (2), 291 (1984).
- [35] Cook, R.L., Herbst, C.A., King Jr, H.E., High-pressure viscosity of glass-forming liquids measured by the centrifugal force diamond anvil cell viscometer. *J Phys Chem* 97, 2355 (1993).
- [36] Venner, C.H., Multilevel Solution of the EHL Line and Point Contact Problems. PhD thesis, University of Twente, Enschede, The Netherlands (1991).

- [37] Venner, C.H., Napel Ten, W.E, Multilevel solution of the elastohydrodynamically lubricated circular contact problem part 2, Smooth surface results. *Wear* 152, 369-381 (1992).
- [38] Venner, C.H., Lubrecht, A.A., Numerical simulation of a transverse ridge in a circular EHL contact under rolling sliding. *Trans. ASME J Tribol* 116, 751-761 (1994).
- [39] Chang, L., A deterministic model for line-contact partial elastohydrodynamic lubrication, *Tribology International*, 1995
- [40] Cheng, H.S., Ai, X., Jiang, X., Hua, D.Y., Lee, S.C., A mixed elastohydrodynamic lubrication model with asperity contact, *Journal of tribology*, 1999.
- [41] Hooke, C.J., The elastohydrodynamic lubrication of heavily loaded contacts, *Journal of Mechanical Engineering Science*, 1977
- [42] Lubrecht A.A., Ioannides E., A Fast Solution to the Dry Contact Problem and the Associated Sub-surface Stress Field, Using Multilevel Techniques. *ASME J Tribol* 113, 128-133, 1991.
- [43] Venner, C.H., Lubrecht, A.A., Amplitude reduction of anisotropic harmonic surface patterns in EHL circular contacts under pure rolling. In: *Proceedings of the 25th Leeds-Lyon Symposium on Tribology*, 151–162, 1999.
- [44] Ehret, P., Bauget, F., Observation of Kaneta's dimples in elastohydrodynamic lubrication contacts, *Proceedings of the Institution of Mechanical Engineers, Part J: Journal of Engineering Tribology* vol. 215, 3, 289-300, 2001.
- [45] Kaneta, M., Cameron, A., Effects of asperities in elastohydrodynamic lubrication, *Journal of Lubrication Technology*, 1980.
- [46] Kaneta, M., Wang, J., Thermal and non-Newtonian numerical analyses for starved EHL line contacts, *Journal of tribology*, 2006.
- [47] Kaneta, M., For the establishment of a new EHL theory, *Tribology Series*, Elsevier, 1999.
- [48] Schwarz, U.D., ACNP Posseduto Biblioteche A generalized analytical model for the elastic deformation of an adhesive contact between a sphere and a flat surface, *Journal of colloid and interface science*, 2003
- [49] Anuradha, P., Kumar, P., EHL Line Contact Central and Minimum Film Thickness Equations for Lubricants with Linear Piezoviscous Behavior. *Tribol Int* 44, 1257-1260, 2011.
- [50] D'Agostino, V., Guida, D., *Fondamenti di Tribologia*, CUEN, ISBN 88-7146-351-X, 2001.
- [51] Timoshenko, S., Goodier. J.N., *Theory of Elasticity*, McGraw-Hill Book Company, 1951.
- [52] Greenwood, J. A., Williamson, J. B. P., Contact of nominally flat surfaces, *Phil. Trans. R. Soc. London, Series A-19*, 1996.

- [53] Williams, M.L., Landel, R.F., Ferry, J.D., The Temperature Dependence of Relaxation Mechanisms in Amorphous Polymers and Other Glass-forming Liquids. *J Am Chem Soc* 77, 3701-3707, (1955).
- [54] Bair, S., The high shear stress rheology of liquid lubricants, PhD Thesis, Georgia Institute of Technology, pp. 30–34, 1990.
- [55] Bair, S., Rheology and high-pressure models for quantitative elastohydrodynamics Proc. IMechE, Part J: J. Engineering Tribology 223, 4, pp. 617-628, 2009.
- [56] Bair, S., Roelands' missing data. *Proc Instn Mech Engrs Part J* 218, 57-60 (2004).
- [57] Hogenboom, D. L., Webb, W., Dixon, J.A., J. Viscosity of several liquid hydrocarbons as a function of temperature, pressure, and free volume. *Chem. Phys.* 46(7), 2586–2598, 1967.
- [58] Bair, S., Roland, C. M., Casalini, R., Fragility and the dynamic crossover in lubricants. *Proc. IMechE, Part J: J. Engineering Tribology*, 221(J7), 801–811, 2007.
- [59] Dowson, D., Higginson, G.R., Archard, J.F., Crook, A. W., *Elastohydrodynamic lubrication* (Vol. 2), Oxford, Pergamon Press, 1977.
- [60] Christopherson, D.G., A new mathematical method for the Solution of Film Lubrication Problems. *Inst Mech Engrs J Proc* 146, 126-135, 1941.
- [61] D'Agostino, V., Guida, D., Ruggiero, A., Russo, C., Optimized EHL piston dynamics computer code. *Proc. AITC-AIT International Conference on Tribology*, 1-6, 2006.
- [62] Gadelmawla, E.S., Koura, M.M., Maksoud, T.M.A., Elewa, I.M., Soliman, H.H., Roughness parameters. *Journal of Materials Processing Technology*; 123, 133–45, 2002.
- [63] Sperka, P., Krupka, I., Hartl, M., The Behavior of Surface Roughness in EHL Contacts Under Small Slide to Roll Ratios. *Tribol Lett*, 47, 357–366, 2012.
- [64] Wen-zhong, W., Hui, C., Yuan-Zhong, H., Hui W., Effect of surface roughness parameters on mixed lubrication characteristics. *Tribol Int* 39, 522–7, 2006.
- [65] Tayebi, N., Polycarpou, A.A., Modeling the effect of skewness and kurtosis on the static friction coefficient of rough surfaces. *Tribology International*, 37, 491–505, 2004.
- [66] Menezes, P.L., Kishore, Kailas S.V., Effect of directionality of unidirectional grinding marks on friction and transfer layer formation of Mg on steel using inclined scratch test. *Materials Science and Engineering*; A429(1–2), 149–60, 2006.
- [67] Menezes, P.L., Kishore, Kailas SV., Effect of roughness parameter and grinding angle on coefficient of friction when sliding of Al–Mg alloy over

- EN8 steel. Transactions of the ASME, Journal of Tribology; 128(4), 697–704, 2006.
- [68] Hu, Z.M., Dean, T.A., A study of surface topography, friction and lubricants in metal forming. International Journal of Machine Tools and Manufacture; 40, 1637–49, 2000.
- [69] Lundberg, J., Influence of surface roughness on normal-sliding lubrication. Tribology International; 28(5), 317–22, 1995.
- [70] Wieleba, W., The statistical correlation of the coefficient of friction and wear rate of PTFE composites with steel counterface roughness and hardness. Wear; 252(9–10), 719–29, 2002.

CHAPTER 5

Investigation on nanoparticle mechanical behaviour through finite element simulation

5.1 Introduction

As showed in the previous chapters, IF nanoparticles made by layered metal dichalcogenides, MX_2 ($\text{M} = \text{W}, \text{Mo}, \text{Ti}; \text{X}=\text{S}, \text{Se}$) hold great promise as additives in oils because of their low surface energy, high chemical stability, nanometric size, spherical shape, and weak intermolecular bonding [1]. It was shown that the addition of small amounts of IF- MoS_2 or IF- WS_2 into a lubricating oil and grease greatly improve the tribological properties of the lubricant [2–5]. This behavior can be explained by superposition of three main mechanisms: rolling, sliding, and exfoliation-material transfer (third body). Since non-disputable answer and key parameters favoring any of these mechanism are not yet known in this study several simulations have been performed using finite element method to study the behavior of a hollow and a bulk IF- MoS_2 nanoparticle under an uniaxial compression and shearing force.

In the early studies, the great lubricating properties of these nanoparticles were attributed to a gradual exfoliation of the external sheets of the particles during the friction process leading to their transfer onto the asperities of the reciprocating surfaces and a shearing of the basal planes. Exfoliation and transfer of MoS_2 nanosheets (designated third body) [6] were considered to be the predominant mechanism for reducing both friction and wear in the case of IF-nanoparticles. It was shown that under large mechanical loads and shear forces, the nanoparticles are deformed and compressed. This structural deformation gives rise to dislocation and dislodging of MX_2 nanosheets from the nanoparticles surface. The external nanosheets of the IF-nanoparticles, a

few monolayers thick each [1], are gradually transferred onto the substrate, thus reducing the friction between the two mating surfaces.

Recently, Tenne and co-workers [7] suggested that an additional rolling process for well-crystallized and round-shaped particles could enhance the lubricating properties of the IF nanoparticles. A recent trend in the synthesis of the fullerenes is to prepare faulted and strained IF nanostructures to facilitate their exfoliation in the tribological contact and thus to optimize the tribological properties of the lubricant [8-10]. When the rolling mechanism is effective, the nanoparticles act as nanoscopic ball bearings between the contact surfaces and could provide extremely low friction coefficients.

It was postulated that the quasi-spherical IF NP are ideally suited to provide this kind of friction mechanism [11]. Recently, in situ uniaxial nanocompression tests of individual IF-WS₂ (MoS₂) nanoparticles using TEM [12] and high resolution scanning electron microscope (HRSEM) [5] renewed the discussion on the significance of rolling friction on the tribological behavior of IF-nanoparticles.

Thus, in some previous works [12-13], the authors suggested that an additional rolling friction process could also play a role together with exfoliation and enhance the good lubricating properties of the particles, but with care of the nanoparticles properties and loads. The aim of this chapter is to investigate the structural response of IF-MoS₂ particles on pressure and shear within the sliding contact, and to analyze the potential friction mechanisms of fullerene-like nanoparticles.

In this chapter, hollow- and full-core nanoparticles were studied using theoretical approach of finite element model (FEM) analyses. In particular, in the first section we have focused our work on comparison of the hollow-core nanoparticle with common properties found in literature and applications, with the full-core nanoparticles, which are much less common, but represent an extreme opposite case to hollow ones. Furthermore, by employing the FEM technique, we aimed to investigate if IF-MoS₂ particles have a potential for providing a rolling support in smooth and parallel surface contacts under different loads.

Moreover, in the second part of the chapter the behavior of a hollow core nanoparticle is investigated under loading and shearing condition in the case of a real rough steel surface, acquired by means of an atomic force microscope (AFM).

5.1 EFFECT OF PRESSURE AND SHEAR ON THE STRUCTURAL BEHAVIOUR

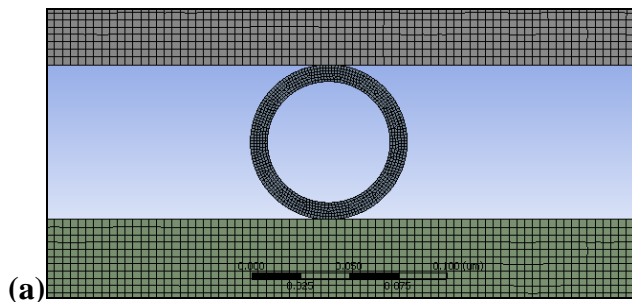
5.2.1 Numerical model

The selected contacts in this work consists of two perfectly smooth and plane steel discs, pressing and shearing a single nanoparticle in between them.

The nanoparticles used in the simulations were nanoparticles of molybdenum disulphide (MoS_2) with two different structures: a hollow core nanoparticle, also called fullerene-like (IF) MoS_2 , which is often synthesized and used; and a bulk nanoparticle with a full core, which is used mainly for comparison due to structural distinction to hollow-core nanoparticles, rather than direct practical need, because such particles are not common.

The size of nanoparticles was selected based on typical data of these nanoparticles published in recent literature on the synthesis of IF-molecules [14]. For the hollow nanoparticles, the external diameter has been set to 80 nm and inner diameter to 60 nm. In this way obtained for the volume and mass of the MoS_2 nanoparticles are close to those found in many publications [15] without taking into account the spaces between the different layers of dichalcogenide material.

The diameter for the full-core bulk nanoparticle was set to 80 nm. Furthermore, the geometry of the nanoparticles was perfectly spherical as shown in Figures 5.1a and 5.1b for hollow-core and full-core bulk nanoparticle.



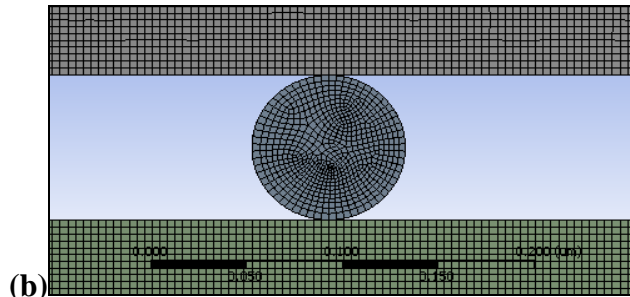


Fig. 5.1– (a) Undeformed geometry of the hollow and the bulk **(b)** MoS₂ nanoparticle used for the finite element simulations

The mechanical properties of the material used in the simulations to model the MoS₂ nanoparticles and the steel surfaces are obtained from literature, presented in Kaplan-Ashiri et al. [16], Table 5.1.

	MoS ₂ -NP	Steel surfaces
Density [kg/m³]	5060	7850
Young's Modulus [GPa]	238	200
Poisson's Ratio [-]	0.35	0.3

Tab. 5.1 – Mechanical properties of the materials used to model the surfaces (steel) and the nanoparticle (molybdenum disuphlide)

The mechanical behavior of the IF-MoS₂ nanoparticle with hollow core has been modeled by using a hyperelastic behavior of the IF-nanoparticles [17-18], since linear elastic models do not accurately describe the observed material behavior of such structures [19]. Namely, Tevet et al. [13] have shown that layered inorganic material, such as MoS₂ and WS₂, that form seamless hollow closed nanostructures are, due to their small size and layered structure, able to withstand very high elastic stress. Therefore, for the hollow-core nanoparticles, hyperelastic, i.e. Green elastic material is employed [16], which represent a constitutive model for ideal materials for which the stress-strain relationship derives from a strain energy density function.

Among different models to describe the hyperelastic behavior of material (a special case of a Cauchy elastic material) the Mooney–Rivlin model was selected. This is a hyperelastic material model that can be used for predicting the nonlinear stress-strain behavior of materials undergoing

large deformations. The model was proposed by Rivlin in 1948 [20]. In contrast to linear elastic materials, the stress-strain curve of a Mooney–Rivlin solid material is not linear. Instead, the relationship between applied stress and strain is initially linear, but at a certain point the stress-strain curve will plateau. In this model the strain energy density function is a linear combination of two invariants of the left Cauchy–Green deformation tensor [21–23]. The strain energy potential, W , is defined as follows:

$$W=c_{10}(\underline{I}_1-3)+c_{01}(\underline{I}_2-3)+c_{11}(\underline{I}_1-3)*(\underline{I}_2-3)+(J-1)^2*(1/d) \quad (5.1)$$

where:

\underline{I}_1 = first deviatoric strain invariant; \underline{I}_2 = second deviatoric strain invariant; J = determinant of the elastic deformation gradient; c_{10} , c_{01} , c_{11} = material constants characterizing the deviatoric deformation of the material; d = material incompressibility parameter. The initial shear modulus is defined as:

$$\mu = 2(c_{10} + c_{01}) \quad (5.2)$$

and the initial bulk modulus is defined as:

$$K = 2/d^3 \quad (5.3)$$

where:

$$d^3 = (1-2*\nu)/(c_{10} + c_{01}) \quad (5.4)$$

Moreover, to avoid any computational problems related to material penetration between the IF-nanoparticle and the flat surfaces, a Normal Lagrange formulation [22–23] has been used for the contact pair computation.

This algorithm enforces zero penetration when contact is closed making use of a Lagrange multiplier on the normal direction and a penalty method in the tangential direction. Normal Lagrange adds contact traction to the model as additional degrees of freedom and requires additional iterations to stabilize contact conditions.

For modeling the full-core bulk nanoparticle a more typical linear elastic model has been used.

In this research, the particle is considered to be perfectly spherical and with a high crystallinity, for this reason it was considered an isotropic behavior of the nanoparticle.

5.2.2 Numerical simulation testing procedure

The simulation consisted of two different phases: the first phase is compression only, while the second phase adds a sliding motion, which induces shear to already loaded particle.

A schematic of the loading and shearing processes are presented in Figure 5.2, while the details on the parameters used in simulation of loading hollow and bulk nanoparticles are seen in Figures 5.3a and 5.3b, respectively.

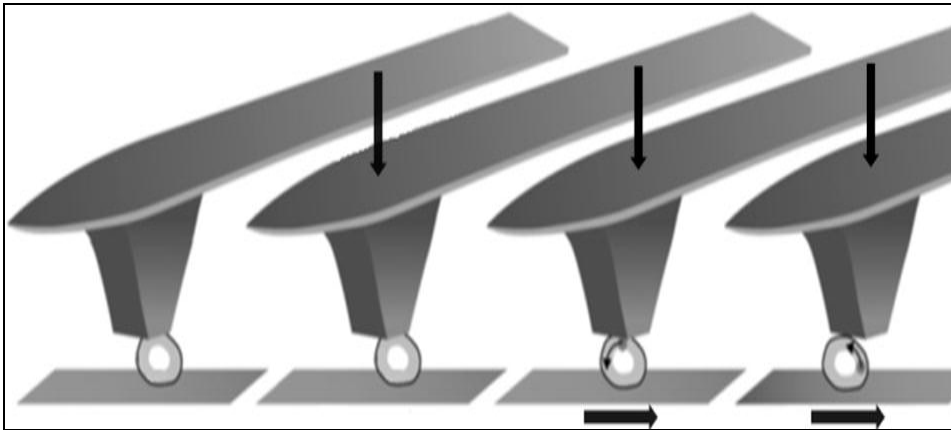


Fig. 5.2 - Displacements scheme performed in the finite element simulation: uniaxial compression and shearing.

Load to nanoparticle was applied by reducing the displacement between the two steel plates – in between which, the nanoparticle was placed. In this way, we could simulate how the two selected types of nanoparticles would respond in a given (the same) gap between the two contacting surfaces.

In terms of normal load, this could represent lubricated or non-lubricated contact.

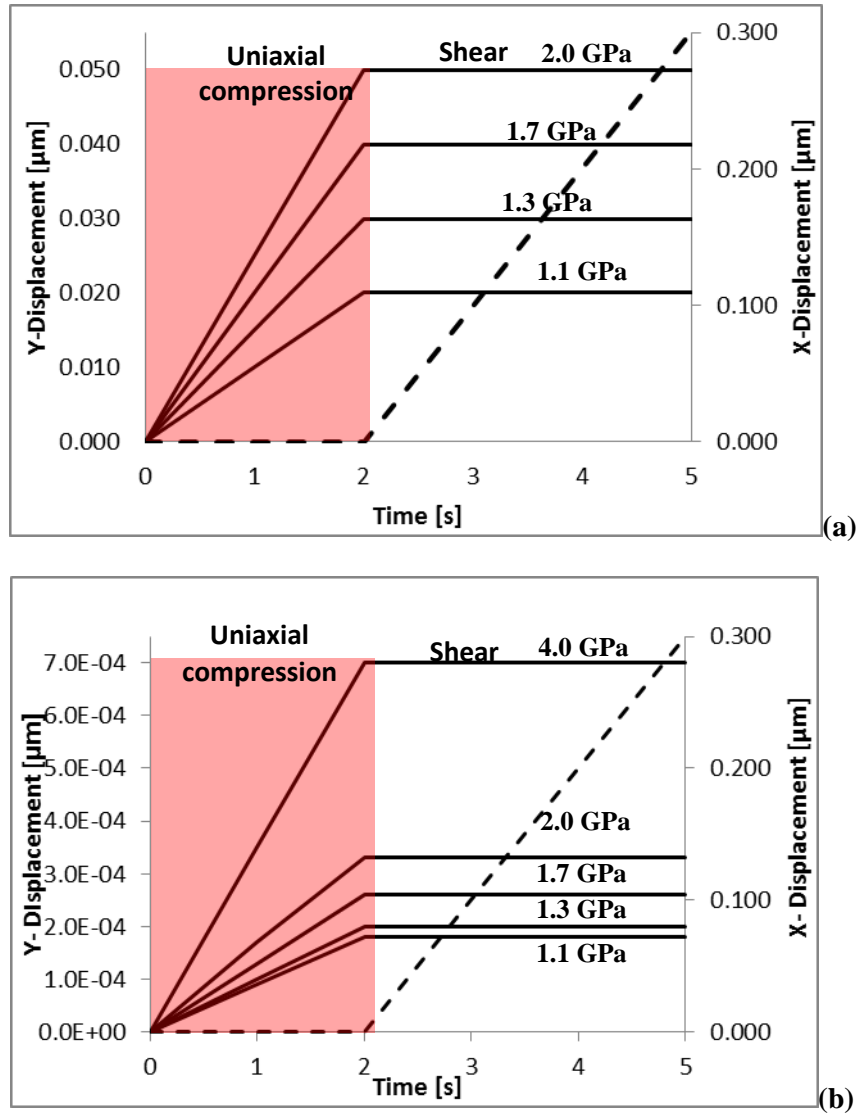


Fig. 5.3 – Displacement-time curves. The solid curves represent different time-Y displacement resulting in different contact pressures, **(a)** from 1.1 GPa up to 2.0 GPa for the hollow-core nanoparticle and **(b)** up to 4.0 GPa for the bulk-core (b), while the dashed line represents the displacement in X direction (300 nm) during the shearing phase

In the first part of simulation, i.e. in compression phase, a normal force was applied to the upper surface (by reducing the gap between the plates in y-direction). In order to investigate the effect of the pressure on the structural behavior of hollow-core MoS₂ nanoparticle, four different levels of Y-displacements were used: 20 nm, 30 nm, 40 nm and 50 nm by which the corresponding average pressures of 1.1 GPa, 1.3 GPa, 1.7 GPa and 2.0 GPa were achieved for the hollow nanoparticles. Instead for the bulk nanoparticles the simulating Y-displacements ranged from 0.18 to 0.70 nm, in order to obtain the same values of contact pressure compared to the hollow one. Therefore, at the time t=0s the upper steel surface is brought into contact with the nanoparticle and during the different simulation loads (upper disc displacements) the loading rate ranges from 10 to 25 nm/s, for 20 nm to 50 nm Y-displacement on the hollow nanoparticles, while the loading rate for the bulk core sphere ranges from 0.09 nm/s to 0.35 nm/s, for the 0.18 nm and 70 nm Y-displacement (Figures 5.3a and 5.3b).

At time t=2s the compression-only phase ends and the shear phase starts with a sliding speed of the lower surface equal to 100 nm/s. The contact between the nanoparticle and the steel disc surfaces is supposed to induce frictional energy dissipation with a coefficient of friction set equal to 0.05, which is a common average value for this class of materials, as reported in the literature [5].

5.2.3 Comparison of the load at a nanoparticle in FEM simulation and loads in typical macroscopic tribological experiments

The loads applied to single nanoparticle in our FEM simulations were calculated from the typical tribological contact conditions, which enable us approximate, but direct comparison of the current numerical simulation with the macro-scale tribological tests. To set the loads, a hollow nanoparticle (i.e. IF-MX₂) was used as model nanoparticle, which is more common than bulk nanoparticle, as mentioned before. Therefore, this comparison is valid only for IF-MoS₂ nanoparticles with hollow core, while for the bulk nanoparticle, the same displacement were used (gap between the plates) to mimic the same geometrical macro-scale contact conditions – but these led to very different loading of nanoparticles, as

seen already from Figure 5.3. A pin-disc experiment with a ball-on-disc configuration, using a 19.05-mm (3/4 in) diameter ball at a normal load of 35 N, which corresponds to a maximum Hertzian contact pressure of 1 GPa (mean 0.7 GPa) and a hertzian contact area of $5.23 \times 10^4 \mu\text{m}^2$ (with an hertzian contact deformation radius of 130 μm) has been used as a reference contact condition [24-26].

A typical and often used concentration of IF-MX₂ nanoparticles in the oil of 1 wt. % was used [5, 24]. By considering typical size of IF-MoS₂ nanoparticle of 80 nm [14] and a specific weight of 5.06 g/cm³ [16], this results in around 6×10^4 IF-MoS₂ nanoparticles trapped in the projection area of the elastic contact if a uniform distribution in the dispersion is assumed and considering a lubrication film thickness in the contact area of 1 μm . Accordingly, at perfectly flat surfaces and perfectly spherical shape of the hollow-core IF-MoS₂ nanoparticle, each nanoparticle would carry the load of 6 μN , which corresponds to 1.7 GPa of contact pressure at this nanoparticle. These values correspond also very well with previous experiments where loads ranging from 4 μN to 10 μN were used in AFM tests [27].

In view of this suggested concept for selected loads, a reasonable variation of the contact pressure in a range between 1.1 and 2.0 GPa was thus used for hollow nanoparticle. As explained above, the contact loading conditions are quite different for full-core nanoparticle, since the same displacement was used for hollow and full-core nanoparticle.

5.2.4 Numerical Results

5.2.4.1 Hollow-core MoS₂ nanoparticle: Compression phase

The force-time curves obtained during the simulations are reported in Figure 5.4. Only three loads are shown, i.e. 1.1, 1.3 and 1.7 GPa, corresponding to a maximum applied forces of 1.0 μN , 3 μN and 5.5 μN . Namely, with the highest pressure of 2.0 GPa used, the simulation did not get a converging solution indicating a complete deformation and shape degradation of nanoparticle, clearly showing it cannot resist the applied load. The simulation results show that as soon as the particle is loaded, it also deforms. At the end of the compression phase, i.e. when sliding/shearing step starts since the tangential load is additionally

applied, important morphological changes were observed in the nanoparticle. These structural/morphological changes are accompanied by a sudden drop of the normal force, as seen for all three cases in Figure 5.4.

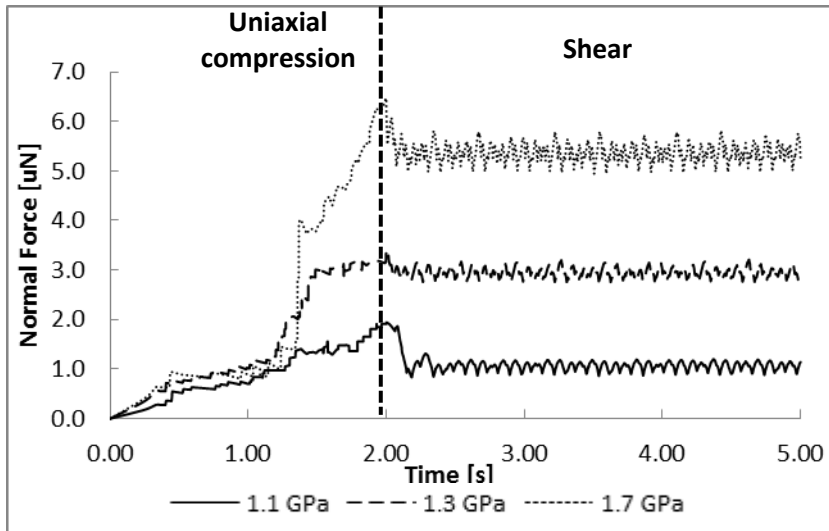


Fig. 5.4 – Force-time curves as function of testing time for different contact pressure used

Table 2 depicts the deformation of the nanoparticle depending on the normal load at the end of the compression phase, i.e. at the maximum normal load.

Hollow-core MoS₂ nanoparticle clearly cannot withstand high contact pressures, which is seen also from the geometrical changes defined by “deformation ratio” (ratio between semiaxes: a/b), presented in Table 5.2. Geometrical changes of the nanoparticles are between 35 % and 60 %, depending on the load.

At 2 GPa the MoS₂ nanoparticle failed as it was completely broken, as mentioned previously. The contact diameter between the nanoparticles and the disc was from 30 nm to 62 nm for the contacts that successfully carried the load.

			FAILURE
P=1.1 GPa	P=1.3 GPa	P=1.7 GPa	P=2.0 GPa
d=30 nm	d=50 nm	d=62 nm	Failure
a/b=0.65	a/b=0.52	a/b=0.40	Failure

Tab. 5.2 - Deformation ratio, maximum average contact pressure and hertzian deformation width for different presented Y-displacements

5.2.4.2 Hollow-core MoS₂ nanoparticle: shear phase

In the second phase of the simulation, the lower steel surface started to slide and introduce the shear force in the contact. During this sliding stage the normal force applied to the nanoparticle was kept constant. The behavior of the nanoparticle during the simulation of tribological sliding is discussed from snapshot taken at different sliding times, Figure 5.5. A white spot was placed as a marker on the nanoparticle in order to easier observe its movement.

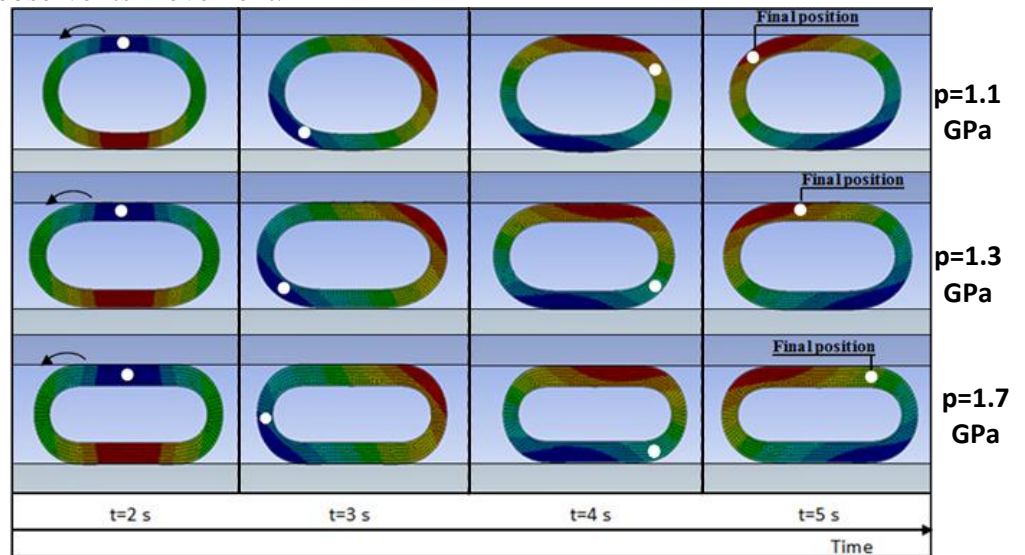


Fig. 5.5 – Sliding snapshots of the hollow nanoparticles at different sliding times for the different presented contact pressure.

As can be clearly seen, the motion of the nanoparticle depends on the load and thus it is not uniform. Namely, the nanoparticle does not only slide or only roll, but the motion is a combination of the two – depending on normal load. To further reveal the actual behavior, a diagram of “slide-to-roll” ratio (SRR), as defined with Eq. 5.5, is developed for the shearing phase and is presented in Figure 5.6.

$$SRR = \frac{u_{disc} - u_{NP}}{u_{disc}} \quad (5.5)$$

where u_{disc} is the speed of the upper surface while u_{NP} is the nanoparticle speed. As seen from Figure 5.6, in the first part of the sliding the particle “sticks” on the surface more strongly (larger portion of sliding compared to rolling) and so it has higher SRR value than at later stage of sliding, which is true for all loads. After certain time, portion of sliding is reduced on account of more rolling and SRR is reduced.

It can be seen that at higher loads, the nanoparticles experience more than 2-times greater portion of sliding compared to rolling at the start of sliding (note 35 % vs. 15 % SRR for 1.7 and 1.1 GPa, respectively), but it also take less time to achieve steady state shear conditions (0.2 seconds vs. 0.6 seconds for 1.7 and 1.1 GPa, respectively). It is further of great importance to observe that in the steady-state sliding, the shearing is much higher at high pressure conditions with about 19% SRR at 1.7 GPa, while this value is much lower at low pressure, being only about 3% SRR at 1.1 GPa, indicating that low loads promote rolling at these conditions, while high loads the shear.

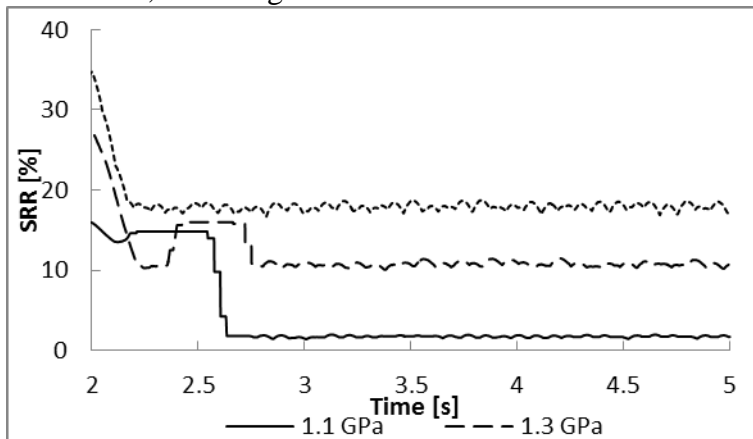


Fig. 5.6 – SRR at different sliding time for the presented pressure contact

5.2.4.3 Full-core bulk MoS₂ nanoparticle: Compression phase

The force-time curves obtained during the simulations of bulk full-core nanoparticles are presented in Figure 5.7. Unlike with the hollow-core nanoparticles, five loads are shown, i.e. those for pressures from 1.1 to 4.0 GPa, corresponding to a maximum applied force ranged from 4 nN to 140 nN. As it can be clearly seen in Figure 5.7, unlike the hollow particle that at the pressure of 2.0 GPa crashed, for the bulk-core nanoparticle the spherical shape was preserved and the failure value in terms of contact pressure was equal to the bulk MoS₂ compressive strength, 4.0 GPa (almost 140 nN).

Although the bulk nanoparticle started to deform immediately after the introducing the normal load, the deformation is slow, namely much lower compared to hollow nanoparticles, as can be seen from slope of deformation curves in Figure 5.7. The value of the deformation area for the bulk nanoparticle is also close to those predicted from the hertzian theory for the contact mechanics. At the end of the compression phase, i.e. when sliding/shearing step starts at time $t=2s$, tangential load did not induced any significant changes in the normal force or deformation of the nanoparticles, which was – the contrary – the case for hollow nanoparticles (compare Figures 5.4 and 5.7).

In Table 5.3 are shown the simulation results obtained at the end of the uniaxial compression phase ($t=2s$) are reported in order to observe in detail the deformation of the full-core bulk nanoparticle at different maximum contact pressures.

As expected, with increasing the contact pressure, the deformation also increase and so a decrease of the deformation ratio a/b has been observed. Depending on the contact pressures, the bulk nanoparticles deformed only between 0.4 and 1 %, which remarkably lower than for hollow nanoparticles at the same contact pressure.

Accordingly the deformation area diameter ranges from 1.6 nm to 3.1, almost 2000 times less than those obtained for the hollow nanoparticle. This is can clearly explain e bulk nanoparticle could be considered as a massive ball of dichalcogenide material instead of the hollow nanoparticle closer to a rubber material than to a massive one. Due to this

consideration the load-carrying capacity of bulk nanoparticle is lower compared to hollow nanoparticles one, while the pressure failure value is higher (compare a/b ratios in Tables 5.2 and 5.3).

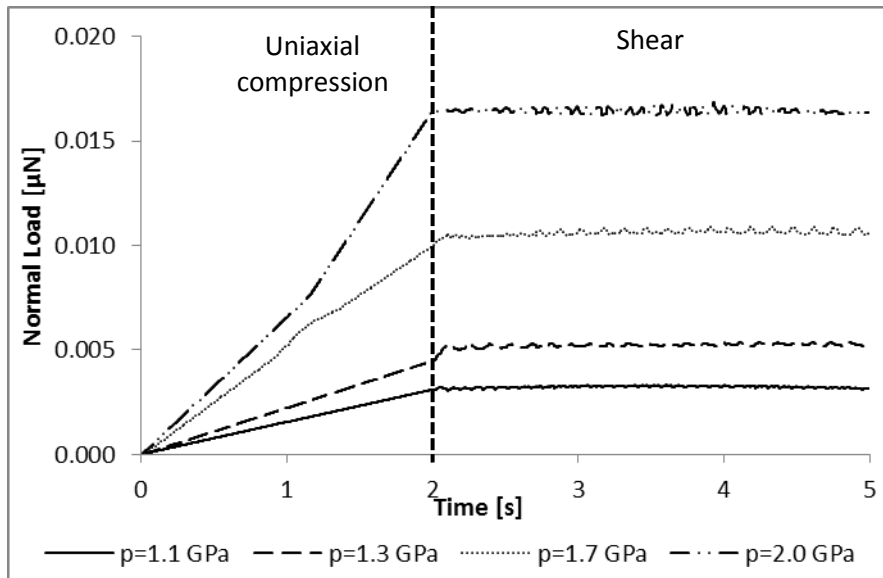


Fig. 5.7 – Force-time curves as function of testing time for different contact pressure used

Y-disp=0.18 nm	Y-disp=0.22 nm	Y-disp=0.29 nm	Y-disp=0.34 nm	Y-disp=0.70 nm
p=1.1 GPa	p=1.3 GPa	p=1.7 GPa	p=2.0 GPa	p=4.0 GPa
d=1.6 nm	d=1.9 nm	d=2.4 nm	d=3.1 nm	FAILURE
a/b=0.996	a/b=0.995	a/b=0.993	a/b=0.991	FAILURE

Tab. 5.3 - Deformation ratio, Y-displacement and hertzian deformation width for different maximum average contact pressures presented obtained for the bulk nanoparticle

5.2.4.4 Full-core bulk MoS₂ nanoparticle: shear phase

The behavior of the nanoparticle during the second phase, i.e. during the sliding, where shear is introduced, is discussed from snapshots taken at different times from $t=2\text{s}$ to 5s , as shown in Figure 5.8. A white point marker was placed on the particle in order to facilitate observing the movement of the particle from the simulation.

The white point on the bulk-core accomplishes a number of revolutions lower than the hollow-core sphere, although the SRR is lower for the bulk nanoparticle and the rolling component of the motion is greater than the hollow one. This result is possible to explain considering that due to its greater deformation the hollow-core nanoparticle has a radius less than massive nanoparticle (40 nm), but the lower surface moves at a constant sliding speed leading to a higher rotation speed for the hollow-core nanoparticle.

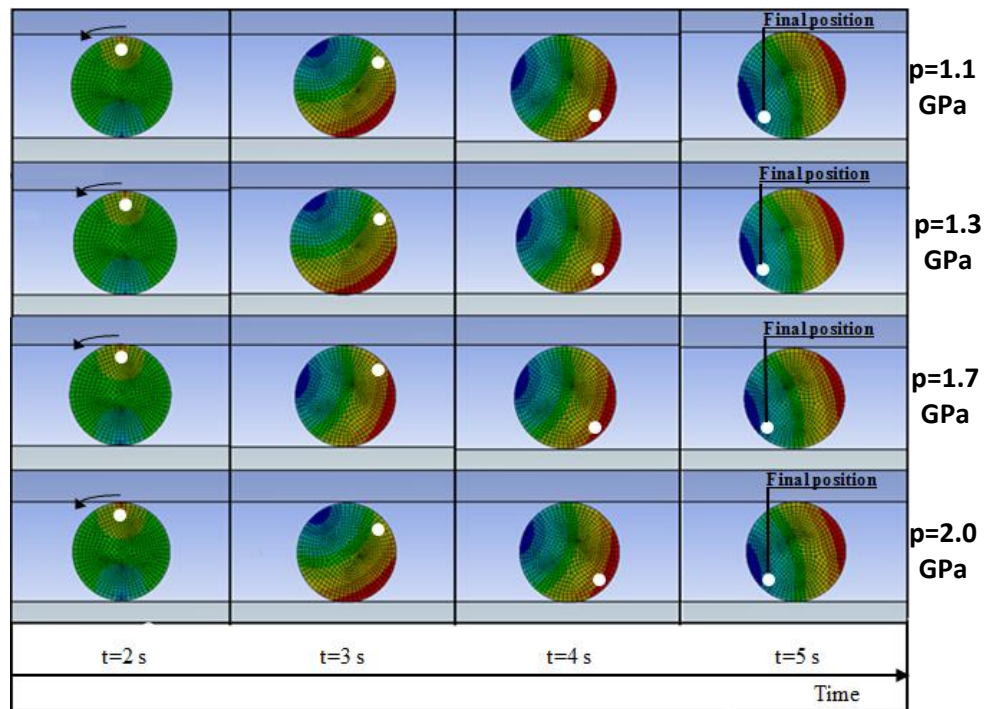


Fig. 5.8 – Sliding snapshots of the hollow nanoparticles at different sliding times for the different presented contact pressure. The white point in the different snapshots allows to follow the rolling of the hollow nanoparticle

The nanoparticle motion in this case is quite different due to the remarkably different shape deformation. As expected the rolling part of the motion is predominant for the bulk nanoparticle due to its almost preserved spherical shape. Slide-to-roll ratio (Eq. 5.5), plotted in Figure 5.9, indicates that sliding component of the motion ranges only from 0.8% to 2% much more sliding occurs at the very beginning of the sliding/shearing phase, i.e. between 2% and 4% depending on the load, which later comes to a steady-state tribological contact with SRR of only about 0.5% and 1.5% at lower and upper limit-pressures of 1.1 GPa and 2.0 GPa, respectively (Figure 5.9). The results are almost perfectly compared with those obtained in a ball bearing for the ball-plate simulation contact [28]. Again, lower loads promote rolling, while higher loads promote shear (compare Figures 5.6 and 5.9).

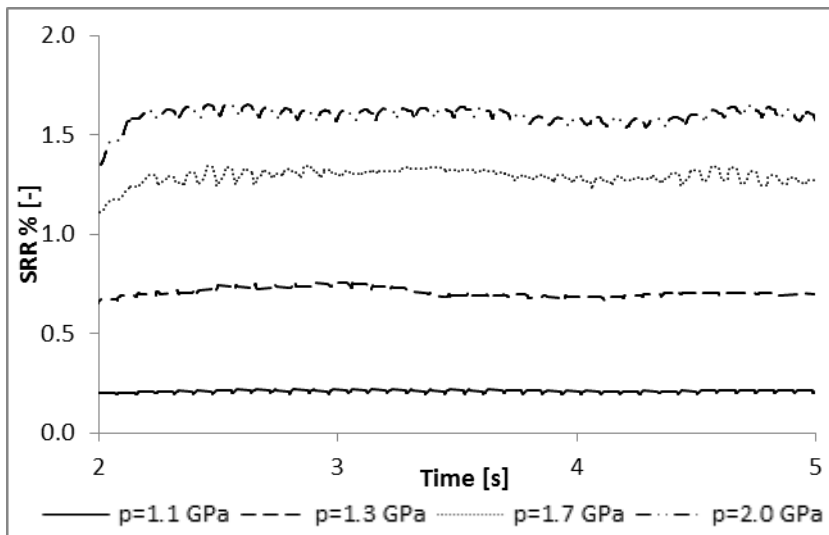


Fig. 5.9 - Slide to roll ratio at different sliding times for the presented contact pressure

5.2.4.5 Effect of nanoparticles structure (hollow-core vs. full-core) on their mechanical response to external loads

In this section mechanical and tribological results obtained in the simulations are compared in order to clarify the effect of the two different structures (hollow-core and full-core) on the nanoparticle behavior.

First, it should be emphasized that for both types of nanoparticles the simulation could not converge at the highest contact pressure, 2.0 GPa and 4.0 GPa for the hollow and the bulk nanoparticle respectively, which suggests that the nanoparticles could not resist the loads.

This occurred at 11.1 μN and 140 nN for hollow-core and full-core nanoparticles, Tables 5.2 and 5.3. Regarding the nanoparticles deformation, it is interesting that our FEM results of hollow-core particles are quite similar to those of Lahouij et al. [27] using AFM tests with similar hollow nanoparticles. Namely, they observed a nanoparticle compression of 45% at a contact pressure close to 2.2 GPa and also report that the shape of a single hollow MoS_2 nanoparticle can be almost preserved at around 1.1 GPa. Our calculations show 35-60 % deformation in the range of 1.1 to 1.7 GPa, Table 5.2.

These results of course depend on thickness, size and some other nanoparticle properties, but in general - within the order of magnitude – confirm good agreement of nano-scale behavior found in experiments and simulation. From the presented results it is possible to observe significantly smaller deformation, but higher pressure, generates at full-core bulk nanoparticle. Hollow-core nanoparticles are therefore able to withstand higher external loads compared to bulk nanoparticles due to its structure and mechanical behavior.

This would apply increasing the number of dichalcogenide layers in the nanoparticle and subsequently the volume occupied by the MoS_2 (in this way the nanoparticle become more massive), the nanoparticle increase the compressive failure strength. In this way the nanoparticle can withstand higher contact pressure but with a lower load-carrying capacity.

Furthermore, Figure 5.10 shows the values of the normal loads carried by the nanoparticles for different displacements imposed in the simulations, clearly confirming much higher load-carrying capacity of hollow-core nanoparticles. The failure loads were 11.1 μN for the hollow-core nanoparticle and 140 nm for one with a full core, which makes almost 80-times difference. Furthermore, in Figure 5.11, the different values for the Y-displacement of the upper surface simulated to achieve the presented contact pressures are shown.

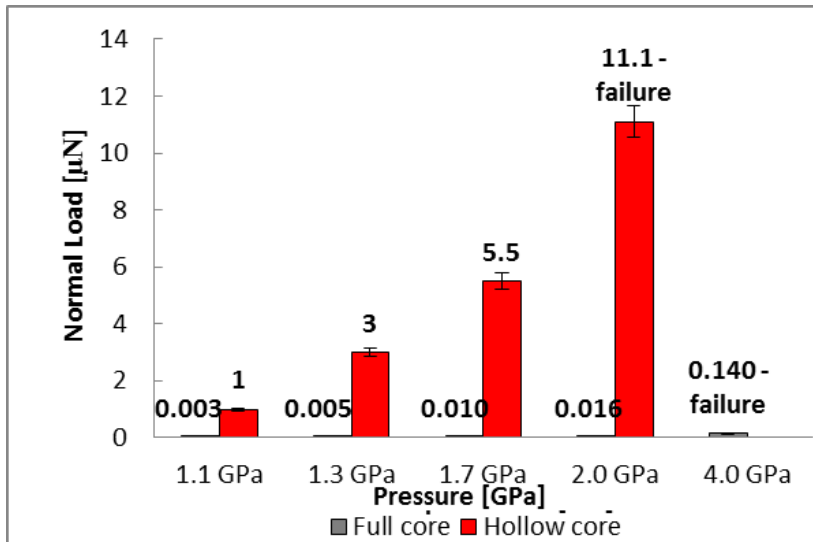


Fig. 5.10 – Normal load comparison for the different core structure (hollow and bulk) of the particle for the presented contact pressure

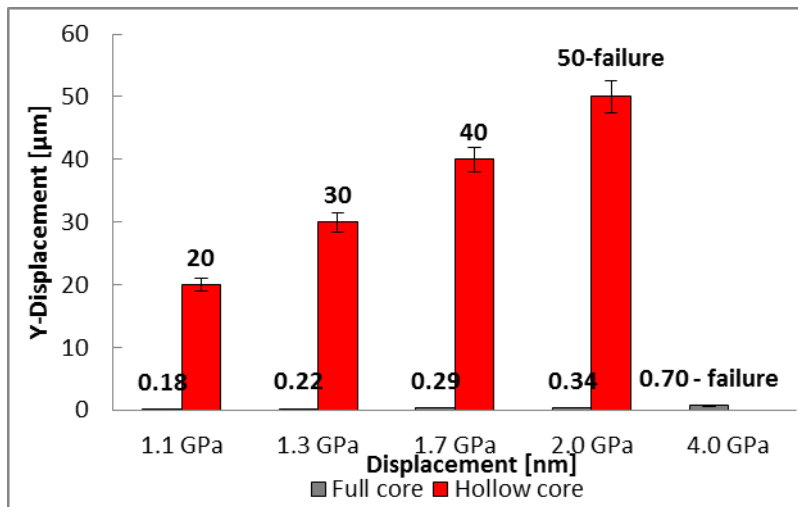


Fig. 5.11 – Upper surface displacement comparison for the different core structure (hollow and bulk) of the particle for the presented contact pressure

Finally, the shear stress of both, full-core and hollow-core nanoparticle has also been compared. As for the equivalent Von Misses stress, also in

this case the distribution of the shear stress is deeply influenced by the structure of the core. Snapshots of the types of two nanoparticles at the end of the simulation for the three loads are presented in Figure 5.12. While the snapshots show the distribution of the shear stress along all the nanoparticles, Figure 5.13 presents the values of the maximum shear stresses during the sliding phase for both nanoparticle structures at different loads. A higher value of the shear stress for the hollow-core particle can be clearly noticed, especially with increasing the load (obtained through contact y-displacement), which is in our case as high as more than two-fold.

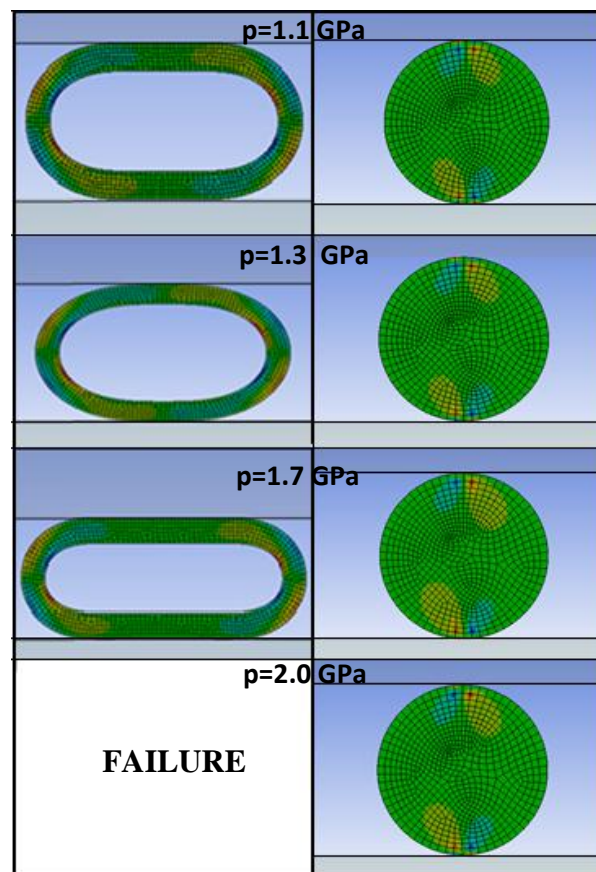


Fig. 5.12 – Shear stress snapshots comparison at the end of test ($t=5s$) for the different presented contact pressures

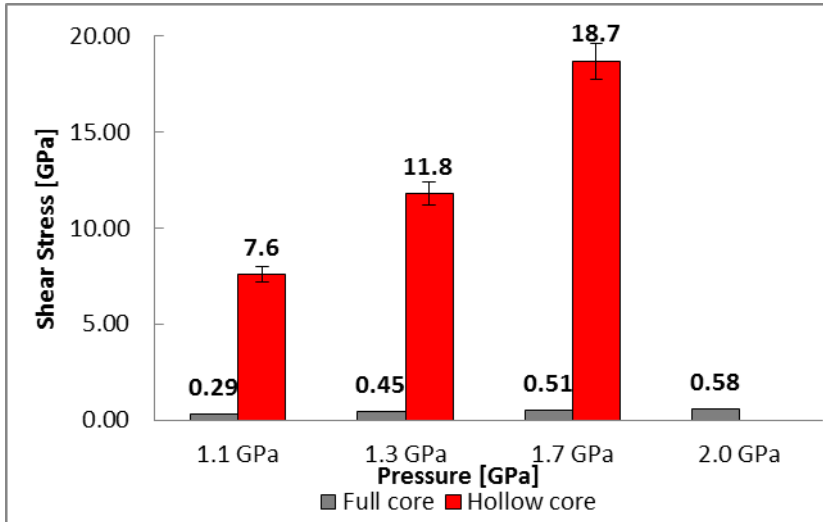


Fig. 5.13 – Shear stress comparison for the different core structure (hollow and bulk) of the particle for the presented contact pressure

5.2.4.6 Friction behavior of hollow- and full-core nanoparticles

This results show that the hollow nanoparticles are subjected to significantly higher value of shear stresses than bulk ones at the same contact pressure (Figure 5.13). This means that the hollow-core nanoparticles will tend to exfoliate and lose the outer layers of its laminar structure at significantly lower values of loads. Therefore, the thin layer nanoparticles promote exfoliation lubrication mechanisms. This property is a direct consequence of the lower stiffness that thin-wall particles possess, leading to much larger deformation of the hollow nanoparticle compared to full-core nanoparticle. In view of the above finding, is of great importance to analyze how much of shear and how much of rolling is induced to different particles at different contact pressure. Clearly, the sliding vs. rolling depends significantly on these variations, as well as on the static or dynamic conditions.

The obtained results for the SRR clearly show the influence of the structural characteristics of the nanoparticle on the rolling and sliding component of the motion, Figure 5.14.

The hollow-nanoparticle shows a greater percentage of deformation that leads to a significantly higher SRR compared to the bulk nanoparticle. Accordingly, for the massive nanoparticle the spherical shape is almost totally preserved for normal loads and pressures analyzed in the simulations (1.1 GPa - 4.0 GPa).

Moreover, the bulk MoS₂ nanoparticle is subjected to lower strain before its failure due to the achievement of the compressive strength value. The different results of the two different structures analyzed in the FEM simulations lead to two different tribological behaviors assumed for the IF nanoparticles and in particular to their mechanism of lubrication.

Accordingly, the bulk particle having almost unchanged its spherical shape behaves essentially like a ball bearing inside the tribological contact, with a predominant percentage of rolling motion (from 99.2% up to 96% for 1.1 to 2.0 GPa, respectively). Instead, regarding the hollow nanoparticle the motion behavior is more complex because its deformation causes an increase in the sliding motion percentage.

The component of the sliding motion of the particle, in particular, increases with the contact pressure due to loss of the spherical shape and a ball bearing behavior. However, by considering that much higher shear and sliding motion are induced to hollow-core particles, this will result in significantly higher exfoliation rate and deposition of MoS₂ sheets at the tribological contact surfaces, thus enable formation of the MoS₂ tribofilm, which reduces friction and wear [25,26]. In agreement to this, it was reported in the recent literature that higher rate of deformation and exfoliation of nanoparticles significantly promotes improvement in tribological performance [29,30].

Furthermore, even if the bulk particle could behave as a sphere of a bearing, it shows unlike the hollow nanoparticle a reduced load-carrying capacity. In this way the massive nanoparticle collapse at lower loads compared to the hollow nanoparticle, losing the tribological advantages due to the spherical shape. For this reason, the hollow-core nanoparticles appear better type of lubricating particles compared to full-core.

Figures 5.6 and 5.9 further provide the answer on the motivation of this section, which relates to potential of nanoparticles to provide the rolling mechanism in the tribological contacts. By calculating the percentage of sliding vs. rolling, the results clearly show significant,

even predominant, rolling action over sliding in steady-state sliding conditions. This is true for both types of nanoparticles, and is more pronounced for full-core nanoparticles and for lower loads. In summary, this work has shown that the lubrication mechanism proposed by Tenne et al [5], in which the spherical shape of the nanoparticle would allow them to behave as a nano-ball bearing, could be enforced under ideal surface conditions as used in these simulations.

Under this assumption, the nanoparticle with its rolling friction process could enhance the lubricating properties of the tribopair. Moreover, the hollow nanoparticle due to the possibility to withstand higher deformation shows a higher load-carrying capacity before collapse and it should be an important advantage in terms of tribological performance.

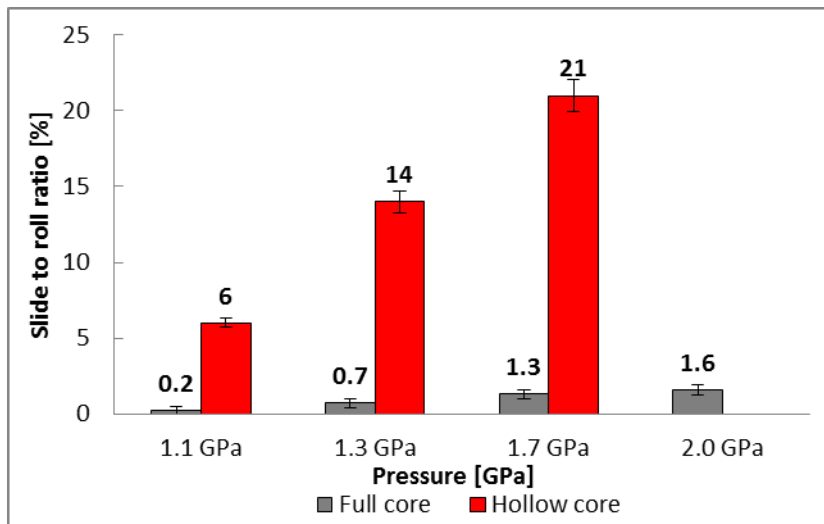


Fig. 5.14 – Slide to roll ratio for the different nanoparticle core structures (hollow and bulk) for the presented contact pressure in steady state sliding (time: 5 sec)

Of course, it should be clearly emphasized that all our surfaces (plates and fullerenes) are ideally smooth, which cannot be achieved in real tribological situation. Moreover, the results are also affected by assumed (fixed) coefficient of friction (0.05). However, the study of these

parameters is beyond the scope of this work and is a part of our on-going research.

These results point out the strong influence of the intrinsic characteristics of the nanoparticles, in particular the influence of the hollow and full core in the center of the MoS₂ nanoparticle on their tribological properties.

In the light of the generally good qualitative agreement between the experimental and simulated results is extremely encouraging for the future outlook.

Actually, the presence of the hollow core at the center of the particles explains the lower stiffness and, therefore, the ability for the hollow-core particles to have a greater deformation than the full core MoS₂ nanoparticle.

From the present simulations it is possible to conclude that for spherical MoS₂ nanoparticles, rolling is a predominant mechanism in the range of pressure from 1.1 to 1.7 GPa for the hollow and massive MoS₂ nanoparticle.

Moreover, sliding is shown to be relevant for higher pressure for the hollow nanoparticles, where the displacement of the upper surface strongly deform the nanoparticle and does not permit its free rolling. Furthermore, even if it has been not simulated in this study, the exfoliation process of the IF nanoparticles could become the dominant mechanism at high values of contact pressure; above 2 GPa and (slow) shear for the hollow core nanoparticle, while for the full-core nanoparticle the spherical shape is almost preserved.

These failure values for the normal load are equal to 11.1 μN for the hollow-core nanoparticle and 0.140 μN for full core, over these limits the simulation were interrupted due to the non-convergence of the solution, this probably means that the nanoparticles collapse at these normal force values.

The hollow nanoparticle is subject to a higher value of shear stress this means that the particle tends to exfoliate and lose the outer layers of its laminar structure for rather low values of the contact pressure

5.3 ANALYSIS OF THE MoS₂ NANOPARTICLE DEFORMATION AND MOTION BEHAVIOR: THE INFLUENCE OF A SOFT ROUGH SURFACE

5.3.1 Experimental simulation: Surfaces and nanoparticle

The selected contact in this section consists in two steel discs pressing and shearing a single nanoparticle in between them. The upper disc was perfectly smooth and plane while the lower disc presented a real rough profile.

The nanoparticle used in the simulations was an individual nanoparticle of molybdenum disulphide with a hollow core nanoparticle, the same described in par. 5.2.1. An atomic force microscope (AFM) was used to acquire the rough profile of a steel disc. This profile was successively used to model the 2D profile of the lower disc for the finite element simulations.

The surface roughness was measured using a CP-II AFM (Veeco, USA). The scans were made along a length of 20 μm .

The analyses were made using ProScan 1.8 Data Acquisition image-analyzing software, associated with the AFM [17]. In Figure 5.15a is reported the acquired surface profile used for the lower disc. The average arithmetic roughness measured by the AFM was 0.005 μm .

Future works will be performed using a higher average roughness, 0.05 μm , in order to evaluate the behavior of the nanoparticles when it approaches peaks or valleys with a size comparable or even bigger than the average nanoparticles radius.

For the finite element simulations an area, highlighted in red in Figure 5.15b has been chosen in order to model a surface disc with 2 μm length.

The red area has been selected in order to simulate the approaching of the nanoparticle with a peak with a height of 7 nm and a slope equal to 2.4%.

As for the simulation presented in the previous section, the size of the nanoparticle was selected based on typical data of these nanoparticles published in recent literature about the synthesis of IF-molecules [16].

The external diameter has been set to 80 nanometers and inner diameter to 60 nanometers.

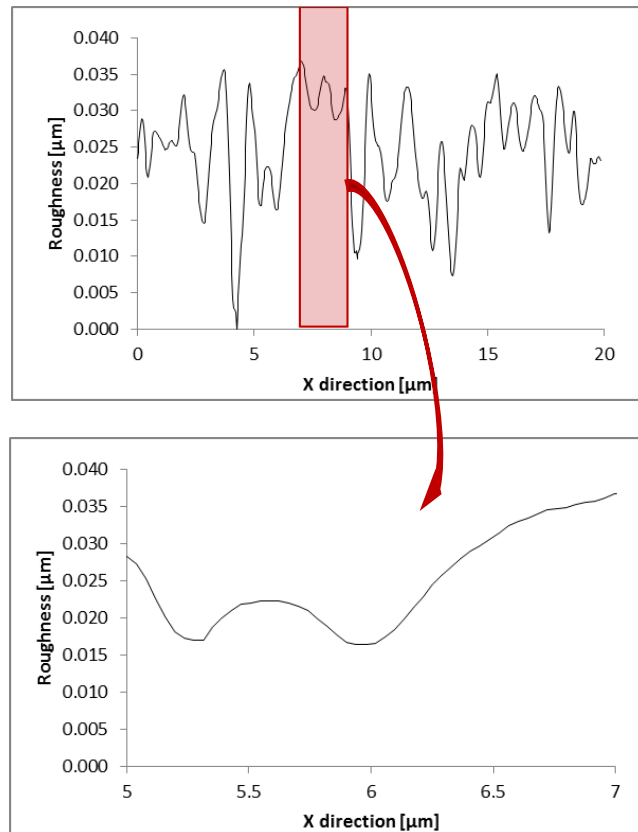


Fig. 5.15 – (a) Surface roughness profile acquired through AFM. The average arithmetic roughness measured by the microscope is $0.005 \mu\text{m}$. The acquired data cover a width of $20 \mu\text{m}$, in red the roughness profile chosen for the finite element simulations. (b) Particular of the surface roughness chosen for the finite element simulations.

Accordingly, in Figure 5.16 is reported the undeformed initial geometry of the hollow MoS_2 nanoparticle used for the finite element simulations. The area interested by the hollow MoS_2 nanoparticle displacements used for the finite element simulations is highlighted in red.



Fig. 5.16 – Undeformed geometry of the hollow MoS₂ nanoparticle used for the finite element simulations. The area interested by the hollow MoS₂ nanoparticle displacements used for the finite element simulations is highlighted in red

5.3.2 Numerical simulated testing procedure

In the same way of the previous paragraph, the simulation loading scheme consisted in two different steps: a compression and a shear-sliding test. In the first step a normal force (set in the simulation in terms of displacement of the upper plate in the y-direction) was applied to the upper surface. In the second, for the sliding phase, a displacement was applied in the x-direction. The aim of these numerical simulations is to evaluate the influence of a soft surface roughness on the nanoparticle behavior. In this way, the simulated results, for a “real smooth surface”, i.e. with a very low roughness, can be compared with those obtained using two perfectly ideal smooth and plane surface. The value of the contact pressure has been set equal to 1.7 GPa. The compression and shear rate used in the two motion phase of the loading scheme are almost the same those used in the previous paragraph for the highest contact pressure value on the hollow core nanoparticle, 1.7 GPa. The contact between the IF-nanoparticle and the surfaces is supposed frictional and the friction coefficient has been set equal to 0.05, a common value class of materials reported in the literature [3].

5.3.3 Numerical results

5.3.3.1 Compression phase

The simulation results show that as soon as the particle started to be loaded it also deforms. At the end of the compression phase, i.e. when sliding/shearing step starts, important morphological changes were observed. The shape of the particle progressively changes to an ellipsoidal shape. The results, shown in Figure 5.17, indicate that the particle is oblate after compression and accommodates the contact

pressure. The normal force value increases during the shearing phase due to the changing of the free space between the two contact surfaces. For this reason, in order to keep constant the value of the contact pressure, an increase of the applied normal load is necessary. As showed in the previous section of this chapter, hollow MoS_2 nanoparticle cannot withstand high contact pressure, which is seen also from the “deformation ratio” (ratio between semiaxes: a/b), presented in Table 5.2. Geometrical change is between 35% - 60%. Due to rough profiles of the surface, the maximum contact pressure, applied on the particle, changes during the simulation. Actually, the nanoparticle during the motion changes its contact area with the surface, so that to keep the displacement in Y-direction constant during the shear phase, the normal force and the contact pressure increase. In particular, the contact pressure at the end of the simulation was estimated to be equal to 2.2 GPa, also highlighted in a red circle in Figure 5.18. For such a pressure, a smashed particle was observed. Such observations are consistent with the results obtained by Tevet et al. [32]. A similar result has been also found in Lahouij et al. [26] in AFM tests for a contact pressure equal close to 2.2 GPa and a percentage of compression of 45%. Under 1.1 GPa uniaxial pressure, it was found, in both ref. [27] and the present work, that the shape of a single hollow MoS_2 nanoparticle was almost preserved.

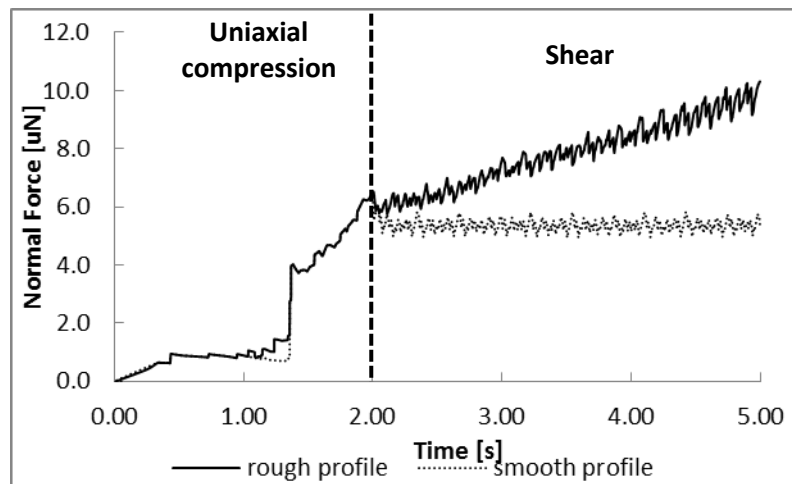


Fig. 5.17 – Normal force comparison at different sliding times between the roughness surface (solid lined) and the ideal smooth surface (dashed line) for the hollow nanoparticle

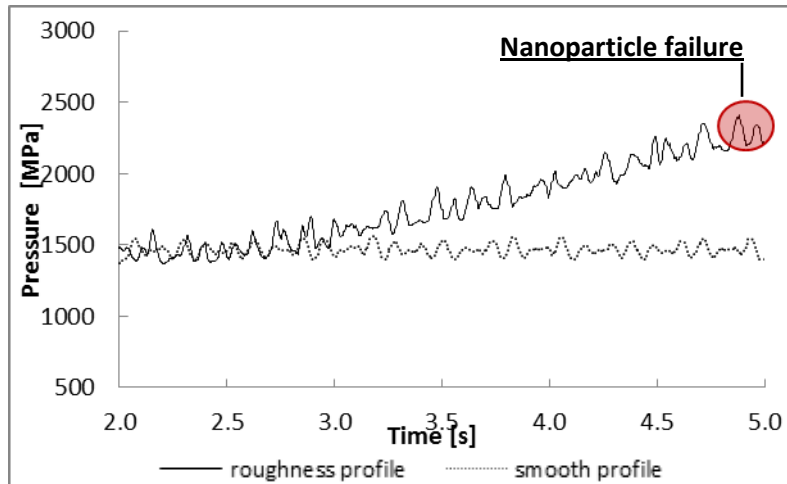


Fig. 5.18 – Pressure comparison at different sliding times between the roughness surface (solid lined) and the ideal smooth surface (dashed line). In the red circle is possible to observe the failure point of particle. At that pressure the nanoparticle collapse and the finite element problem does not converge to a solution.

5.3.3.2 Numerical results: shear phase

In the second stage of the simulation, the lower steel rough surface was moved to slide and introduce the shear force. During this sliding stage the normal force applied to the nanoparticle was kept constant. The behavior of the nanoparticle during this simulation of tribological sliding test is discussed from snapshot taken at different sliding times, Figure 5.19.

A white point was placed on the particle in order to easier follow the movement of the particle. As can be clearly seen, the nanoparticle does not only slide or only roll, but the motion is a combination of the two.

Moreover, the share of sliding and rolling depends on the rough profile of the lower surface and on the normal load. It is possible to note, in Figure 5.18, that when the nanoparticle approaches the beginning of the asperity it starts to deform heavier due to the decrease of the space between the steel surfaces. Accordingly, a diagram of “slide to roll” ratio, according to Eq. 5.5, is showed in Figure 5.20.

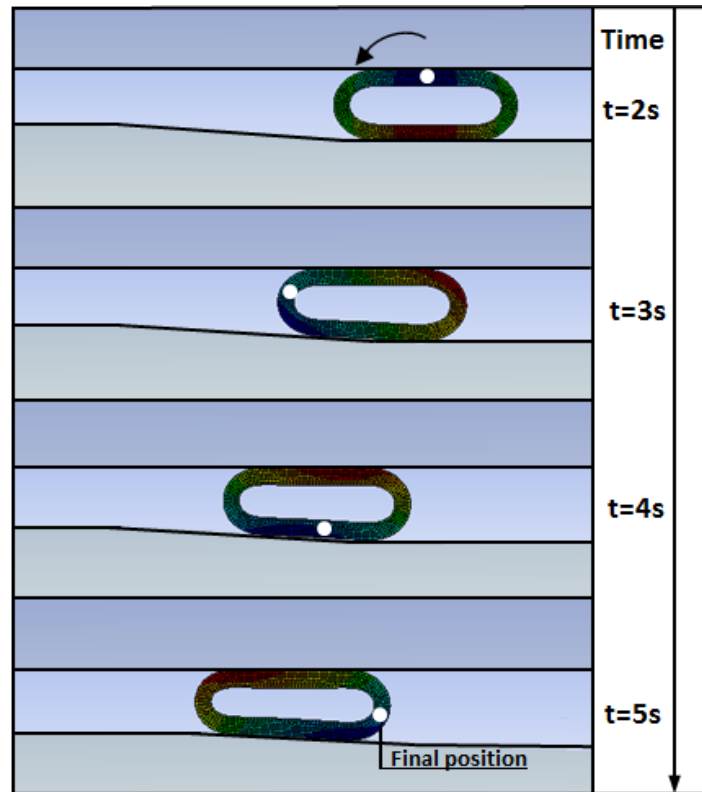


Fig. 5.19 - Sliding snapshots of the hollow nanoparticles at different sliding times for the presented contact pressure with a $Ra=0.005\mu\text{m}$. The white point in the different snapshots allows to follow the rolling of the hollow nanoparticle.

In the first part of the sliding stage the particle sticks on the surface more strongly with higher SRR value, later it starts to take part of rolling and SRR is partially reduced. The behavior between the plane case and the one with the presence of roughness, differs from $t=2.1$ s. In fact, in the case with perfectly smooth surfaces the SRR ratio is kept almost constant during the entire phase of sliding, with an average value of 19% as result of the simulation at 1.7 GPa, with a strong predominance of the rolling component. While in the case with rough surfaces it is possible to note an increase of the sliding component during the second phase, i.e. shearing, of the test. Accordingly, due to the slope of the surface profile related to the roughness of the lower surface, which also leads to a greater

deformation of the nanoparticle, the sliding component of the nanoparticle motion assumes a role much more important than in the case with perfectly smooth surfaces.

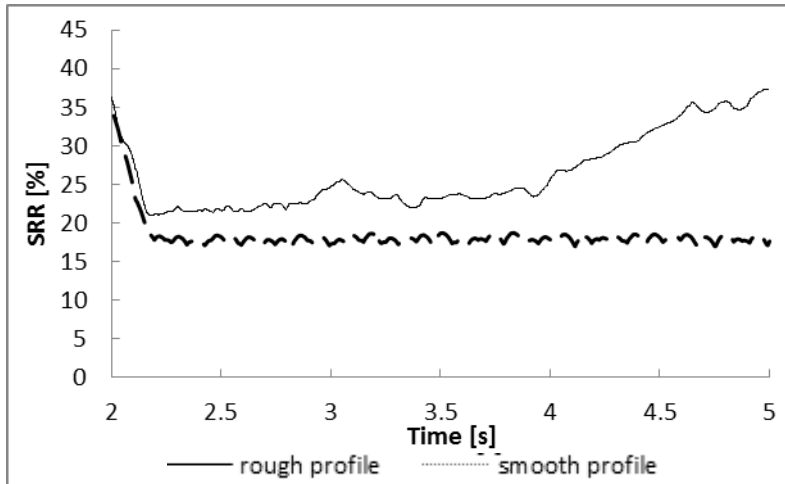


Fig. 5.20 – Slide to roll ratio comparison at different sliding times between the roughness surface (solid lined) and the ideal smooth surface (dashed line) for the hollow nanoparticle

5.3.4 Comparison between rough and smooth surfaces

In this section some mechanical and tribological results obtained in the simulations have been compared in order to investigate the effect of soft roughness of the surfaces on the nanoparticles behavior with respect to the smooth surfaces case. The Figures 5.21a and 5.21 show the different behavior of the two MoS₂ nanoparticle structure in terms of equivalent stress calculated through the Von Mises criteria during the compression and the shearing phase. It is clearly possible to observe the different distribution of the maximum equivalent stress in the spherical shape due to the difference in core structure and during the different phases of the finite element simulations.

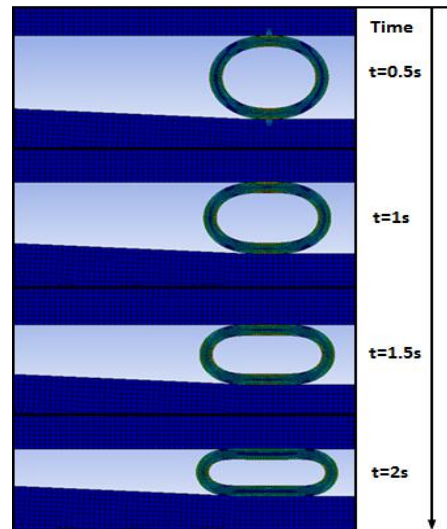


Fig. 5.21a - Finite element results of Von Mises equivalent stress for the hollow core structure during the compression phase

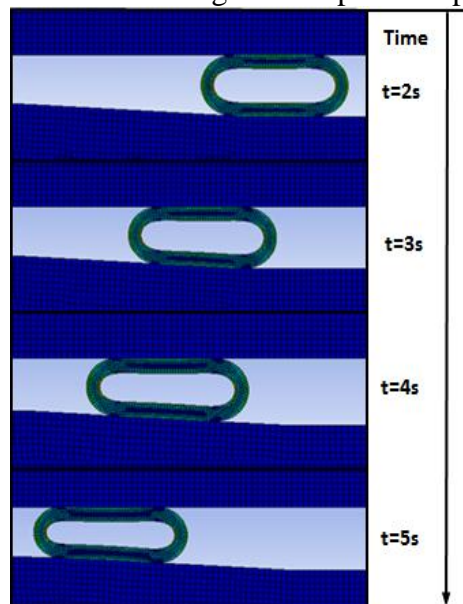


Fig. 5.21b - Finite element results of Von Mises equivalent stress for the hollow core structure during the shearing/sliding phase

Making a comparison between the different values achieved by the normal load on the nanoparticle in the case of smooth and rough, is

possible to note the value for which the simulations were interrupted due to the non-convergence of the solution, due to the destruction of the nanoparticle. The average normal loads applied on the hollow nanoparticle were 5.5 μN and 7.8 μN for the rough and smooth profile, respectively.

It is important to observe that the sliding component of the nanoparticle motion significantly increases with the presence of a rough surface profile that influence the deformation of the nanoparticle and the way in which the nanoparticle itself move in the gap between the two tribopair contact surface. Accordingly the average SRR percentages were 19% and 27% for the hollow nanoparticle structure in the case of smooth and rough surface, respectively.

Finally, the shear stress of both full and hollow core nanoparticle has also been compared for the smooth and rough simulating contact. The result shows that the hollow nanoparticle is subject to a higher value of shear stress, i.e. 18.7 GPa and 21.0 GPa for the smooth and rough profile, respectively, which means that the nanoparticles will tend to exfoliate and lose the outer layers of its structure at significantly lower values of load (contact pressure) than the bulk core nanoparticle. This evidence is important to understand as the exfoliation could play, over a threshold of contact pressure, for a real tribopair, with rough surface, an important role in the nanoparticle lubrication mechanism.

From the results shown in this chapter some consideration about the mechanical of the simulated nanoparticles in presence of rough and smooth surface can be made. The compression failure strength and the elastic behavior of the nanoparticles under uniaxial compression were studied. It was shown that hollow closed nanostructures were able to withstand very elastic stress. The compression failure strength of these nanoparticles was found to be as high as 2.2 GPa.

The possible mechanism of lubrication, shown in this work as result of finite element simulations, is related to the spherical (or spheroidal) shape of the fullerenes that would allow them to behave as microscopic ball bearings. Thus, the author suggested that an additional rolling friction process could also play a role and enhance the good lubricating properties of the particles. According to the author, this process could play a more predominant role for well-crystallized particles, as also suggested by Tenne et al. [3].

Moreover, these nanoparticles would present higher mechanical resistance and would behave as genuine nano-ball bearings precluding gradual deformation and exfoliation. The resistance of the IF-MoS₂ to exfoliation was attributed to its good mechanical properties due to its well crystallized structure and the round shape of the particle. It is extremely difficult to attribute the only to the shear stress imposed to the particle. Adhesion forces must also be considered. In his work, Schwarz et al. [33] used a scaling approach based on continuum elasticity theory for shells and pairwise summation of Van der Waals interactions to investigate theoretically the effect of adhesion, pressure and shear on the deformation, and mechanical stability of spherical nanoparticles. This scientific work theoretically confirmed the possibility of delaminating of IF-MeS₂ (Me = metal) and they also showed that Van der Waals interactions cause strong adhesion to the substrate, which favors the release of delaminated layers onto the surface.

The author concluded from their simulations that rolling was an important lubrication mechanism for IF-MoS₂ in the relatively low range of normal stress (1-2 GPa). Sliding was shown to be relevant under slightly higher normal stress, where the spacing between the two mated surfaces does not permit free rolling of the nanoparticles. A uniaxial pressure higher than 2 GPa was necessary to crush the particles. In the light of the above fact it is possible to speculate that the nanoparticle rolls during the sliding until a certain limit for Y-displacement (contact pressure). When the nanoparticle overcomes this threshold it starts to deform heavily and exfoliate [16]. However, even if sliding is at the origin of the particle exfoliation, the adhesion forces between particles and the substrate may play a significant role in facilitating the exfoliation of the particles. These results are consistent with those obtained by Tevet et al [25] which suggest higher compression failure strength for spherical particles compared to faceted particle, and in Lahouji et al. [34] in which it was shown that the particles behave differently depending on experimental conditions. In some cases, rolling of the particle was clearly observed, whereas sometimes sliding of the particle occurred with or without an exfoliation process.

Moreover, the roughness strongly influences the sliding/rolling motion of the nanoparticle. Increasing the slope of the surface profile, due to its roughness, the space between the two steel surfaces decreases leading to a stronger deformation of the IF-MoS₂. The nanoparticle

assumes a more elliptical shape with a higher percentage of sliding compared to the results obtained for the perfectly smooth surfaces.

REFERENCES

- [1] Golan, Y., Drummond, C., Homyonfer, M., Feldman, Y., Tenne, R., Israelachvili, J., Microtribology and direct force measurements of WS₂ nested fullerene-like nanostructures. *Adv. Mater.* 11, 934–937, 1999
- [2] Rapoport, L., Feldman, Y., Homyonfer, M., Cohen, H., Sloan, J., Hutchison, J.L., Tenne, R., Inorganic fullerene-like material as additives to lubricants: structure-function relationship. *Wear* 975, 225–229 (1999)
- [3] Cizaire, L., Vacher, B., Le Mogne, T., Martin, J.M., Rapoport, L., Margolin, A., Tenne, R., Mechanisms of ultra-low friction by hollow inorganic fullerene-like MoS₂ nanoparticles. *Surf. Coat. Technol.* 160, 282–287 (2002)
- [4] Joly-Pottuz, L., Dassenoy, F., Belin, M., Vacher, B., Martin, J.M., Fleischer, N., Ultralow friction and wear properties of IF-WS₂ under boundary lubrication. *Tribol. Lett.* 18, 477–485 (2005)
- [5] Rosentsveig, R., Gorodnev, A., Feuerstein, N., Friedman, H., Zak, A., Fleischer, N., Tannous, J., Dassenoy, F., Tenne, R., Fullerene-like MoS₂ nanoparticles and their tribological behavior. *Tribol. Lett.* 36, 175–182 (2009)
- [6] L. Rapoport, Bilik, Y., Feldman, Y., Homyonfer, M., Cohen, S. R., Tenne, R., Hollow nanoparticles of WS₂ as potential solid-state lubricants. *Nature*.1997;387, 791–793.
- [7] Tannous, J., Dassenoy, F., Lahouij, I., Le Mogne, T., Vacher, B., Bruhacs, A., Tremel W., Understanding the Tribochemical Mechanisms of IF-MoS₂ Nanoparticles Under Boundary Lubrication *Tribol Lett* (2011) 41:55–64 63
- [8] Tannous, J., Dassenoy, F., Bruhacs, A., Tremel, W., Synthesis and tribological performance of novel Mo_xW_(1-x)S₂ (0 < x < 1) inorganic fullerenes. *Tribol. Lett.* 37, 83–92, 2010
- [9] Yadgarov, L., Petrone, V., Rosentsveig, R., Feldman, Y., Tenne, R., Senatore, A., Tribological studies of rhenium doped fullerene-like

- MoS₂ nanoparticles in boundary, mixed and elasto-hydrodynamic lubrication conditions, *Wear*, 297, 1–2, pp. 1103–1110, 2013
- [10] Deepak, F.L., Popovitz-Biro, R., Feldman, Y., Cohen, H., Enyashin, A., Seifert, G., Tenne, R., Fullerene-like Mo(W)_(1-x)Re_(x)S₂ nanoparticles. *Chem. Asian. J.* 3, 1568–1574 (2008)
- [11] Margolin, A., Popovitz-Biro, R., Albu-Yaron, A., Rapoport, L., Tenne, R., Inorganic fullerene-like nanoparticles of TiS₂. *Chem Phys Lett.* 2005, 411:162–166.
- [12] Lahouij, I., Dassenoy, F., de Knoop, L., Martin, J.M., Vacher, B., In situ TEM observation of the behavior of an individual fullerene-like MoS₂ nanoparticle in a dynamic Contact. *Tribol Lett.* 2011;42:133–140.
- [13] Tevet, O., Goldbart, O., Cohen, S.R., Rosentsveig, R., Popovitz-Biro, R., Wagner, H.D., Tenne, R., Nanocompression of individual multilayered polyhedral nanoparticles. *Nanotechnology*, 21, 365705–365711, 2010.
- [14] Feldman, Y., Frey, G.L., Homyonfer, V., Lyakhovitskaya, L., Margulis, L., Cohen, H., Hodes, G., Hutchinson, J.L, Tenne, R., Bulk synthesis of inorganic fullerene-like MS₂ (M= Mo,W) from the respective trioxides and the reaction mechanism. *J. Am.Chem. Soc.* 118, 5362-5367, 1996.
- [15] Rosentsveig, R., Margolin, A., Gorodnev, A., Popovitz-Biro, R., Feldman, Y., Rapoport, L., Novema, Y., Naveha, G., Tenne, R., Synthesis of fullerene-like MoS₂ nanoparticles and their tribological behavior, *J. Mater. Chem.*,19, 4368-4374, 2009.
- [16] Kaplan-Ashiri, I., Cohen, S.R., Gartsman, K., Ivanovskaya, V., Heine, T., Seifert, G., Tenne, R., Mechanical behavior of individual WS₂ nanotubes. *J. Mater.Res.* 19, 254, 2004.
- [17] Saavedra Flores, E.I., Adhikari, S., Friswell, M.I., Scarpa, F., Hyperelastic axial buckling of single wall carbon nanotubes, *Physica E* 4, 525–529, 2011.
- [18] Wang, Z.Q., Zhao, Y.P., Thermo-hyperelastic models for nanostructured materials, *Sci China Phys Mech Astron*, 54, 5, 2011
- [19] Qian, D., Wagner, G.J., Liu, W.K., Yu, M., Ruoff, R.S., Mechanics of carbon nanotubes, *Appl Mech Rev* 55, 6, 2002
- [20] Rivlin, R.S., Large elastic deformations of isotropic materials. IV. Further developments of the general theory. *Philosophical*

- Transactions of the Royal Society of London. Series A, Mathematical and Physical Sciences, 241(835) 379-397, 1948
- [21] Djeridi, R., Ouali, M.O., Numerical Implementation and Finite Element Analysis of Anisotropic Hyperelastic Biomaterials - Influence of Fibers Orientation, *Key Engineering Materials*, 554 - 557, pp. 2414-2423, 2013
- [22] Simo, J.C., Laursen, T.A., An augmented lagrangian treatment of contact problems involving friction, *Computers & Structures*, 42, 1, pp. 97-116, 1992.
- [23] Simo, J.C., Wriggers, P., Taylor, R.L., A perturbed Lagrangian formulation for the finite element solution of contact problems, *Computer Methods in Applied Mechanics and Engineering*, 50, 2, pp. 163-180, 1985.
- [24] Kogovsek, J., Remskar, M., Mrzel, A., Kalin, M., Influence of surface roughness and running-in on the lubrication of steel surfaces with oil containing MoS₂ nanotubes in all lubrication regimes. *Tribology International* 61, 40-47, 2013.
- [25] Kalin, M., Kogovsek, J., Remskar, M., Mechanisms and improvements in the friction and wear behavior using MoS₂ nanotubes as potential oil additives, *Wear*, 280-281, pp. 36-45, 2012
- [26] Kogovsek, J., Remskar, M., Kalin, M., Lubrication of DLC-coated surfaces with MoS₂ nanotubes in all lubrication regimes: Surface roughness and running-in effects, *Wear*, 303, 1-2, pp. 361-370, 2013
- [27] Lahouij, I., Dassenoy, F., Vacher, B., Martin, J.M., Real time TEM imaging of compression and shear of single fullerene like MoS₂ nanoparticle, *Tribol Lett* 45, 131-141, 2012.
- [28] Jiang, Z., Liu, X., Bu, J., Contact Simulation of Thrust Ball Bearing Based on ANSYS *Advanced Materials Research*, 154 - 155, pp. 1629-1633, 2010.
- [29] Lahouij, I., Vacher, E., Martin, S.M., Dassenoy, F., IF-MoS₂ based lubricants: influence of size, shape and crystal structure, *Wear*, 296, 1-2, 558-567, 2012.
- [30] Lahouij, I., Bucholz, W., Vacher, E., Sinnott, B., Martin, S.M., Dassenoy, F., Lubrication mechanisms of hollow-core inorganic fullerene-like nanoparticles: coupling experimental and computational works, *Nanotechnology*, 23,37, 375701, 2012.
- [31] Feldman, Y., Frey, G.L., Homyonfer, V., Lyakhovitskaya, L., Margulis, L., Cohen, H., Hodes, G., Hutchinson, J.L., Tenne, R.,

- Bulk synthesis of inorganic fullerene-like MS₂ (M= Mo,W) from the respective trioxides and the reaction mechanism. *J. Am.Chem. Soc.* 118, 5362-5367, 1996.
- [32] Tevet, O., Von-Huth, P., Popovitz-Biro, ., Rosentsveig, R., Daniel, H., Tenne, R., Friction mechanism of individual multilayered nanoparticles, *PNAS* | December 13, 2011 | vol. 108 | no. 50 | 19901–19906.
- [33] Schwarz, U.S., Komura, S., Safran, S.A., Deformation and tribology of multi-walled hollow nanoparticles, *Europhys. Lett.*, 50, 6, pp. 762–768, 2000.
- [34] Lahouij, I., Dassenoy, F., de Knoop, L., Martin, J.M., Vacher, B., In situ TEM observation of the behavior of an individual fullerene-like MoS₂ nanoparticle in a dynamic Contact. *Tribol Lett.* 2011, 42:133–140.

CHAPTER 6

Conclusions

Most of lubricant oils at present contain several critical lubricant additives, including antiwear additive, dispersant, detergent, friction modifier, viscosity index improver and antioxidant. Traditionally, lubricant oils are presented as a single phase material in order to maintain a good consistency and dispersibility of the lubricant additives in the base oil. However, a great amount of research has been focused on introducing solid particles as a friction reduction or antiwear lubricant additive over recent years due to a number of incomparable advantages of the two-phase lubricant oils (liquid-solid), such as the superior thermal conductivity, the high pressure standing ability, high resistance to decomposition at temperature, low environmental impact, etc. Some of the solid lubricant additives, particularly in nano or submicron size, have even demonstrated better tribological performances than the traditional organic additives, Zinc dialkyldithiophosphates (ZDDP) for instance.

In this Ph.D. dissertation, several tests have been carried out on samples formulated with organic and inorganic nanoparticles as lubricant and grease additives in order to investigate their tribological performances in terms of friction and wear. Furthermore, in the aim of a better understanding of the nanoparticle lubrication mechanism and the piezoviscosity effect of the lubricant numerical simulations have been also performed.

The tribological tests presented in Chapter 2 confirm the scientific literature observations that the performance of base oils formulated with organic and inorganic nanoparticles as solid lubricants, lead to significant reduction in both friction and wear in both boundary and mixed lubrication regimes under severe test conditions. The first part of the Chapter 2 showed the role of the intrinsic properties of MoS₂ and WS₂ nanoparticles on their lubricating properties. In a lubrication test in presence of steel surfaces, it was shown that the MoS₂ nanoparticles containing defects were much easier exfoliated than the perfect structures.

The ability of the particles to exfoliate is directly related to the fast formation of a tribofilm made of MoS₂ nanosheets that protects the surface against wear and contributes to reduce friction. The exfoliation of perfect nanoparticles is more difficult and consequently there is a progressive decrease of the friction coefficient in the friction test.

For all the tested samples, the CoF showed a tendency to decrease with increasing contact pressure. Additionally, in all studied samples the CoF increased with the temperature.

Their small size and round like configuration facilitates their access to the tribological interface. Another important contribution to the lower CoF and WSD is due to the “mending effect”, i.e. the healing of the surface during the tribological test. This effect can be attributed to a series of mechano-chemical phenomena which lead to smoothing of the surface during the test. For instance, with average contact pressure of 1.68 GPa and temperature in the range 25-80 °C, the average CoF decreased by more than 40% compared with the base lubricant value.

In the chapter it has been also shown that the best results for the samples formulated with inorganic nanoadditives were achieved by the inorganic fullerene-like nanoparticle of molybdenum disulphide doped with rhenium. Using IF-WS₂ nanoparticles also resulted in rather low friction and wear, however the tendency for agglomeration and oxidation is an important disadvantage when compared to the Re doped IF. It is noteworthy to mention that all the rhenium doped nanoparticles dispersed in the lubricant did not require chemical activation and show a clear effect already at room temperature.

On the other hand, the tribological tests performed on the samples formulated with carbon-based additives, such as graphene oxide (GO) platelets and graphite showed a remarkable effect in terms of friction wear parameters reduction. Moreover, a tribological film of reduced GO nanosheets after the tribological test covers the ball wear scar.

The good friction and anti-wear properties of graphene sheets may possibly be attributed to their small structure and extremely thin laminated structure, which offer lower shear stress and prevent interaction between metal interfaces. The results clearly prove that graphene platelets in oil easily form protective deposited films to prevent the rubbing surfaces from coming into direct contact and, thereby, improve the entirely tribological behaviour of the oil.

In Chapter 3 the tribological effects of nanoparticles dispersions in

Calcium and Lithium based greases have been investigated. For the samples formulated with inorganic fullerene like nanoparticles the tribological results showed a marked decreasing in friction coefficient both in boundary and mixed/EHL lubrication regimes achievable through dichalcogenides nanosheets dispersion. Actually, remarkable results have been achieved by the synthesis and the tribological test of a new hybrid organic–inorganic nanocomposite, made by an organic core of CNT covered by MoS₂ nanosheets. This kind of hybrid nanostructures conjugates and enhances, through a unique synergy, the performances of CNT and nanochalcogenides, with the organic coating that promotes the compatibility in a-polar matrix (solvent, oil, grease).

In Chapter 4 the pressure and film thickness variations in one and two dimensional contacts and the numerical results in EHL simulation using a Full MultiGrid approach with different pressure-viscosity relationship for the lubricant has been presented. In the simulations, the Roelands model, usually used for modelling the pressure-viscosity relationship of the lubricants, has been observed to fail in capturing the real film thinning behaviour while the more realistic pressure–viscosity relationship described by the Yasutomi-Doolittle free-volume model yields results very close to the experimental literature data, with a higher value of viscosity in the low pressure area than those obtained by the Barus and Roelands models. Higher viscosity in the low-pressure area results in a larger central film thickness. The fact that film thickness is formed mainly by the entraining action at the inlet area significantly weighs the importance of viscosity variation from different models in this area. This finding can help explain the inconsistency between experiment data and simulation results encountered in the past, where the computed film thickness was always smaller than the corresponding experimental value. It was also found that the film thickness becomes thicker using the free-volume model and the pressure spike magnitude increases significantly.

The second part of the Chapter has analyzed in detail the influence of roughness parameters on the pressure and film thickness variations using a more realistic model to describe the lubricant piezoviscosity based on the free volume model developed by Doolittle and improved by Yasutomi firstly and Bair, later. The simulations showed the advantages of a quick and comprehensive analysis of the roughness parameters effect on the behavior of film thickness and pressure in

lubrication EHL, showing also that roughness plays a pivotal role in deciding the tribological behavior of the contacting surfaces, in particular by skewness and kurtosis.

The lubrication mechanism and the mechanical behavior of a spherical MoS₂ nanoparticle between steel surfaces have been investigated in Chapter 5 by means of finite element simulations. From the presented results it is possible to observe hollow-core nanoparticles are therefore able to withstand higher external loads compared to bulk nanoparticles due to its structure and mechanical behavior. Furthermore, hollow nanoparticles are subjected to significantly higher value of shear stresses than bulk ones at the same contact pressure. This means that the hollow-core nanoparticles will tend to exfoliate and lose the outer layers of its laminar structure at significantly lower values of loads. Therefore, the thin layer nanoparticles promote exfoliation lubrication mechanisms.

The hollow-nanoparticle, also, shows a greater percentage of deformation that leads to a significantly higher slide to roll ratio compared to the bulk nanoparticle. Actually, by considering that much higher shear and sliding motion are induced to hollow-core particles, this will result in significantly higher exfoliation rate and deposition of MoS₂ sheets at the tribological contact surfaces, thus enable formation of the MoS₂ tribofilm, which reduces friction and wear.

Accordingly, the possible lubrication mechanism, shown in this work as result of finite element simulations, is related to the spherical (or spheroidal) shape of the fullerenes that would allow them to behave as microscopic ball bearings. Thus, the author suggested that an additional rolling friction process could also play a role and enhance the good lubricating properties of the particles. This process could play a more predominant role for well-crystallized particles.

Furthermore, the roughness strongly influences the sliding/rolling motion of the nanoparticle. Increasing the slope of the surface profile, due to its roughness, the space between the two steel surfaces decreases leading to a stronger deformation of the IF-MoS₂. The nanoparticle assumes a more elliptical shape with a higher percentage of sliding compared to the results obtained for the perfectly smooth surfaces.

ANNEX A

PAPERS ON INTERNATIONAL JOURNALS:

1. Oil lubricant tribological behaviour improvement through dispersion of few layer graphene oxide. **Journal of Nanoscience and Nanotechnology**, ISSN: 1533-4880, 2013 (accepted for publication).
2. New 'chimie douce' approach to the synthesis of hybrid nanosheets of MoS₂ on CNT and their anti-friction and anti-wear properties. **Nanotechnology**, Vol. 24, 12, 2013.
3. Experimental Investigation of the Tribological Effects of Radial Grooves on Slider Bearings. **International Journal of Mechanical Engineering and Industrial Design**, Volume 2(1): 2013, pp. 1-6, ISSN: 2280-6407, 2013.
4. Tribological studies of rhenium doped fullerene-like MoS₂ nanoparticles in boundary, mixed and elasto-hydrodynamic lubrication conditions. **Wear**, Vol. 297, 1–2, pp. 1103–1110, 2013.
5. Effect of an improved Yasutomi pressure-viscosity relationship on the elastohydrodynamic line contact problem, **ISRN Tribology**, Volume 2013, Article ID 149451, 7 pages, 2013. doi:10.5402/2013/149451, 2013.
6. Graphene Oxide Nanosheets as Effective Friction Modifier for Oil Lubricant: Materials, Methods, and Tribological Results. **ISRN Tribology**, Volume 2013, Pag.1-9 ISSN:2090-889X, 2013.

7. Effects of the lubricant piezo-viscous properties on EHL line and point contact problems. **Tribology Letters**, Vol.49, pp. 385–396, 2013.
8. Experimental investigation and neural network prediction of brakes and clutch material frictional behavior considering the sliding acceleration influence. **Tribology International**, vol. 44, no. 10, pp. 1199-1207, 2011.

PAPERS IN CONFERENCE PROCEEDINGS:

1. The influence of the roughness parameters on the EHL line contact using the free volume model. **ASME 2013- International Mechanical Engineering Congress and Exposition**. Edited by: American Society of Mechanical Engineers, San Diego, USA, 2013
2. On the friction reduction mechanism introduced by graphene nanosheets as additive in oil lubricated contacts. **Proceedings of the World Tribology Congress 2013** - Edited by: AIT - Italian Association of Tribology (ISBN: 9788890818509), Torino, Italy, 2013.
3. Finite element analysis of IF-MoS₂ deformation under uniaxial compression and shear between real nanorough surfaces. **International Workshop Multi-Scale Modeling and characterization of Innovative Materials and Structures**. Edited by: Università di Salerno, Cetara, Amalfi Coast, Italy, 2013.
4. The influence of piezo-viscous lubricants on EHLline and point contact problems. **ASME 2012- International Mechanical Engineering Congress and Exposition**. Edited by: American Society of Mechanical Engineers, Houston, USA, 2012.
5. Tribological behavior of graphene nanosheets as a lubricant additive. **Proceedings of the 15th International Conference on**

Experimental Mechanics ICEM15 - Edited by: Prof. Ferreira, INEGI Edicoes, (ISBN: 978-972-8826-25-3), Porto, Portugal, 2012.

6. Influence of surface roughness and piezo-viscous lubricant properties on the EHD line contact lubrication. **Proceedings of Proceedings of ECT 2012, the Eighth International Conference on Engineering Computational Technology**, (ISSN: 1759-3433, ISBN: 978-1-905088-55-3), Dubrovnik Croatia, 2012.
7. Friction and wear performances of lubricating greases with inorganic nanoadditives. **AIT Workshop - Italian Association of Tribology**, Milano, Italy, 2012.
8. Tribological and rheological behavior of lubricating greases with nanosized inorganic based additives. **3rd European Conference on Tribology ECOTRIB 2011-VIENNANO 2011** - Edited by: F Franek, WJ Bartz, A Pauschitz, J Vizintin, E Ciulli, R Crockett. 903-908 OETG (ISBN: 978-3-901657-38-2), Vienna, Austria 2011.
9. Testing dry sliding contacts for brakes and clutch applications. **Proceedings of Proceedings of ECT 2010, the Seventh International Conference on Engineering Computational Technology** Edited by: B.H.V. Topping, J.M. Adam, F.J. Pallarés, R. Bru and M.L. Romero, (Editors), Civil-Comp Press, Stirlingshire, Valencia, Spain, 2010.

POSTERS:

1. Nanosized molybdenum disulphide as affective additive for lubricant grease: synthesis, rheological and tribological characterization. **NanotechItaly**, Venezia, Italy, 2011.

-
2. Tribological and rheological properties of tungsten disulphide nanosheets as additive in lubricant mineral. **NanotechItaly**, Venezia, Italy, 2010.